Three dimensional mechanical mapping of nano- and bio-composite materials using a combination of AFM and FIB

Russell John BAILEY

Submitted in partial fulfilment of the requirements of the Degree of

Doctor of Philosophy

I, Russell John BAILEY, confirm that the research included within this thesis is my own work or that where it has been carried out in collaboration with, or supported by others, that this is duly acknowledged below and my contribution indicated. Previously published material is also acknowledged below.

I attest that I have exercised reasonable care to ensure that the work is original, and does not to the best of my knowledge break any UK law, infringe any third party's copyright or other Intellectual Property Right, or contain any confidential material.

I accept that the College has the right to use plagiarism detection software to check the electronic version of the thesis.

I confirm that this thesis has not been previously submitted for the award of a degree by this or any other university.

The copyright of this thesis rests with the author and no quotation from it or information derived from it may be published without the prior written consent of the author.

Signature: Russell John BAILEY

Date:20/06/2016

Details of collaboration and publications:

Bailey, R.J., et al., Evaluating focused ion beam induced damage in soft materials. Micron, 2013. 50: p. 51-56

Bailey, R.J., et al., Extending AFM Phase Image of Nanocomposite Structures to 3D using FIB. MRS Online Proceedings Library Archive, 2012. 1421: p. mrsf11-1421-pp07-09

Abstract

Composites used in engineering applications are being made from smaller and smaller component phases; from macroscopic through micro- to nanometre length-scales. This trend has led man-made composites to mimic the length-scales and structures that biocomposites have developed in nature through millions of years of evolution. Biocomposites have evolved to perform specific engineering functions, such as piercing and grinding with wear resistance, impact resistance, and compressive load bearing. This work aims to map the 2D and 3D mechanical distribution in composite structures with a broad variation in localised stiffness in order to better understand the links between short and long scale mechanical performance.

The approach undertaken in this work is to explore the use of Atomic Force Microscopy (AFM) to probe the mechanical performance of a specimen surface. The AFM can build a 2D map of the variation in contact stiffness at a resolution of the order of nanometres. Focussed Ion Beam (FIB) is used to precisely mill flat surfaces into specimens, which allows for the 2D mechanical mapping to be conducted on a flat plane. Quantitative AFM phase imaging is exploited to evaluate the elastic modulus variations on a simple FIB prepared nano-layered polymer composite surface, with variations in the elastic modulus exhibiting a bimodal distribution that is representative of the two polymers in the composite. Further demonstration of quantitative AFM phase imaging is made by evaluating the layered nanocomposite structure of snail shell. Extension of 2D nanomechanical imaging to 3D is presented by using FIB followed by subsequent AFM imaging to provide a stack of 2D AFM phase information that is reconstructed into a 3D map. This work therefore provides methods to systematically translate AFM phase information into quantitative elastic modulus measurements in 2D and 3D using FIB preparation, with examples of engineering and biological nanocomposites highlighting broad applicability.

Table of Contents

1 Introduction 1
2 Literature Review 2
  2.1 Atomic Force Microscopy 2
  2.2 Focussed Ion Beam 11
  2.3 Model materials 24
3 Materials and Methods 34
  3.1 Preparation of sample materials 34
  3.2 Atomic Force microscopy 39
  3.3 Clamping sample holder for AFM and SEM 69
  3.4 Secondary electron microscopy 71
  3.5 Preparation of FIB milled cross-sections 77
  3.6 Tensile testing 86
4 Assessing FIB damage in soft materials 88
  4.1 Phase contrast AFM 88
  4.2 EDS analysis 94
  4.3 Conclusions 97
5 Quantifying the phase signal 98
  5.1 Aims 98
  5.2 Background 101
  5.3 Methodology and Results 115
  5.4 The effect of reduced contact modulus on AFM phase 131
  5.5 Conclusions 132
6 Quantitative phase imaging of nanocomposite materials 131
  6.1 Aims 131
  6.2 Preparation of a model polymer nanocomposite 131
  6.3 AFM phase imaging of the nanocomposite 133
  6.4 AFM Force-distance measurements of a polymer nanocomposite 140
  6.5 Measurement of elastic modulus of polymer nanocomposite by tensile testing 151
  6.6 Comparison of results from different measurement techniques 155
7 Imaging a bio-composite 159
  7.1 Introduction 159

7.2 Experimental ... 164
7.3 Results ... 171
7.4 Discussion ... 176
7.5 Conclusions ... 179
8 Three dimensional reconstruction of a nanocomposite ... 180
8.1 Aims ... 180
8.2 Introduction ... 180
8.3 Experiment ... 181
8.4 Results ... 184
8.5 Conclusions ... 186
9 Conclusions ... 188
References ... 189
Appendix ... 195
MatLab code for simulating AFM cantilever dynamics and calculating phase lag ... 196
Python code for calculating Force/Displacement and moduli from AFM deflection/distance data ... 205

1 Introduction

Materials characterisation is a field of study that is critically important in both the development of high performance engineering materials, and in the understanding of naturally evolved structures. The increase in utilisation of nanocomposite and biomimetic materials has meant that in order to fully understand their function and behaviour, there is an increased demand for higher resolution analytical techniques. Atomic Force Microscopy is one such technique that can achieve near atomic resolution whilst sampling a range of signals, including topography, frictional force, electrical conductance, magnetic domains and contact stiffness. A limiting factor of AFM, however, is that it is surface specific, and therefore cannot tell us about bulk behaviour.

Another developing microscopic technique is the Focused Ion Beam microscope, which utilises positively charges ions to image in much the same way as a Scanning Electron Microscope, but because the ions carry significantly more momentum than an electron, they cause the specimen atoms to sputter from the surface. By taking advantage of the destructive nature of the accelerated ion beam, it can be used to machine specimens and produce cross-sections.

The aim of this work is to develop a way of quantifying the phase contrast AFM image, so that the contact stiffness and Young's modulus can be extracted, to assess the damage caused by the FIB when machining soft materials, and to utilise the FIB to take serial cross-sections and extend AFM data into 3 dimensions.

2 Literature Review

2.1 Atomic Force Microscopy

2.1.1 Origins and development of the AFM

Atomic Force Microscopy (AFM) is a scanning probe technique that was originally developed in 1986 by Binnig, Quate and Gerber [1]. They were interested in developing a method to measure the ultra-small forces that existed between particles as small as individual atoms and overcome the obvious drawback with the scanning tunnelling microscope (STM) [2]; that it can only image conducting samples. In their original AFM this was achieved using a diamond tip mounted on a gold foil cantilever to probe the sample surface; the gold cantilever in turn became the sample for an STM probe, which was used to monitor its deflection. As the sample was scanned under the diamond tip a feedback system maintained the tunnelling current between the cantilever and the STM probe by altering the z position of the AFM sample and maintaining the force on the cantilever. This movement in z was used to build the 3D topographical images of the surface.

AFM was shown to be able to achieve atomic resolution, with Binnig et al publishing images of graphite [3]. Marti et al, as well as producing atomic resolution on graphite, were able to resolve monatomic steps on an oil covered sample of sodium chloride [4]. Perhaps more importantly, Albrecht used AFM to produce atomic resolution images of the surface of highly oriented pyrolytic boron nitride, which is a non-conducting sample [5]. This demonstrated that AFM could fill the gap left by STM.

AFM has since become a popular tool for the atomic and nanometre scale characterisation and manipulation of a wide variety of samples. It has been continually used to image hard surfaces of both conducting and non-conducting samples with atomic resolution [3-8]. And

with the

introduction of dynamic or “tapping mode” [9] (Described in section 2.1.2.5) the AFM has been successful at imaging soft materials with high resolution, such as polymers [10], membrane bounded proteins [11], isolated proteins [12] and even DNA [13]. But AFM’s uses aren’t limited to imaging. Because it’s basic function is the detection of small forces with high resolution it is very effective at performing micro and nanomechanical tests. This has been demonstrated through tensile and composite fibre pull-out tests [14] and its use as a nanoindenter [15].

2.1.2 Imaging modes

There are several ways in which the AFM can be operated depending on the type of sample being studied and/or the information that is to be examined. They all involve monitoring an interaction between the sample and the tip, which is used as the parameter for a feedback loop that controls the stage/head position in the z direction. The parameter used is dependent on the mode, but the feedback loop will move the stage/head up and down to maintain a user defined value, termed the “set point”. The x and y stage/head directions are used in imaging to scan the tip relative to the sample in a raster pattern, sampling each data point in sequence.

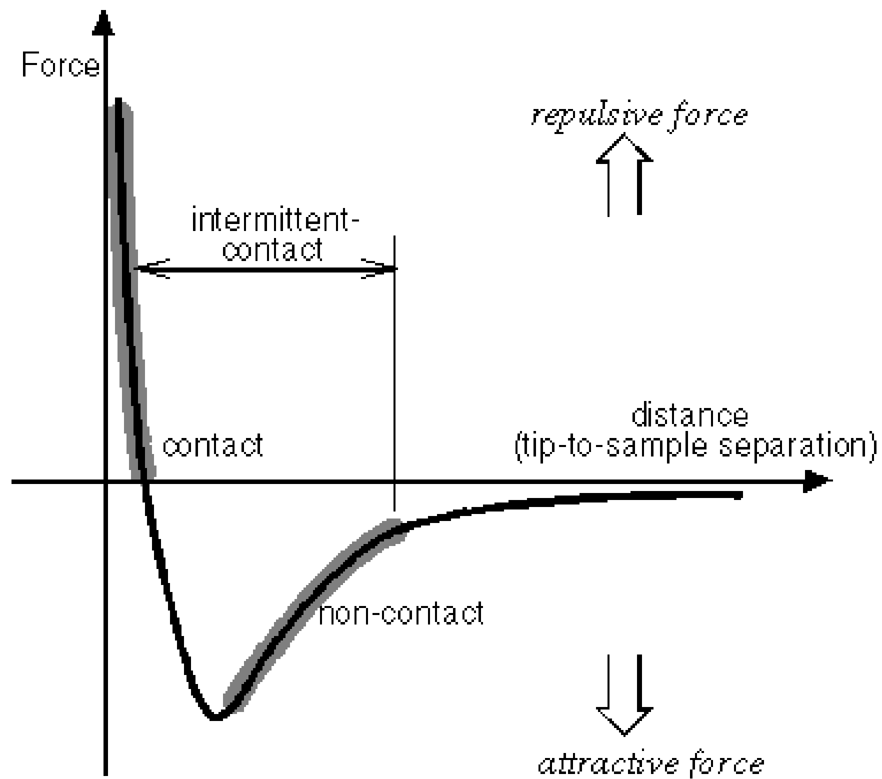

Figure 2.1 Lennard-Jones Force plot

The different modes take advantage of the different attractive and repulsive forces that the tip experiences as it approaches the sample.

Figure 2.1 is a Lennard-Jones plot that shows forces influencing the AFM cantilever, and highlighted are the regions of the curve that are utilised in each mode.

2.1.2.1 Contact

In contact mode the tip is lowered onto the sample until a set level of cantilever deflection is achieved. The deflection of the cantilever away from the sample is typically used as the setpoint. Therefore, a repulsive sample-AFM interaction is examined using contact mode AFM. Cantilevers of low spring constant (~0.01 N/m) are used in order to minimise the applied load on the sample. The sample or tip is then scanned in a raster pattern within the x-y plane in order to form a sample's image using piezoelectric positioners. As the sample is being scanned

the feedback loop maintains the deflection, and therefore the applied force, by moving either the stage or scan head in the z direction. This movement in z is used to provide the height information in the topographical image [1]. Another useful way of imaging in this mode is contact error, which displays the actual deflection during feedback and provides enhanced edge contrast.

2.1.2.2 Lateral force

Lateral force microscopy (LFM) measures the frictional forces on the surface [16]. It is a contact technique, but it is the torsion of the cantilever that is measured during the scan, rather than the deflection. Using this technique, it is possible to obtain qualitative contrast between areas of higher or lower friction.

2.1.2.3 Non-contact

Non-contact mode (or Frequency Modulation AFM, FM-AFM) is the first mode that relies on the cantilever being oscillated [17]. The frequency of the oscillating cantilever is used as an input signal in order to define a setpoint value during imaging. The natural resonance frequency of the cantilever is monitored as the sample is brought closer to the oscillating tip using a z-piezo positioner. The oscillating AFM tip will begin to interact in the attractive regime of the Lennard-Jones curve, resulting in a shift in the resonance of the AFM cantilever and the feedback loop will vary the tip-sample distance in order to maintain a set frequency shift. Selection of a suitable setpoint can allow the AFM tip to oscillate close to the surface without actually contacting. The forces between the sample and tip are of the order of pN, and detection is based on measuring changes in the resonant frequency of the cantilever whilst the amplitude remains constant. Using FM-AFM it is possible to achieve true atomic resolution whilst in Ultra-high vacuum (UHV).

2.1.2.4 Force modulation

Force modulation is a method used to probe material properties through tip/sample interactions. The cantilever, or in some cases the sample, is driven to oscillate at high frequency and then pushed into the repulsive regime. The slope of the resultant force distance curves are measured and correlated to the elasticity of the sample [18].

2.1.2.5 Dynamic AFM

In tapping or semicontact mode (also known as Amplitude Modulated AFM, AM-AFM) the cantilever is driven at or near to its resonance frequency. The motion of the cantilever can be considered as sinusoidal with an amplitude and a phase lag with respect to the driving force. Typically, the amplitude of the oscillation is monitored and used as the parameter for the feedback loop. Figure 2.2 shows the response of amplitude and phase angle to increasing tip sample interaction. (a) is representative of the freely oscillating cantilever while the tip and sample are far apart; the peak amplitude is at resonance (represented by the vertical line) and the phase angle at resonance is 90° (represented by the horizontal line). In (b) the sample has been moved towards the tip until the amplitude dropped to 70% of the free amplitude (A0), whilst oscillating at resonance. The amplitude plot shows a cut-off and the resonance has shifted to the left; which can be seen more clearly from the phase angle plot and would suggest that the AFM is operating in the attractive regime. As the sample is brought closer (c & d) the amplitude peak broadens and shifts to the right along with the phase angle curve.

If the cantilever is driven at its resonant frequency, then this apparent drop in amplitude can be monitored by the AFM software and used to determine the separation of the tip and sample. By choosing a set point amplitude (Asp) and using it as the parameter for the feedback loop, the software will alter the separation in response to changing topography, so as to maintain Asp.

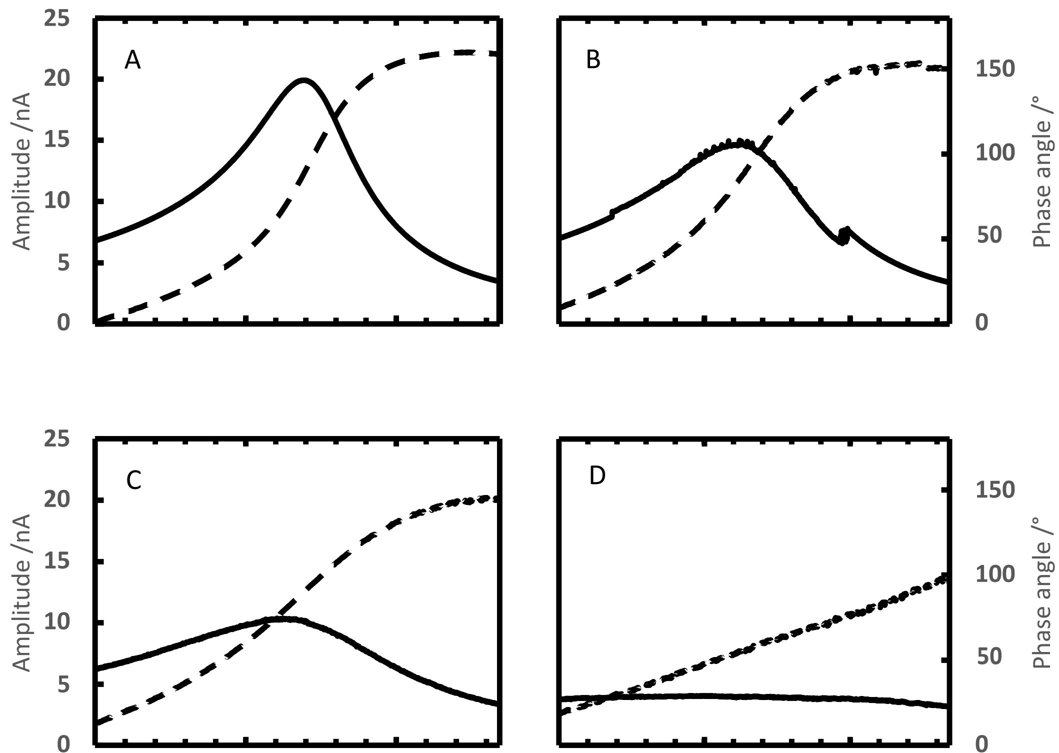

Figure 2.2 Amplitude vs. frequency (solid) and phase angle vs. frequency (dotted) recorded at different set point ratios. a) Asp/A0 = 1 b) Asp/A0 = 0.7 c) Asp/A0 = 0.5 d) Asp/A0 = 0.2.

Unlike FM-AFM, AM-AFM is operated in the repulsive regime; the tip makes intermittent contact with the surface and the average interaction is repulsive. As with contact mode the topographical information is provided by the signal from the z positioner as it responds to the feedback system. Again there are other imaging modes that can be employed. Similar to contact error, semicontact error records the actual amplitude that is being measured under feedback, giving enhanced edge contrast. Another mode of imaging that is available whilst in semicontact mode is phase contrast imaging, which is of particular interest in this report and will be looked at in more detail.

Tapping mode AFM has advantages to contact mode in that the lateral forces that occur when in contact are virtually eliminated [9]. This leads to improved lateral resolution and reduced damage to soft materials. As a result, this mode of operation has become a favoured

technique among biologists because of its ability to produce high resolution images of organic materials without the need for staining, fixing or UHV [11, 12].

2.1.2.6 Phase contrast AFM

Phase imaging is a technique that utilises the AM-AFM mode of operation and can be performed whilst recording topography simultaneously. In AM-AFM the motion of the tip can be considered to be (almost) sinusoidal; with amplitude that's maintained under feedback and a phase lag with respect to the external driving force. This oscillation can be described by

$$z = A\cos(\omega t - \varphi)$$

Equation 1

During imaging the phase lag is monitored and recorded while the amplitude remains fixed. The relationship between phase shift and the driving frequency is given by the equation

$$\tan\varphi = \frac{\omega . \omega_0 / Q}{\omega_0^2 - \omega^2}$$

Equation 2

This shows that when driven at resonance the phase lag is 90°. The shift in phase lag can be attributed to a number of factors including adhesion, contact area and contact modulus. Measures can be taken to place emphasis on any particular property of interest, and this report is interested in using the phase shift to measure the contact modulus between the sample and the tip. It has been shown that high amplitude is favourable, as this gives the tip more energy to overcome any adhesion. Also, a low set point ratio (i.e. set point amplitudes equal to ~50% of the free amplitude) means that there is increased interaction and a greater dependence on modulus [19, 20]. As with the other AFM imaging modes, the variation of

phase across a sample can be measured using raster scanning of the tip or sample. The tip moves in the x-y plane across the sample's surface in a semi-contact imaging mode. However, the phase shift at each point on the sample's surface during the semi-contact imaging can be used as a z-coordinate to produce a resultant phase image. Figure 2.3 gives an example phase imaging, which has been used to observe the layers in a laminate film of polypropylene containing both high and low elastic modulus layers. The topography image in Figure 2.3a shows a relatively rough surface with no indication of the sample being a laminate, while the phase image in b shows distinct light and dark bands that range from 150 – 1000nm across. The differing colourations indicate variations in the phase shift when the AFM-tip is in semi-contact with the sample.

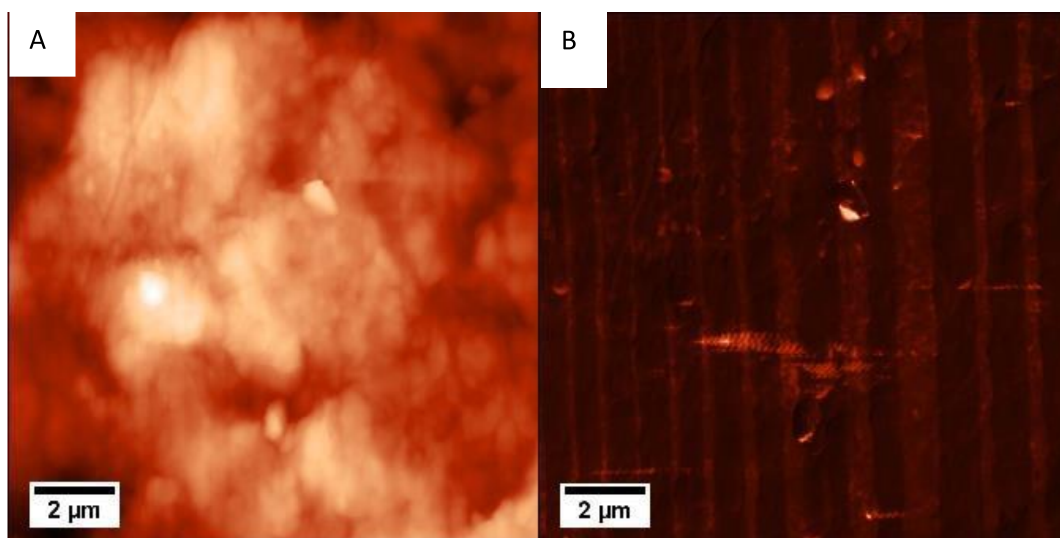

Figure 2.3 Comparison of AFM topography and phase contrast imaging. A) Topography image showing surface roughness, with little indication of the laminate structure. B) Phase contrast image highlighting the variation in contact stiffness of the surface and the laminate structure of the composite.

At the moment phase imaging is only a qualitative measurement of the stiffness of a sample due to the complex motion of the cantilever and a number of factors that affect the contrast. However, some efforts have been made to model the motion of the tip during AM-AFM and to relate material properties to the phase signal [20-23].

2.2 Focussed Ion Beam

2.2.1 The origins of FIB

The Focused Ion Beam (FIB) microscope is a powerful tool with a wide range of applications including secondary electron imaging, secondary ion imaging, material deposition, sample sputtering/etching, ion spectroscopy, material doping and resist development.

As early as the 1960s high energy ion guns have been used for the fine polishing of material surfaces, such as those of optical lenses[24] and, at a much smaller scale, for the thinning of Transmission Electron Microscope (TEM) samples.[25-27] A typical ion polishing system for TEM sample preparation will utilise Ar^{+} ions from two Penning ionisation sources, set at shallow angles of incidence (1 - 10°), to sputter away the surface of the sample and produce an electron transparent section at thicknesses of the order of 100 nm.

In the 1970s the first field emission ion sources were developed for FIB applications.[28-30] These ion sources were developed for the semiconductor industry in order to use FIBs for maskless doping of surfaces. The original field emission ion sources used gas phase field ionisation, whereby the neutral gas of the element to be ionised is fed to the tip of a sharp electrode. A large positive potential is applied to the electrode and the high field strength, due to the sharpened tip, causes tunnelling of electrons from the gas atoms, and repulsion of the generated ions. In 1974, Seliger and Fleming demonstrated a FIB system that could achieve a spot size of 3.5 µm at a beam energy of 60 keV, which would be suitable for maskless doping.[31]

At about the same time, interest in FIB systems grew as an alternative to electron beam lithography (EBL) of resist layers in microfabrication. The achievable pattern resolution when using an electron beam for exposure is limited by the proximity effect,[32, 33] which causes a broadening of the distribution of the exposure dose as a result of the electron beam's

interaction with the resist layer and substrate. This will cause an uneven exposure of the desired pattern and a non-zero exposure at the edges. The broadening of the dose distribution occurs because as the electron beam passes through the light resist layer there will be low angle deflection of the beam, and when the beam reaches the substrate (likely to be heavier nuclei) there will be backscattering of the primary electrons as well as secondary electron production.

Ions are intrinsically higher resolution because they do not suffer from the proximity effect, produce secondary electrons of only very low energy and field emission ions have an order of magnitude shorter wavelength then Field-emission Electron Sources (FES).[34, 35] Ion beams suffer less lateral- and back-scattering than electron beams and sensitivity is increased due to higher deposited energy density.[36]

An important development in FIB technology was that of the Liquid Metal Ion Sources (LMIS). The LMIS is capable of producing beams with greater brightness and a higher current density than the standard field ionisation or duoplasmatron sources,[37, 38] which allows them to achieve higher sputtering rates and higher resolutions. LMISs utilise the principle of field evaporation from a liquid surface, whereby the application of a strong electrical field reduces the potential barrier and atoms/ions evaporate. Atoms that evaporate are then ionised in the field at the source tip. LMISs use either a crucible or needle point source, coated which the ion source liquid, which is fed to the tip from a reservoir. However, a tungsten needle point is generally preferred as it offers greater beam stability.[35, 39]

Field evaporation occurs upon application of an extracting voltage to the sharp source needle, which results in a large electric field of the order of 1×10^{8} V.cm^{-1}. The liquid metal in the presence of the extraction field distorts and balances the effects of surface tension and the electrostatic forces by forming a Taylor cone.[40] Taylor cones stabilise at a half angle of 49.3° and a further increase in field strength begins the field evaporation process.

It was found by Komuro and Kawakatsu in 1981 that if a bias electrode was introduced around the source needle that this could be used to stabilise the emission current,[41] and this also allowed the current to be varied whilst maintaining a constant beam energy.[42]

The metal used in a LMIS should ideally have a high surface tension and a low vapour pressure at melting. A number of potential metals have been trialled, however it was shown by Krohn and Ringo in 1975 that gallium offers the highest brightness and the greatest suitability compared to caesium and mercury; having an effective source size of 200 nm.[43] Since then the majority of LMIS FIB study has focused on the use of gallium as the metal ion source. Improved ion optics led to gallium ion beams that could be focused to 100 nm with a brightness of 1.5 $A.cm^{-2}$,[44, 45] and continued development into the 1990s produced probe sizes of sub 50 nm[46, 47] until reaching todays reported ion beam resolution of 5 nm.[48]

The Taylor cone formation in gallium has been observed by a number of researchers in order to understand the dynamics of liquid metal field evaporation. In 1981 Wagner *et al.* reported a cone formation with a radius of curvature of 350 Å, when operating at an emission current of 25 µA and an extraction voltage of 2 kV.[49] However, since then cone apices have been reported to have a radius of curvature in the order of 5 nm after inspection of “frozen” LMISs under SEM.[50, 51]

FIBs suffer from the Boersch effect, which can be described as an energy spread or distribution is due to mutual repulsion of charged particles in close proximity, resulting in local deceleration and acceleration. This means that the energy of any one ion within the beam will fall within a distribution of energies, and will not necessarily reflect the applied accelerating voltage. This energy distribution leads to aberration, and is therefore undesirable. Studies into the emission behaviour of LMISs and gallium in particular have revealed that the beam current is more stable and produces less noise at emission currents below 30 µA.[52] They have also shown that the lowest total energy distribution and highest current density are

achieved at a low total emission current, and therefore high angular intensity can be combined with low energy distribution and low chromatic aberration.[50, 53] In 1980, Swanson, Schwind and Bell established that 1 µA was the critical emission current for Ga LMIS field evaporation, below which no emission would occur.[54] And so it is recommended that a gallium LMIS should be operated at an emission current of 1-2 µA.[35]

Another area of interest in the development of stable LMISs has been the issue of backsputtered contaminants. Material sputtered from electrodes and apertures can become deposited on the source metal and influence the emission current and stability of the beam. Studies looking at a variety of aperture materials have measured the rate of emission decay due to contamination and have found that although tungsten causes a reduction of total emission current, the beam current stabilises without a total loss of emission.[55] It has also been shown that at certain concentrations Sn/In contamination can improve LMIS stability.[56]

To counter the effects of source contamination, Galovich showed that the heating of the ion source via resistive heating can cause the desorption of contaminants.[55] However, repeated or continual heating of the metal ion source can lead to an increase in the energy spread and therefore chromatic aberration.[57]

As well as a high performance source, developments were required in the optic systems that were to focus and control the beam.

In 1987, Orloff compared the use of two different lens systems on the performance of a focused ion beam. He showed that a two lens system operating in a collimated beam mode, with a varying aperture size, was superior to a system operating with an intermediate crossover in terms of beam diameter when operating at a fixed beam current and working distance.[58]

In 1988, Narum and Pease demonstrated their development of a variable energy FIB system for use in microfabrication that could achieve beam energies in the range of 0 – 50 keV.[59] The suggested applications for this variable energy system include using a high energy beam to sputter or machine and a low energy beam to write.[60]

2.2.2 Applications

2.2.2.1 Scanning Ion Microscope

The beam of primary ions incident on a material surface produces sputtered neutral atoms, secondary electron emission, and secondary ion emission (both positive and negative). The electrons or positive ions can be collected for imaging by applying either a positive or negative bias to the detector respectively. With the increasing lateral resolution of FIBs there is growing interest in using them for imaging and not just specimen preparation. Different ion yields can give compositional and crystallographic contrast, which is enhanced through the channelling effect and topographic contrast.[61]

2.2.2.2 Secondary Ion Mass Spectrometry (SIMS)

Secondary Ion Mass Spectrometry uses an ion beam to sputter surface atoms from a sample. Those atoms that are ionised by the beam (secondary ions) are then collected by a mass spectrometer, allowing for the elucidation of the elemental composition.[62] This technique is inherently destructive, as it requires the surface material to be sputtered and ionised in order to be counted in the analysis. As there are only a finite number of atoms in a given volume of material, and only a percentage of the atoms sputtered from the surface are ionised and collected in the spectrometer, a high yield of ions is desirable to increase the sensitivity of the SIMS technique, and in 1983 Barofsky *et al.* showed that there was an increased abundance of secondary ions when using a LMIS.[63]

Gallium LMIS FIB has been used by NASA for SIMS analysis of micro-particle impact sites on spacecraft returning from Low Earth Orbit (LEO).[64]

2.2.2.3 Ion Induced Auger

As well as sputtering sample material, incident ion beams cause the emission of electrons. Low energy secondary electrons can be used for imaging the sample surface, as is done in SEM. Some elements also emit Auger electrons, which allows for identification of the sample composition. By measuring the Auger electron emission during ion beam exposure a depth profile of the sample can be recorded as the surface is sputtered. The was described by Maydell *et al.* as Dynamic Ion-Induced Auger Spectroscopy.[65]

2.2.2.4 Ion Scattering Spectroscopy or Low Energy Ion Spectroscopy (ISS or LEIS)

This technique uses an energy analyser to measure the energy loss of primary ions from a low energy source (~1 keV) scattered from a sample surface. Energy analysis of the scattered primary ions can provide information on the mass of the atomic species in the outermost layer of the sample, when the mass of the primary ion, the primary beam energy and the scattering angle are all known. Because this technique requires a measurable energy loss and scattering of the primary ion it is generally used with a light primary ion; ^{4}He and ^{20}Ne are commonly used.[66]

2.2.2.5 Rutherford Backscattering Spectroscopy or High Energy Ion Spectroscopy (RBS or HEIS)

Like LEIS, this technique measures the energy loss of scattered primary ions. However, as the name suggests, the energy of the primary beam is much higher, in the order of 1 MeV. This means that the primary ions penetrate deeper into the sample surface and can provide a depth profile of the sample.[66]

2.2.2.6 Micromachining/Nanomachining/Cross-sectioning

One of the major applications of the FIB, especially with regard to the high brightness beams produced by LMIS, has been micro- and nano-machining. The ability to sputter material accurately, reproducibly and with high resolution means that it has found application within a number of fields, such as modern semiconductor and other electronics,[67-69] high performance optics[70] and specimen preparation for other high resolution imaging techniques.[39, 71-73]

Harriot *et al.* (1987) demonstrated that FIB could be used to mill optical cavities for use in laser systems.[70] Their study used a 20 kV Ga FIB to polish the optical surfaces, and they found that laser performance was good compared to other preparation techniques. However, the mill times they required were long, 20 min for a single mirror surface, and so they surmised that FIB would only be suitable for unique, high value devices, or for prototyping and research.

An application of particular interest in this study is the use of FIB for the preparation of specimens for high resolution microscopy. Previous methods of specimen preparation involved the use of microtomes, polishing discs and polishing ion systems, which could be quite crude and didn't allow for specific areas of the sample to be selected. With the use of FIB microscopy, specific sites of interest can be selected, exposed and examined in a number of ways, depending on the final technique to be used.

Two distinct methods of preparing specimens for TEM are described by Giannuzzi *et al.* [39] The "Trench" method is best used to thin a sample that has already be produce mechanically. The method requires the use of the FIB to mill parallel trenches into the edge of a film, on opposite sides, so that a thin foil is left between them, supported by the walls of the trench. This method of specimen production still isn't ideal; if the trench isn't wide enough there can be shadowing and signal contamination from the sidewalls, but it allows accurate selection of regions within a mechanically prepared sample.

The “lift-out” method is a technique that has been developed for use with Small Dual Beam (SDB) systems, which consist of a FIB and SEM combined. The advantage of having both beams within one system is that the electron beam can be used to observe the progress of the FIB, with little or no damage to the sample. The “lift-out” method uses the FIB to mill parallel trenches normal to the surface of the sample. This bulk material around the site of interest is removed rapidly using high beam currents, leaving a thin section, containing the site of interest, between the trenches. The sample section is then thinned further using lower beam currents (smaller probe size) and tilted into the beam for the final polishing step[72, 73] to reduce damage and compensate for the formation of the “Classic V-shape” respectively. The final TEM foil is then tilted relative to the FIB so that it can be detached from the side walls, and the sample it attached to a micromanipulator before the final cut is made across the base of the sample. The TEM specimen is the lifted from the bulk material by the manipulator and deposited onto a TEM grid ready for transfer to the TEM.

Another unique application of the FIB in an SDB system is the development of “Slice and view” or 3D FIB Tomography. This three dimensional technique uses the FIB to prepare sequential cross-sections of a sample that can be imaged using the in situ SEM. The series of images obtained by SEM can then be aligned and reconstituted into a three dimensional model of the sample.

Slice and view has been used to visualize the internal structure of semiconductors and other solid devices.[61] It has also been used to study and characterise the deformation and damage due to nanoindentation of multi-layered composites.[74]

3D FIB tomography has also recently drawn interest from the biological sciences, because of the ability to create three dimensional reconstructions of whole cells and tissues.[75, 76]

In 2006, Heymann *et al.* demonstrated the abilities of 3D FIB tomography by imaging a number of biological samples. Cross-sections and 3D reconstructions were generated of embedded

and critical point dried yeast cells. Similar results were also achieved through the use of cryogenically frozen yeast cells. The study also demonstrated the reconstruction of a section of embedded tumour tissue, lift-out of embedded yeast cells for TEM and the production of cylindrical specimens for electron tomography.[75]

In 2009, Schroeder-Reiter *et al.* demonstrated the real potential of 3D FIB tomography by imaging the structural elements in critical point dried chromosomes[77]

2.2.3 Beam damage/interactions

When using a FIB for specimen preparation and analysis, consideration has to be made of the effect that the beam's interaction with the sample will have on the structure and/or properties of interest. FIB techniques are innately destructive; some of its main applications, as described above, involve the removal of sample material, and so a lot of research has been dedicated to understanding what unintended damage is being done to the sample around the area of interest and how it can be best limited.

When an ion beam is incident upon a sample surface there are two types of collisions that can occur; nuclear and electronic.[78] Nuclear collisions are when the ion collides or interacts with the atomic nuclei of the surface material. These collisions are elastic, with the conservation of energy and momentum (unless nuclear reactions or nuclear resonances occur). Electronic collisions involve the interaction of the primary ion with the electrons of the sample material. These interactions are inelastic, with energy being lost during each collision. Electronic collisions cause the primary ions to lose less of their energy than nuclear collisions, but they are a lot more frequent, due to the lower probability of an ion colliding with an atomic nucleus. However, as the primary ion loses its energy and decelerates it becomes more likely to collide with a nucleus.

If the primary ion has sufficient energy when it collides with an atomic nucleus it will displace it from its position within the lattice (assuming the sample material is crystalline). This energy threshold is exceeded by FIB microscopes and hence they can be used for the machining of the sample surface. Nuclear collisions induced by a FIB can impart considerably more energy than is required to displace an atom from its lattice position. As a result, the displaced atom will travel through the material and can go on to displace further atoms from the lattice, giving rise to a "displacement cascade".[79] this is one of the reasons why material removal and "damage" can extend further than the direct interaction with the primary ion beam.

The rate and efficiency of sputtering from a sample surface can be influenced by the topography of the starting surface. Prenitzer *et al.* have described how surface topography can affect the sputter rate in different areas due to the sputter yield being dependant on the angle of incidence.[80] An angle of 0° from the surface normal has the lowest sputter yield as the displaced sample atoms are generally deeper in the sample and are less likely to escape from the surface, but the yield increase as the angle moves away from the normal. Peak sputter yield has been modelled for a range of samples using TRansport of Ions in Matter (TRIM) and is shown to be achieved at 80° ± 5°. Above this optimal angle there is an increased likelihood of the primary ion being deflected away from the surface, as so the sputter yield drops rapidly. This angular dependence means that rough topography at the surface will lead to a self-exaggerating selective etch that will produce morphological artefacts in the final milled surface.

The fate of the primary ion is dependent on a number of factors, such as accelerating voltage, angle of incidence and the mass and density of the sample material. The ion could either be scattered backwards and escape the surface (or sideways depending on the geometry of the sample and angle of the beam), or it could come to rest within the surface of the sample.

In 2007 Kiener *et al.* described the potential for surface hardening in the order of GPa due to the formation of a precipitate layer, while studying the effect of gallium ion beam exposure on a copper sample.[81]

A major issue with the use of FIB for preparing cross-sections of a sample surface is that the distribution of energy, resulting from the Boersch effect, causes chromatic aberration of the probe. This aberration generates tails of low intensity around the spot that irradiate the sample away from the target region and result in indiscriminate damage of the sample surface. Frey *et al.* (2003) described the energy distribution of the beam as a Gaussian and showed that the tails produced regions of differential sputtering and deposition surrounding the desired patterning area.[82] In 2008 Pallecchi *et al.* performed an evaluation of the beam profile, operating at 30 kV and 100 pA, which indicated that the effects of irradiation from the tails of the beam spanned a distance of 130 nm from the edge of a feature milled to a depth of 20 nm.[83]

In order to minimise the interaction and damage caused by the beam tails, it has become common practice to deposit a layer of metal, typically platinum, via ion beam assisted Chemical Vapour Deposition (CVD) above the area of interest.[39] The process of ion beam assisted CVD involves the injection of a metallo-organic gas into the chamber at the site of interest (normally within 200 µm of the sample surface). The gas adsorbs to the surface before being exposed to the ion beam. As the beam rasters over the designated area, the gas is degraded, leaving only the metal deposited on the surface. As a result of having a layer of platinum (of the order of 1 µm thick) over the feature to be cross-sectioned, the high intensity centre of the ion beam will be able to mill down through the platinum and the sample, while the low intensity tails are limited to impacting on the layer of platinum. This provides a clean cross-section of the sample, without the ion implantation and rounding of edges that would normally occur with exposure to the beam tails. However, if the feature of interest is very

superficial within the sample (within the first 100 nm of the surface) then platinum coating alone will not offer the desired protection. Because of the way in which the gas is decomposed there will inevitably be exposure of the sample to the ion beam prior to deposition of the protective metal layer. This was shown quite neatly by Rubanov and Munroe in 2003 when they studied the effect of the ion beam during platinum deposition on an AlAs-InAs superlattice structure. In their study five alternating layers of AlAs and InAs were deposited onto an AlAs substrate. The layers had measured thicknesses of between 2 and 10 nm, clearly visibly under the TEM. Their layered sample had been sputter coated with a layer of gold, prior to platinum deposition and cross-sectioning with the FIB, and the gold layer was of an inconsistent thickness. Where there were thin regions (~15 nm) and gaps in the gold coating the layered structure of the sample had become mixed, as the ion beam had penetrated the gold and displaced the atoms within the sample lattice during platinum deposition. From this evidence they postulate that prior gold coating, to a thickness of ∼60 nm, is essential where the near surface structure of a specimen is to be examined.[84]

Using an ion current of 50 pA, FIB milling of magnetite thin films is possible without damaging the magnetic properties of the film. Higher beam currents produce considerable damage to the magnetite layer, resulting in misoriented grains around the ion-milled structure.[85]

Rubanov et al. performed a study looking at the effect of ion beam exposure on a diamond cross-section. Ga^+ implantation in diamond was investigated by intentional surface exposure followed by TEM sample prep, and showed that damage accumulation results in an amorphous layer below the exposed surface, that can be easily seen using TEM, with a volume increase of around 50%. The data presented also showed the TEM samples could be prepared without measurable damage in the sample sidewalls, compared to the obvious amorphisation resulting from 0° beam incidence.[86]

2.2.3.1 Semiconductor studies

The majority of studies that consider the damage caused by FIB have focused on hard materials, such as Si and GaAs, because of the FIBs applications in the semiconductor industry. There is therefore an abundance of studies that relate FIB damage in Si with accelerating voltage and spot size, and observed damage has been shown to be reduced through the use of lower beam energies, and by increasing the angle of incidence, relative to the surface normal. [87-90] And a defect study in GaAs showed that low energy beams produce less damage when used for maskless etching[91]

Scanning spreading resistance microscopy (SSRM) and scanning capacitance microscopy (SCM) were used to analyse focused ion beam (FIB) induced lateral damage around milled structures on silicon. FIB induced lateral damage on silicon around purposely irradiated regions has been observed experimentally using SCM and SSRM. It has been shown that the extension of this lateral damage is much larger than reported in previously. It is probably due to large beam broadening and increases with both increasing dose and irradiated structure diameter.

Considers damage in the incident surface (perpendicular to the beam), which is obvious. Damage surrounding the patterns is due to the beam tails, which is why it correlates with spot size[92]

2.2.3.2 Artefacts in biological samples

Drobne *et al.* studied the effects of ion beam exposure on a biological sample (digestive glands of *Porcellio scaber*).[93] They describe a “melt-like” effect at the incident surface of gold coated samples, “sweat-like” effects in conductively stained samples, morphological deformation and Ga^+ implantation at the incident surface and the exposed sidewall. The “sweat-like” artefacts they postulate as being the local redeposition of metallic material or the reaction of Ga^+ with the conductive stain to form various intermetallics. The morphological

deformations observed were caused by the selective milling of uneven samples. And the Ga^+ implantation was observed indirectly by a reduction in charging effects and an increase in signal and contrast in both SE and BSE imaging. The artefacts described by this study were reduced by the use of Pt deposition prior to ion beam exposure.

2.3 Model materials

2.3.1 Polycarbonate

Polycarbonates are polyesters of carbonic acid, in which the carbonate group recur along the polymer chain. They were first discovered in 1898 by Alfred Einhorn at the University of Munich, but it wasn't until 1953, when Hermann Schell of Bayer patented the first linear polycarbonate, that PC went into commercial production under the trade name of MAKROLON. Parallel development of PCs was being undertaken at General Electric, who went on to produce PC under licence in 1960, using the trade name LEXAN.

The repeat structural unit of polycarbonate (as used in this study) is shown in Figure 2.4, and is produced by the condensation polymerisation of bisphenol A (BPA) with phosgene ($COCl_2$).

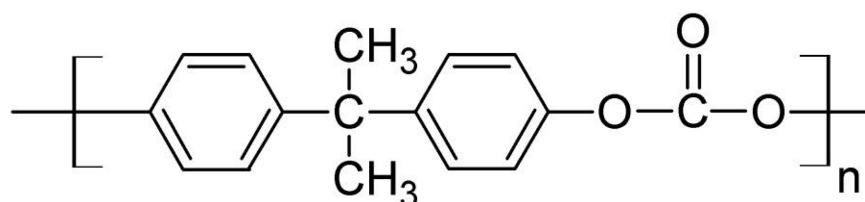

Figure 2.4 Repeat structural unit of polycarbonate

The presence of benzene rings in the polymer chain, resulting from the bisphenol A, gives polycarbonate stability against thermal and oxidative degradation, and increased chain stiffness.

2.3.2 Snail shell

Snail shell has been chosen here as the model bio-composite system, because it has an interesting biphasic nanoscale 3D structure, which would be ideal for testing the application of AFM-SDB phase imaging. Snail shell also has a primary mechanical function that is critically dependent on both the mechanical properties and organization of its constituents. As such, snail shell is of interest to those developing bio-mimetic composites.

2.3.2.1 Periostracum

The periostracum is the outermost layer of a snail shell. It is mainly organic, proteinic, and offers a protective barrier to prevent the erosion of the mineralised layers beneath. In freshwater snails it is usually made up of two layers; the outer layer being proteinaceous and the inner layer calcified, and often brittle. As well as being protective, the periostracum plays a role in shell formation, organising the shell layers; acting as a matrix.

2.3.2.2 Crossed-lamellar layer (CLL)

The crossed-lamellar arrangement is the most frequent microstructure found in gastropods. It is formed from layers of either fine prismatic or lath like aragonite crystal. The layers form interdigitating sheets at varying angles. Figure 2.5 is a schematic drawing illustrating the organisation of CLL, taken from Dauphin et al [94].

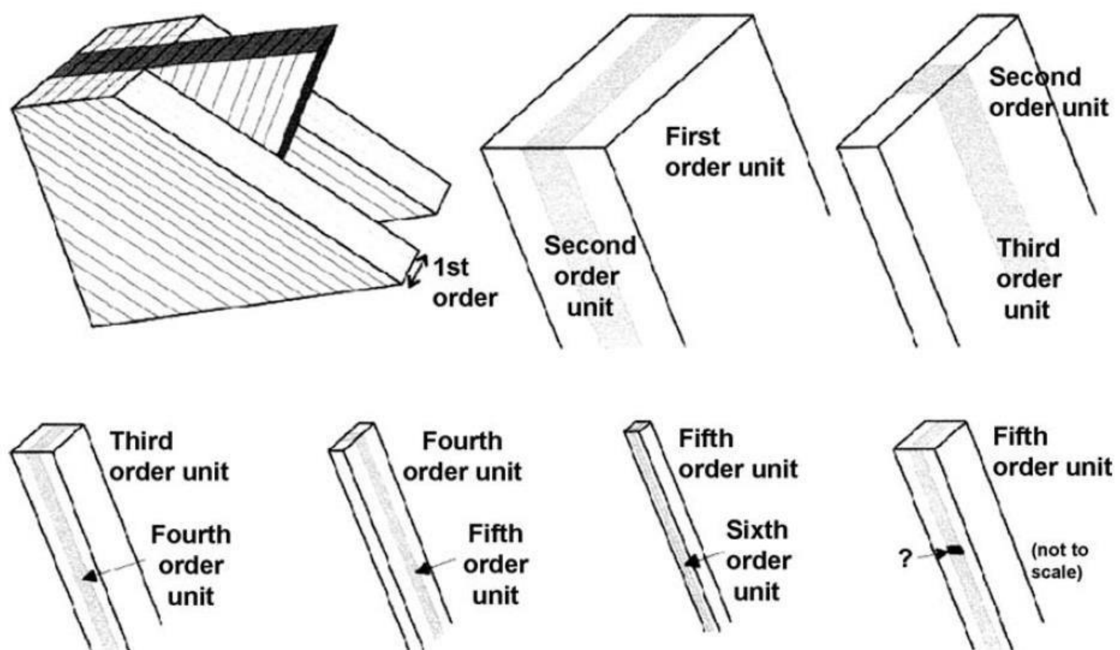

Figure 2.5 Schematic drawing to illustrate the organisation of the crossed-lamellar layer (CLL) in shell of gastropoda. Each lamellar is made of successively smaller units, down to the individual rod-like crystals

The first order structure forms the alternating layers. The layers are angled between 45-60°, which makes it difficult for cracks to propagate through the shell [95].

2.3.2.3 Nacreous structure

The nacreous layer is the innermost layer of a molluscan shell. It is always aragonitic in nature and forms a laminated structure. The crystals form sheets that are generally around 500nm thick and have a uniform spacing of ~30nm, which is filled with biological material. In Bivalvia and Cephalopoda the layers stack in the sheet nacre model, which resembles a “brick and mortar” arrangement. However, in Gastropoda a “columnar stacking” arrangement occurs where the newly deposited mineral plates stack directly on top of each other in vertical alignment [96]. This arrangement of stacked crystal and organic matrix (which makes up < 5%

of the layer) gives nacre very high tensile, compressive and bending strengths. It is thought to be the presence of a chitin-protein complex in the organic framework of the matrix that acts as a guide for mineral deposition and gives the layer its mechanical properties [97].

2.3.2.4 The shell matrix

The shell matrix is made up of proteins, carbohydrates, polysaccharides and lipids. It is intimately associated with the mineral phase and binds the crystals together. Making up < 5% of the total volume of the shell [98]it forms the framework on which the crystals are deposited. The matrix is crucial in the process of crystal nucleation and growth and gives shell its unique physical properties. Figure 2.6 shows the model proposed by Levi-Kalisman et al [97] for the biological matrix. It shows strands of highly ordered β-chitin in a periodic arrangement. Between these β-chitin sheets are layers of a silk fibroin gel, which contain aspartic acid-rich glycoproteins. The glycoproteins bind and stabilise the chitin layer, forming a membrane. Upon mineralisation the aragonite crystallises in the space between the chitin sheets and forms a composite of outstanding mechanical properties.

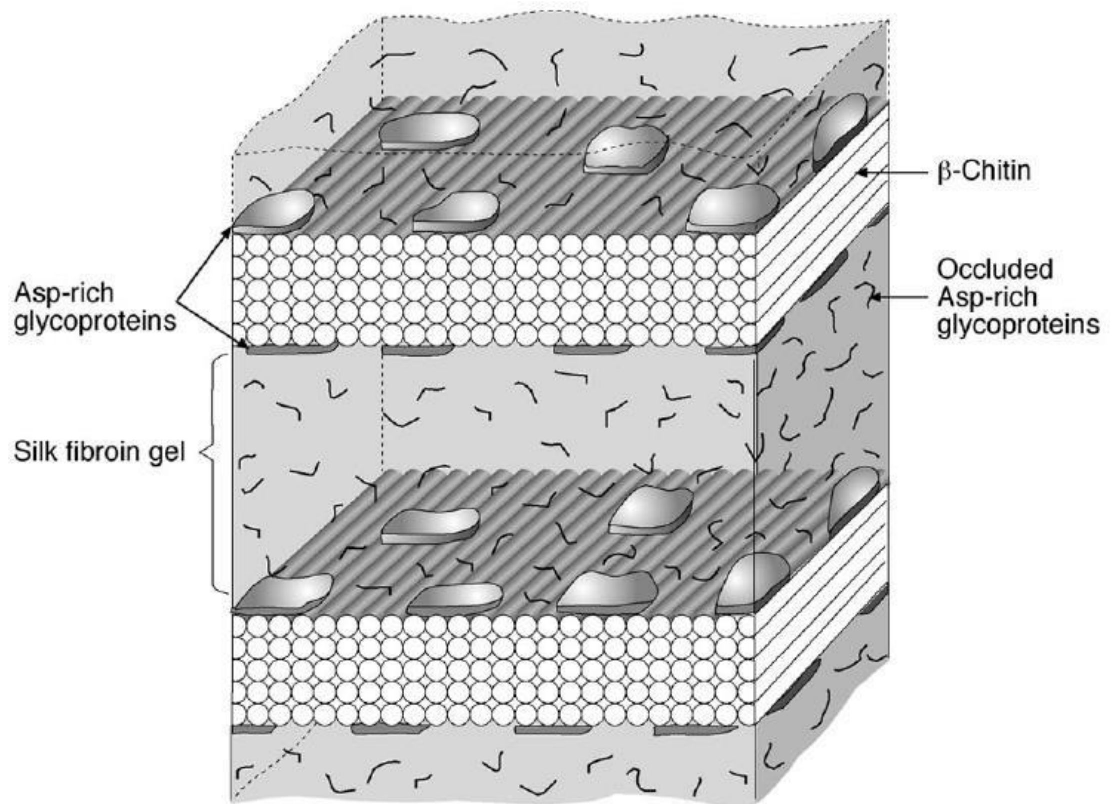

Figure 2.6 Three-dimensional model of the biological matrix proposed by Levi-Kalisman et al (2001)

3 Materials and Methods

3.1 Preparation of sample materials

3.1.1 Polycarbonate film

Polycarbonate (PC, Lexan, SABIC Innovative Plastics) was chosen as the sample material when investigating the effects of Focused Ion Beam exposure on soft polymeric materials due to its homogeneous amorphous structure. Samples of uncoated polycarbonate were prepared from a solution cast film, which had a film thickness of 200 µm as measured by SEM, and was supplied by Nanoforce Technology Ltd. Small polycarbonate sections of dimensions 10 mm x 5 mm x 200 µm were cut from the parent PC film by hand using a razor blade. These smaller PC sections were freeze-fractured under liquid nitrogen to produce a brittle fracture, which reduced the amount of post yield material at the cross-section when compared to a surface produced through mechanical shearing. The freeze fractured surface also provided a relatively flat starting surface for FIB milling. The film was mounted onto a standard Scanning Electron Microscopy (SEM) stub using carbon cement/adhesive tabs, and gold coated to provide an electrically conductive pathway and reduce charging of the polymer under the focused ion and electron beams. This coated and mounted sample, shown in Figure 3.1, was transferred into a Small Dual Beam (SDB) (Quanta 3D FEG, FEI, EU/USA) so that the fractured surface was parallel to the electron beam for subsequent platinum deposition and FIB milling, which will be described in section 3.5. The methodology for AFM based imaging and measurements will be covered in section 3.2 and for the purpose of imaging the cross-sections of film/tape samples a custom made clamping sample holder was used, which is described on section 3.3.

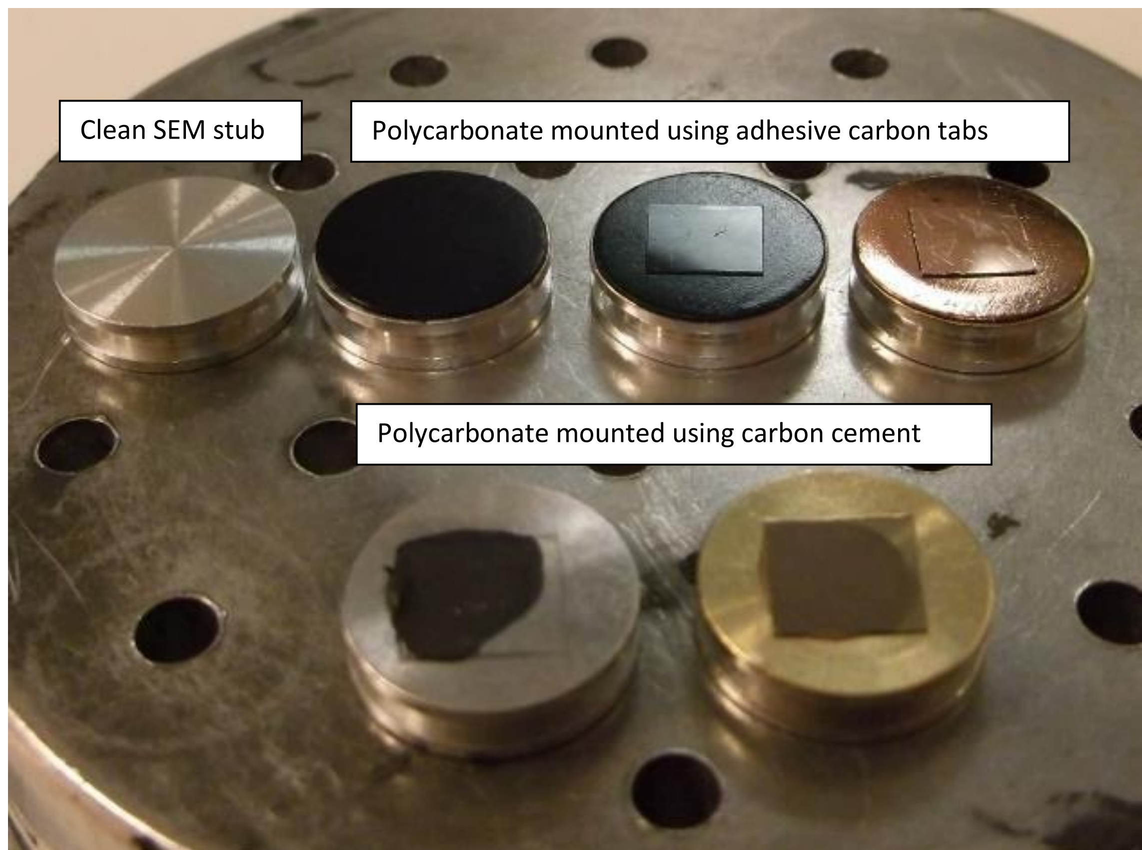

Figure 3.1 Polycarbonate film samples being prepared for SEM-FIB. The top row of samples shows the stages of preparation using carbon adhesive tabs; from left to right, a clean stub, a stub with a carbon tab, a sample of polycarbonate film stuck to the carbon tab and a gold coated sample. The bottom row shows samples prepared using carbon cement; the left sample is yet to be coated and the right sample has been coated with gold.

3.1.2 Silicon

Silicon was chosen as a model sample for the calibration and quantification of the AFM phase image as a cleaved silicon surface is very flat, thereby minimising the effects of topography on the AFM phase signal. Silicon has a well-defined literature value of elastic modulus. Also, silicon has been established as a good model material in the literature for the purpose of standardising microscopy data.

Samples of silicon were prepared from a standard silicon wafer using a straight edge and a diamond scribe. Any particulate contamination was removed from the silicon surface by sonication in an ethanol bath and drying with high pressure nitrogen gas. The silicon samples

were mounted onto standard AFM sapphire sheets by use of double-sided adhesive carbon tape, and the sapphire sheets were clipped to the AFM sample holder, as shown in Figure 3.2.

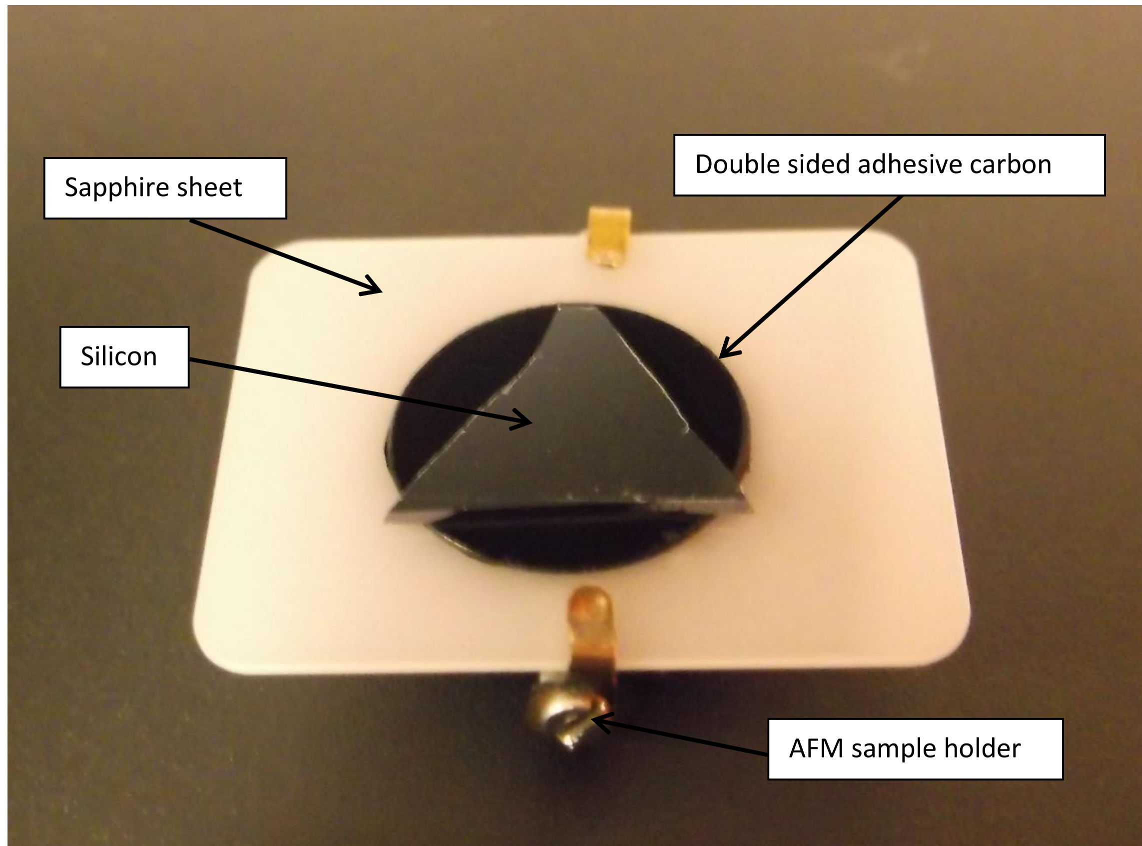

Figure 3.2 Image of silicon wafer sample on an AFM sample holder

3.1.3 Polypropylene/elastomer nanocomposite tape

A nanocomposite tape of polypropylene and an elastomer (Versify 2300, Dow, US), manufactured by Nanoforce technology Ltd, was used as the sample material in order to demonstrate AFM phase imaging's ability to resolve nanoscale components of a material with varying elastic moduli. The nanocomposite tape was manufactured through a process of coextrusion and layering. The image to the right of Figure 3.3 shows the two single screw extruders that were used in the construction of the nanocomposite tape, feeding into a dye, which causes the two polymers to flow together to form a flat bilayer tape. Two lengths of the

bilayer tape were then layered on top of each other and fed into a heated roller system, shown to the left of Figure 3.3, which fused the two tapes and then used differential roller speeds to draw the newly combined tape. This layering or mixing step was repeated a further 11 times to produce a nanocomposite tape containing 8192 (2^{13}) layers.

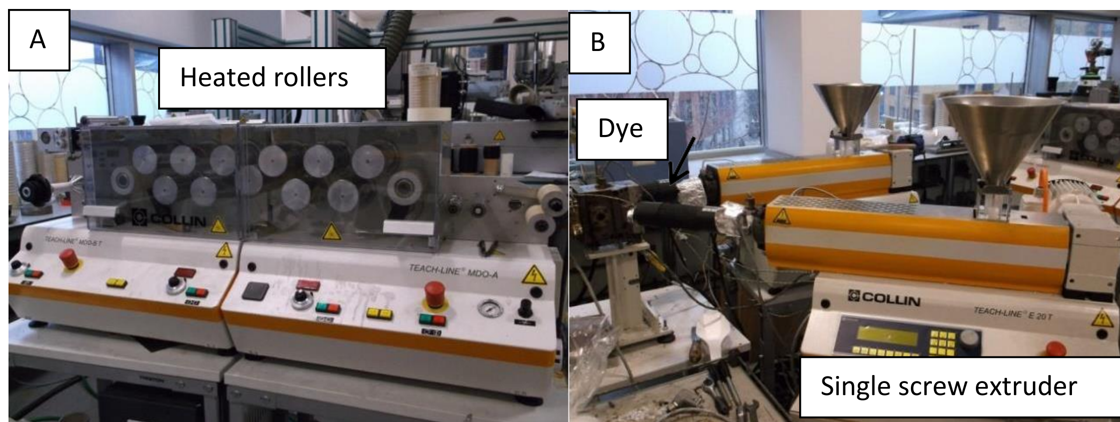

Figure 3.3 The polymer processing equipment used to prepare the polymer nanocomposite sample. b) The two single screw extruders, which feed into a dye, combining the two polymers into a bilayer tape. a) The heated roller unit that draws the nanocomposite tape.

Short sections of the polymer nanocomposite tape were taken for the preparation of samples and are shown in Figure 3.4. Samples of the nanocomposite tape were cut using a razor blade, freeze fractured under liquid nitrogen, and mounted on SEM stubs as described for the polycarbonate samples in section 3.1.1. For the purpose of imaging the cross-section of the nanocomposite tape using AFM, and for when the sample was repeatedly transferred between the AFM and the SDB, the sample was mounted using a custom made clamping sample holder, which is described in section 3.3.

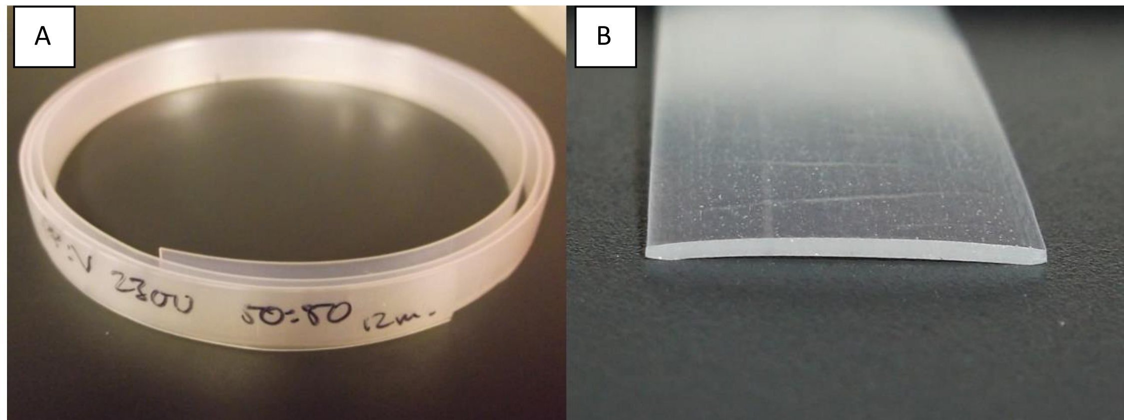

Figure 3.4 Images of the polymer nanocomposite tape. a) A length of the composite tape and b) a cross-section of the tape prepared with a razor blade.

3.1.4 Biocomposite material (Snail shell)

Snail shell was selected as an example of a biocomposite material due to its complex, but regular structure, which consists of regions of stiff mineral platelets and soft protein layers holding the platelets together. The two different component materials should offer enough variation in elastic modulus to provide contrast in the phase signal of the dynamic AFM imaging, whilst the length scales of the protein region will challenge the resolution if the AFM.

A fresh water snail, *Pomacea diffusa,* or spiked-topped apple snail was purchased from a local pet shop. A section of the shell was removed from the opening by first allowing the snail to retract into its shell. As the snail retracts it covers the shell opening with the operculum, shown in Figure 3.5. Tapping on the operculum with a pair of tweezers makes sure that the snail was securely retracted, leaving several millimetres of shell overhanging. A section of the overhanging shell was fractured using a small set of pliers. Figure 3.5 is a photograph of the snail, subsequently named Eric, having had a section of its shell removed. Eric was given a home in the aquarium in the Physics department at QMUL.

The sample of shell was fragmented into smaller sections and mounted in a custom made clamping sample holder, which is described in section 3.3. The mounted samples were coated

with gold and examined under SEM. Cross-sections of the snail shell samples were created using the FIB as described in section 3.5 and were imaged using the AFM as per section 3.2.

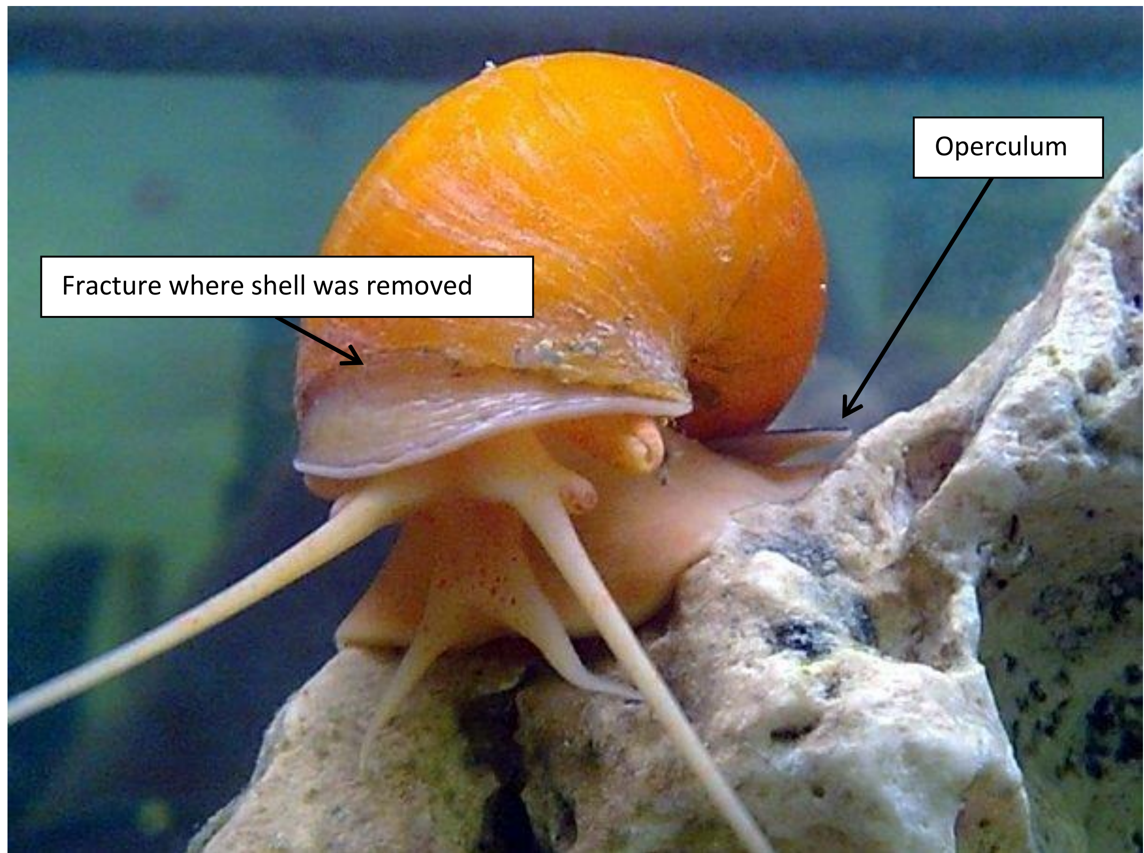

Figure 3.5 Eric the snail (post donation) enjoying his new home in the Physics Department. The operculum can be seen folded back against the base of the shell.

3.2 Atomic Force microscopy

Atomic Force Microscopy is a scanning probe technique, which forms the basis of majority of the sample imaging in this thesis. The main benchtop AFM setup in the NanoVision centre is the NTegra platform by NT-MDT (Russia).

3.2.1 NT-MDT NTegra

The NTegra is a modular setup with various interchangeable sample stages and heads. Each head contains the cantilever holder and the laser optics and can be lifted on and off the main stage for easy access to the sample. A schematic of the optical system is shown in Figure 3.11. There are different heads for different applications and imaging modes; some are static heads that require the sample to be mounted on a scanning stage in order to image, others contain scanning piezos that move the cantilever and provide the feedback response, whilst there are others for special applications such as imaging in liquid and imaging at extremes of temperature. Figure 3.6 is a photograph of the AFM setup in the scanning head configuration. All of the AFM heads contain a laser system that projects a red laser onto the reverse of the cantilever. This laser light is reflected (often enhanced by an Al or Au reflective coating on the cantilever) back into a segmented photodiode that allows the software to monitor the deflection of the cantilever, shown in Figure 3.11. All of the AFM heads, including the static ones, contain a dither piezo under the chip holder so that oscillations can be applied to the AFM cantilever.

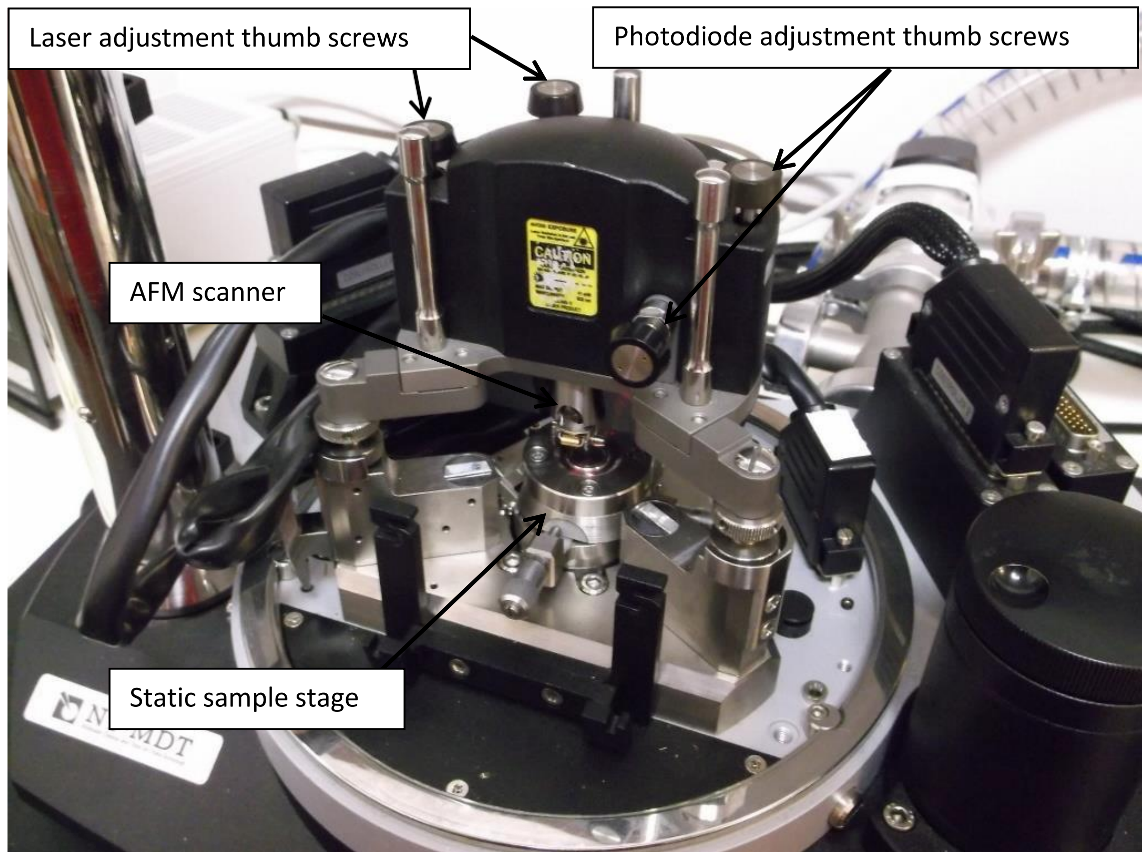

Figure 3.6 NT-MDT NTegra AFM. This is the main benchtop AFM used throughout the project, shown here with the scanning head and static sample stage.

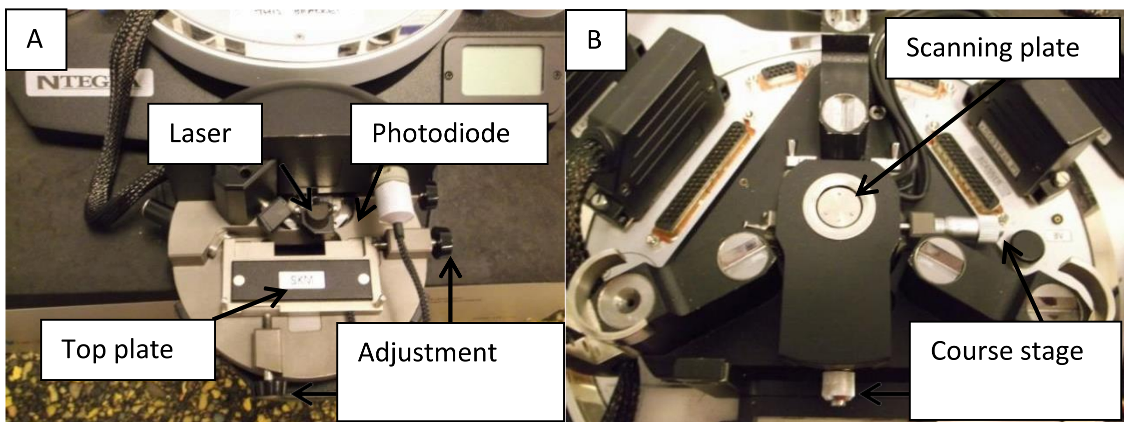

Figure 3.7 a) Static head for the NTegra AFM. b) Scanning sample stage for the NTegra AFM

The sample stages can either be static; requiring the use of a scanning head to image, or they can contain scan piezos. Figure 3.7a is a photograph of the static head for the NTegra AFM and

Figure 3.7b is an example of a scanning sample stage that is use in conjunction with the static head. There are different scanning stages with different ranges of movement that allow the user to adjust for increased scan range or a reduced step size (and therefore greater potential resolution). For maximum scan range a scanning head and scanning stage can be used in combination and run simultaneously. The sample stages are mounted onto a course stage for large scale movement, with manually controlled movement in the x- and y-direction and a software controlled, motor driven z-axis for automated tip-sample approach. Figure 3.8 contains photographs of the AFM cantilever chip holders that are used to mount the AFM cantilever onto the AFM head. Figure 3.8a is the AFM cantilever chip holder on the scanning head and Figure 3.8b is the AFM cantilever chip holder on the static head. Both of the AFM chip holders have the same structure, and function in the same way. The AFM cantilever chip is held in place against the dither piezo by a metal spring clip, which can be seen in Figure 3.8b. The spring clip is opened and closed using the lever on the side of the AFM chip holder, which turns a cam underneath the spring clip. With the spring clip held open the AFM chip can be positioned on the dither piezo, underneath the clip, and then the spring clip is released, securing the AFM chip in place. The top surface of the dither piezo is coated with a layer of sapphire, which has a square recess cut into it, allowing for the AFM chip to be more easily aligned under the spring clip.

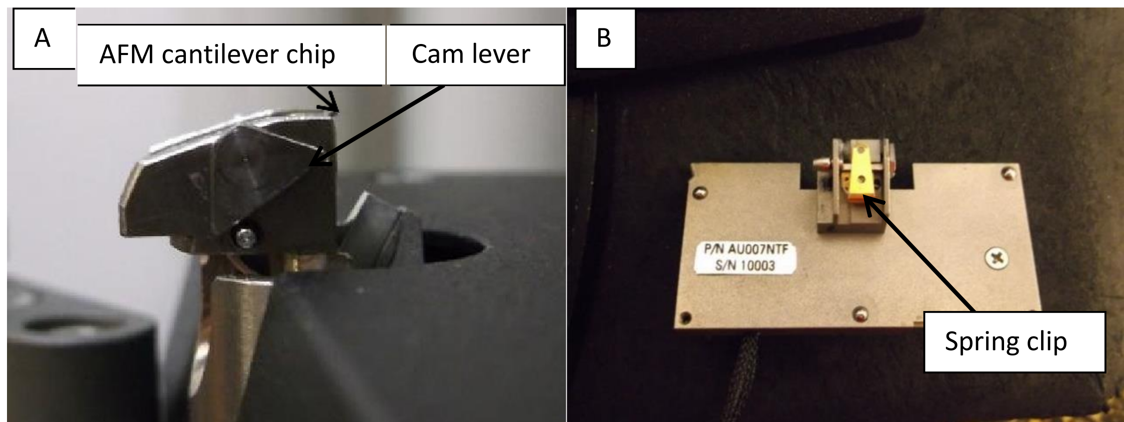

Figure 3.8 AFM cantilever chip holders for the NTegra AFM. a) Scanning head chip holder is exposed by inverting the whole head piece. b) Static head chip holder is exposed by detaching and inverting the top plate.

With the AFM cantilever chip in position in the holder the laser is aligned onto the back of the AFM cantilever. The laser alignment is achieved by observing the shadow cast by the AFM cantilever when the laser is projected against the bench. Using the alignment thumbscrews shown in Figure 3.6 and Figure 3.7a the alignment of the laser relative to the AFM cantilever is altered in x and y until a shadow is cast by the laser. The first shadow seen during the alignment is typically the main AFM chip, but by following the edge of the chip in the shadow the cantilever can be located. The laser is aligned on the cantilever in this way such that the laser is centred relative to the width of the cantilever and towards the free end of the AFM cantilever. The AFM head can now be mounted onto the main AFM stage.

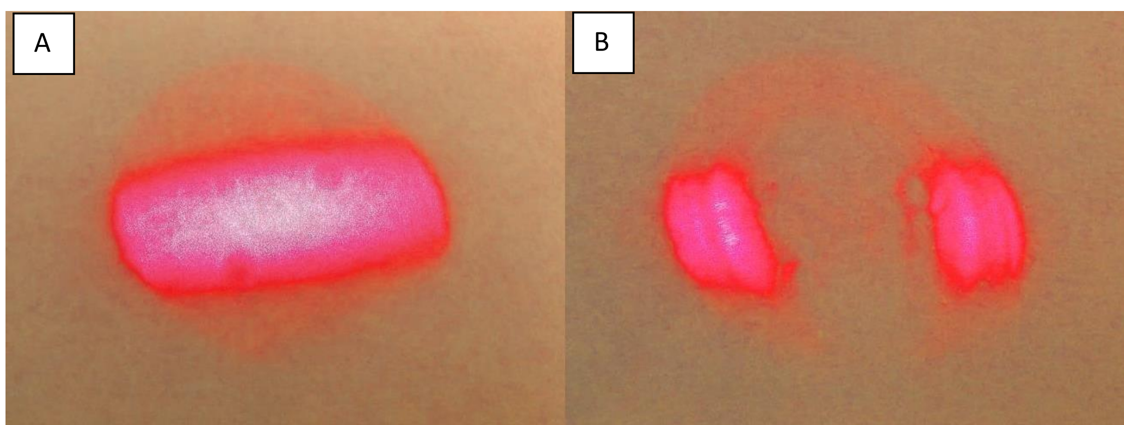

Figure 3.9 a) A photograph of the AFM laser spot projected onto the workbench. B) A photograph of the AFM cantilever casting a shadow in the red laser light of the AFM.

The whole AFM setup is positioned on an anti-vibration table to reduce the influence of environmental noise, and if required there is a lid that covers the head and stage to reduce the effects of light and sound from within the lab. Figure 3.10 is a photograph of the NTegra AFM with its cover in place, seated on the anti-vibration table.

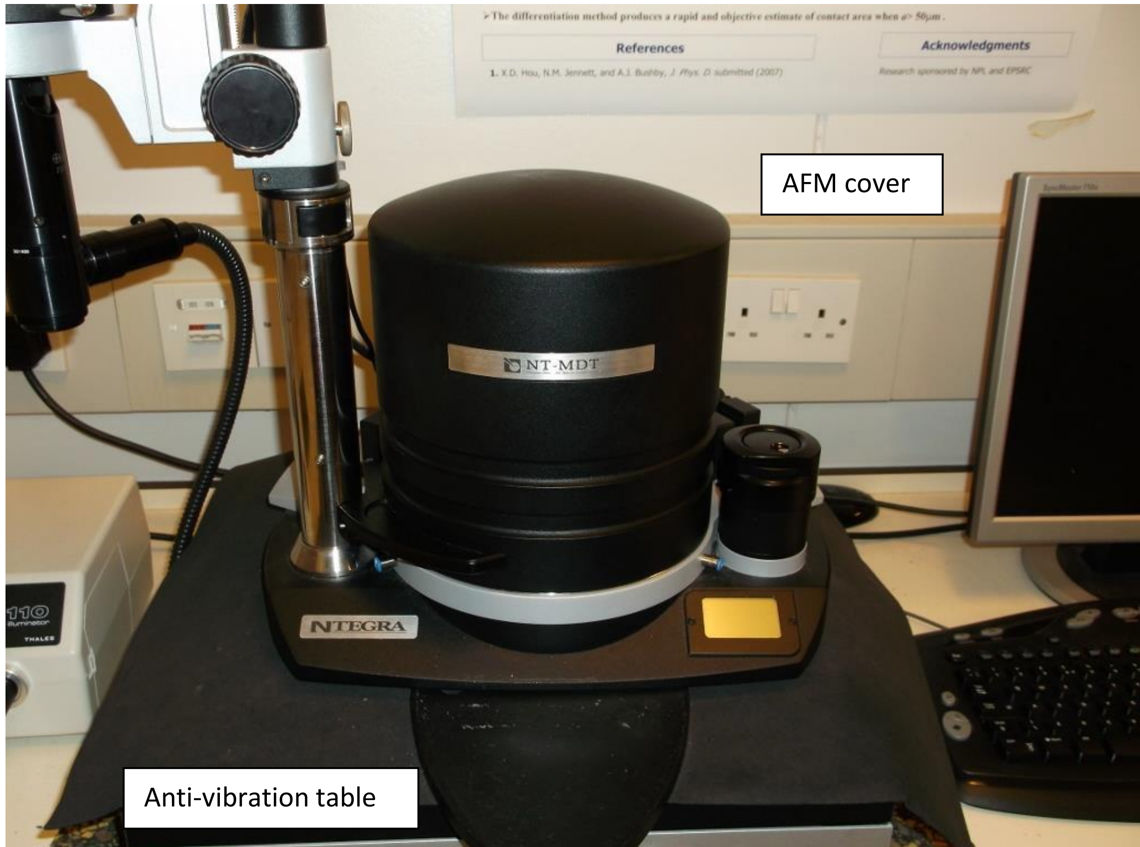

Figure 3.10 The NTegra AFM with its cover in place.

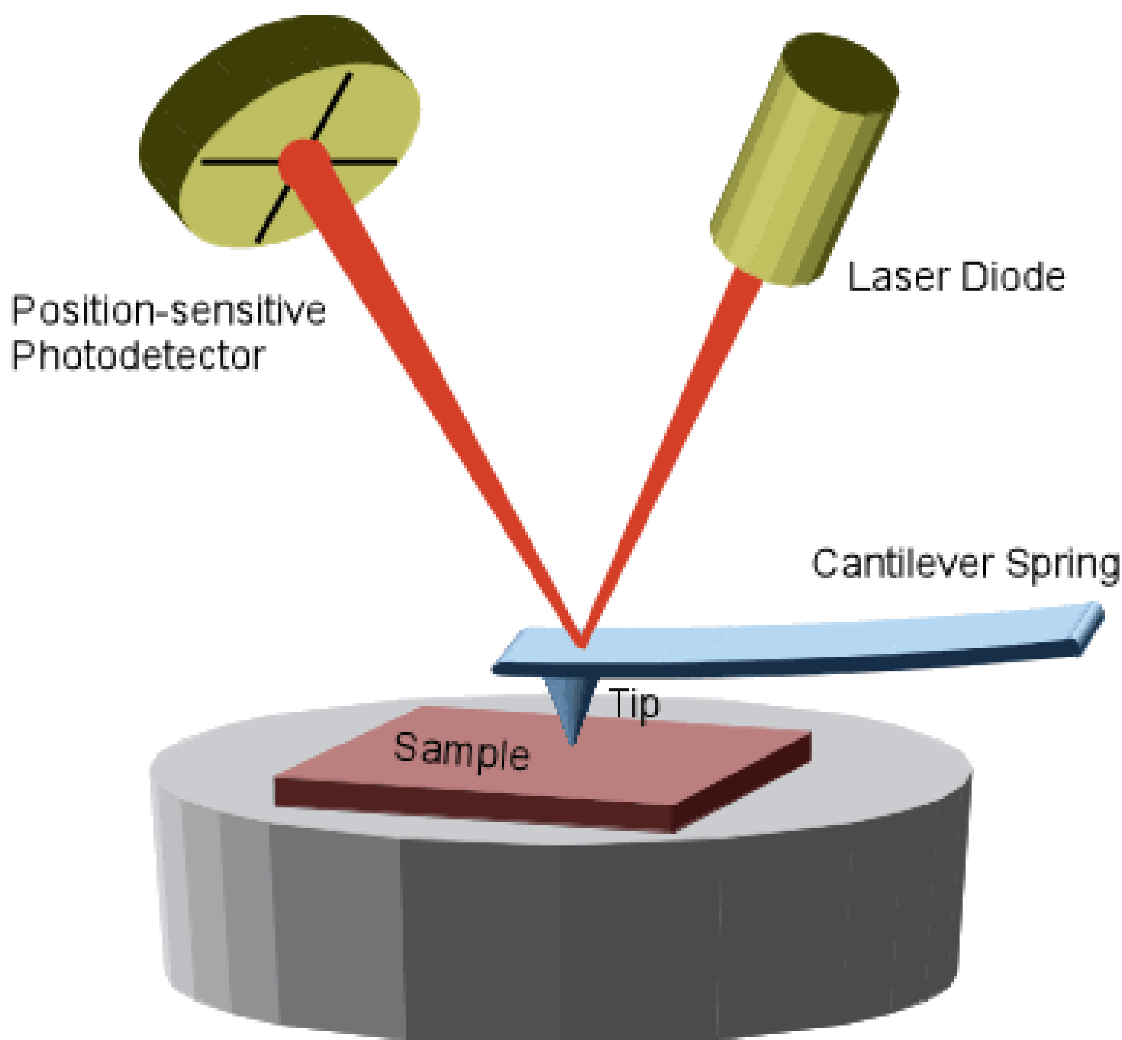

Figure 3.11 Schematic of the optical setup in a typical AFM whereby the AFM cantilever deflection is measured via the displacement of a reflected laser spot on a segmented photodiode.

After the laser has been aligned with the AFM cantilever the photodiode needs to be aligned with the reflected laser in order to accurately measure the deflection of the cantilever. In order to align the photodiode, the signal being received by the software needs to be monitored. The NOVA software that is supplied with the NT-MDT NTegra AFM has a page that is designed to aid in the alignment of the photodiode and is shown in Figure 3.12. It contains a graphical representation of the four quadrants of the photodiode, along with a red dot to represent the position of the laser reflection. The position of the red dot is based on the signal received by each quadrant of the photodiode. The laser alignment, or “Aiming”, page of the

NOVA software also displays a numerical readout of the deflection (DFL) and lateral force (LF) signals, based on the alignment of the photodiode, which aids in the fine alignment.

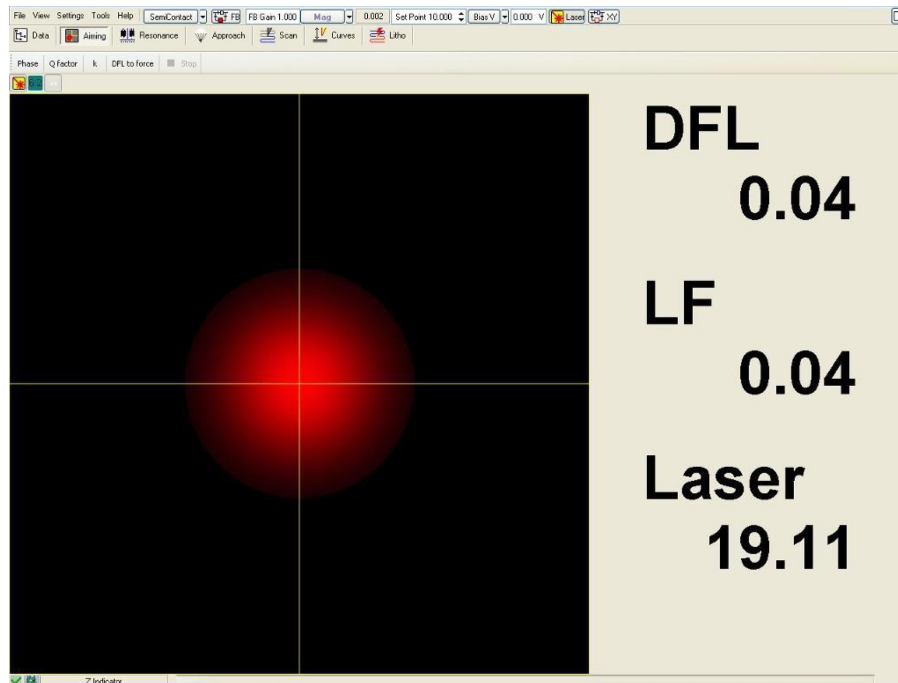

Figure 3.12 Laser alignment page of the NOVA AFM software, showing a graphic representation of the photodiode segments and the laser spot to the left and laser deflection and intensity readings on the right.

With the laser and photodiode aligned the AFM is now able to provide a qualitative measure of the deflection of the AFM cantilever, which is recorded as the current output from the photodiode (nA). At this stage in the setup of the AFM the microscope is ready to start imagining in contact mode. However, for imaging in dynamic mode the AFM cantilever needs to oscillate. The “Resonance” page in the NOVA software is where the dither piezo is controlled and a driving oscillation can be generated. The “Resonance” page allows the AFM user to sweep the dither piezo through a range of oscillation frequencies and records the oscillation amplitude of the AFM cantilever as measured by the photodiode. Figure 3.13 is a screenshot of the “Resonance” page in the NOVA software and the resonance peak of the AFM cantilever can be seen in the centre of the frequency rage. The “Resonance” page allows the

user to alter the amplitude of the oscillation generator, as well as the gain on the lock-in amplifier recording the deflection signal, and has the option of automatically

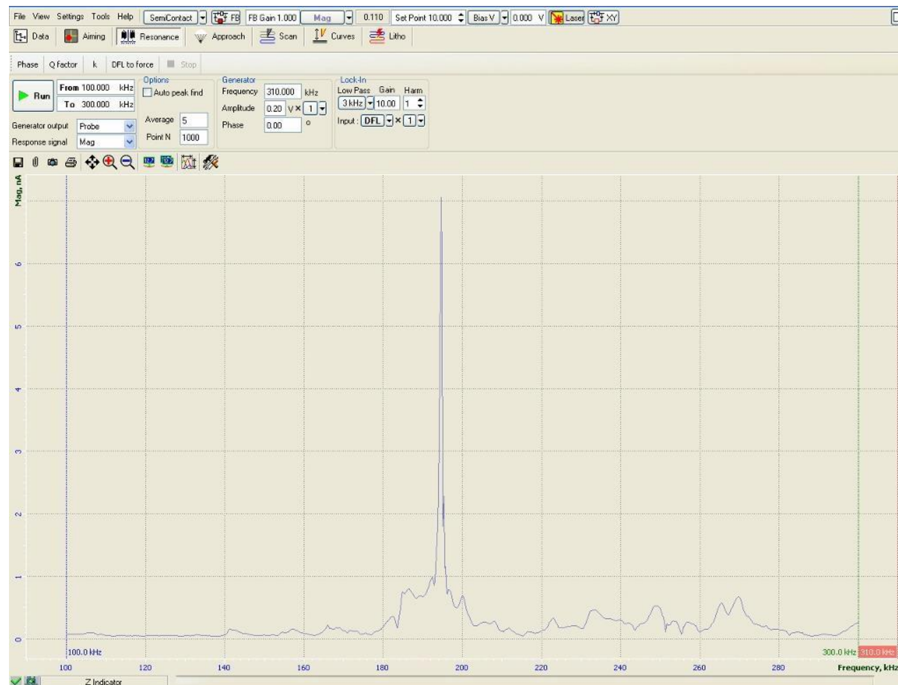

Figure 3.13 Cantilever resonance page in the NOVA AFM software.

locating the resonance of the cantilever within the defined range and setting the oscillation of the piezo to the cantilever resonance. Figure 3.14 is a screenshot of the “Resonance” page with the frequency range automatically centred on the resonance of the AFM cantilever and the generator frequency set to the AFM cantilever resonance. The generator amplitude is altered such that the recorded amplitude at resonance falls between 20 and 25 nA; the working range of the photodiode is 0 to 40 nA.

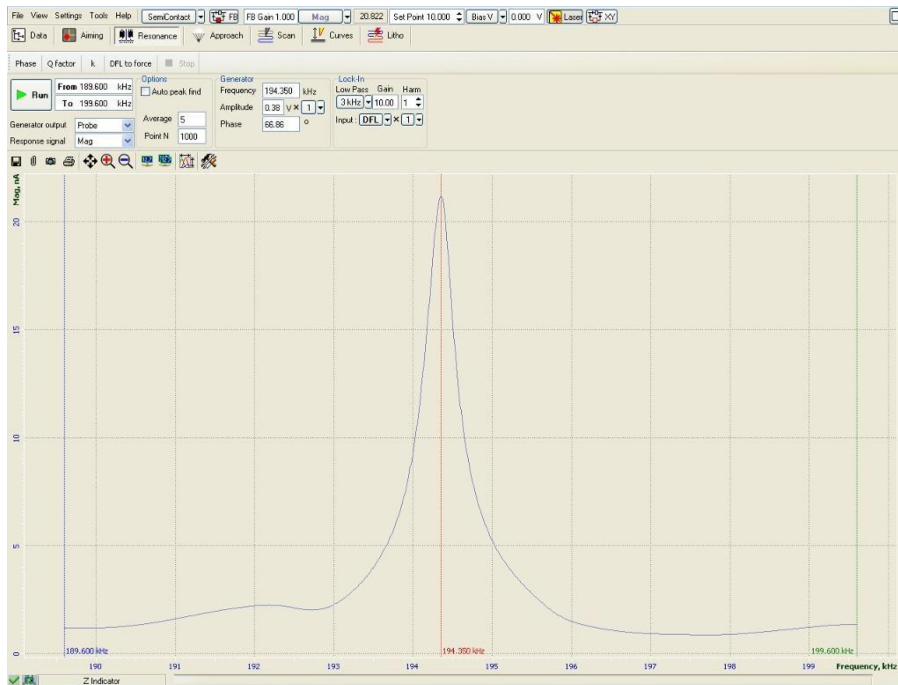

Figure 3.14 An isolated AFM cantilever resonance peak.

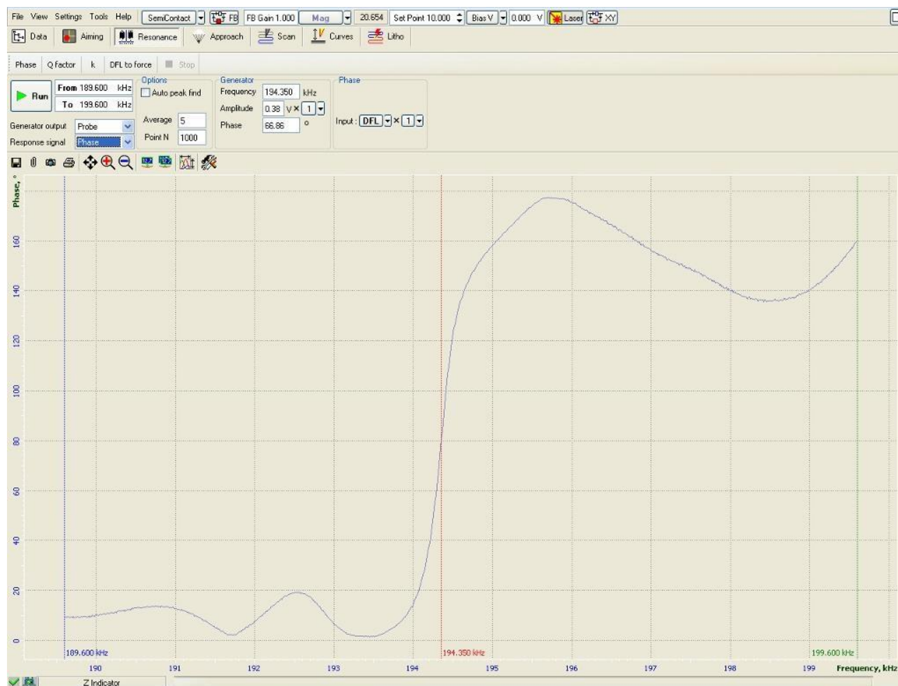

Figure 3.15 The phase response of the AFM cantilever across the resonance peak shown in Figure 3.14

When using the AFM to record phase information in dynamic mode AFM the “Resonance” page is also used to normalise the phase signal. Once the resonance of the AFM cantilever has been located and the generator frequency set, a frequency sweep is repeated, but on this occasion the phase of the AFM cantilever is recorded instead of the amplitude. The phase of the generator is then altered, either using the automated function or manually using a dialogue box, such that the AFM cantilever phase is recorded as 90° at resonance, as shown in Figure 3.15.

The approach of the AFM probe to the sample surface is achieved using the “Approach” page of the NOVA software. The “Approach” page controls the motorised z movement of the sample stage. Prior to approaching the sample, the setpoint for the feedback system needs to be specified. The setpoint value depends on the mode of operation and the signal that is being used in the feedback loop. Typically, if operating in contact mode then the setpoint is set as a positive deflection, such that the cantilever is being deflected away from the sample.

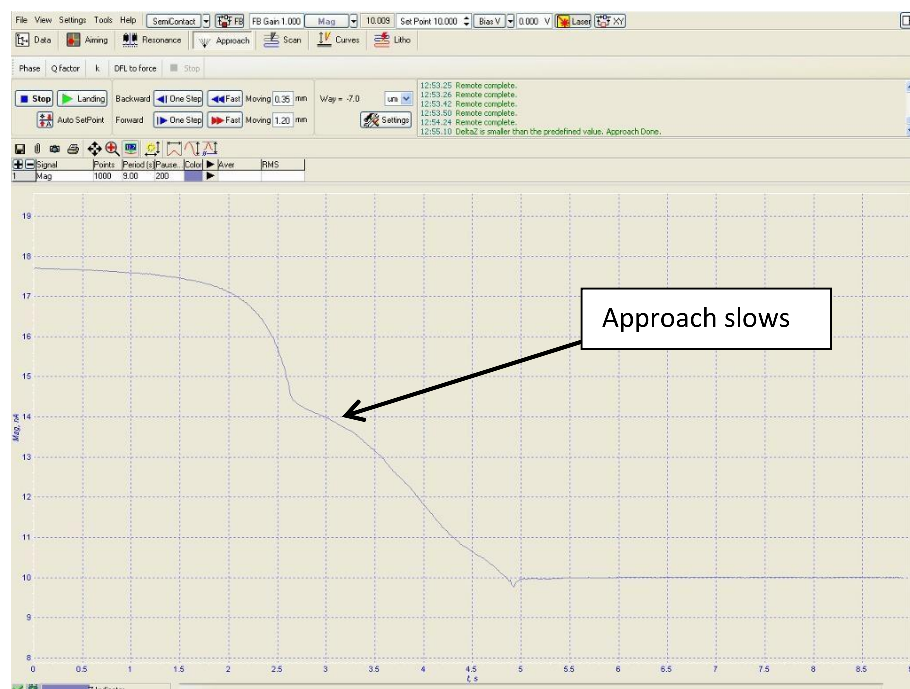

Figure 3.16 The sample approach page of the NOVA AFM software showing the amplitude drop of the oscillating cantilever as the sample is moved towards the probe. The AFM is in amplitude modulated feedback and the approach therefore stops when the amplitude of the cantilever reaches the predefined set point.

When operating in Amplitude Modulated dynamic AFM mode the setpoint is an amplitude value less than the free amplitude of oscillation.

Figure 3.16 is a screenshot of an approach when operating in dynamic mode AFM. The amplitude of the AFM cantilever decreases rapidly as the sample approaches the AFM cantilever. The software slows the approach as the amplitude begins to decrease and stops when the setpoint value is reached. The software aims to achieve the setpoint value when the AFM scanner's z piezo is in the middle of its range, thereby allowing for movement of the AFM scanner in either direction along the z axis. Once the approach sequence is complete the AFM is ready to begin imaging.

3.2.2 Attocube AFM

The attocube AFM system (Munich, Germany) is a customised setup, built from existing components, designed to provide a unique form factor which allows access to the sample from both beams of a small dual beam microscope, as well as the AFM probe. Figure 3.17 is a photograph of the attocube AFM system, which has been adapted so that it can be mounted directly onto the sample stage of a small dual beam microscope (FEI Quanta 3D FEG, Eindhoven, NL) The sample stage of the attocube AFM is composed of three stick-slip positioners, which allow for long range movement of the sample relative to the AFM head. Two attocube ANPx-101 positioners, mounted at 90° to each other, provide movement in the x and y direction. An attocube ANPz-101 positioner provides movement in the z direction.

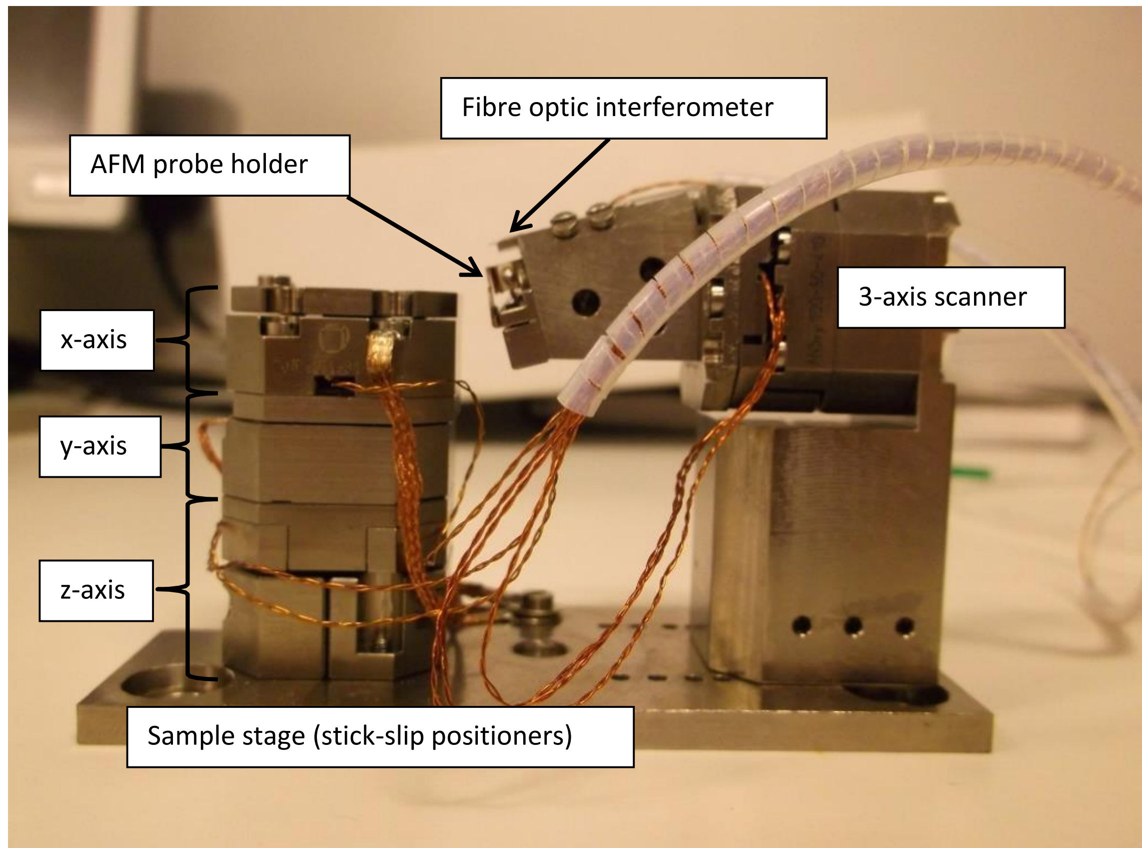

Figure 3.17 A photograph of the attocube AFM. The sample stage is comprised of three independent stick-slip positioners, one for each axis. The scanning AFM head is a support unit mounted onto a three dimensional scanner, consisting of an x-y scanner and a z scanner.

Each of the sample stage positioners has a range of 5 mm. The AFM head unit is mounted onto a 3 axis scanner, which consists of an x-y scanner and a separate z scanner. The attocube ANSxy-100 provides movement of the scanner in x and y directions. The attocube ANSz-100 scans in the z direction. The scanners operate by using a piezo stack to deform the scan frame in a smooth motion, as opposed to the stepping motion of the sample positioners. Samples are mounted to the AFM sample stage through the use of sample blocks, which bolt to the top plate of the x-positioner. Examples of the sample blocks are shown in Figure 3.18 and Figure 3.25.

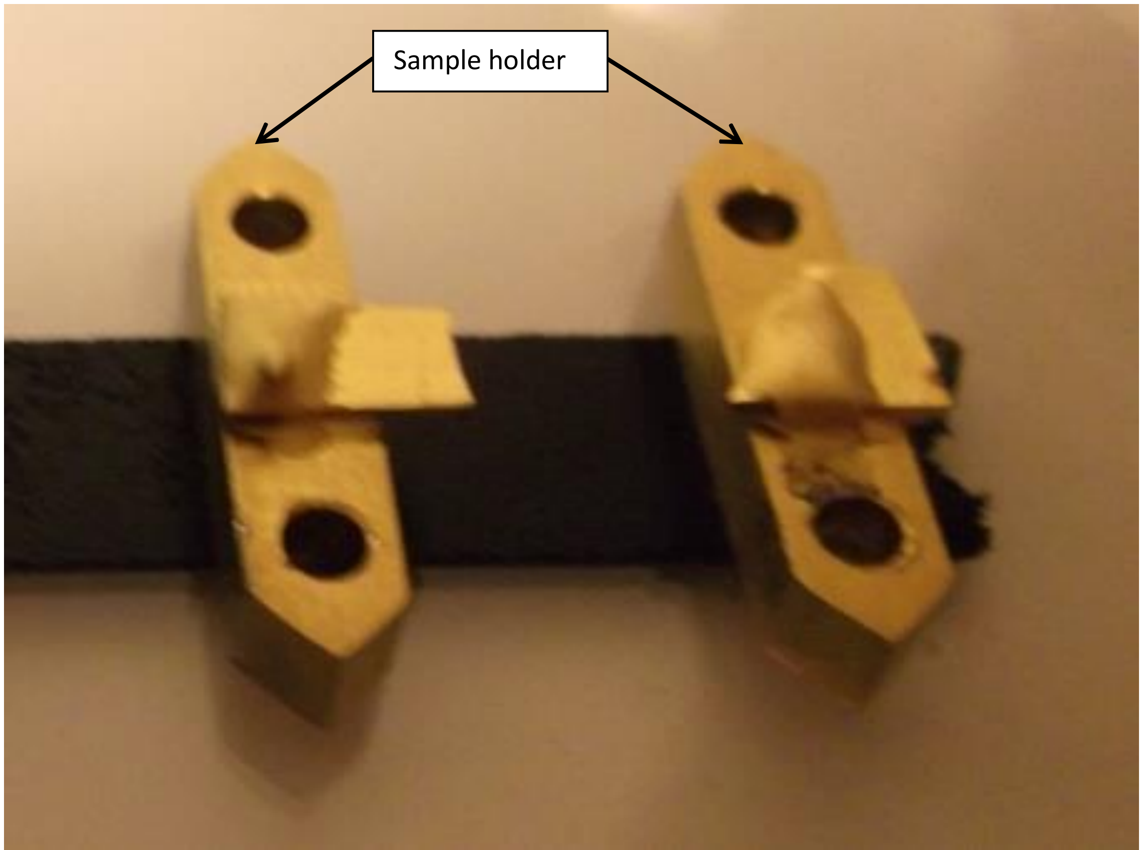

Figure 3.18 Image of polymer nanocomposite samples mounted on attocube AFM sample holders using carbon cement and coated with gold.

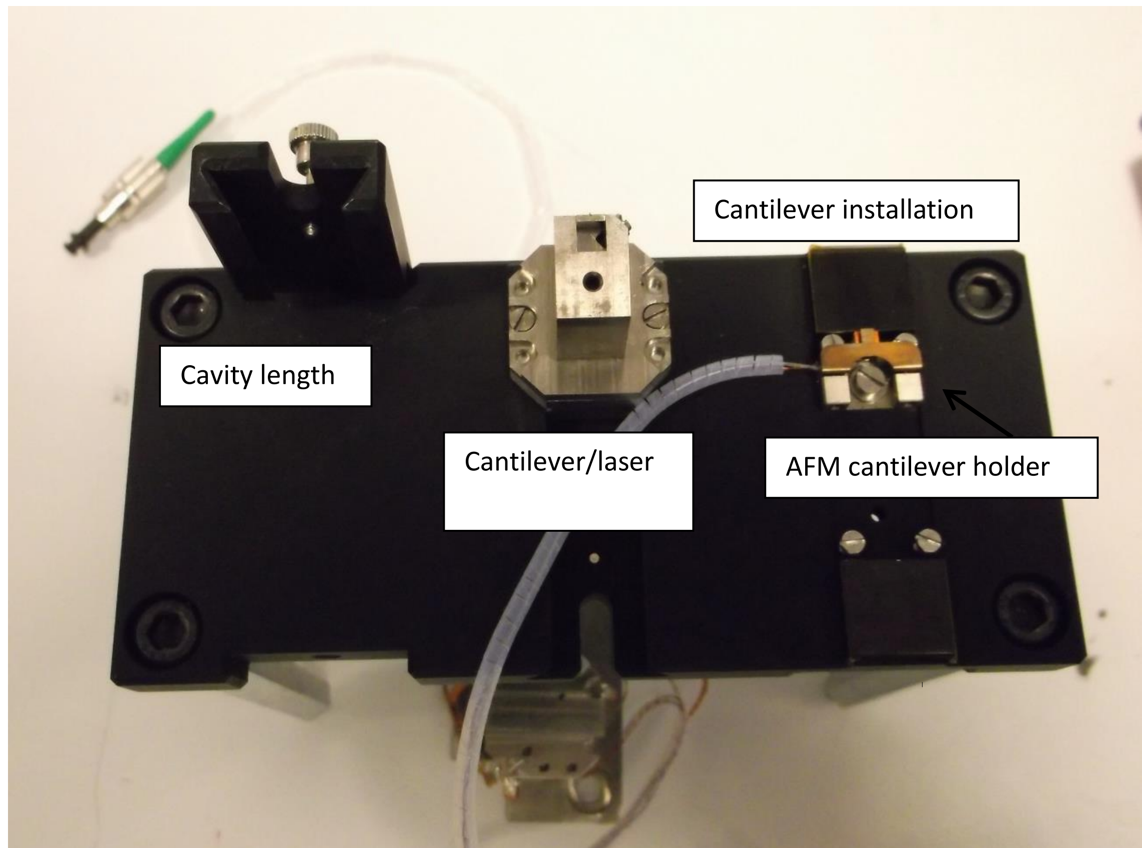

Figure 3.19 The attocube's cantilever alignment table for installing and aligning the AFM cantilever. The right hand station is for installing the cantilever, the middle station for aligning the cantilever with the optical fibre and the left hand station for setting the cavity length between the optical fibre and the AFM cantilever.

The attocube AFM head is attached to the scanning unit by two bolts. The AFM head is removed from the scanners when installing and aligning the AFM cantilever. An alignment table, shown in Figure 3.19, is used to install and align the AFM cantilever. The alignment table has three workstations for different steps in the alignment process. The first workstation, shown to the right of Figure 3.19 and in Figure 3.20, is setup to facilitate AFM cantilever installation. The AFM cantilever holder consists of a dither piezo, for oscillating the AFM cantilever, and a spring clip to secure the AFM cantilever in place. The AFM cantilever installation workstation has two adjustable bolts that hold the spring clip open when the AFM cantilever holder is bolted into place. The workstation also has a support table that is level

with the top surface of the dither piezo, allowing the AFM cantilever chip to be positioned more easily.

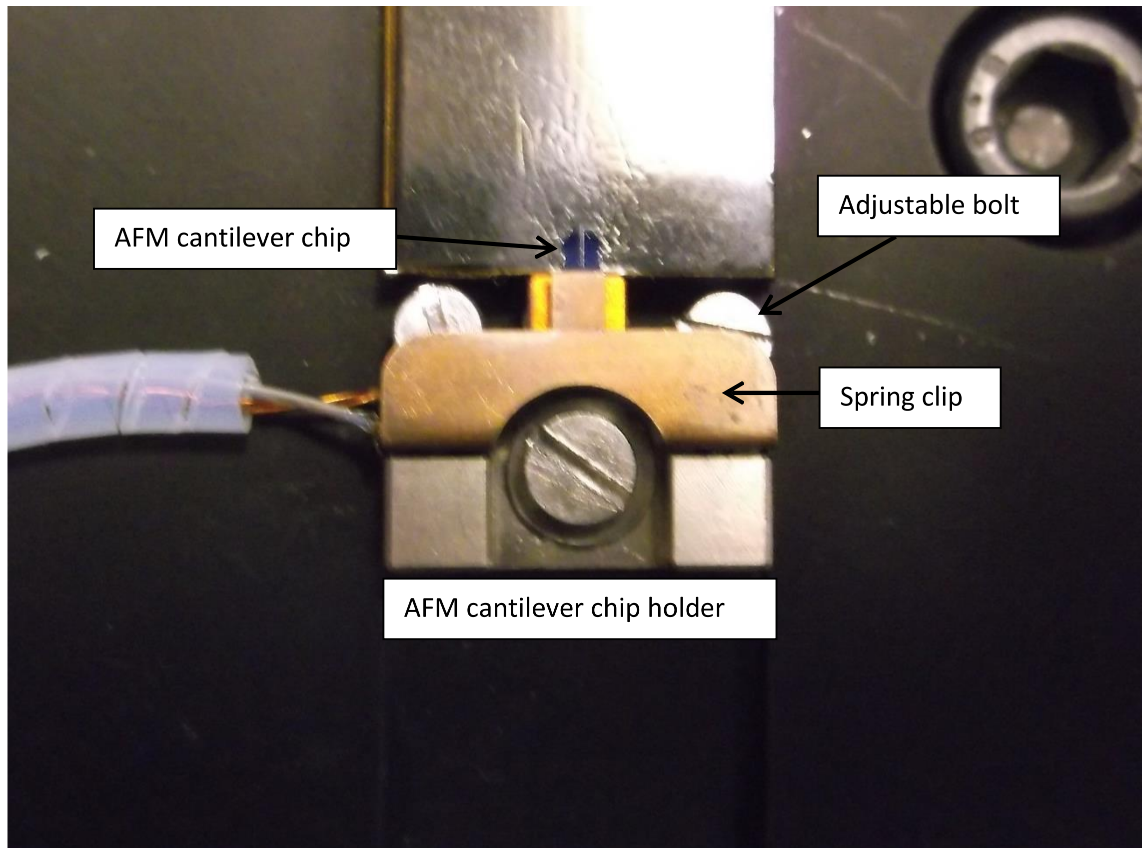

Figure 3.20 The AFM cantilever chip holder from the head of the attocube AFM. The AFM cantilever chip is held against the dither piezo by a spring clip, which is held open by the adjustable bolts of the alignment table when the chip holder is bolted to the work station.

Once the AFM cantilever chip has been installed in the holder the centre workstation is used to support the AFM head while the AFM chip holder is reattached and the AFM cantilever is aligned with the laser fibre optic. Figure 3.21 contains photographs of the AFM chip holder having been reattached to the AFM head piece. Figure 3.21a shows the position of the optical fibre relative to the AFM cantilever chip.

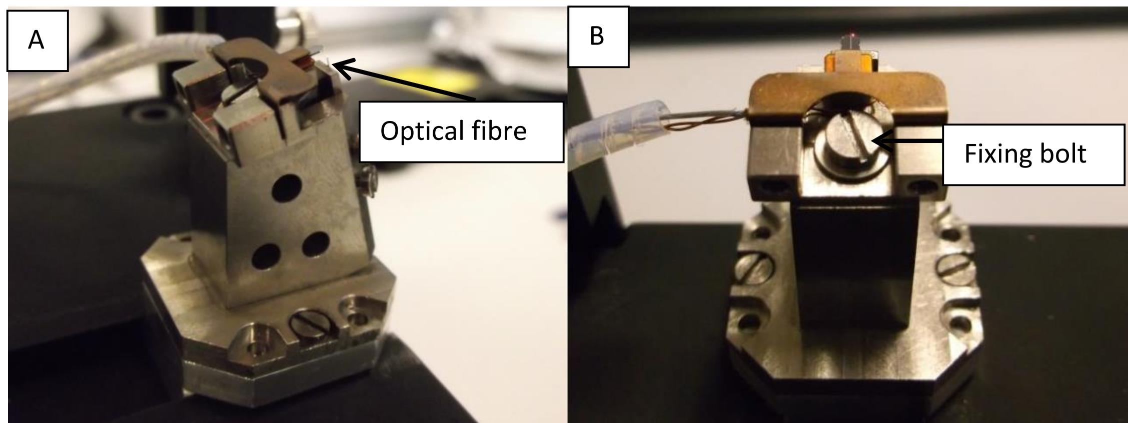

Figure 3.21 The AFM chip holder mounted onto the attocube AFM head piece.

A red laser is used to align the AFM cantilever with the optical fibre. A piece of scrap paper is attached to a screw driver, shown in Figure 3.22 and this then acts as a screen onto which an image of the AFM cantilever is projected by the laser light. The screw driver is used to loosen the fixing bolt, which holds the AFM chip holder to the head piece, allowing for movement of the AFM chip holder. The AFM chip holder is manually positioned such that a shadow of the AFM cantilever can be seen on the paper. The AFM cantilever should be positioned so that the long axis of the shadow is in line with the centre of the laser spot and should extend beyond the centre of the laser spot, as shown in Figure 3.22. With the AFM cantilever correctly aligned, the fixing bolt is tightened again to prevent movement of the AFM chip holder.

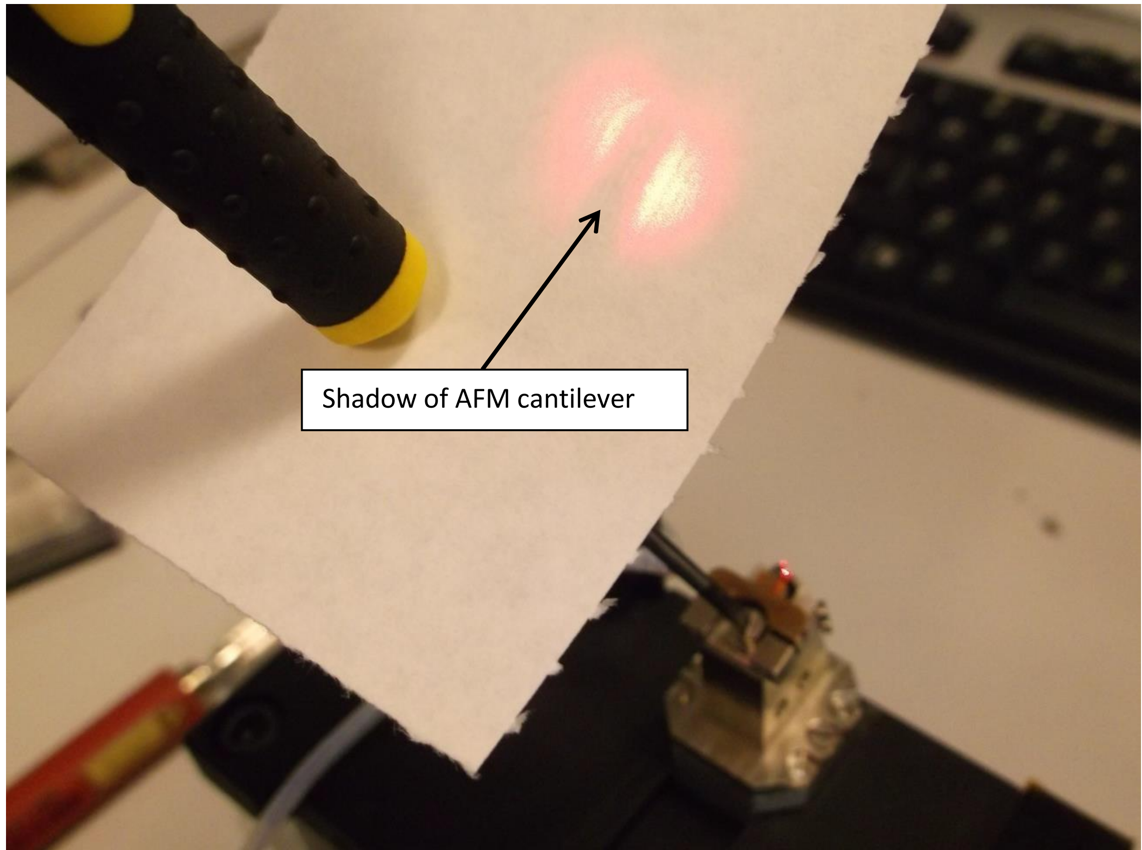

Figure 3.22 Red laser light is used to align the AFM cantilever by projecting a shadow of the AFM cantilever onto a piece of paper. The paper is attached to a screwdriver which is used to tighten the chip holder in place once aligned.

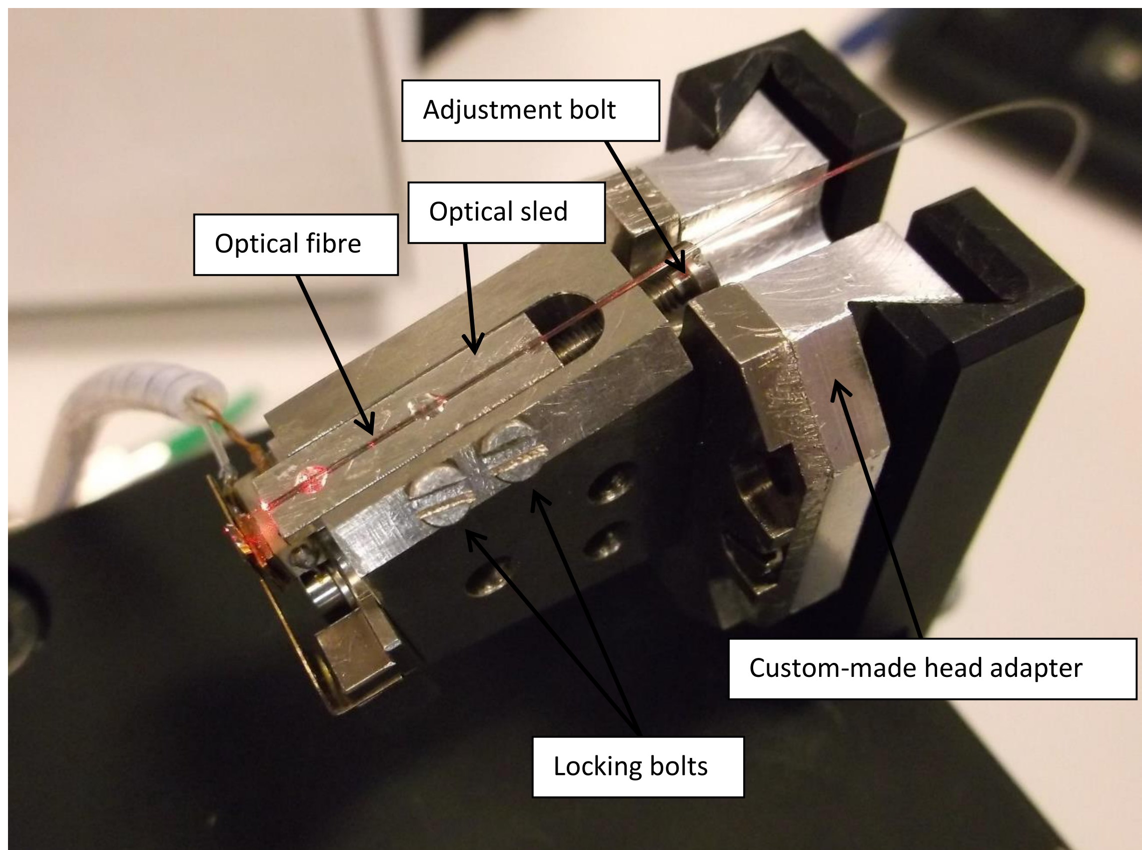

Figure 3.23 The attocube AFM head and chip holder in the final work station of the alignment table. The optical fibre working distance is set by using the adjustment bolt at the rear of the head to push the sled supporting the optical fibre towards the AFM cantilever. The laser intensity reading is monitored using the AFM software in order to determine the correct distance.

With the AFM cantilever installed and aligned with the optical fibre the AFM head piece is transferred to the final workstation of the alignment table, shown in Figure 3.23, which allows for the setting of the optical fibre working distance. The free end of the optical fibre should be positioned within 50 to 150 µm of the back of the AFM cantilever in order to maximise the amount of reflected light being collected by the interferometer without contacting the AFM cantilever. In order to set the working distance, the optical fibre is connected to the infrared (1310 nm) laser unit of the AFM control electronics. The attocube AFM software is used to monitor the interferometer signal as the optical fibre is moved towards AFM cantilever. The laser intensity is set to between 0.035 and 0.04 mW while setting the working distance. The

locking bolt shown in Figure 3.23 secure the optical sled in place during operation and therefore need to be loosened before the working distance can be altered. The front locking bolt is loosened off first and then tightened again to the point when it first contacts the optical sled. The rear locking bolt is loosened off completely. By having some pressure on the optical sled from the front locking bolt the optical sled is prevented from moving due to gravity, but is free enough to move with an application of force from the adjustment bolt. Whilst monitoring the laser intensity signal in the AFM software the adjustment bolt is tightened so that the optical sled and fibre are pushed towards the AFM cantilever. The typical laser intensity signal observed during the alignment process is shown in Figure 3.24. The laser intensity detected by the control electronics oscillates sinusoidally as the gap between the fibre and the AFM cantilever is closed, and the interference switches between constructive and destructive. The average intensity of the detected laser light increases as the gap is closed, and the approach is completed when the laser intensity reaches 10 V. The locking bolts are tightened fully to prevent slippage of the optical sled and the adjustment bolt is backed off. The AFM head piece is now ready to be mounted onto the AFM scanner.

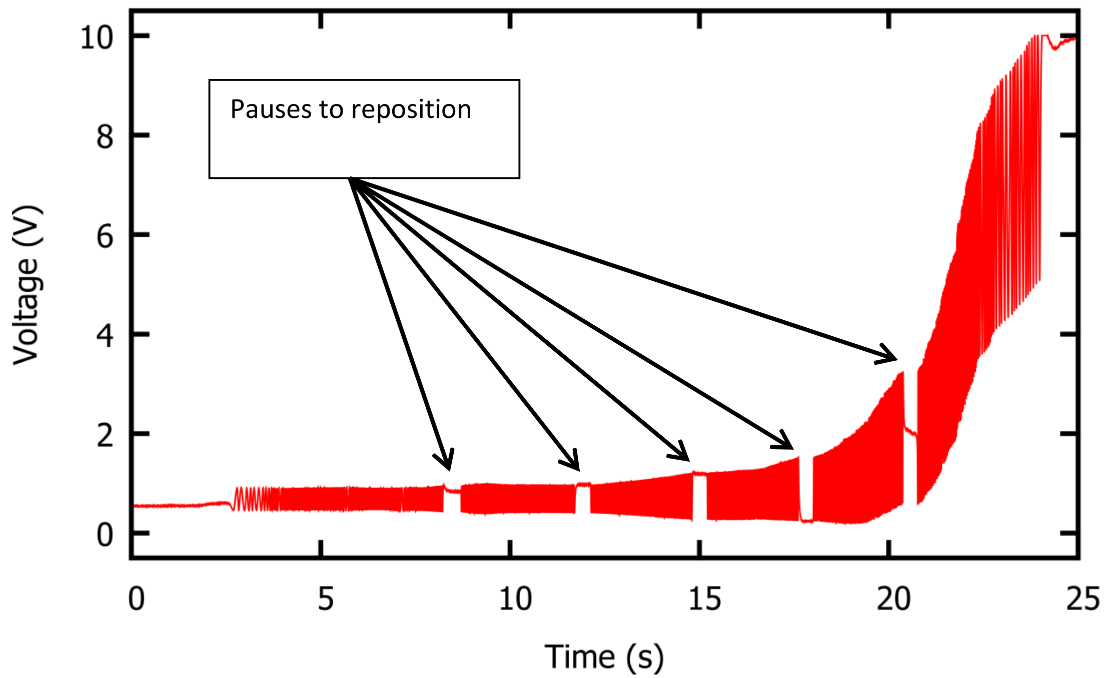

Figure 3.24 The laser intensity recorded whilst setting the fibre-cantilever working distance. The attocube AFM records the laser intensity as a voltage from the photodiode, which is plotted on the y-axis. The fibre optic acts as an interferometer, with interference occurring between the light reflected from the AFM cantilever and the light internally reflected at the end of the fibre. The interference leads to the oscillating intensity seen here as the optical fibre is moved towards the AFM cantilever.

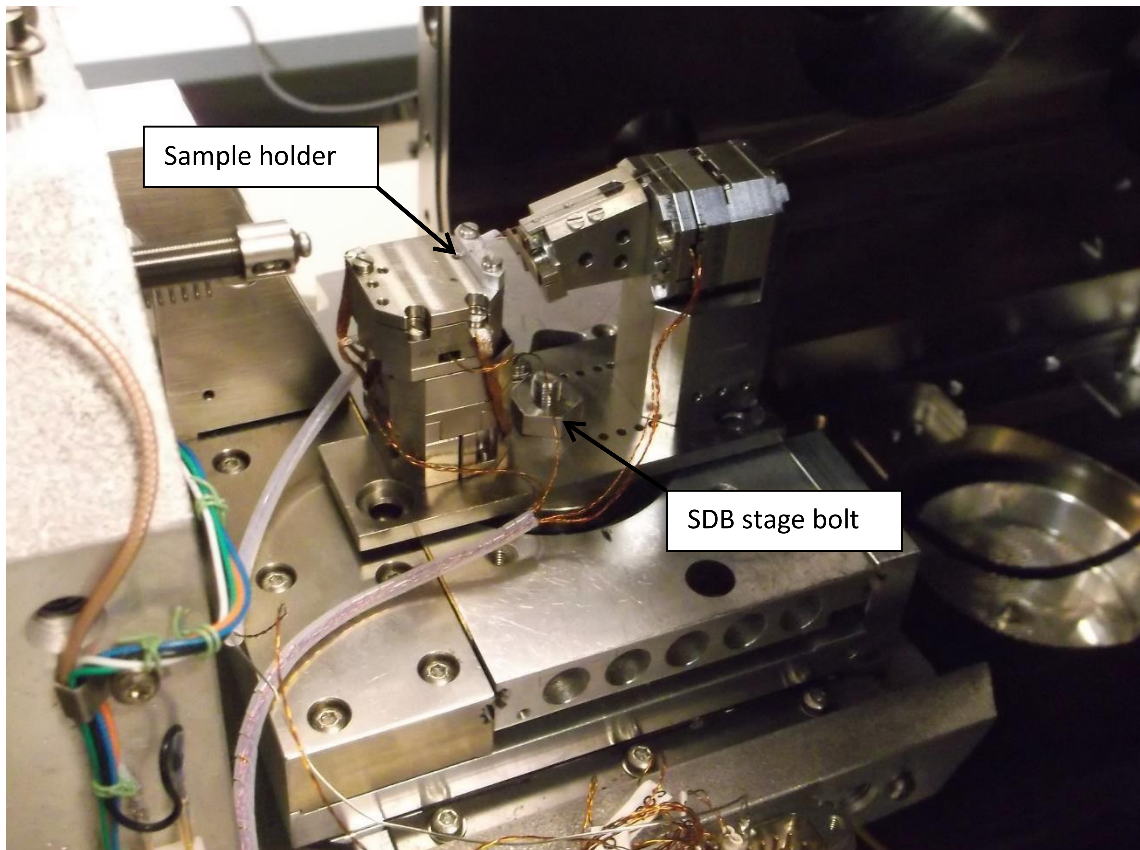

Figure 3.25 The attocube AFM mounted onto the mechanical sample stage of the FEI Quanta 3D FEG Small Dual-Beam microscope. The base plate of the AFM has been adapted so that it can be bolted directly into the stage.

The baseplate of the attocube AFM has a hole through the centre, which allows the AFM to be bolted to the mechanical stage of the SDB microscope. The AFM can be moved in x, y and z and tilted as required. Small rotations are also possible, but care must be taken not to strain the optical fibre or the electrical connections. Figure 3.25 is a photograph of the attocube AFM mounted on the mechanical stage of the FEI Quanta 3D FEG. A feed-through port is used pass the wiring and optical fibre through the microscope chamber door.

3.2.3 Calibration of AFM cantilevers

The spring constants of AFM cantilevers were calculated using the method described by Sader *et al*.[99]. The cantilevers to be used were first observed optically and the dimensions of width

(b) and length (L) were measured using a CCD camera and ImagePro Express software, having first been calibrated against a standard reticule. An example optical image of an AFM cantilever is given in Figure 3.26. The width of the cantilever was measured at 5 positions along its length, with two measurements at each position (the inner and outer width as marked in Figure 3.26) to account for the trapezoid cross-section. The mean average of all of the measured widths was used for the spring constant calculation. The length of the cantilever was measured from the base where the cantilever meets the supporting chip to the centre of the probe tip, as shown in Figure 3.26.

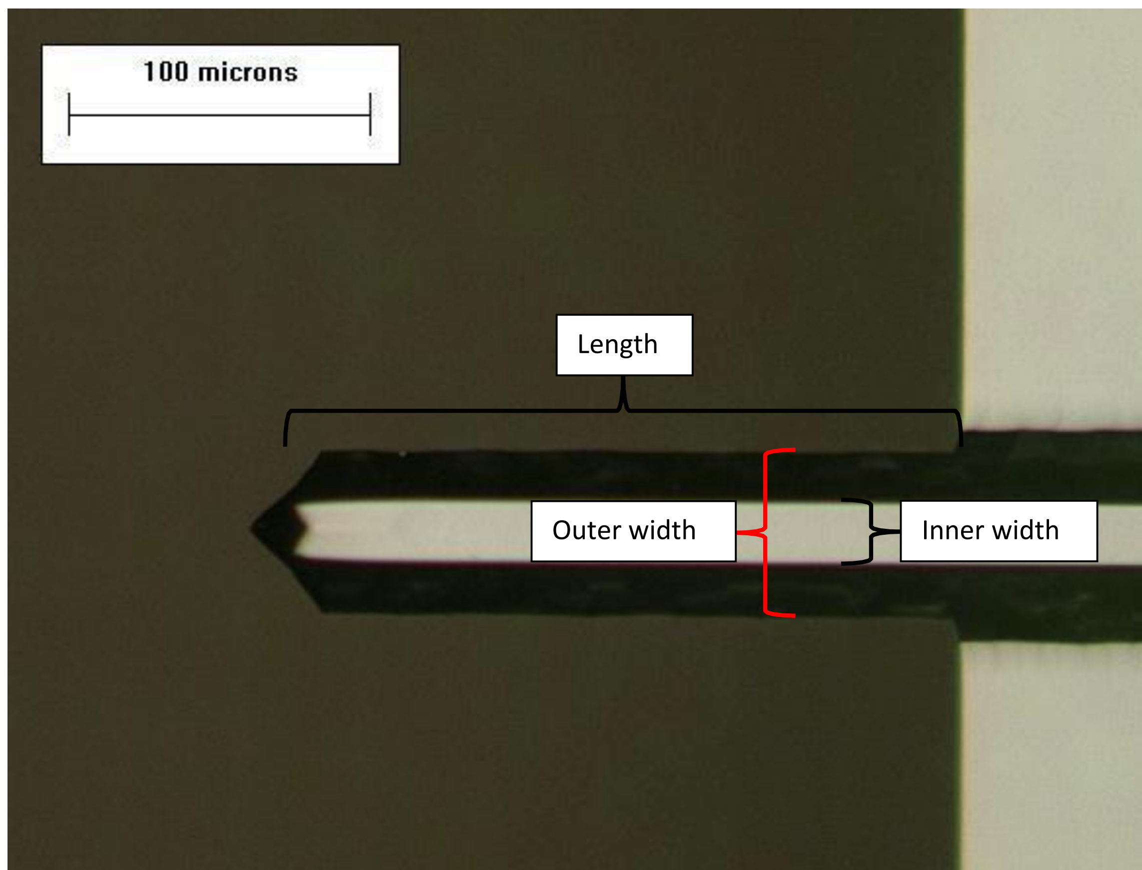

Figure 3.26 An optical image of an AFM cantilever being measured for calibration.

With the width and length of the cantilever known, it was installed into the NTegra AFM and the primary resonance peak identified. A script within the NOVA software of the NT-MDT AFM was used to calculate the spring constant based on user input values for the dimensions of the

AFM cantilever and the measured resonance frequency and quality factor. The script assumes that the density (ρ_f) and viscosity (η) of air are 1.18 and 1.8 x 10^{-5} kg/(m.s) respectively, and uses these values to calculate the imaginary part of the hydrodynamic function with respect to frequency (Γ_i). The spring constant is then calculated using Equation 3 as described by Sader. [99]

$$k_z = 0.1906\rho_f b^2 L Q_f \omega_f^2 \Gamma_i(\omega_f)$$

Equation 3

The script outputs the value of k as a popup dialogue box.

3.2.4 Imaging

The NTegra AFM is capable of imaging in contact, semi-contact and noncontact modes, as well as outputting a variety of signals depending on the type of AFM tip-sample interaction that is of interest. Contact and semi-contact modes were used in this thesis and are therefore described in more detail here.

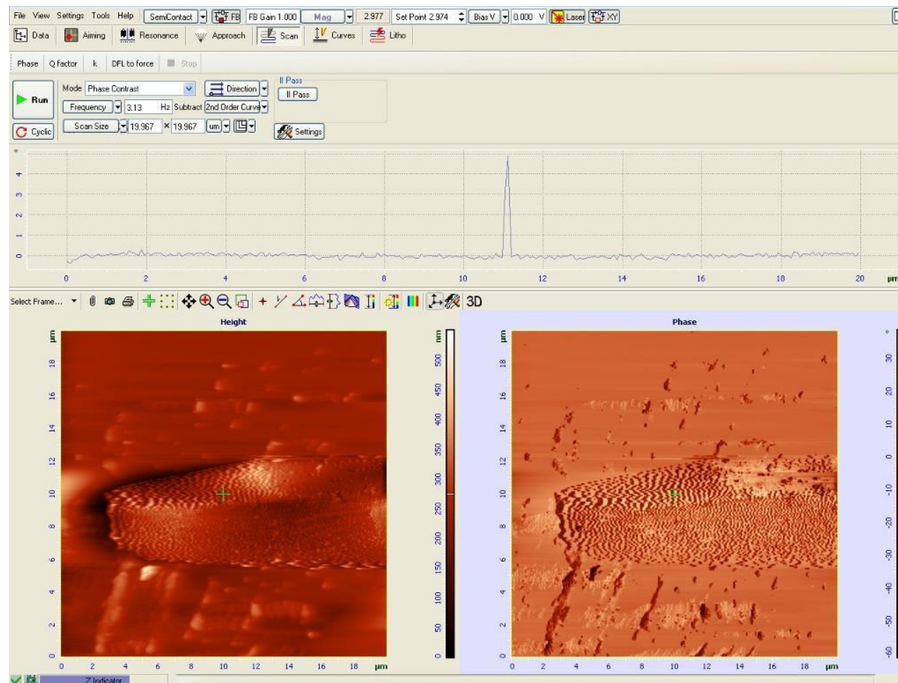

Figure 3.27 The imaging page of the NOVA software. Each line trace in the scan is displayed as 2D data at the top of the page, whilst the 3D datasets are presented underneath with up to 4 datasets being collected at once (two channels in each scan direction)

3.2.4.1 Contact mode

Contact mode AFM uses the AFM cantilever deflection signal for the z scanner feedback loop and thereby maintains a constant contact force between the AFM tip and the sample surface. As the AFM cantilever is scanned in x and y relative to the sample surface the deflection is maintained by the feedback loop by altering the extension of the z scanner. The relative extension of the z scanner at each point in the image is recorded as the height of the sample. Contact mode typically is not used for imaging polymeric or biological samples as the shear stresses at the sample surface during scanning plastically deform the sample. However, contact mode is used during force/displacement spectroscopy measurements and can be used during scanner calibrations, which requires the imaging of Silicon standards. Force displacement measurements are described in section 3.2.5 and scanner calibration is described in section 3.2.6

3.2.4.2 Semi-contact mode imaging

Semi-contact, or dynamic AFM imaging, is used for relatively soft samples, such as polymeric or proteinaceous materials, as the intermittent contact forces are lower than those experienced during contact mode imaging and the shear forces during imaging are negligible.

During dynamic AFM imaging the AFM cantilever is driven by the dither piezo to oscillate at or very near its resonance frequency. The amplitude of the AFM cantilever is then monitored and a setpoint amplitude maintained by the feedback system. As the separation of the AFM cantilever and the sample surface is reduced, the interaction between the AFM tip and the sample damps the oscillation of the AFM cantilever and the amplitude of the AFM cantilever is reduced. In order to maintain the setpoint amplitude of the AFM cantilever, the feedback loop modulates the extension of the z scanner in much the same way as described for contact mode in section 3.2.4.1.

3.2.4.3 Phase contrast imaging

Phase contrast imaging is an imaging mode based on dynamic AFM imaging. The phase signal recorded by the AFM is a measure of the lag between the oscillation of the end of the AFM cantilever and the oscillation of the dither piezo that drives it. After collecting a topography/height image of the area of interest on a sample, the feedback loop was turned off so that the z scanner was fully retracted. When the z scanner is fully retracted it is pulled away from the sample surface. The phase signal being recorded by the AFM software could then be normalised as described in section 3.2.1. A second channel was set to record the phase signal during imaging, which was collected simultaneously with the height information. The feedback loop was then reactivated and was still maintaining setpoint amplitude. Whilst scanning the sample the amplitude of the AFM cantilever oscillation was maintained and the height and

phase information recorded to form two simultaneous images. An example of phase contrast imaging is shown in Figure 3.27.

3.2.5 Mechanical measurement by AFM z-spectroscopy

Force/displacement measurements were carried out using the AFM z-spectroscopy. The AFM cantilever is a force sensor with a force resolution of the order of piconewtons, and coupled with the positioning accuracy of a piezo actuated scanner makes an ideal nanomechanical testing rig. The scanners in the NTegra AFM are fitted with capacitance sensors and a closed loop system, which means that the AFM probe can be repeatedly positioned over an area of interest on the sample with sub-nanometre accuracy.

An image of the sample was first recorded using semi-contact mode to be used as a reference map for subsequent spectroscopy. In order to perform force/displacement measurements the AFM needs to be in contact mode, so the tip was retracted from the sample surface and the mode switched. When switching to contact mode the oscillation generator is automatically turned off and the signal for the closed loop is switched to cantilever deflection. The setpoint for the feedback loop was set to a deflection signal of 2 nA and the position of the test defined using the reference image. The feedback was restored and the AFM probe landed on the sample surface. With the AFM now in contact mode the range of motion in z was specified relative to the setpoint condition and the testing rate was defined. The spectroscopy page of the NOVA software can be seen in Figure 3.28. The spectroscopy page of the NOVA software displays the reference image to the left of the page and the results of the force/displacement test to the right. The reference image includes a marker to show were the test was carried out. The spectroscopy page records both the landing and retraction curves, which can be more clearly observed in Figure 3.29.

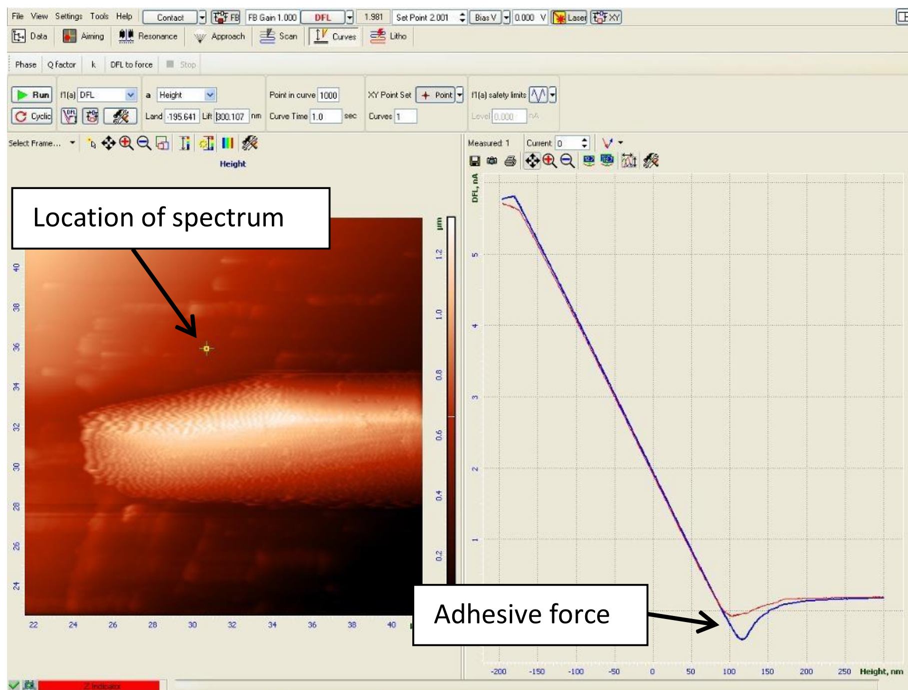

Figure 3.28 The spectroscopy page of the NOVA software. In this instance the data collected is AFM cantilever deflection against height.

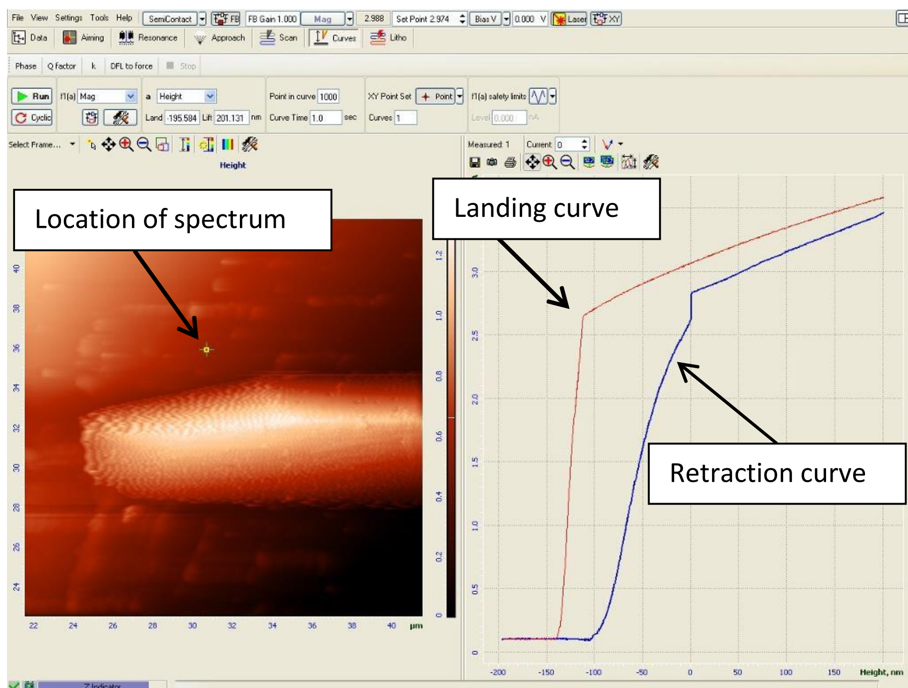

Figure 3.29 The spectroscopy page of the NOVA software. The right hand window shows an amplitude against height plot and the left hand window indicates where on the sample the data was collected from.

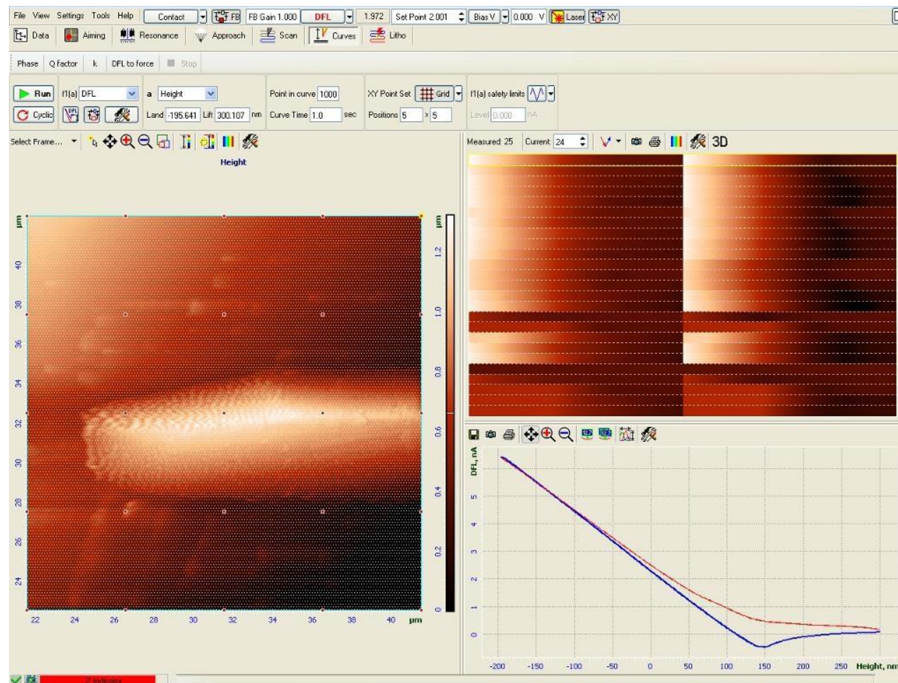

Figure 3.30 The spectroscopy page of the NOVA software, showing a grid array of deflection against height curves.

3.2.6 Calibration of AFM piezo scanners

AFM piezo scanners are capable of fine movement, but the hysteretic nature of piezo crystals means that they require calibration and compensation. The NTegra AFM uses capacitance sensors to measure the position of the piezo scanners in order to cancel out these effects and minimise drift in the scanning system. The scanners require calibration against known standards to maintain their accuracy. Two types of calibration standard are used for calibrating the AFM scanners; an x/y calibration standard and a z standard.

3.2.5.1 x/y calibration

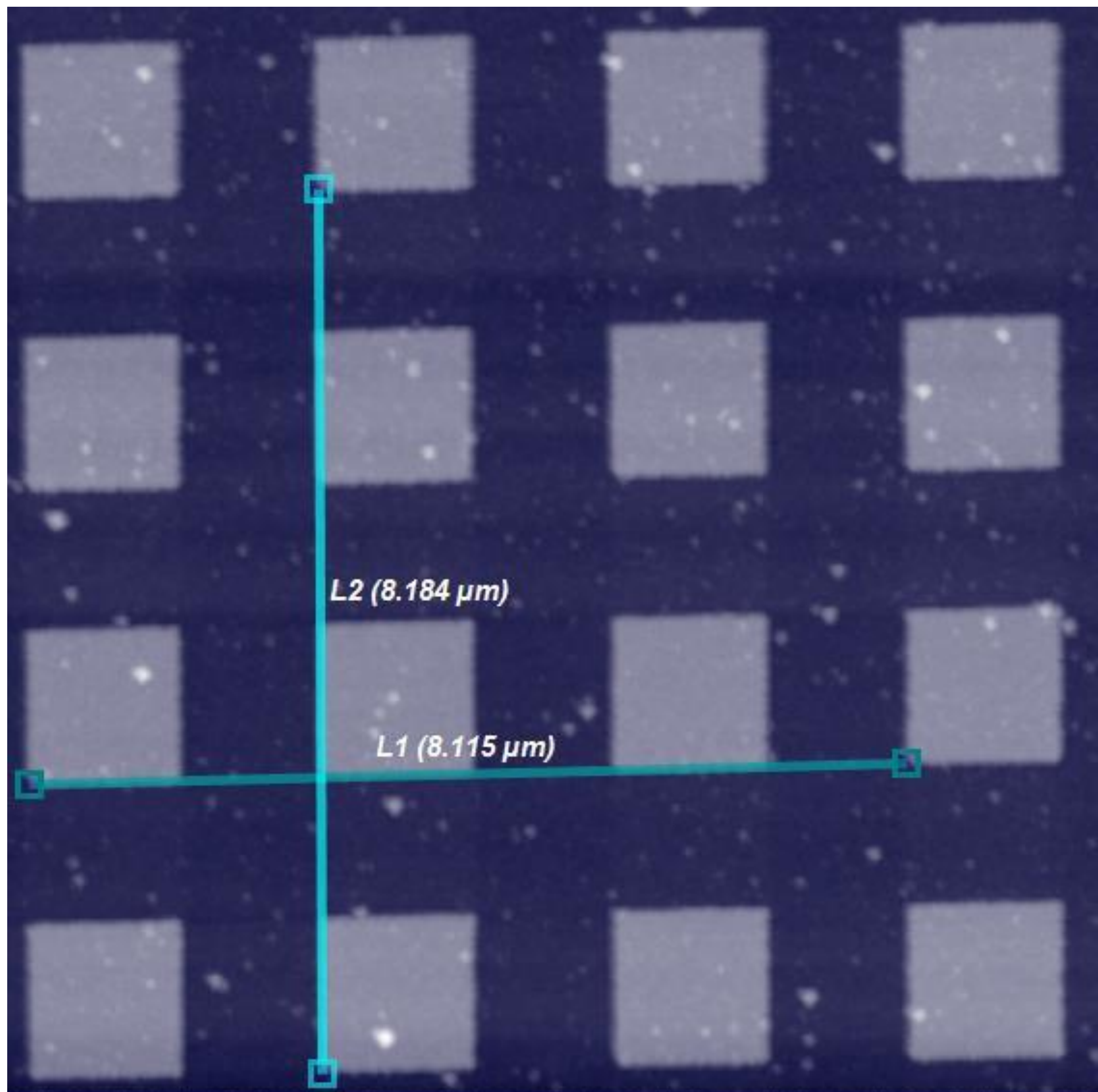

Figure 3.31 AFM height image of an AFM xy calibration grating. The spatial frequency of the squares is 3 µm.

The x/y calibration standard is a section of silicon wafer that has had a regular pattern etched into the SiO_2 layer on the surface. The pattern in the standard is a grid of square islands that have a periodicity of 3.0 ± 0.05 µm, shown in Figure 3.31. The line measurements shown in Figure 3.31 each span 3 periods in the calibration grating and therefore should measure 9.0 µm. However, they are both underestimating the distance, and so the scaling factors in the NOVA software need to be redefined.

3.2.6.1 *z calibration*

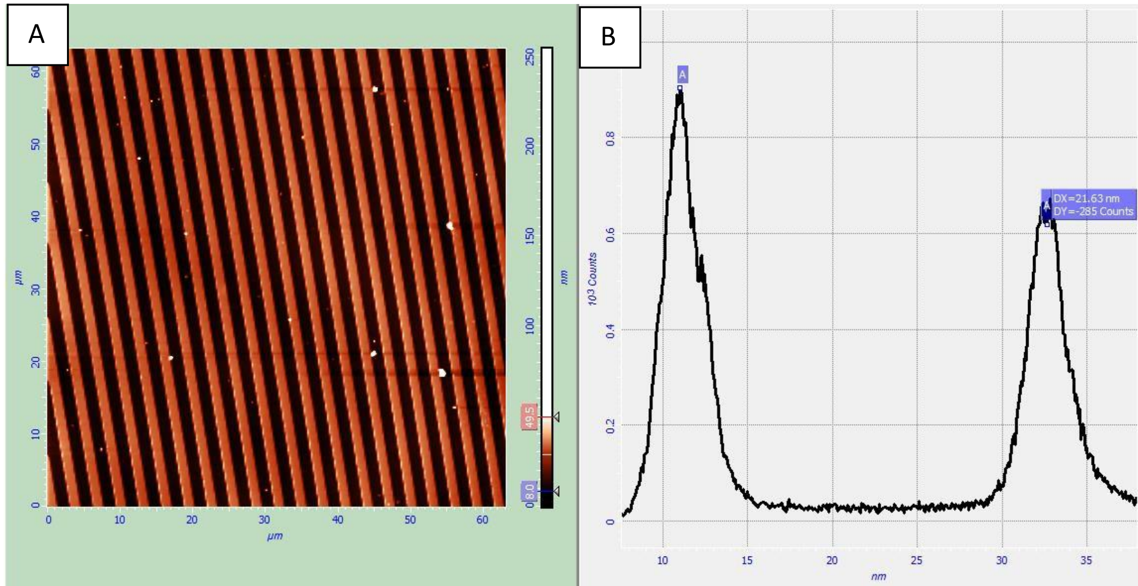

Figure 3.32 a) AFM height image of an AFM z calibration grating. The height of each ridge is 18.5 nm. b) histogram of the height distribution of the calibration grating image.

The z calibration grating is a section of silicon wafer with periodic trenches etched into the SiO_2 layer on the surface. The trenches have a spatial frequency of 3.0 ± 0.05 µm and a step height of 18.5 ± 1 nm. Figure 3.32a is a baseline corrected AFM height image of the z calibration grating. To calibrate the z scanner, the height data is plotted as a histogram of counts against height, shown in Figure 3.32b, and the separation of the two peaks is measured in nanometres. A comparison of the measured step size and that reported on the standard was used to adjust the scaling factor for the z scanner.

3.3 Clamping sample holder for AFM and SEM

In order to image the cross-sections of thin films and shell in both the AFM and the SEM without the need to remount the sample, a customised sample holder was designed and manufactured in the QMUL workshop. The sample holder was designed to clamp the sample vertically, between two flat surfaces, such that the cross-section becomes the top surface. The

base of the sample holder is flat so that it can be placed on the stage of the AFM. A threaded pin, that screws into the base of the sample holder, allows the sample to be mounted on the standard sample stage of the FEI SEMs. Figure 3.33 contains four different views of the clamping sample holder. Figure 3.33a is a photograph of the threaded SEM pin, mounted in a plastic support, that can be attached to the base of the sample holder. Figure 3.33b is a photograph of the clamping sample holder mounted on the threaded SEM pin. Figure 3.33c & d are photographs of the clamping sample holder, without the SEM pin, from a top down and elevation view respectively. The clamp is held against the sample by a grub screw and a recess around the base allows the sample holder to be handle with standard SEM pin stub grippers.

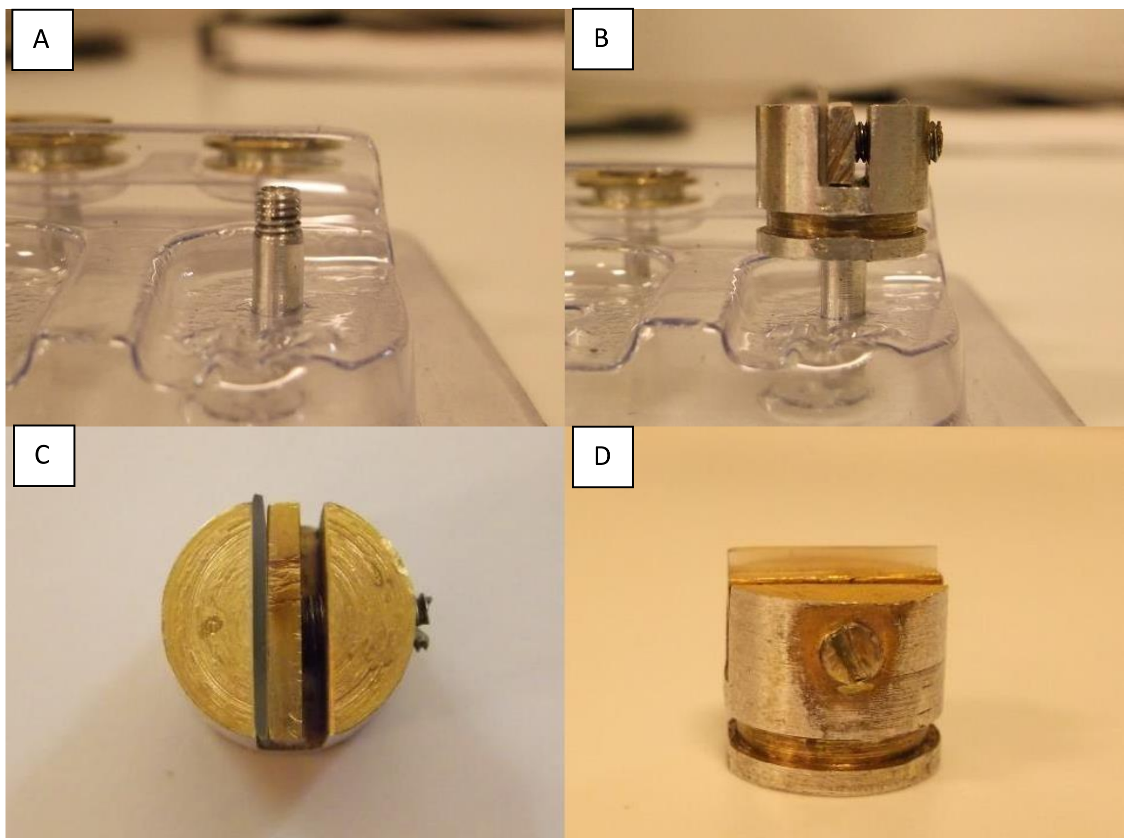

Figure 3.33 Images of the clamping sample holder. a) The removable pin for mounting the sample holder in the SEM. b) The sample holder on the removable pin. The sample is held in place by tightening the grub screw against the clamping plate. c) A top down view of the sample holder. d) The side view of the sample holder.

3.4 Secondary electron microscopy

Secondary electron microscopy was used for imaging and elemental analysis of samples. The two analytical SEMs in the NanoVision Centre are shown in Figure 3.34. Figure 3.34a is a photograph of the FEI Quanta 3D FEG, which is a Small Dual Beam (SDB) system. Figure 3.34b is a photograph of the FEI Inspect F, which is the main analytical system. Both SEMs have Field Emission Gun (FEG) sources. The Inspect F operates at high vacuum and images with either an Everhart-Thornley secondary electron detector or an annular backscattered electron detector. In addition to the electron imaging detectors, the Inspect F is fitted with Energy Dispersive Spectroscopy (EDS) and Wavelength Dispersive Spectroscopy (WDS) for elemental analysis, and an Electron Backscatter Diffraction (EBSD) detector.

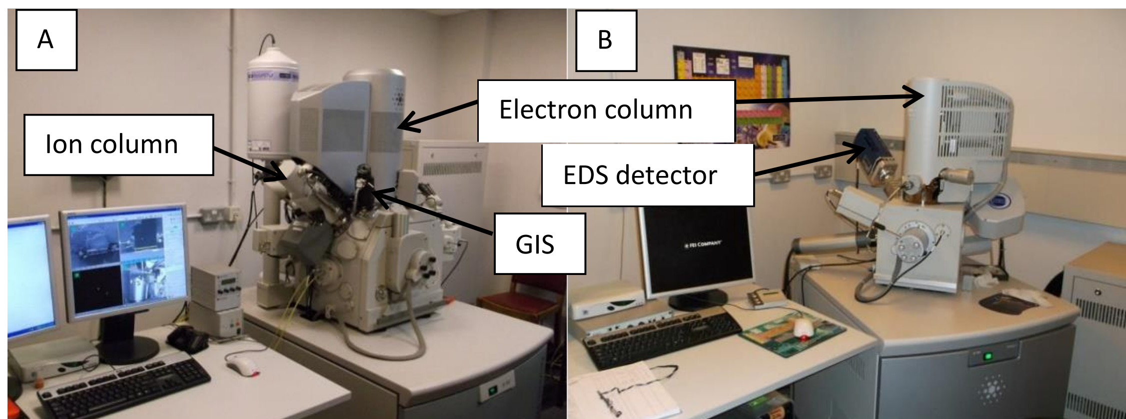

Figure 3.34 a) FEI Quanta 3D FEG, the FIB-SEM that was used for all FIB work and SEM-AFM work. b) FEI Inspect F, the analytical SEM, used for SEM and EDS.

The Quanta 3D FEG is an SDB system with a Gallium Focussed Ion Beam (FIB) and a large, variable pressure chamber. At high vacuum the Quanta is able to image using an Everhart-Thornley secondary electron or backscattered electron detector when scanning with the primary electron beam, or with the secondary electron detector when scanning the sample with the FIB. The Quanta also has an EDS detector for elemental analysis and a cryostage for the preparation cryogenically frozen samples. When operating in low vacuum and

Environmental SEM (ESEM) mode, imaging is achieved using a Low Vacuum Secondary Electron Detector (LVSED) or a Gaseous Secondary Electron Detector (GSED) respectively. The FIB can only be used in high vacuum mode, and although it is capable of being used for sample imaging, it is primarily used for sample machining as sputtering occurs in areas exposed to the beam. A Gas Injection System (GIS) on the Quanta allows for Platinum deposition on the sample surface by injecting methylcyclopentadienyl-trimethyl platinum $(CH_3)_3Pt(C_pCH_3)$, an organometallic precursor gas which adsorbs onto the sample surface and degrades under the FIB, leaving a build-up of Platinum on the sample surface.

3.4.1 Imaging with the SEM

When imaging with the SEMs, the image quality is greatly dependent on the alignment of the electron beam and the apertures. The path of the electron beam down the electron column passes through a fixed beam limiting aperture followed by the first condenser lens (C1). The beam then passes through the second condenser lens (C2) and through a variable aperture. The C1 and C2 lenses de-magnify the crossover of the electron beam within the column to produce a smaller spot size. After the variable aperture the beam passes through the objective lens, the magnification control and the scanning coils, which control the focus, magnification and scanning of the final beam respectively. Altering the variable aperture control the amount of current reaching the sample. For the Quanta the aperture for standard imaging is 30 µm in diameter, and for high resolution imaging a 20 µm aperture can be used. However, reducing the aperture size, and therefore the beam current, also has the effect of reducing the signal to noise ratio.

The FEI Quanta 3D FEG has an additional condenser lens (C0) prior to the fixed beam limiting aperture, which directs more of the electrons emitted from the FEG through the fixed aperture, resulting in higher beam currents. The first step in aligning the electron beam when

using the Quanta is therefore to align the C0 lens to maximise the number of electron entering the column. The C0 lens alignment application page of the Quanta control software (xTUI) is shown in Figure 3.35.

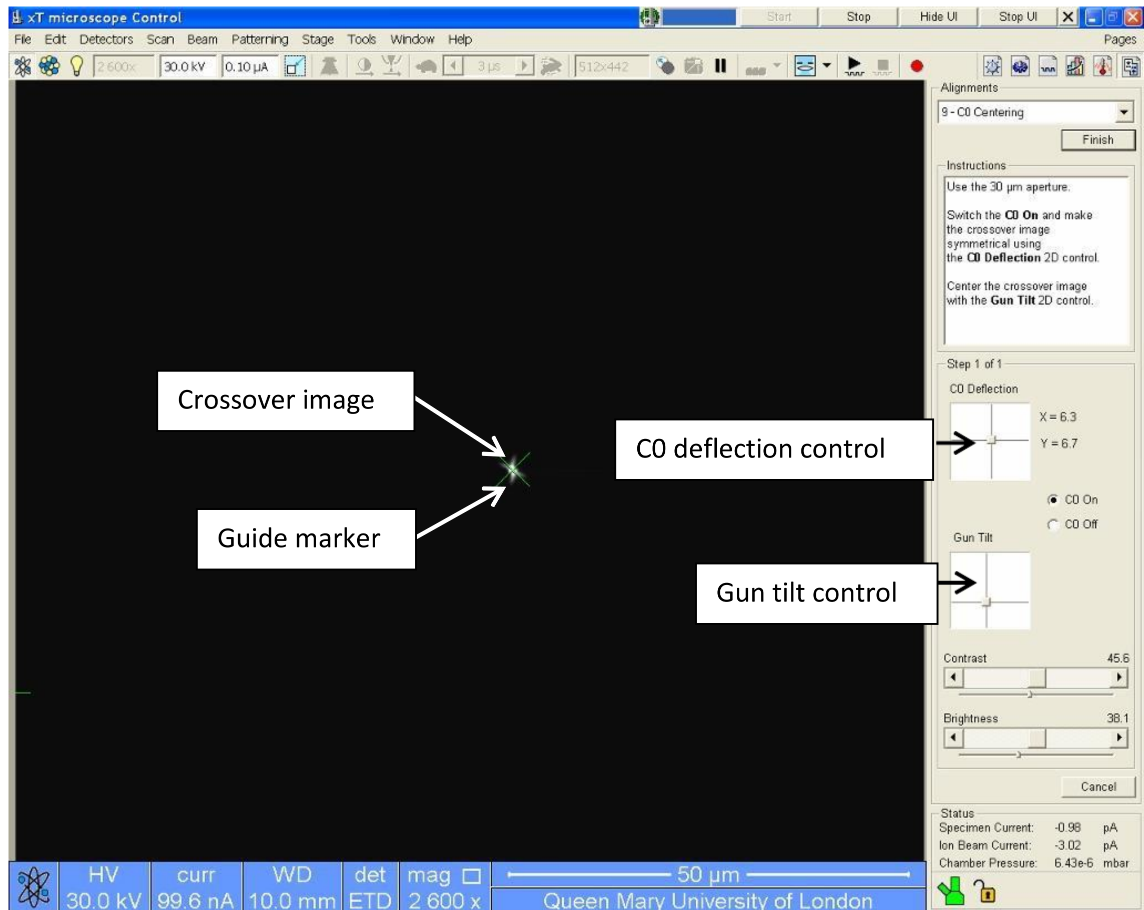

Figure 3.35 The C0 alignment application page of the Quanta 3D FEG software. This page provides the deflection and gun tilt controls for centring the C0 lens.

The C0 lens was aligned by using the C0 deflection control to produce a symmetrical crossover image, adjusting the contrast and brightness as necessary. The crossover image was then aligned with the centre of the electron column by using the gun tilt control to align it with the green guide marker seen in Figure 3.35.

The crossover image of each electron beam spot size is aligned with the centre of the column in a similar fashion, by aligning the image with a green guide marker using the source tilt controls shown in Figure 3.36.

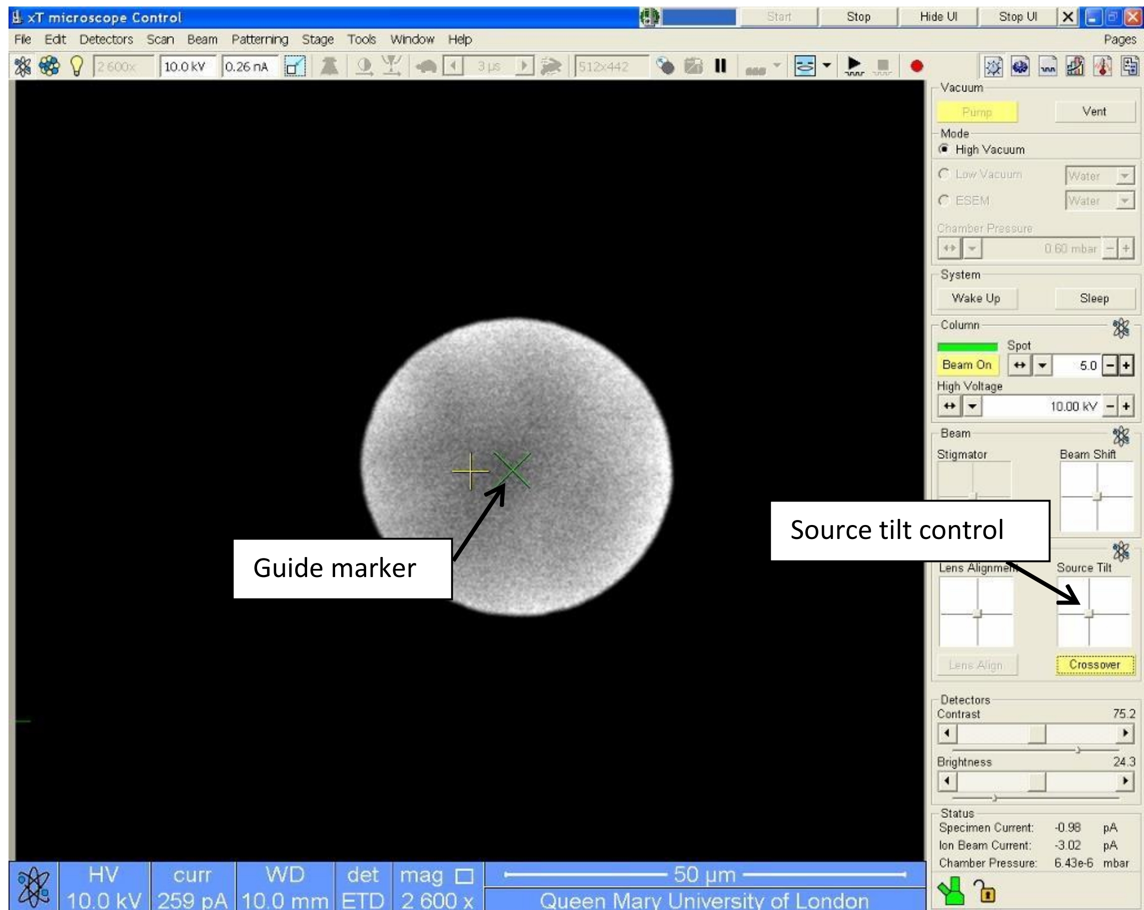

Figure 3.36 The crossover view in the Quanta 3D FEG software, which allows for crossover centring using the source tilt control.

The variable SEM apertures are aligned with the beam in order to maximise the current making it through and also to prevent deflection of the beam when focusing. Imaging alignments and calibrations were performed using the FEI standard sample shown in Figure 3.37, which is a section of silicon with crosses etch into the top surface in a regular pattern. The SEM variable apertures were aligned by activating a “wobble” in the focus of the image, such that the image would move periodic through focus from under- to over-focus and back

again. The apertures were adjusted laterally relative to the electron until any shifting in the image while the focus wobbled was kept to a minimum.

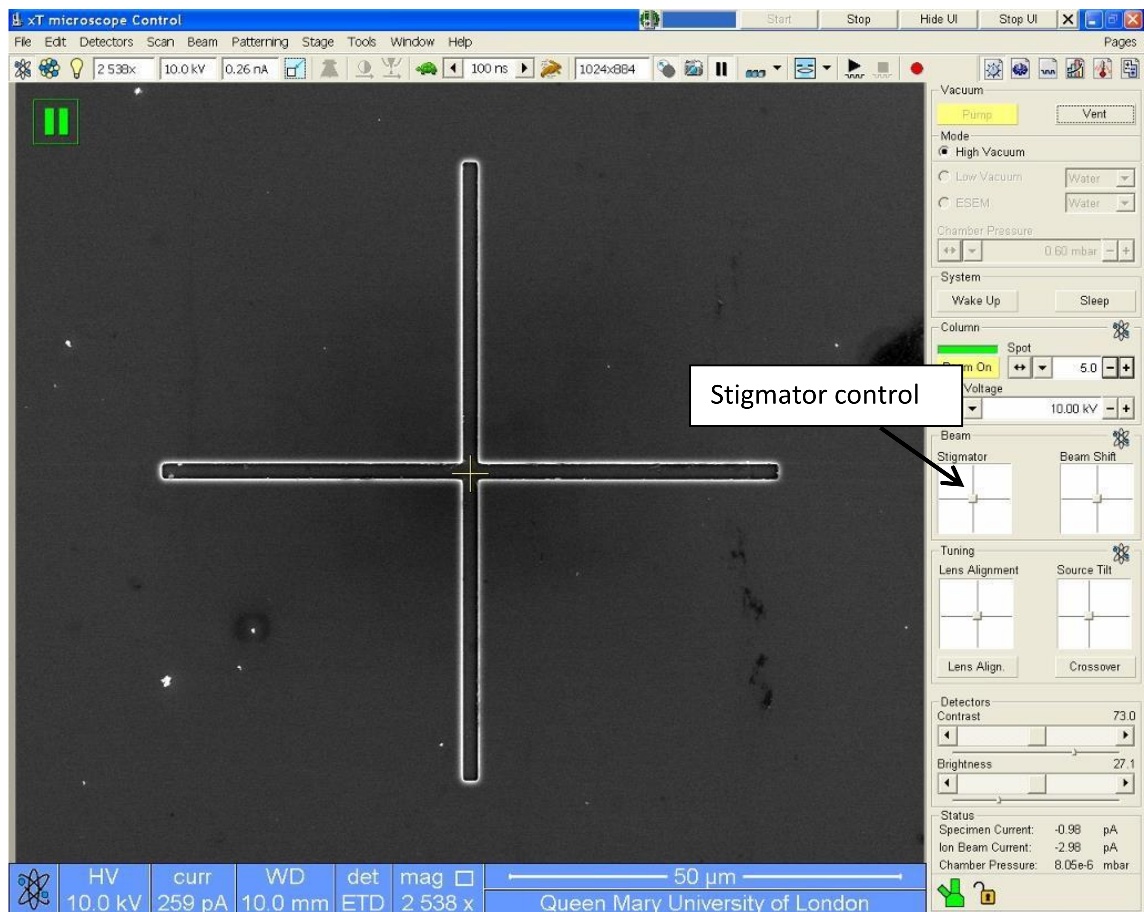

Figure 3.37 Standard view of the Quanta 3D FEG software with an image of the calibration and alignment sample.

Astigmatism in the electron beam was corrected by using the stigmator coils. An astigmatic beam produces an elliptical spot shape, which cannot be focused. The stigmator control shown in Figure 3.37 was used to correct the astigmatism and produce a round electron beam spot.

3.4.2 Energy Dispersive Spectroscopy

Energy Dispersive Spectroscopy (EDS) (x-stream, Oxford Instrument, UK) was used to identify the elements present in a sample surface. EDS utilises the characteristic X-rays emitted by

atoms after excitation by the electron beam to identify the elemental composition of the sample surface. To increase the count rate (the number of x-rays reaching the detector per second) the variable SEM aperture was switched to a 50 µm diameter aperture in order to allow more current to reach the sample. The electron beam spot size was also increased to provide a higher count rate. The beam current used for EDS was limited by saturation of the EDS detector, which slows spectrum acquisition time, the reduced imaging resolution of using larger spot sizes, and the damage that high currents do to the sample surface.

The INCA software (Oxford Instruments, UK) that controls the EDS detector records an SEM image of the sample by taking external control of the SEM. INCA provides a variety of ways of collecting spectral data, including "point ID" where the electron beam is held constant on a single spot, "Grid" where a series of spectra are collected from a series of spots in a grid, and "Area" where a defined area is raster scanned and the averaged spectrum of the whole scan is collected. An example EDS spectrum is shown in Figure 3.38, with x-ray peaks identified as originating from Carbon, Calcium, Oxygen, Fluorine, Sodium, Silicon and Phosphorous. Standards of pure elements and known compound stoichiometry were used to optimise the quantitative data acquisition.

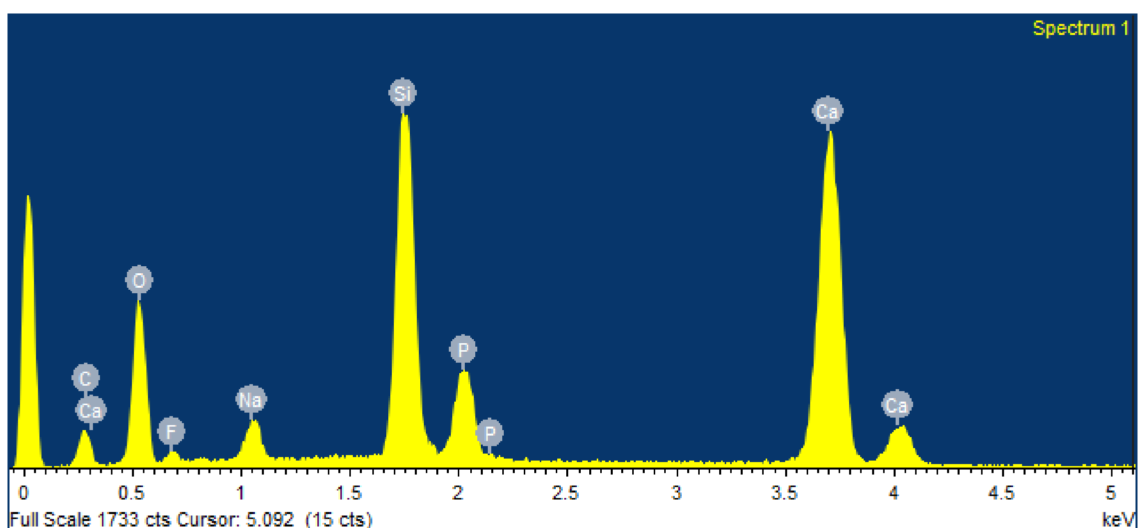

Figure 3.38 An example spectrum obtained by Energy Dispersive X-ray Spectroscopy. Each peak represents a characteristic energy of x-rays being emitted by the sample upon excitation by the electron beam, and can be assigned to the relevant element.

Samples of polycarbonate were examined using EDS after being cross-sectioned by FIB. Area spectra were collected to get an averaged overview of the surface composition, including unexposed regions away from the cross-section. Point ID spectra were collected in specific regions to identify differences in the areas exposed to the FIB compared to unexposed regions.

3.5 Preparation of FIB milled cross-sections

3.5.1 Optimisation of the FIB

The alignment of the FIB was performed in the same way as the electron beam alignment, described in section 3.4.1, with the exception that the FIB does not have a C0 lens and is a collimated, and therefore does not require crossover alignments.

3.5.2 FIB cross-sectioning of sample materials

Samples were prepared as described in section 3.1. Samples were gold coated to provide a conductive pathway from their surface to the SEM stage, and also to provide protection from the electron beam and the initial exposure to the FIB.

3.5.2.1 Samples mounted on standard SEM pin stubs

The samples that were mounted on standard stubs were mounted onto the sample stage of the Small Dual Beam (SDB) (Quanta 3D FEG, FEI Company, USA/Netherlands) so that the top surface was perpendicular to the direction of the electron beam. The sample was imaged with the electron beam and the height of the stage was altered so that the sample surface was at a working distance of 10 mm. The 10 mm working distance in the Quanta is the height at which the electron and ion beam converge and is also the eucentric height of the tilt stage. Fine

adjustments of the height to better achieve a eucentric position were determined by aligning a recognisable feature under the electron beam and then maintaining that alignment after tilting the sample stage by adjusting the height of the stage. At eucentric height the electron and ion beams converge, so with the sample in this position both beams are incident on the same region. Having the sample at eucentric height allows for imaging of the sample with the electron beam to monitor the progress of milling with the ion beam. Figure 3.39 is a schematic representing the position of the sample relative to the electron and ion beams when at eucentric height. Figure 3.39a represents the geometry when the stage is at zero tilt and the top surface of the sample is perpendicular to the electron beam. Figure 3.39b represents the condition when the stage is tilted to 52° so that the top surface of the sample is perpendicular to the ion beam.

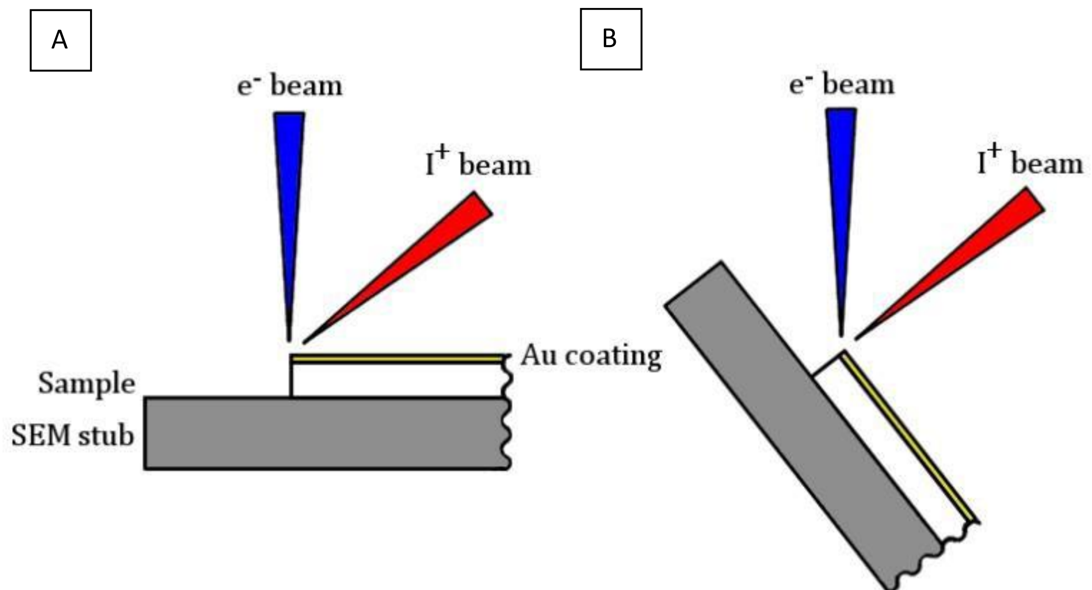

Figure 3.39 Schematic representation of beam geometry and sample position. a) Sample stage at 0° so that the top surface of the sample is perpendicular to the electron beam. b) Sample stage at 52° so that the top surface of the sample is perpendicular to the ion beam.

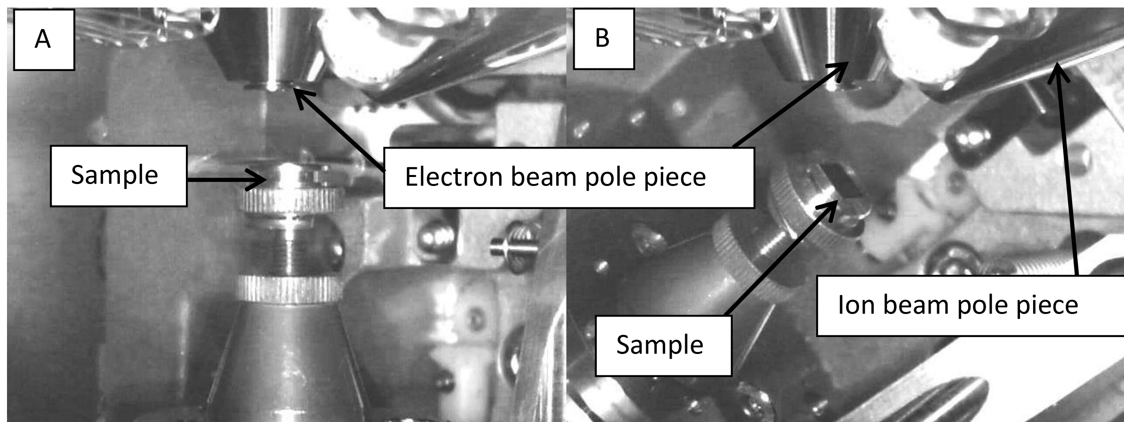

Figure 3.40 CCD images of the sample stage in the Quanta 3D FEG at the a) 0° and b) 52° position.

Figure 3.40 contains images collected from the infrared (IR) CCD camera at the back wall of the Quanta's chamber. The IR images show the position of the sample relative to the beam pole pieces when at 0 and 52° of stage tilt.

Before milling the cross-section of the sample, a layer of platinum was deposited on the top surface by ion beam assisted chemical vapour deposition. The layer of platinum was deposited in order to provide a more resilient conductive path compared to the gold coating, and to offer protection from the low intensity tails of the ion beam profile. The GIS needle was inserted into the chamber using a compressed air system controlled by the xTUI software. The end of the GIS needle was positioned within 200 µm of the sample surface to be coated. Figure 3.41a is an IR image of the sample, tilted to 52°, with the GIS needle in position. Figure 3.41b is a secondary electron micrograph of the end of the GIS in position over the sample surface ready to begin Platinum deposition.

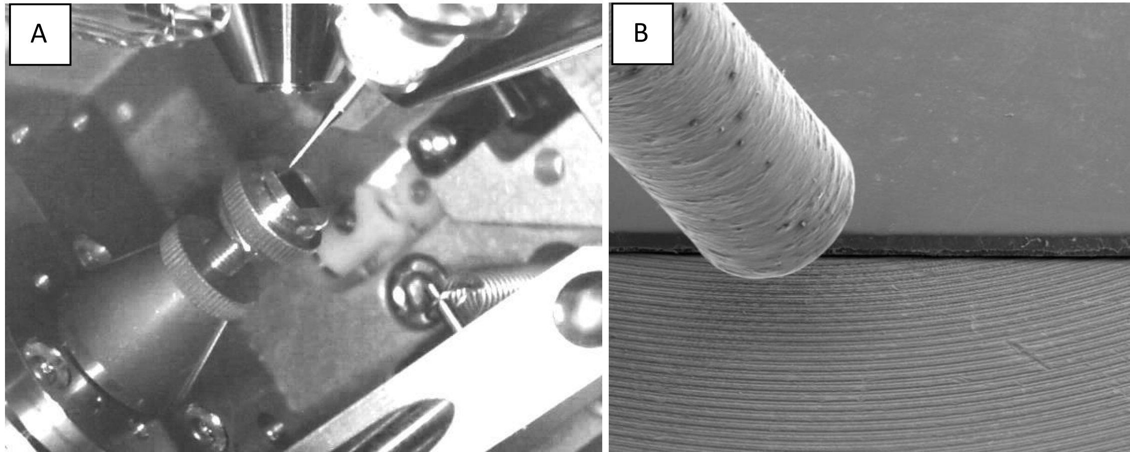

Figure 3.41 a) CCD image and b) secondary electron micrograph of the Gaseous Inject System (GIS) needle for the deposition of platinum.

Prior to Platinum deposition the precursor gas was warmed, and a rectangular pattern was defined in the FIB imaging quadrant of the xTUI software. Platinum is only deposited on the surface where the FIB has been scanned, and therefore the shaped of the deposited layer is defined by the FIB scan pattern. The deposition rate of Platinum is highest when the FIB is operating at a current density of 2 to 6 $pA.\mu m^{-2}$. At current densities below 2 $pA.\mu m^{-2}$ the Platinum deposition is very slow and the sample surface will be damaged by the incident ion beam. AT current densities above 6 $pA.\mu m^{-2}$ the platinum starts to sputter faster than it is deposited and the sample surface is eroded. The FIB aperture that was used during Platinum deposition was therefore chosen on the basis of the current that it allowed to reach the sample in order to achieve a desirable current density.

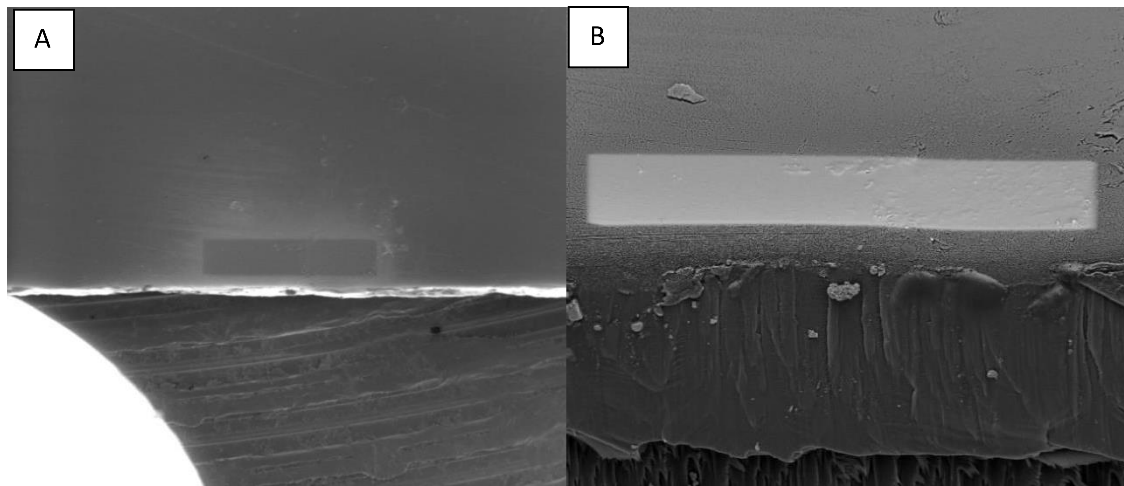

Figure 3.42 a) Ion Beam induced secondary electron image of deposited platinum strip. b) A mixed secondary and backscattered electron image of the same platinum strip.

Platinum was deposited in strips along the edge of samples that were to be cross-sectioned so that the final cross-section would fall within the region of the strip. Figure 3.42 contain images of a completed Platinum strip. Figure 3.42a is a FIB induced secondary electron image of the Platinum strip viewed top down. Figure 3.42b is an electron micrograph of the same Platinum strip imaged using a combined signal from the ETD secondary electron detector and retractable BSE detector. The electron image of the Platinum strip is viewed at a shallow angle and also shows the sample cross-section.

Cross-sections were prepared in samples in sequence of FIB milling steps. Firstly, large areas of material were cleared using a FIB accelerating voltage of 30 kV and high beam currents in order to remove the material as quickly as possible and produce a flat starting point for further polishing steps. The maximum beam current used was dependant on the material, but for polymers and biological material was typically no higher than 15 nA. After the starting surface had been prepared, each subsequent polishing step was conducted over a smaller area and at a lower current. A schematic of a cross-sectioned sample is represented in Figure 3.43, showing the platinum layer on the top surface and a sequence of FIB polished surfaces receding into the surface. Example FIB beam conditions are labelled on each cross-section

surface of Figure 3.43. The final polishing step results in the final cross-section to be analysed or imaged, and it the case of Figure 3.43 has been achieved at a FIB accelerating voltage of 16 kV and a beam current of 100 pA.

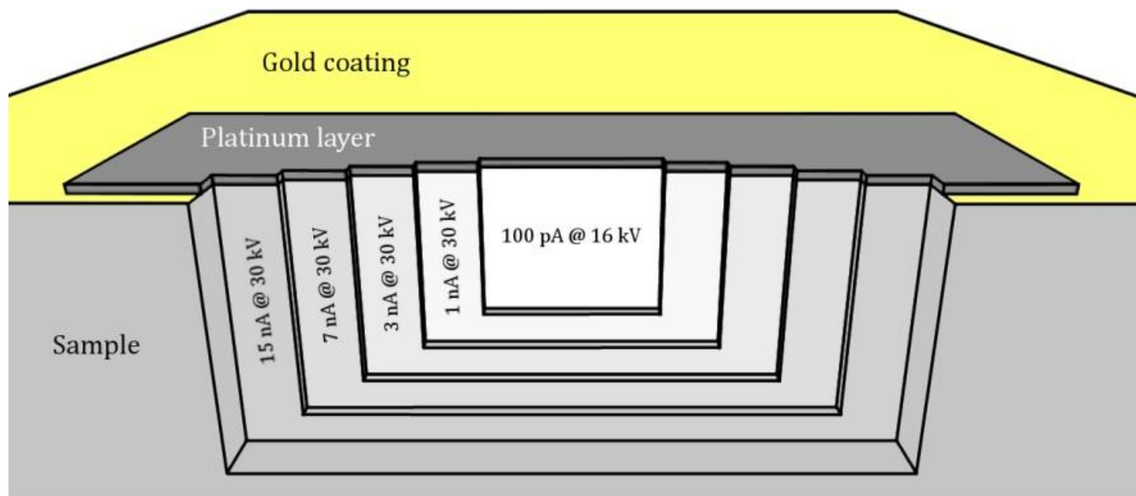

Figure 3.43 Schematic representation of a FIB prepared surface. The platinum strip on the top surface is there to protect the top surface of the sample from low intensity ion beam tails. Each cross-section surface has been prepared using different FIB condition and has been labelled accordingly.

3.5.2.2 Samples mounted in the clamping sample holder

The clamping sample holder described in section 3.3 was used for samples that needed to be transferred to the AFM after FIB milling and made it easier to image the cross-sections of thin samples. Because the sample was supported vertically in the clamp, a 45° pre-tilt SEM stage was used to align the cross-section of the sample with the FIB. A 7° tilt of the main SEM stage was applied to get the sample to the necessary 52°. Once aligned, samples in the clamping sample holder were FIB milled in the same way as described in section 3.5.2.1. The added benefit of the 45° pre-tilt stage is that by rotating the main stage through 180°, the sample is switched through 90° relative to the beams. In this ways the cross-section of a sample can be

easily switched between being perpendicular or parallel to the ion beam without having to remove the sample and remount it.

3.5.3 Polycarbonate

Polycarbonate was used as a model material to investigate the effects of FIB exposure of the mechanical response of the polished polymer surface when imaged using phase contrast AFM. Cross-sections of polycarbonate film were prepared using FIB as described in section 3.5.2.1. Each cross-section prepared was done so using the same initial set of beam conditions, but the final polishing step was varied so that a range of accelerating voltages and beam currents were considered. Accelerating voltages used were 5, 10, 15, 20 and 30 kV, while the beam currents used were in the range of 50 pA to 5 nA. The absolute values of beam current were dependent on the accelerating voltage and the beam limiting aperture. An example of a cross-section prepared in polycarbonate is presented in Figure 3.44.

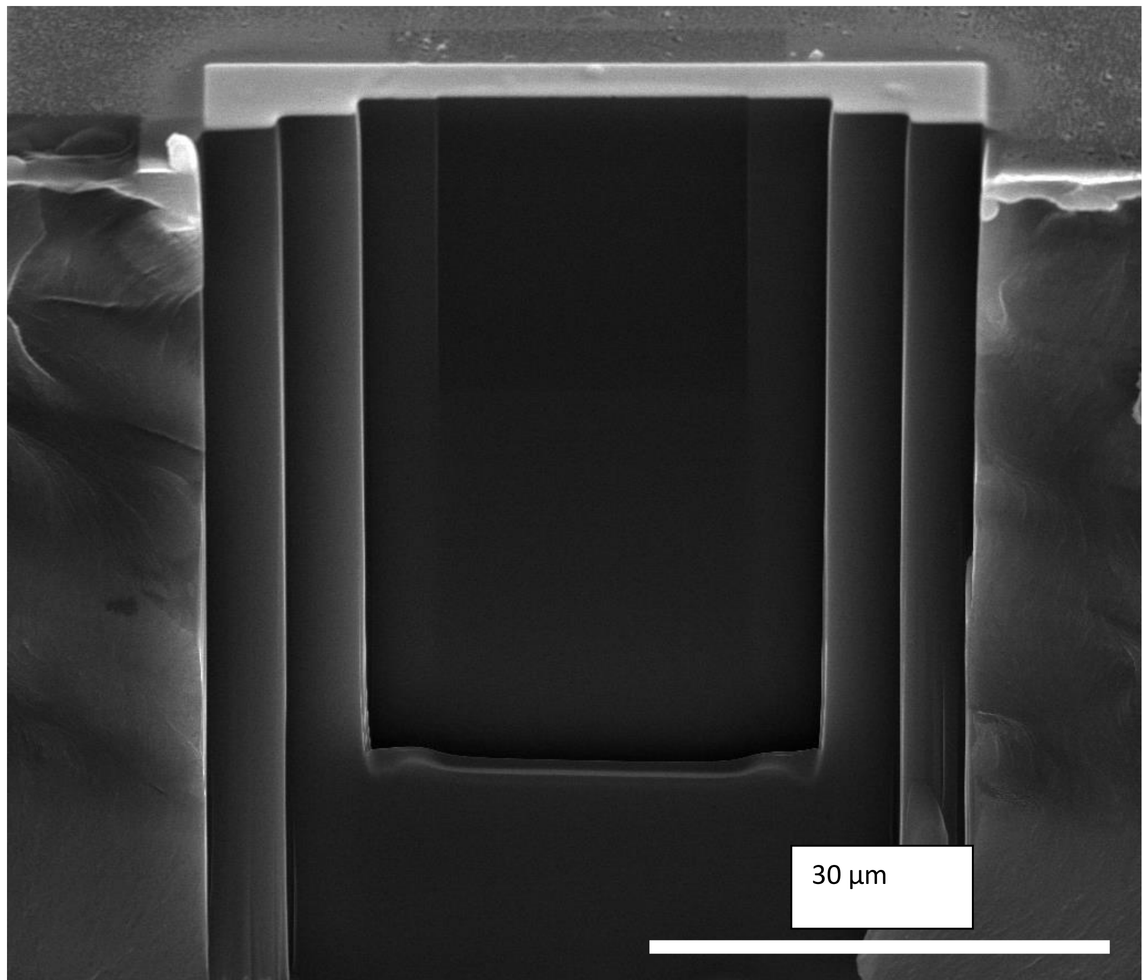

Figure 3.44 Secondary electron micrograph of a FIB prepared cross-section of polycarbonate. The final cross-section was polished using a 30 kV ion beam with a beam current of 100 pA.

The size of the cross-sections milled into the polycarbonate film was kept large enough so that the AFM probe could easily image a sufficient area of the surface without contacting at the edges.

3.5.4 Polypropylene/elastomer

Cross-sections of the polypropylene/elastomer nanocomposite were prepared in the same manner as for the polycarbonate film in section 3.5.3 with the exception that the nanocomposite was mounted either in the clamping sample holder or on the sample stage of

the attocube AFM. Both the clamping sample holder and the attocube AFM sample stage allow ample access for the GIS needle in order to deposit a strip of Platinum.

3.5.5 Snail shell

The fracture surfaces of the snail shell were coarse in comparison to the polymer surface and therefore required larger areas of material to be cleared during the initial FIB milling cross-sections. The initial clearance cross-section of a snail shell sample is shown in Figure 3.45. Figure 3.45a is a secondary electron image of the FIB milled snail shell and Figure 3.45b is the corresponding Ion beam image viewed from the top down. The large sloped sides of the FIB milled trench have been milled out to allow access to the cross-section by the AFM probe.

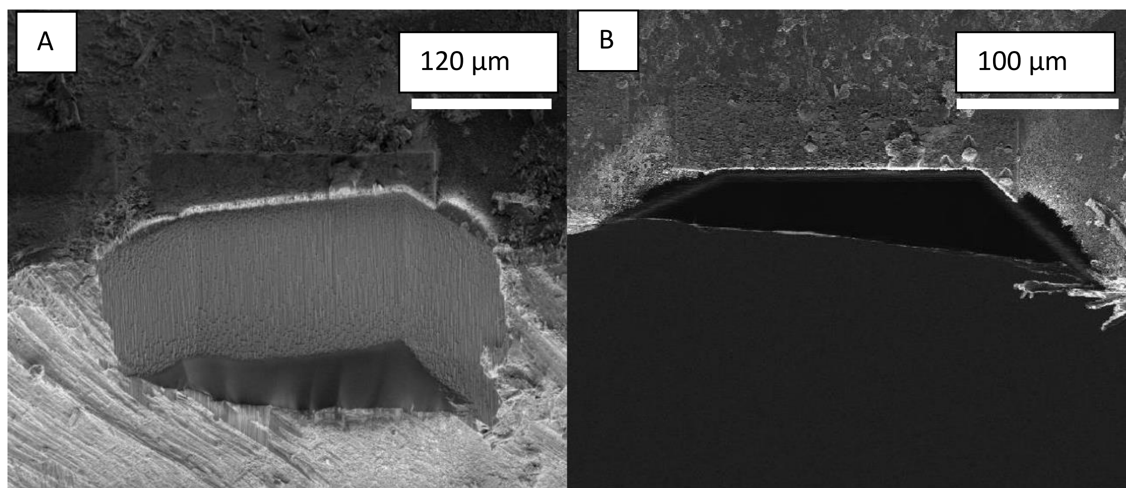

Figure 3.45 a) Secondary electron micrograph of a course cross-section of snail shell prepared using the FIB. b) An Ion Beam induced secondary electron micrograph of the snail shell sample.

As with the polymer samples, the area and beam current for each subsequent cross-section was reduced in order to produce a smoother finish in the final cross-section surface. Figure 3.46a and Figure 3.46b are secondary electron images of intermediate and final cross-sections respectively. The intermediate cross-sections can be seen to still contain milling artefacts, such

as curtaining and areas of material redeposition. The final cross-section surface in Figure 3.46b is a much smoother surface, and it would appear that there are no longer any milling artefacts.

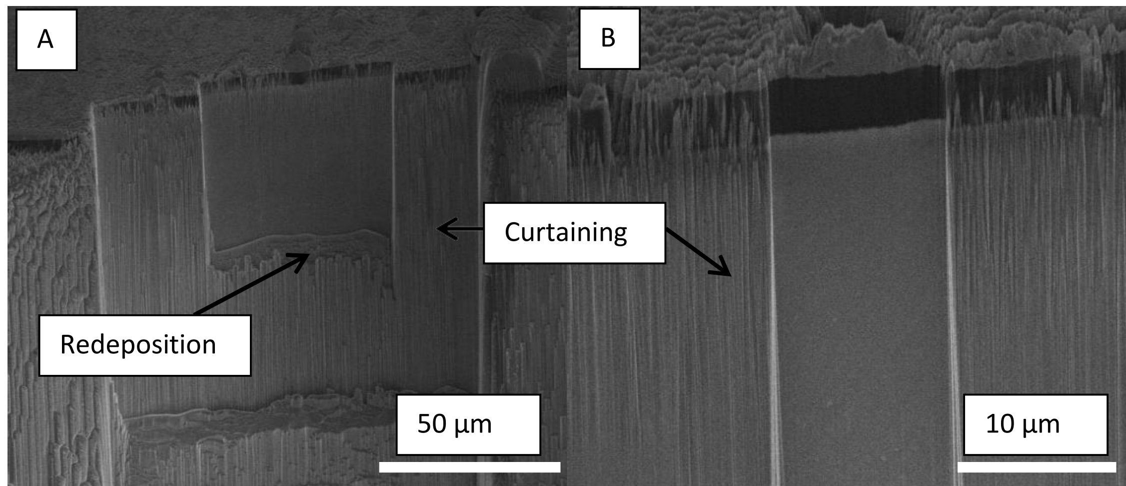

Figure 3.46 a) Secondary electron micrograph of the reduced area, low current cross-sections of snail shell, still showing signs of milling artefacts. b) Final polished cross-section of the snail shell with all major surface topography removed.

3.6 Tensile testing

Tensile mechanical testing was carried out on the polymer nanocomposite samples of polypropylene and elastomer in order to evaluate the elastic modulus of the bulk composite. An Instron model 5566 load frame (Instron, MA, USA), shown in Figure 3.47, was used to carry out the macroscopic mechanical tests, and all tensile testing was carried out in accordance with ASTM standard D 882. ASTM standard D 882 was used because the nanocomposite tape had a thickness of less than 1.0 mm (approx. 750 µm) and so for the purpose of tensile testing is defined as thin plastic sheeting. All samples of the nanocomposite tape were measured to have a width of approximately 11 mm and therefore had a width to thickness ratio greater than 8 as stipulated in the standard. The samples of nanocomposite tape were held in place using file-faced, air-actuated grips in order to reduce slippage during testing. A static weighing test method was used, whereby the crosshead separation was set at a constant rate. The load applied to the sample was recorded using a 1 kN load cell. Tests were performed at a strain

rate of 0.1 mm/mm.min. The gauge length of the samples used was 250 mm and therefore the crosshead speed was set to 25 mm/min. All data was collected and analysed using the Bluehill software that was supplied with the Instron frame.

Figure 3.47 Photograph of Instron load frame used to strain polymer nanocomposite samples

4 Assessing FIB damage in soft materials

4.1 Phase contrast AFM

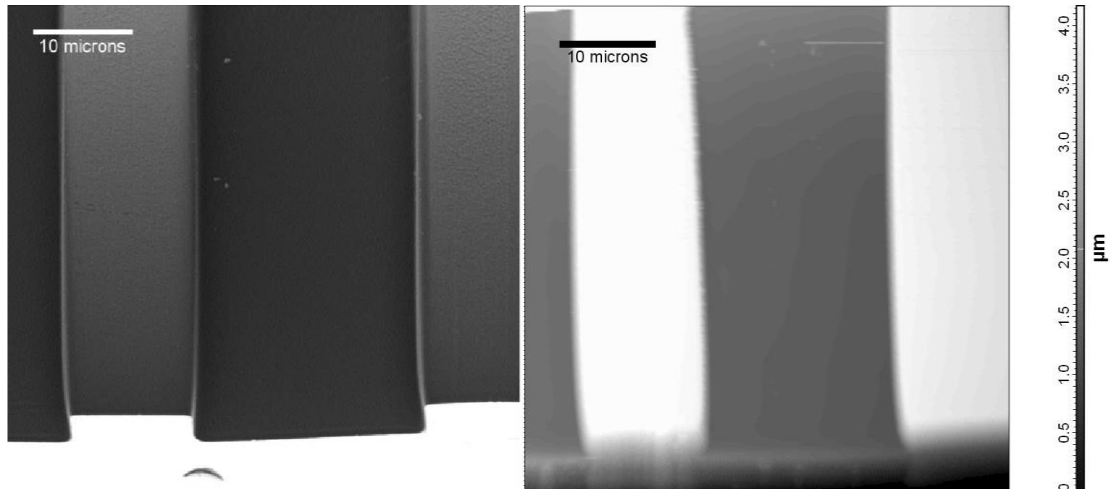

Figure 4.1 Scanning electron micrograph (left) and AFM topography image (right) showing the milled surfaces of the polycarbonate film using an accelerating voltage of 20 kV.

Phase contrast AFM is a mode of semi-contact/tapping mode AFM whereby the phase lag of the cantilever's response with respect to the driving signal is recorded. The recorded phase angle is influenced by the amount of energy dissipated during the probes interaction with the sample;[100, 101] the greater the energy lost from the cantilever, the larger the recorded shift in phase angle. The amount of energy dissipated is dependent on a number of factors including AFM tip-sample contact area, adhesion at the surface and the contact modulus between the tip and the sample; which in turn is a function of their respective elastic moduli.[23, 102] AFM phase imaging measures surface specific mechanics [103, 104] and is considered superior to other mechanical testing techniques, such as nanoindentation where the sampling volume is greater and a convolution of surface and sub-surface bulk behaviour is recorded.[105]

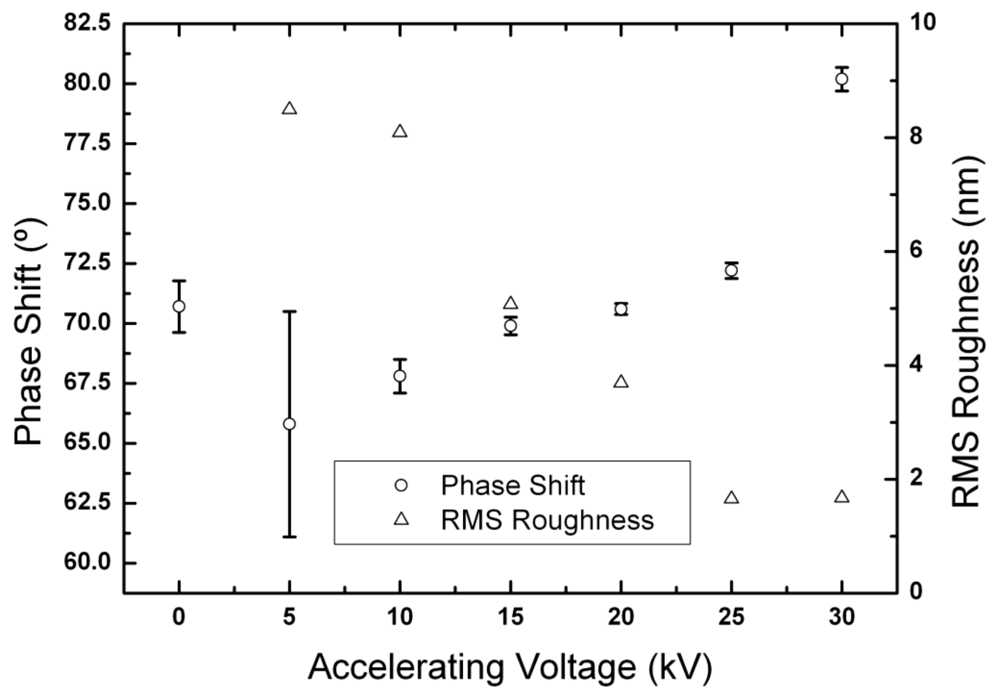

Figure 4.2 Plot showing the relationship between the accelerating voltages used to FIB mill platinum coated PC and the resulting AFM phase shift angle and RMS roughness measurements. The value at 0 kV represents the bulk PC material.

Figure 4.2 shows the resultant phase shift angle at the FIB milled trench surface recorded by the AFM. The data in Figure 4.2 indicates a large variability in the phase shift for PC surfaces prepared at FIB accelerating voltages of 5 kV, which decreases as the FIB accelerating voltage increases. The RMS roughness of the surfaces was highest for the 5 kV FIB milled PC surface but dropped as the accelerating voltage increased, indicating that a rougher surface gave a larger phase shift variability. This observation is expected as the phase shift will be strongly dependent on the contact area between the AFM probe and the sample surface. A rough surface will provide peaks and troughs in topography, providing a relatively small and large AFM probe-sample contact area respectively, resulting in large phase shift variability for a homogeneous sample. An increase in the FIB accelerating voltage produced PC surfaces with corresponding phase shift values that converged towards the phase shift value of the

unmodified bulk PC surface, denoted as 0 kV. Therefore, our data indicates that the phase shift for the PC surfaces milled at FIB accelerating voltages of 15, 20 and 25 kV is the same as that of the bulk material. Increasing the FIB accelerating voltage above 25 kV produces an increase in the phase shift above the bulk value. This indicates a softening of the PC surface, possibly due to kinetic damage between the impinging Ga^+ ion and the sample. Conversely a drop in the phase shift below the bulk value for samples milled at 5 and 10 kV highlight a stiffening of the PC surface. Mechanisms to support the observed changes in PC surface mechanics have been reported in previous literature.[106-110] Ion beams have generated both free radical induced cross-linking and chain scission in polymeric materials. Therefore, softening of the PC surface at 25 kV and above is due to ion beam induced degradation and shortening of the PC chains, whereas cross-linking of the polymer chains at 10 kV and below promote PC surface stiffening. Optimal FIB milling conditions must therefore produce surfaces with a phase shift comparable to the bulk PC, as well as a small RMS roughness to minimise variability in phase shift values. Figure 4.2 shows that FIB accelerating voltages from 15 to 25 kV provide a comparable phase shift to the bulk PC, with the higher accelerating voltages in this range producing the smoothest surfaces. This work highlights how FIB milling with higher energy Ga^+ ions creates surfaces representative of unmodified PC, which is contrary to previous work that suggests less damage in silicon using lower energy FIB. [87-90]

4.1.1 Simulations

The AFM phase shift data from Figure 4.2 highlights how Ga^+ ions accelerated at low voltage produce surfaces that are unrepresentative of the PC sample. The reduced phase shifts of the lower accelerating voltages, when compared to those of bulk PC, indicate that the surface has an increased elastic modulus. This would suggest that at lower beam energies the Ga^+ ions are embedded within the PC sample, which causes this surface stiffening effect. A series of simulations were run using SRIM (Stopping and Range of Ions in Matter) and TRIM (TRansport

of Ions in Matter) software (www.srim.org) in order to support the hypothesis that Ga^+ implantation is leading to a stiffening of the exposed PC surface. SRIM and TRIM simulations calculate the interactions of ions with matter using Monte Carlo methods. The simulation examined the interaction of Ga^+ with PC at an incidence angle of 89°, representing an almost parallel ion beam to a flat polymer surface. We note that a completely parallel ion beam to the polymer surface cannot be used as no interaction will occur. The resulting ion paths and secondary recoils for accelerating voltages ranging from 1 to 30 keV are shown in Figure 4.3. Ga^+ ion penetration ranges perpendicular to the surface are shown in Figure 4.4 as ion range. The plot in Figure 4.4 clearly shows an almost linear positive correlation between the accelerating voltage and the ion range, indicating how increasing the accelerating voltage deposits Ga^+ ions deeper into the polymer surface. The deposition of Ga^+ ions below the polymer surface can be described by ion density, which is the amount of ions per volume per number of incident Ga^+ ions. The ion density in Figure 4.4 is a maximum at 5 kV, but reduces linearly above 15 kV. Examination of both the ion range and ion density shows a low accelerating voltage provides a high density of Ga^+ ions with a low penetration depth into the polymer (2-10 nm). An increase in FIB accelerating voltage lowers the ion density but increases the penetration depth. Figure 4.4 highlights an increased dispersion of Ga^+ ions within the polymer at higher accelerating voltages. The relationship between FIB accelerating voltage and ion density seen in Figure 4.4 can be directly related to the phase shift shown previously in Figure 4.2; the higher Ga^+ concentration at the near surface is causing the stiffening of the polymer surface, which in turn is causing the shift in phase shown in Figure 4.2.

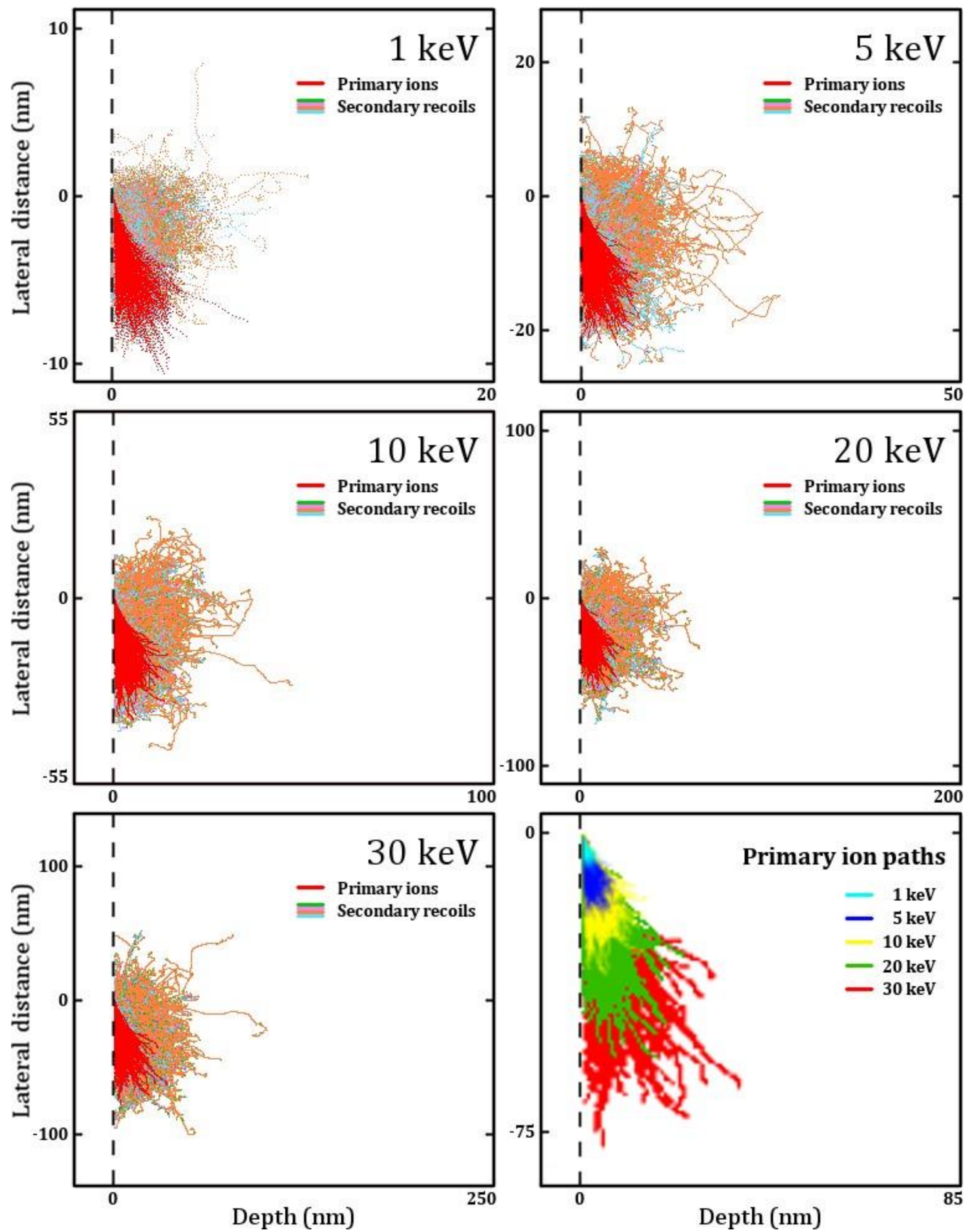

Figure 4.3 Interaction volumes obtained from TRIM simulation for a Ga^+ beam incident on a polycarbonate surface at 89° from normal.

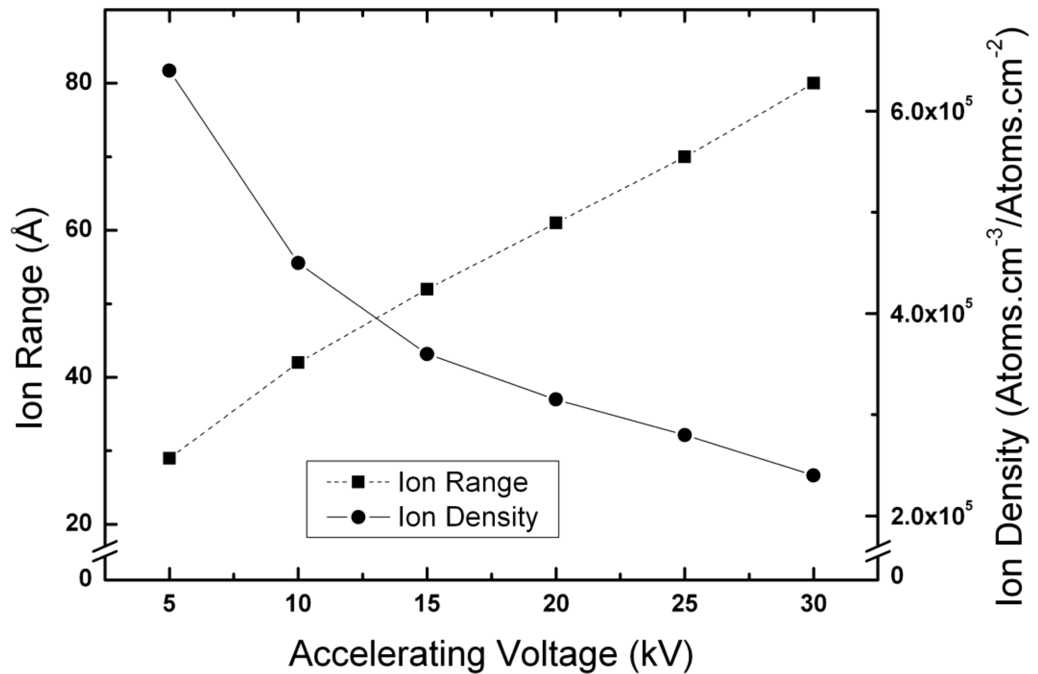

Figure 4.4 Results of TRIM modelling of ion beam interactions with polycarbonate at varying accelerating voltages. The ion range represents the average depth of Ga^+ ions beneath the surface and the ion density is representative of the concentration of Ga^+ at the surface.

The FIB is being used in this work to generate cross sections of the PC surface and therefore considerations must be made for the sputtering efficiency with which material is removed from the polymer at each accelerating voltage. Figure 4.5 shows how the sputter yield varies with FIB accelerating voltage, based on the results of the SRIM calculations. The simulation was carried out for polycarbonate and compared to silicon, a model material system used in most FIB studies, [87, 111, 112] with an FIB 89° angle of incidence. Sputter yield is found in Figure 4.5 to be a minimum at 5 kV and increases with increasing FIB accelerating voltage. In addition, the rate of change of sputter yield slows as the voltage increases. The sputter yield is greater for PC than for silicon and suggests that the effect of accelerating voltage is more noticeable in the polymeric sample. The sputter yield for polycarbonate will increase with accelerating voltage because each Ga^+ ion is carrying more energy and can therefore displace a

greater number of sample atoms. The path of the Ga^+ through the PC is longer, whereas for silicon the interaction volume of the FIB is smaller and energy is used displacing material. Low energy FIB, represented by the low accelerating voltage experiments, do not carry enough energy to displace the sample atoms of the PC efficiently, thus causing the incident Ga^+ ions to become embedded within the sample volume. The relatively small phase angle shifts measured at the sample surface using AFM signifies a stiffer surface due to this Ga^+ implantation within the probed surface region.

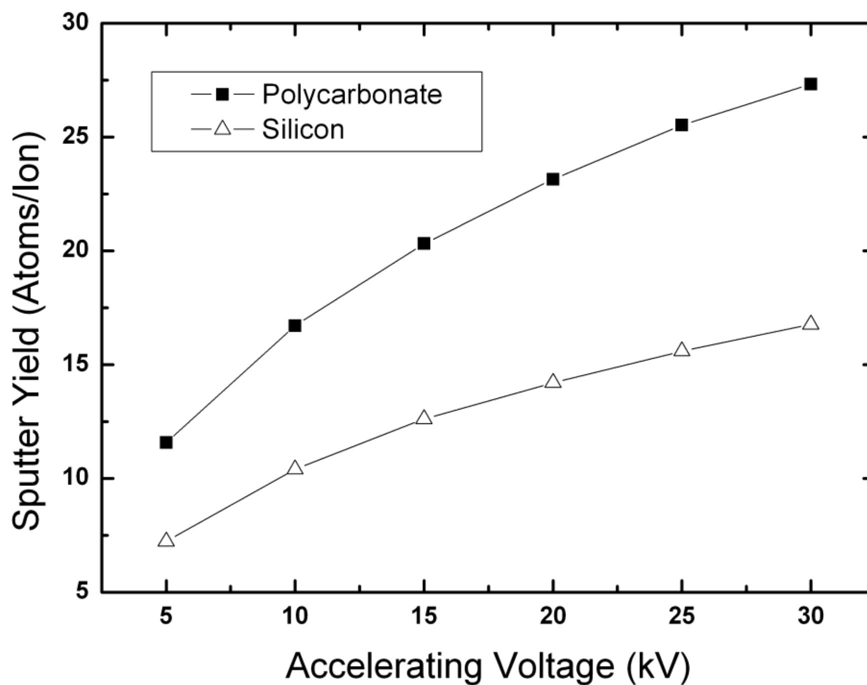

Figure 4.5 Plot of sputter yield against accelerating voltage in polycarbonate and silicon calculated from SRIM simulations.

4.2 EDS analysis

Chemical analysis of the FIB milled PC surfaces was performed in order to determine if embedded Ga^+ ions could be detected. Energy Dispersive Spectroscopy (EDS) measures the energy of X-rays being emitted from a sample while being exposed to an electron beam. The

energies that are recorded are specific to the elements that are present in the sample and can therefore be used to identify the composition of a sample. EDS analysis of the milled PC surfaces was performed in order to confirm the presence of Ga^+. EDS analysis is not surface specific, but is sufficient to measure changes in the gallium concentration at the PC surface. Spectra were gathered over each of the milled surfaces and the supporting software was used to calculate the weight percentage of Ga^+ in the sample area. The spectra in Figure 4.6 show a clear Ga^+ peak at 1.1 keV for a series of FIB milled PC surfaces. The amount of Ga^+ found within each sample was plotted against FIB accelerating voltage as shown in Figure 4.6. The amount of Ga^+ present in the surface layer decreases when milling at higher accelerating voltages. The depth of the layer under analysis with EDS is dependent on the sample and the accelerating voltage of the electron beam; calculated as 5.5 µm using Monte Carlo simulation (Casino v2.42, Can.). This plot can be directly related to the ion densities presented in Figure 4.4 and the sputter yield in Figure 4.5 as the higher FIB accelerating voltages sputter through the sample more efficiently and leave less Ga^+ implanted in the polymer surface. The insert in Figure 4.6 shows a direct comparison of the X-ray peak at 1.1 keV unique to Ga^+ that was used to calculate the surface content.

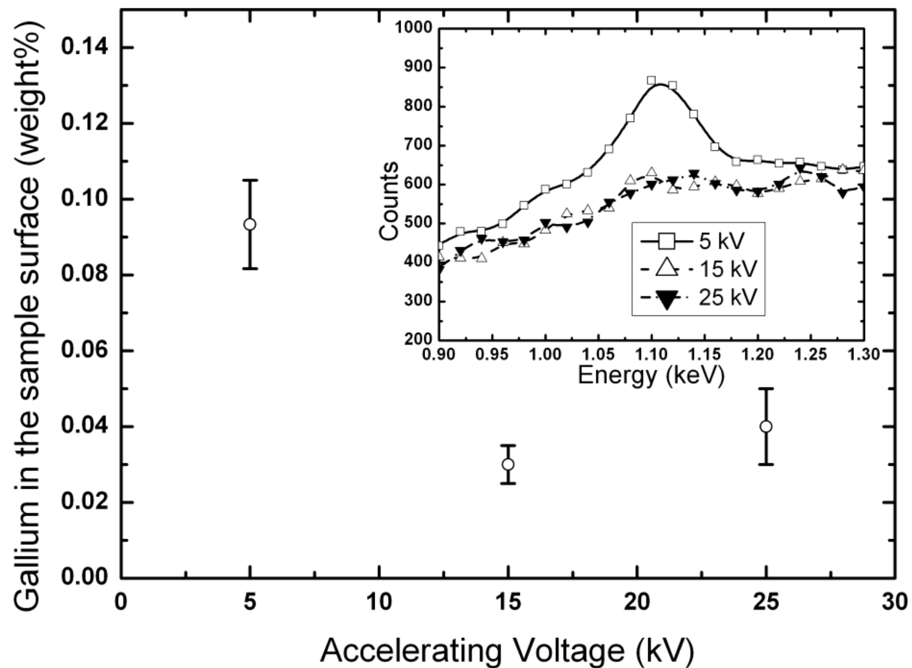

Figure 4.6 Plot showing Ga^+ content variation with ion beam accelerating voltage used to mill PC surfaces. The main plot shows the weight% of Ga^+ as calculated by the EDS software, taken from the EDS spectra insert for the different FIB milled surfaces showing the Ga peak at 1.1 keV.

Both the ion density in Figure 4.4 and the weight percentage of Ga^+ in Figure 4.6 appear to approach a limiting value as the accelerating voltage increases. Here we propose a phenomenological model that accounts for these effects. As the ion beam interacts with the edge of a sample there are a number of pathways that the incident ion can take. The sum of these potential pathways is represented by an interaction volume. The interaction volume for a 5 kV ion beam is relatively small, with fewer ions escaping from the polymer surface. However, the beam energy is too low to efficiently sputter away the sample atoms and we see Ga^+ implantation. An increase in the accelerating voltage causes an increase in the energy available per ion to displace sample atoms, as well as an increase in the sample interaction volume with the beam. This increase in the Ga^+ ion energy will increase the amount off sample sputtered from the surface and increase the volume the imbedded Ga^+ ions will be found in.

4.3 Conclusions

A PC sample was milled using FIB to expose a relatively smooth surface using various ion beam parameters. Surfaces parallel to the milling ion beam direction were imaged using phase contrast AFM. This phase imaging showed how FIB accelerating voltages within the range of 15 to 25 kV gave similar phase shifts to bulk PC, whereas lower accelerating voltages gave significant deviations in the phase signal, indicative of Ga^+ ion implantation at the PC surface. The data presented in this study supports the hypothesis that low accelerating voltage ion beams have reduced sputter yield and result in higher Ga^+ concentrations at the sample surface, directly measured using EDS. The presence of Ga^+ at the sample surface is therefore responsible for increased polymer elastic modulus, detected through phase contrast AFM. Therefore, this work demonstrates ion beam preparation of polymeric samples requires higher energy FIB milling up to a threshold of 25 kV to produce surfaces that are more representative of the parent material.

5 Quantifying the phase signal

5.1 Aims

This chapter considers an established model of the motion of an AFM cantilever during dynamic AFM (dAFM) imaging. MatLab is used to solve the equations of motion presented in the model and simulate the motion of an AFM cantilever when imaging surfaces with a variety of Young's moduli of elasticity. The position of the AFM tip is calculated as a function time for several hundred oscillations of the AFM cantilever and the phase of the oscillation is extracted by Fourier Transform. The effects of AFM operating parameters and other material properties on the recorded AFM phase are also examined through simulation.

5.1.1 AFM Phase Imaging

Phase contrast imaging with dynamic AFM is a powerful tool for observing the variation in the mechanical behaviour of nano-composite surfaces with high spatial resolution. However, the raw phase shift data recorded during dynamic AFM measurement is dependent on a number of factors, such as the force of adhesion between the sample surface and the AFM tip, the contact area between the surface and the AFM tip, the ratio of the free amplitude of the AFM cantilever and the setpoint amplitude of the AFM cantilever whilst imaging and the stiffness of the contact between the AFM tip and the sample surface. Knowledge of these factors is important as, in principle, the recorded phase shift raw data can be subsequently converted into quantitative mechanical information of the sample that is interacting with the AFM probe. Although qualitative assessment of the surface can be useful in standard AFM phase imaging, achieving quantitative results using computer modelling to predict the response of an AFM cantilever under experimental conditions is possible, thereby associating phase shift values with specific mechanics at a sample's surface.

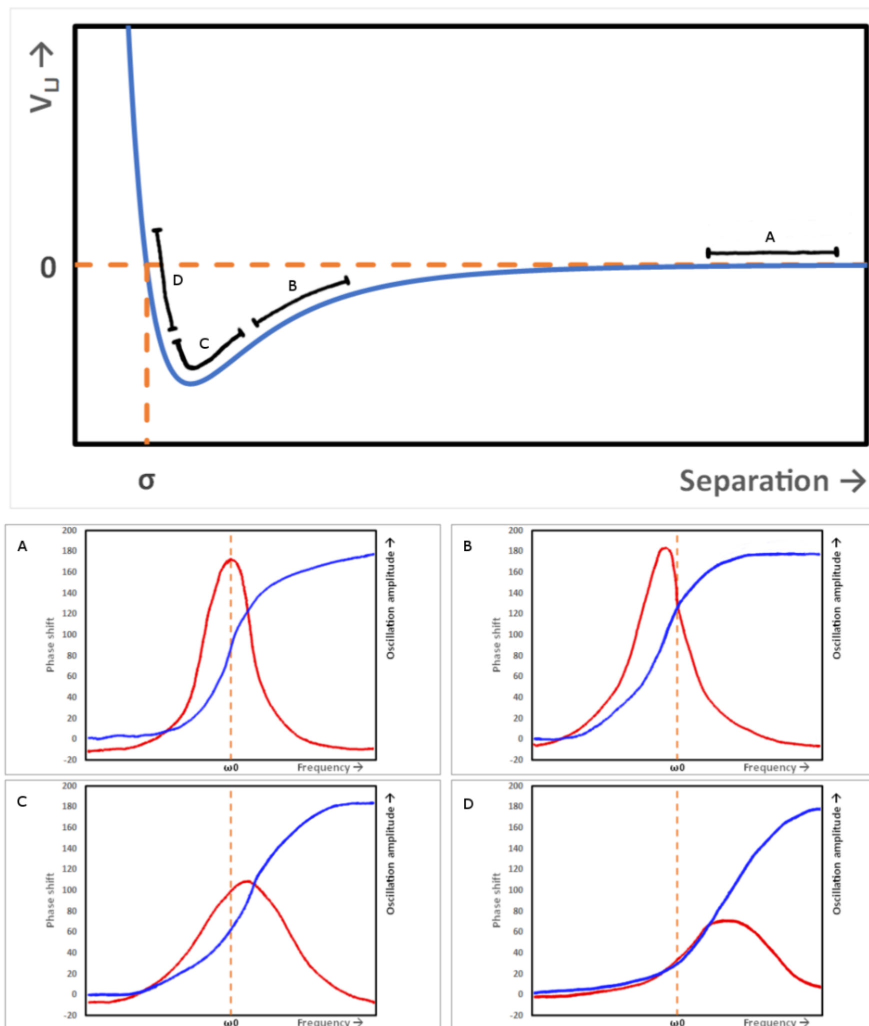

Figure 5.1 Plot of Lennard-Jones potential, highlighting the different interaction regimes, depending on the region of the curve through which the tip is oscillating. σ is the interparticle distance at which the Lennard-Jones potential is zero. The inset plots (A to D) show the phase shift (blue) and oscillation amplitude (red) as a function of frequency for each region. The dashed orange line is the resonance frequency of the freely oscillating cantilever in air, which is represented by region/plot A. Region/plot B represents the purely non-contact regime, where the tip is experiencing only attracting forces. Region/plot C represents the semi-contact regime, where the tip is making intermittent contact and experiences both attractive and repulsive forces. Region/plot D represents the regime where the tip is experiencing purely repulsive forces.

Figure 5.1 highlights the differing interactions when the AFM tip is oscillating through different regions of the Lennard-Jones (L-J) potential. The main plot at the top of the figure is the L-J potential. The minimum of the L-J plot is where the force experienced by the AFM tip is zero, and therefore represents the point at which the tip contacts the specimen surface. The region to the left of the minimum is where the AFM tip is experiencing repulsive forces, and the region to the right, where

the potential is negative, is where the tip is experiencing an attractive force. Region/plot A represents the condition where the AFM cantilever is freely oscillating in air; the amplitude of oscillation is at a maximum at resonant frequency, and the phase shift is 90°.

Region/plot B represents the regime whereby the AFM tip is oscillating within the attractive region of the L-J potential. The attractive forces experienced by the tip cause an increase in the oscillating amplitude, and a shift in the resonance to a lower frequency. This shift in frequency means that there is an observed increase in the phase shift.

Region/plot C represents the regime whereby the AFM tip is making intermittent contact with the specimen surface, and is therefore experiencing a mixture of attractive and repulsive forces. When the repulsive forces dominate, there is an observed shift in the resonance to a higher frequency, and a reduction in the phase shift. There is also a damping of the oscillation amplitude.

Region/plot D represents the regime where the oscillation is purely in the repulsive region. This results in a further shifting of the resonance and phase than seen in region C.

During imaging in semi-contact (Amplitude Modulated) mode, as represented by plot C, the amplitude is typically monitored slightly off resonance, at a lower frequency, such that the amplitude is 90% of maximum. This is so that the signal is always being measured on the slope of the amplitude peak, as measuring across the peak can lead to bi-stability, whereby the system switches between the two possible setpoint amplitudes, either side of the peak.

5.1.2 Model for Tip-Sample Contact

The aim of this chapter is to take an existing model for an AFM tip-sample contact and simulate cantilever dynamics under equilibrium feedback conditions. It should be possible to describe the influence that sample stiffness has on the AFM phase signal, independent of the other variables, by defining suitable values for the experimental conditions used and varying the reduced contact modulus of the interaction, and thereby quantify the phase signal as a function of stiffness. This would then allow for the stiffness of the sample surface to be calculated based on the phase contrast information.

5.2 Background

5.2.1 The Carpick model

The Carpick group developed perhaps the most comprehensive model for describing the interaction between an AFM tip in intermittent contact with a solid sample surface, capable of simulating steady state imaging conditions.[102] There are a number of models in the literature that take differing approaches to simulate the response of an AFM cantilever to mechanical excitation. Broadly, these models fall into the categories of 1D point-mass, 1D beam, torsional, coupled torsional-bending, 3D point-mass and 3D finite element modal. Each category has advantages when considering specific imaging techniques, e.g. 1D beam models are able to consider higher modes of excitation, and the Carpick model is a 1D point-mass model, which is suitable for this study as all of the AFM imaging was done using the primary resonance of the AFM cantilever and there was no need to measure or model the torsional bending of the AFM cantilever. A number of works from the Carpick group have been used to investigate the effects of sample tilt on the measured phase angle during a standard AFM phase image, where the AFM tip intermittently contacts the sample's surface, and to explain the AFM's ability to resolve in-plane material anisotropy [22, 102] Figure 5.2 is an AFM

micrograph of poly(diacetylene) (PDA) imaged in semi-contact mode, reproduced from Marcus *et al* (2002). Figure 5.2a is the AFM topography image of the polymer surface, containing large regions of monolayer PDA and islands of multilayer PDA. Figure 5.2b is the AFM phase image, which adds contrast to the monolayer PDA regions dependant on the orientation of the AFM cantilever relative to the polymer backbones in the polymer crystals. The contrast in the AFM phase image arises from energy dissipation due to in-plane forces, which in turn is due to motion of the AFM tip parallel to the sample surface.

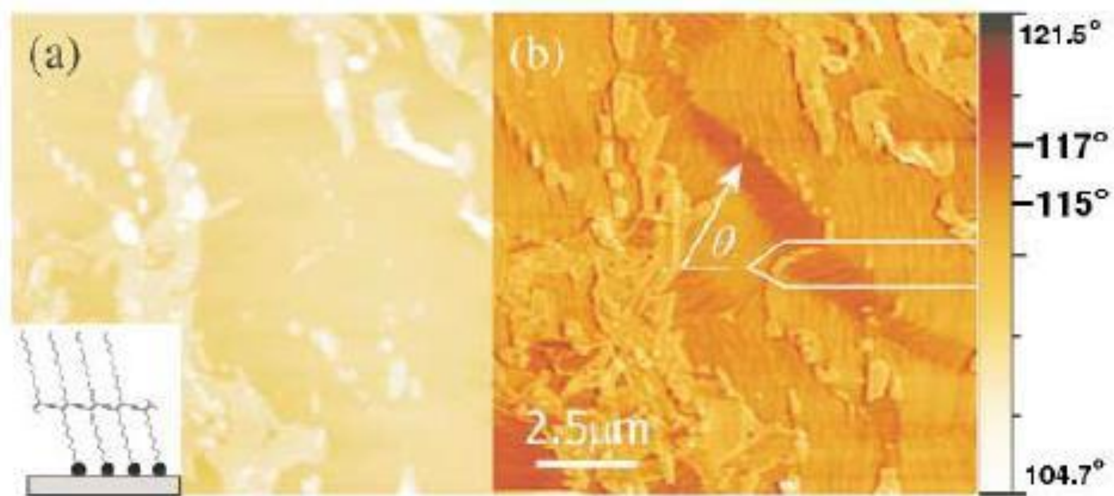

Figure 5.2 (a) AFM topography image acquired in semi-contact mode using amplitude modulation. The inset shows the PDA structure and its backbone. (b) AFM phase image acquired simultaneously with the topography data. The orientation of the AFM cantilever is shown as a white outline to the right of the image and ϑ is the angle between the local PDA backbone striations and the long axis of the AFM cantilever

The Carpick model describes the AFM cantilever as a sinusoidally driven, damped harmonic oscillator and the tip is assumed to be a point mass with an effective mass of $\frac{k}{\omega_0^2}$, where k is the spring constant and ω_0 is the resonance frequency of the AFM cantilever. A diagram of the tip sample interactions is shown in Figure 5.3. The movement of the tip is constrained to the direction normal of the cantilever base (z'), which in all AFM systems is tilted to allow greater separation between the cantilever base and the sample during imaging. Three

conditions are considered during AFM phase imaging depending on whether the tip is some distance away from the sample surface, near to the surface and within a near surface damping layer, or in contact with the sample's surface. The "away from surface" and "near surface" conditions are shown in Figure 5.3. The first condition with the AFM tip away from the sample surface denotes AFM tip interaction with the sample surface through van der Waals forces only. An AFM tip in the 'near surface' condition experiences an extra damping force which, due to the tilt angle of the AFM cantilever relative to the sample surface, is resolved normal and lateral to the sample surface and described by Q_{normal} and $Q_{lateral}$. The values of Q_{normal}, $Q_{lateral}$ and $Q_{cantilever}$ are the quality factors of the system and relate to the damping forces experienced by the AFM tip. The higher the value of Q, the less damping the tip experiences and therefore there is less resistance to cantilever oscillation. Q_{normal} and $Q_{lateral}$ are properties of the near surface damping layer and $Q_{cantilever}$ is the quality factor of the AFM cantilever oscillating in air, which can be measured by dividing the resonance frequency of the AFM cantilever by the Full Width at Half Maximum (FWHM) of the resonance peak.

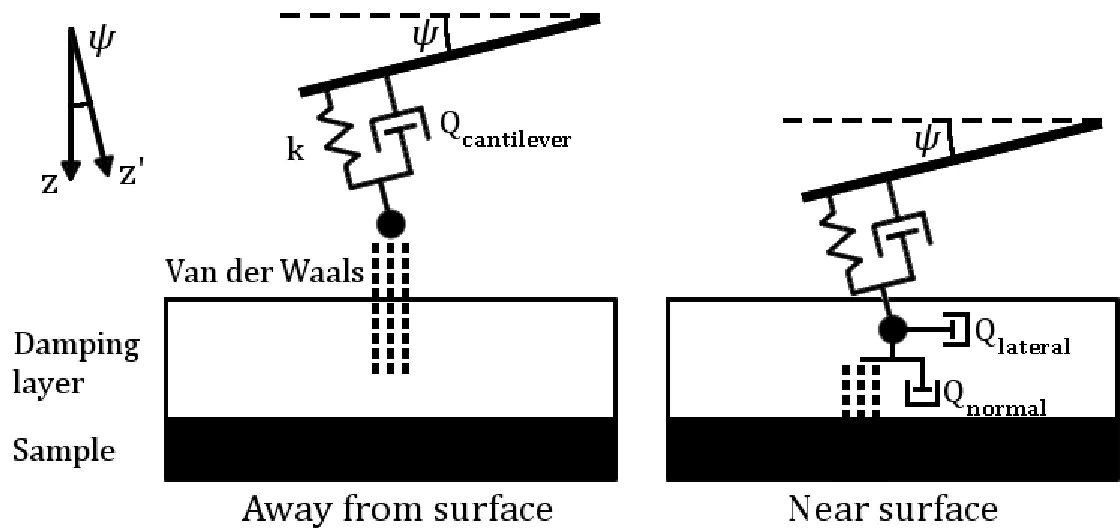

Figure 5.3 AFM tip approaching a surface with a viscous damping layer. The cantilever is tilted (ψ) relative to the surface.

The AFM tip-sample interaction forces can be resolved to the component forces that are acting in the plane of the surface and normal to the surface, as shown in Figure 5.3. The van der Waals forces between the AFM tip and sample surface are modelled as a sphere approaching a plane using adhesive contact mechanics (DMT).[102] Derjaguin-Muller-Toporov (DMT) theory is an extension of classical Hertzian contact mechanics. [113] The Hertzian theory of contact mechanics does not account or allow for an adhesive force. The adhesion and forces of attraction between the AFM tip and the sample surface are an important factor in influencing the phase of the oscillating cantilever, which therefore need to be accounted for in modelling the system. There are two major theories in the literature that are commonly used for modelling adhesive contacts, Johnson-Kendall-Roberts (JKR) theory and DMT. The JKR theory considers the adhesive force as a balance between the stored energy in the elastic deformation of the contact and the surface energy gained through separation. JKR theory limits the contact pressure and adhesive force to within the contact area. DMT theory maintains the same contact profile as Hertzian theory, but the attractive forces extend beyond the area of contact. JKR theory is typically a best fit for large, compliant contacts, whereas DMT theory is best suited for use with small, stiff contacts, which is why it was chosen for this study. The out-of-contact van der Waals term used to define the force F_{vdW} acting on the AFM tip at a distance away from the solid sample surface therefore takes the form of:

$$F_{vdW} = -\frac{AR}{6D^2}$$

Equation 4

Where A is the Hamaker constant, R is the radius of the sphere approximating the shape of the AFM tip and D is the separation between the sphere and the sample plane.

The out-of-contact van der Waals term presented in the Carpick model, which accounts for tilt of the cantilever and the corresponding frame of reference, is represented by:

$$F_{vdW} = \left(\frac{AR\cos\psi}{6(p\cos\psi - \xi_0)^2}\right)$$

Equation 5

Where ψ is the angle of the cantilever relative to the sample surface, p is the position of the tip relative to the surface and ξ_0 is the equilibrium separation. As p is the position of the tip along the z' axis, as shown in Figure 5.3, p has been multiplied by cos ψ in order to find the separation of the tip and the sample along the z axis, which is smaller than the separation along z'.

The out-of-contact van der Waals term is used to model the interaction up to the point of contact. The AFM tip contact with the sample plane is considered to be equivalent to equilibrium separation, where the force experience by the approaching tip is zero as described by the Lennard-Jones equation, which takes the form of:

$$V_{LJ} = \varepsilon\left[\left(\frac{r_m}{r}\right)^{12} - 2\left(\frac{r_m}{r}\right)^{6}\right]$$

Equation 6

A representative plot of the Lennard-Jones equation is shown in Figure 5.4. The value of ξ_0 is therefore subtracted from the position of the AFM tip. The interaction force between the AFM tip and sample plane calculated based on the separation of p cos ψ is then resolved back into the z' axis by multiplying through by cos ψ again.

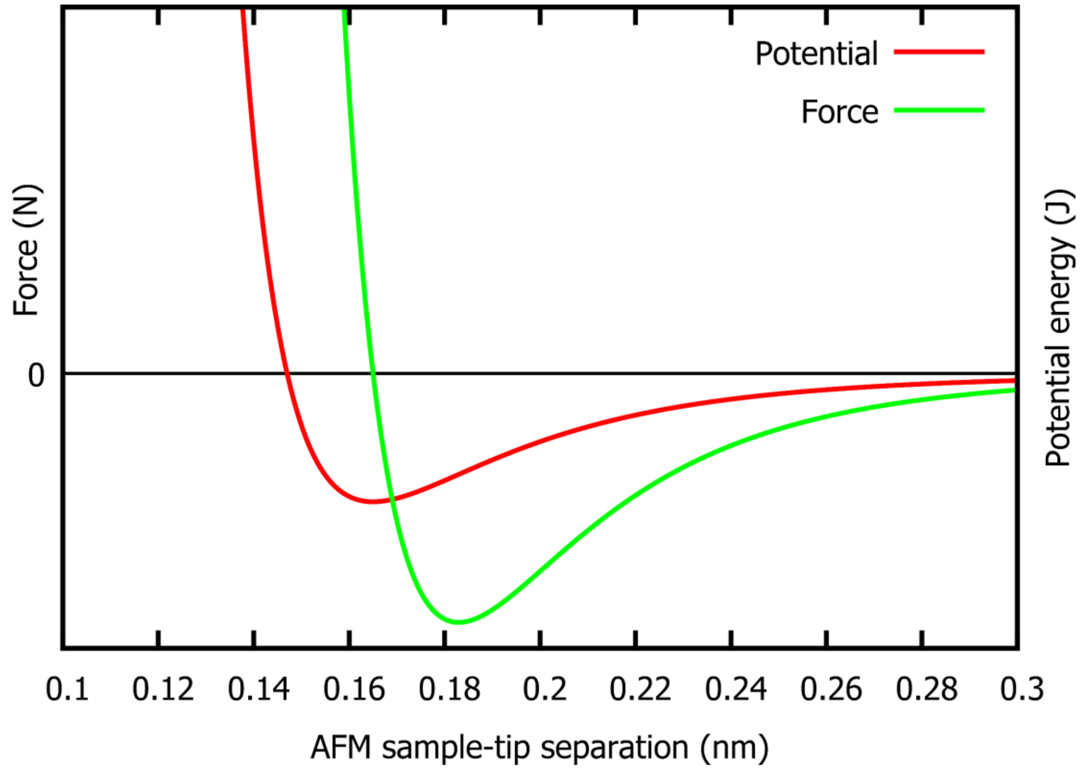

Figure 5.4 Plot of Lennard-Jones potential and corresponding force between an AFM tip and a Sample surface, calculated using Equation 6

For the contact condition, the repulsive contact force, as defined by DMT theory, is given by:

$$F_{DMT} = \left(\frac{4E^*}{3}\sqrt{R}(p)^{3/2}\right)$$

Equation 7

Where E^* is the reduced modulus, R is the radius of curvature of the AFM tip, v_s is the Poisson's ratio of the sample and p is the position of the tip relative to the sample, with an increasing positive value moving into the surface and increasing negative value moving away from the surface (thus, p=0 corresponds to AFM tip contact with the sample plane).

The definition of the reduced contact modulus K is given as:

$$\frac{1}{K} = \frac{3}{4}\left(\frac{(1-v_s^2)}{E_s} + \frac{(1-v_t^2)}{E_t}\right)$$

Equation 8

Where E_s and v_s are the elastic modulus and Poisson's ratio of the sample respectively, E_t is the elastic modulus of the silicon AFM tip and v_t is the Poisson's ratio of the AFM tip. K can therefore be related to E^* by:

$$K = \frac{4E^*}{3}$$

Equation 9

This definition of K is substituted into Equation 7 to give the repulsive force acting between the AFM tip and sample plane in the Carpick model as the term:

$$F_{DMT} = K\sqrt{R}p^{3/2}\cos^{5/2}\psi$$

Equation 10

Again, the value of p has been resolved into the z axis by multiplying by $\cos\psi$ in order to calculate the AFM tip-sample interaction force, which has subsequently been multiplied by $\cos\psi$ to find the magnitude of the component in the z' axis. The term $\cos^{5/2}\psi$ has resulted from multiplying the two $\cos\psi$ terms together thus:

$$(p\cos\psi)^{3/2}\cos\psi = p^{3/2}\cos^{5/2}\psi$$

Equation 11

The DMT force of adhesion is given by:

$$F_a \quad = -2\pi\gamma R \cos\psi$$

Equation 12

Where γ is the work of adhesion and can be related to equilibrium separation and the Hamaker constant by:

$$\gamma = {}^{A}\!/_{12\pi\xi_0^2}$$

Equation 13

Where A is the Hamaker constant and ξ_0 is the equilibrium separation. As the force of adhesion in Equation 12 is independent of p, only one $\cos\psi$ term is used to quantify the force component in the z' axis.

Finally, the in and out-of-plane near surface damping terms, as shown in Figure 5.3 are defined as:

$$F_{nsd} = -\frac{k}{\omega_0 . Q_{norm}} \dot{p} \cos^2\psi - \frac{k}{\omega_0 . Q_{lat}} \dot{p} \sin^2\psi$$

Equation 14

And if the force due to near surface damping is divided by the effective mass of the AFM tip, $\frac{k}{\omega_0^2}$, then the acceleration of the AFM tip due to near surface damping is given by:

$$a_{nsd} = -\frac{\omega_0}{Q_{norm}} \dot{p} \; \cos^2\psi - \frac{\omega_0}{Q_{lat}} \dot{p} \sin^2\psi$$

Equation 15

The near surface damping terms are dependent on the velocity of the AFM tip ($\dot{p}$) rather than

the tip position. The tilt of the AFM cantilever relative to the plane of the sample surface means that the velocity of the AFM tip relative to the sample surface needs to be resolved relative to the z axis, as shown in Figure 5.3, in order to calculate the force and resulting acceleration due to near surface damping. The accelerations due to near surface damping are resolved to find their components acting along the z' axis, which are therefore affecting the dynamics of the AFM cantilever oscillation.

Using the interaction forces defined above and dividing them by the effective mass of the AFM tip to find the accelerations due to those forces, the Carpick group presented the equation of motion for the AFM tip in intermittent contact with the sample as:

$$\ddot{p} + \frac{\omega_0}{Q_{cant}}(\dot{p} - \dot{\zeta}) + \omega_0^2(p - \zeta)$$
$$= \begin{cases} \frac{\omega_0^2}{k}\left(\frac{AR\cos\psi}{6(p\cos\psi - \xi_0)^2}\right) & p \geq 0.5\text{ nm} \\ \frac{\omega_0^2}{k}\left(\frac{AR\cos\psi}{6(p\cos\psi - \xi_0)^2}\right) - \frac{\omega_0}{Q_{norm}}\dot{p}\cos^2\psi - \frac{\omega_0}{Q_{lat}}\dot{p}\sin^2\psi & 0 < p < 0.5\text{ nm} \\ -\cos\psi\left(K\sqrt{R}p^{3/2}\cos^{3/2}\psi - 2\pi\gamma R\right) & p \leq 0\text{ nm} \end{cases}$$

Equation 16

The first condition at the top right-hand side of Equation 16, describes the AFM tip out-of-contact with the sample's surface. The thickness of the near surface damping layer was arbitrarily defined as 0.5 nm so that the out-of-contact condition is when $p \geq 0.5$ nm. The second condition describes the damping when the AFM tip is within the near surface damping layer, where the AFM tip position is $0 < p < 0.5$ nm, and the third condition describes the repulsive and adhesive forces for when the tip is in contact with the surface and $p \leq 0$ nm. These conditions are equated to the position, velocity and acceleration of the AFM tip (p, $\dot{p}$

and $\ddot{p}$ respectively) and the position and velocity of the cantilever base (ζ and ζ) on the left-hand side of Equation 16.

5.2.2 The MatLab Code

The equation of motion shown above was solved numerically using MatLab's ODE113 differential equation solver, and the phase extracted. The MatLab code used was an adaptation of the work of D'Amato *et al.*[102]. ODE113 was chosen over ODE45 and ODE23, as it is more efficient at solving problems with tighter accuracy requirements. The basic functioning of the code is described here, and adaptations to the code will be described in section 5.3.1.

Figure 5.5 is a flowchart providing a high-level overview of the functioning of the Matlab code. The complete script can be found in the appendix on page 196.

The script begins by defining a list of variables relating to the AFM setup and the sample mechanics. Reduced contact modulus, thickness of the near surface damping layer, lateral quality factor of the near surface damping layer, normal quality factor of the near surface damping layer, work of adhesion, equilibrium separation, peak-to-peak free amplitude, cantilever drive frequency, cantilever spring constant, cantilever quality factor, radius of curvature of the AFM tip, initial velocity of the tip, start time for the calculation, sample tilt relative to the AFM stage and the number of oscillation periods to be modelled in the calculation can all be user defined at the start of the script.

The initial parameters are then used by the MatLab script to calculate further additional values that are dependent upon these initial parameters. The angle of the AFM tip relative to the sample surface in Radians is calculated from the user-defined sample tilt and an offset due to the tilt of the AFM chip within the AFM head. The length of a period of AFM cantilever oscillation in seconds is calculated from the cantilever drive frequency. The total

calculation time over which the AFM cantilever oscillation will be modelled is calculated, and the Hamaker constant is calculated as defined in Equation 13.

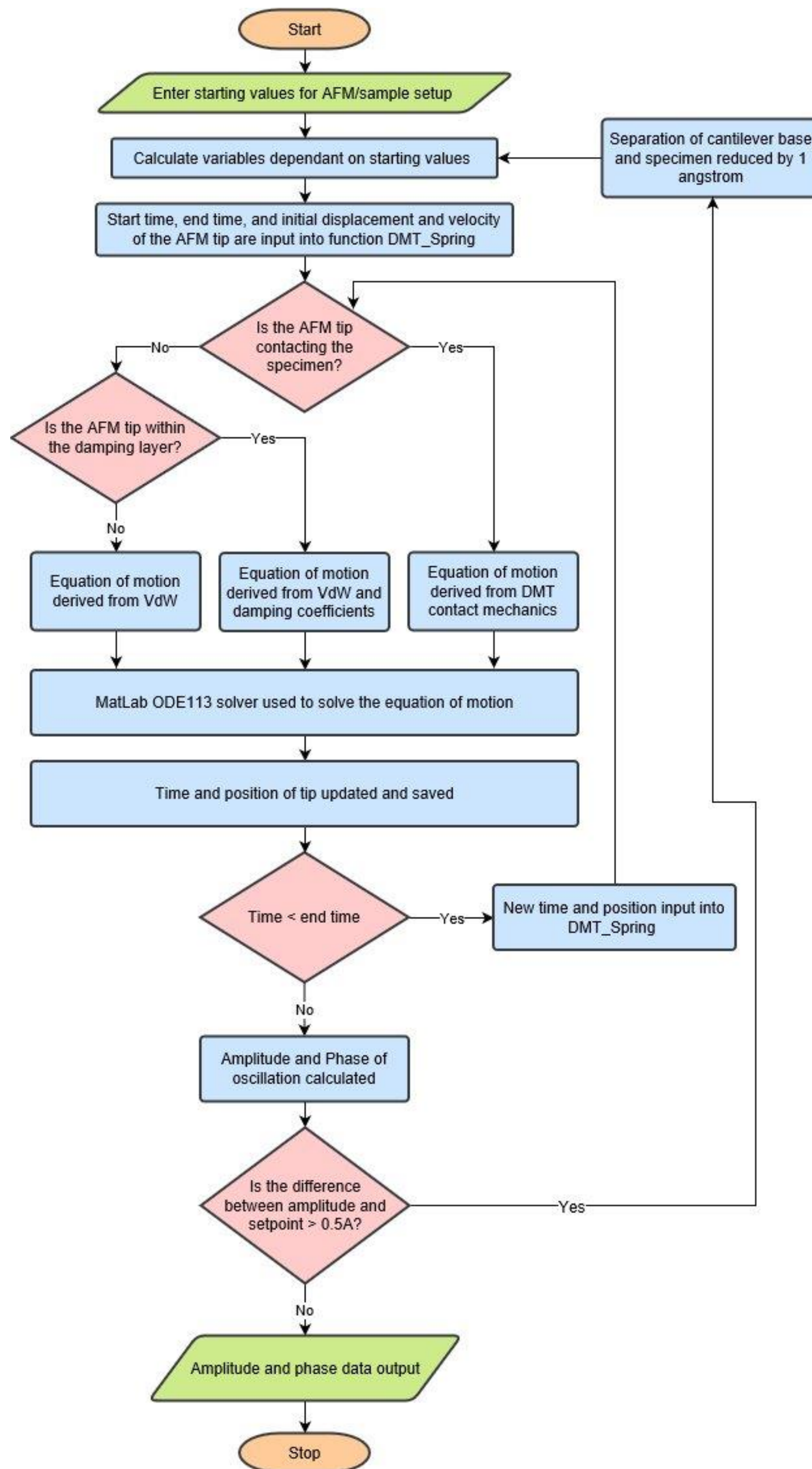

Figure 5.5 Flowchart giving a high-level overview of how the MatLab code modelled the oscillation of the AFM cantilever, dependant on tip-sample interaction, and extracted oscillation amplitude and phase. The tip-sample values input at the beginning of the algorithm include: reduced contact stiffness, thickness of the damping layer, damping layer Q factors, work of adhesion, equilibrium separation, free amplitude of oscillation, drive frequency, cantilever spring constant, cantilever Q factor, tip radius, start time, sample tilt, and the number of oscillation periods to be modelled. Values that are then dependant on these values include the Hamaker constant and starting separation of cantilever base and specimen.

The free amplitude of oscillation, which is measured as the semi-amplitude, is initially given an arbitrary value, as is the initial displacement of the AFM tip. Amplitude is updated with each cycle of the differential equation solver but is used as a terminating condition for a while loop that calls the solver, so therefore requires an initial value.

The ordinary differential equation solver is contained within a while loop, which reduces the value of Z_0 until the desired amplitude is reached.

In this case, the terminating condition for the while loop is when the amplitude, which is updated by the solver after each calculation, is within 0.5 Å of the setpoint value, which is 25% of the peak-to-peak free amplitude or 50% of the free amplitude. At the end of the loop the value of Z_0 is increased by 1 Å, thereby reducing the separation of the cantilever base and the sample within the simulation.

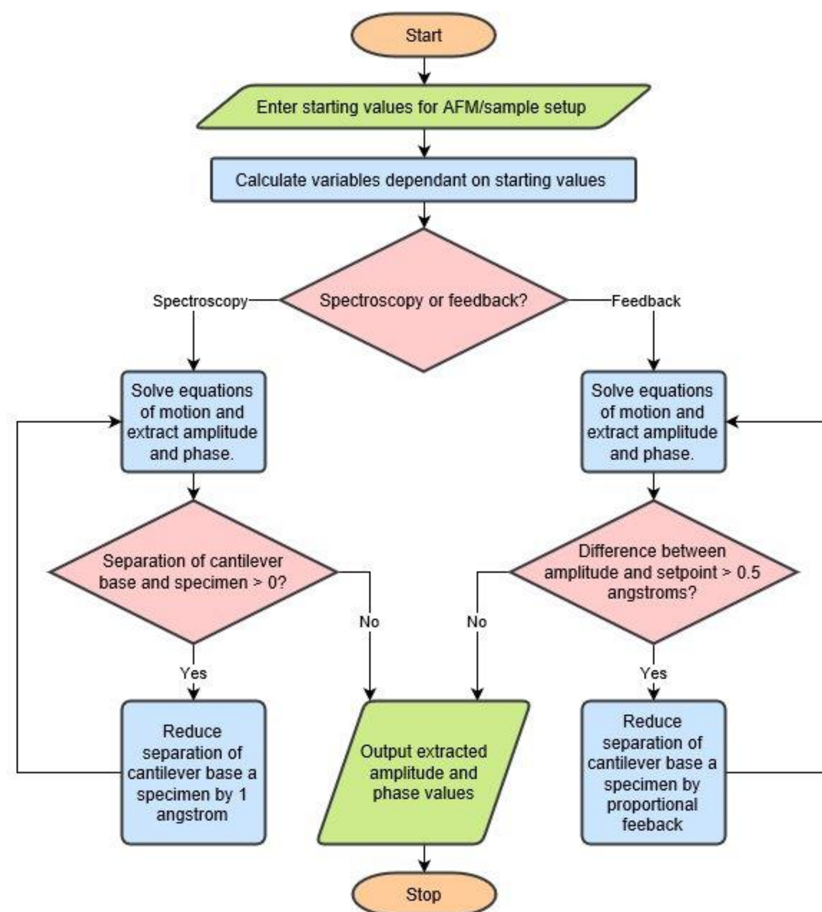

Figure 5.6 Flowchart giving a high-level overview of how while loops around the main body of code were utilised to simulate either z-spectroscopy or tip landing through proportional feedback.

The solver is called within the loop to solve the equation of motion, which is built within the loop, and the components of which are dependent on the instantaneous position of the tip. The function definition requires inputs of time and a position vector and outputs the velocity and acceleration of the tip. The function first defines the position of the cantilever base as a function of time; a sine wave. Then the velocity of the cantilever base is defined by taking the derivative of the position.

Based on the position of the tip, the code calculates whether the AFM tip is in contact with the sample surface. As the surface is defined as being at 0 nm, with negative values of z being above the surface and positive values within the surface.
If the AFM tip is not in contact with the surface, the output force is the out-of-contact van der Waals force. If, however, the tip is in contact with the surface, the output force will be the non-linear DMT contact interaction, which is dependent on tip angle, tip radius, position raised to the power 3/2 and the reduced contact modulus between the tip and the sample.
If the tip is above the surface, but still within the thickness of the near surface damping layer, the function adds the near surface damping terms to the equation of motion.
All of the terms of the equation of motion are subsequently used by the ODE113 solver to output values of time (t) and displacement (d) and return control to the parent script.

As the initial part of the simulated motion of the cantilever will include a period of instability before reaching equilibrium, the script interpolates the last 200 periods of the AFM cantilever oscillation. Using these interpolated datasets, the script extracts the phase of the cantilever using Fourier transform subfunctions.
The amplitude of the cantilever oscillation is then calculated by finding the maximum and minimum values in the interpolated position data, which gives the peak-to-peak amplitude, and dividing the difference by 2 to find the semi-amplitude.
The script calculates values of sample compression under the AFM tip and penetration of the AFM tip through the near surface damping layer based on the amplitude of the AFM

cantilever and maximum displacement of the AFM tip, updates the value of Z_0 and outputs the values of AFM cantilever phase and amplitude.

As stated above, the calculated amplitude is used in the terminating condition for the while loop, and will allow the calculation to repeat, with the position of the cantilever base stepping towards the surface, until the amplitude falls within the desired range.

5.3 Methodology and Results

5.3.1 Modifications to the model/code

The Matlab script as supplied by D'Amato et al was first adapted to meet the requirements of this investigation. Originally, the script would use a single set of starting conditions and output a single phase value for a particular AFM cantilever and sample setup. The simulation was initially evaluated by modifying the while loop around the ODE solver to simulate either a feedback landing of the AFM tip, or a Z-spectroscopy approach curve by solving the equations of motion for a range of values of Z. Also, for loops have been added around the while loop so that the calculations can be repeated while the script steps through values of various parameters.

The feedback landing version of the while loop allows the cantilever base to quickly approach the sample until the value of amplitude reaches the desired setpoint. The first variation in this piece of code is that the starting value of Z_0 is not defined as a point far from the surface, as was the case in previous versions of the script. Instead, the value assigned to Z_0 at the beginning of the loop is dependent on the free peak-to-peak amplitude of the cantilever and the defined setpoint value, which has been created for this purpose.

If the desired end point for the calculation is a setpoint amplitude that is 50% of the free amplitude, then the setpoint value would be defined as 0.5. For an infinitely stiff sample, it is reasonable to assume that the amplitude of the cantilever is equal to the separation of the

cantilever base and the sample, i.e. an amplitude of 100 nm would occur at a separation of 100 nm, if the separation is not greater than the free amplitude. It is for this reason that the script sets the initial separation at this predicted value; for stiff samples this initial value will be close to the desired setpoint condition and for softer samples the separation will need to be reduced further as the surface will be deformed by the AFM tip and result in the amplitude of the AFM cantilever oscillation being greater than the setpoint value.

The while loop uses the deviation of amplitude from the desired setpoint value as the terminating condition and varies the value of Z_0 using a proportional feedback term.
This version of the while loop allows us to observe the effect an experimental parameter, such as the modulus of the sample, has on the cantilever dynamics at a specific setpoint condition by adjusting the step size proportionally to the deviation from the equilibrium condition rather than the gradual approach implemented in the original code. The script will then output the phase, amplitude etc. of this final setpoint condition only before moving to the next value in the for loop.
Figure 5.6 is a flowchart that provides an overview of how the new while loops would simulate either a feedback approach or Z-spectroscopy.

Initial attempts to use this feedback loop resulted in the separation overshooting the setpoint and then snapping back, never reaching the setpoint amplitude. Upon outputting and plotting the displacement/time data from the solver, and thereby visualising the complete series of oscillations, it became apparent that this overshooting was due to several factors. Firstly, the amplitude of the cantilever oscillation was found to oscillate, especially for softer samples. To combat this fluctuation in AFM cantilever oscillation amplitude, the error tolerances for the ODE solver were tightened, and the maximum step size was reduced from 50 ns to 5 ns, which effectively allowed the solver more time to react to the rapidly changing forces when the AFM tip moved in and out of contact with the sample surface. The problem of the oscillating amplitude had been further compounded by the method by which the amplitude was being

calculated. The original code, as described earlier, would simply divide the difference between the highest and lowest position of the tip by 2 and assign this value to amplitude. This original method for calculating the amplitude meant that any instability or fluctuation in the oscillation of the cantilever would result in an artificially high AFM cantilever amplitude value, and this in turn would cause the feedback loop to overshoot. The method of calculating amplitude was therefore updated, separating each of the last 200 periods of the oscillation and interpolating the data for each period before finding the maximum and minimum data point and adding them to a log for each value. These minimum and maximum value lists are then averaged, and it is the mean values of the minimum and maximum that are used to calculate the amplitude of oscillation.

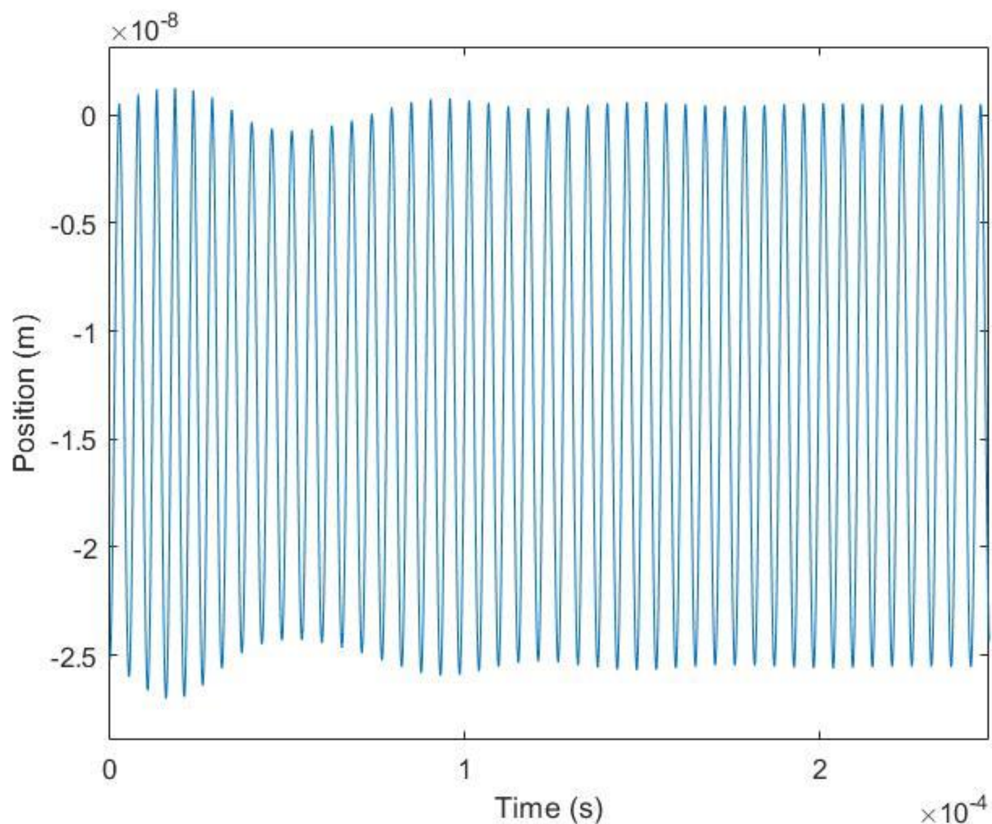

Figure 5.7 An example of raw output from the ODE solver; a plot of tip position as a function of time, showing the first 250 µs of oscillation. There is an initial period of instability where the amplitude fluctuates, before settling out.

Plotting the full series of oscillations also made it apparent that the arbitrary starting conditions of the cantilever were out of phase with the base of the cantilever. This meant that

the initial 20-30 % of the oscillations for each cycle through the while loop were being used as the cantilever phase inverted through 180°. To rectify this, the initial values of tip displacement and velocity were defined as though at the peak of an oscillation. Velocity was therefore defined as 0 and tip displacement as Z_0 minus the amplitude of oscillation. The alterations to solver tolerances, the calculation of amplitude and the starting conditions of the cantilever have resulted in the cantilever oscillations reaching a stable amplitude and doing so more rapidly in terms of the number of oscillations (although the calculation times have increased) to ensure a more realistic feedback loop. This can be seen in the raw output from the solver, shown in Figure 5.7.

The z-spectroscopy loop is simpler than the feedback loop as it steps through values of Z_0, until reaching the predefined Z_0 stop point. This while loop is similar to the original implemented by D'Amato *et al*.[102] except that the terminating condition is independent of the value of amplitude and the loop will continue until it reaches the defined separation (in this case 0 nm). The script keeps a log of phase, amplitude, Z_0, tip penetration and sample compression; which will be output at the end of the calculations, thus allowing complete AFM tip-sample approach curves to be plotted. These new Z-spectroscopy capabilities of the code compare the phase response of the simulation as a function of tip-sample separation to AFM experimental data. Thus, comparison of the simulation with the experimental data was used to validate if the simulation was providing meaningful values of AFM cantilever amplitude and phase.

A number of problems were encountered when providing comparison of the simulation to the experimental data. Several variables, as discussed in detail below, within the model are not easily measured physically and have values set arbitrarily for subsequent tuning for the simulated data to match the experimental. Secondly, whilst working through the MatLab code, a significant inconsistency between the code and the equation of motion presented by D'Amato *et al* for the repulsive term was found. In the paper, the $\frac{\omega_0^2}{k}$ term was noticeably omitted and, as the term has a value in the order of 4×10^{10}, consequently impacted the

magnitude of the repulsive force significantly. The equation of motion therefore was modified as highlighted below:

$$\ddot{p} + \frac{\omega_0}{Q_{cant}}(\dot{p} - \dot{\zeta}) + \omega_0^2(p - \zeta)$$

$$= \begin{cases} \frac{\omega_0^2}{k}\left(\frac{AR\cos\psi}{6(p\cos\psi - \xi_0)^2}\right) & p \geq 0.5\text{ nm} \\ \frac{\omega_0^2}{k}\left(\frac{AR\cos\psi}{6(p\cos\psi - \xi_0)^2}\right) - \frac{\omega_0}{Q_{norm}}\dot{p}\cos^2\psi - \frac{\omega_0}{Q_{lat}}\dot{p}\sin^2\psi & 0 < p < 0.5\text{ nm} \\ -\frac{\omega_0^2}{k}\left(K\sqrt{R}p^{3/2}\cos^{3/2}\psi - 2\pi\gamma R\right)\cos\psi & p \leq 0\text{ nm} \end{cases}$$

Equation 17

5.3.2 Variable Influences on the AFM cantilever phase

The variables in the model that cannot be measured by direct means have been assigned arbitrary values. In order to determine whether these assigned values are realistic, their effects on the phase approach curves have been simulated in MatLab. Specifically, tuning parameters was used to fit a simulated AFM tip approach curve towards a silicon surface with an AFM experimental approach. It should be noted that in Figure 5.8 and similar plots, both phase shift and amplitude are dependant on the z position of the cantilever, but have been presented in this way to simulate a phase shift vs setpoint amplitude z-spectrum, as produced by the AFM. Each variable was tested by looping through a series of values, and simulating a z-spectrum and a feedback condition for each value.

5.3.2.1 Qnormal

Q_{normal} (Q_{norm}) is the quality factor of the near surface damping layer in the direction of the surface normal axis. Q_{normal} is a denominator in the term for calculating the near-surface damping force and therefore lower values of Q_{normal} will result in a larger damping force. Figure 5.8 is a plot of phase against amplitude approach curves where all parameters were kept constant, with the exception of the value of Q_{normal}. The figure shows a decreasing value of Q_{normal} resulting in a phase value increase. Decreasing Q_{normal} also causes the position of the maximal phase peak, which indicates the region where attractive forces are dominating the phase shift, to shift to lower amplitudes. However, the minimum of each approach curve in Figure 5.8 appears to occur at constant AFM cantilever amplitude. In Figure 5.9 the data are presented as phase shift against Q_{normal}, with the amplitude being held constant, thereby simulating the condition within a feedback loop. Figure 5.9 clearly indicates that the relationship between Q_{normal} and phase is nonlinear; as the value of Q_{normal} increases the value of the damping force, and therefore the contribution to the phase shift, tends towards zero. This would imply that, with reference to Figure 5.1, increasing Q_{normal} is causing a shift of the phase response to the right, pushing it further into the repulsive regime. The plot in Figure 5.9

also highlights the boundary condition value of Q_{normal} approaching zero causes a damping force tending toward infinity.

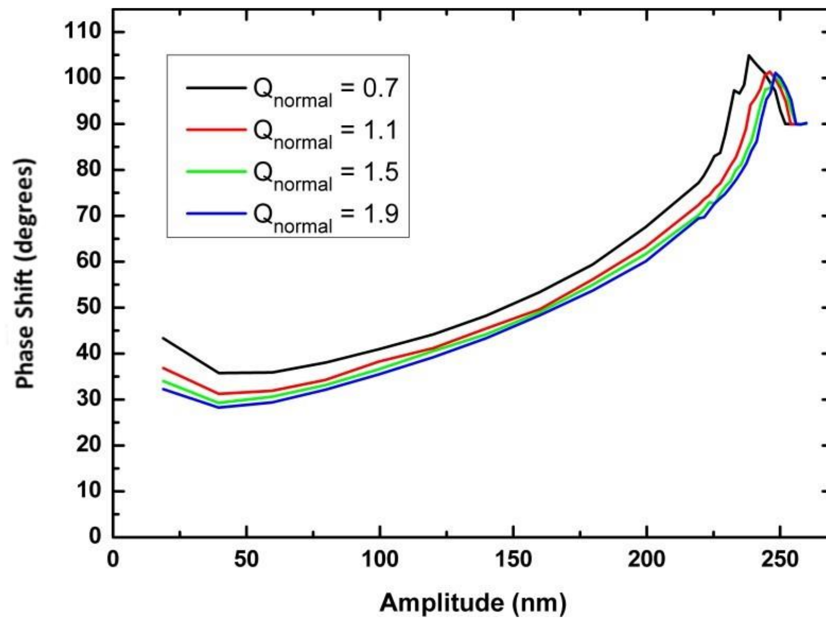

Figure 5.8 AFM cantilever phase vs AFM cantilever amplitude plot showing the effects of varying the value of Qnorm. Decreasing Qnorm causes a corresponding phase shift increase and the positive phase shift peak (above 90° while the attractive forces dominate) moves to the left. The Z position of the cantilever base is the independent variable in this dataset, and the amplitude and phase shift are both dependant on it, but have been presented in this manner to simulate a phase shift vs amplitude z-spectrum

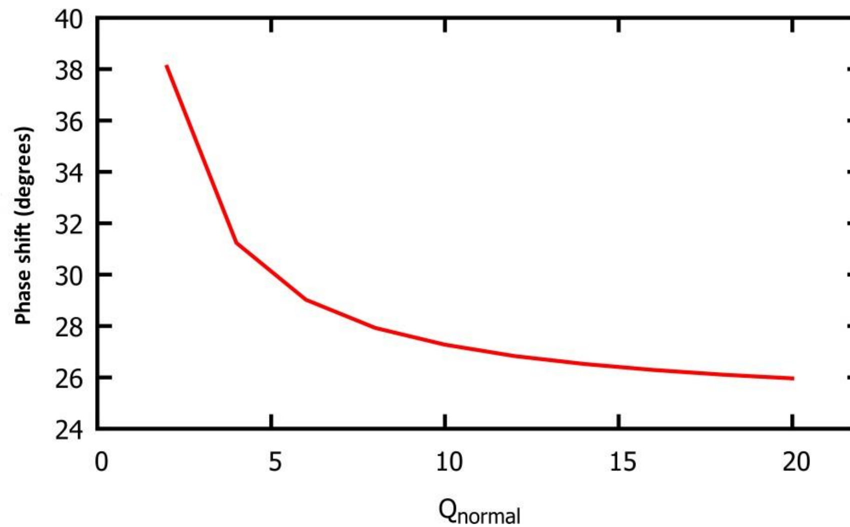

Figure 5.9 Plot of AFM cantilever phase against Q_{norm} at a fixed setpoint amplitude showing that as the value of Q_{norm} increases the phase shift decreases and it is a non-linear relationship.

5.3.2.2 Qlateral

$Q_{lateral}$ (Q_{lat}) is the quality factor of the near surface damping layer in the direction parallel to the sample surface. As is the case with Q_{normal}, $Q_{lateral}$ is a denominator in the term for the near surface damping force and therefore as the value of $Q_{lateral}$ increases the value of the damping force will decrease.

Figure 5.10 is plot of AFM phase shift against AFM cantilever amplitude for a range of values of $Q_{lateral}$ and as with Q_{normal}, reducing the value of $Q_{lateral}$ increases the resulting phase shift and shifts the positive phase peak to lower amplitudes. Figure 5.11 is a plot of phase against $Q_{lateral}$ while the amplitude of oscillation is held constant. As with Q_{normal}, increasing Q_{lat} is causing a shift in the AFM pahse shift values to higher frequencies, or potentially sharpening the resonance peak, implying that the tip is experiencing more repulsive forces. The relationship between $Q_{lateral}$ and the predicted AFM phase shift is non-linear, as might be expected from the non-linearity observed in the effect that varying Q_{normal} had on AFM phase shift. The effect that $Q_{lateral}$ has on the AFM phase shift is less than the effect that Q_{normal} exerts as the contribution of $Q_{lateral}$ to the damping force on the AFM cantilever, when operating at low tilt angles, is smaller when compared to Q_{normal} ($\sin^2(11) = 0.036$, $\cos^2(11) = 0.964$). Note that the scale on the abscissa in Figure 5.9 reaches a value of 20 but a significantly smaller value up to 0.2 in Figure 5.11.

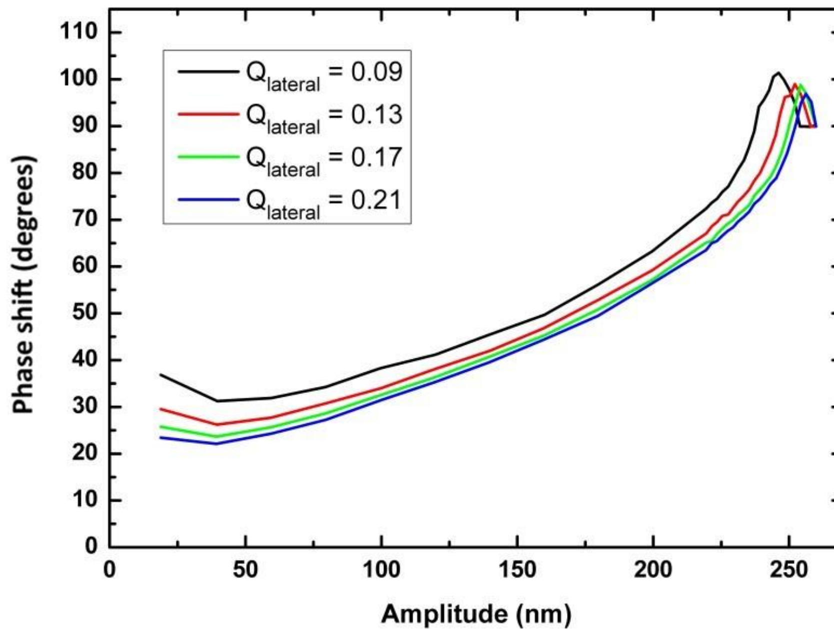

Figure 5.10 AFM cantilever Phase vs AFM cantilever amplitude plot showing the effects of varying the value of Q_{lat}. As Decreasing Q_{lat} causes a corresponding AFM cantilever phase increase and the positive phase shift peak (above 90° while the attractive forces dominate) moves to the left.

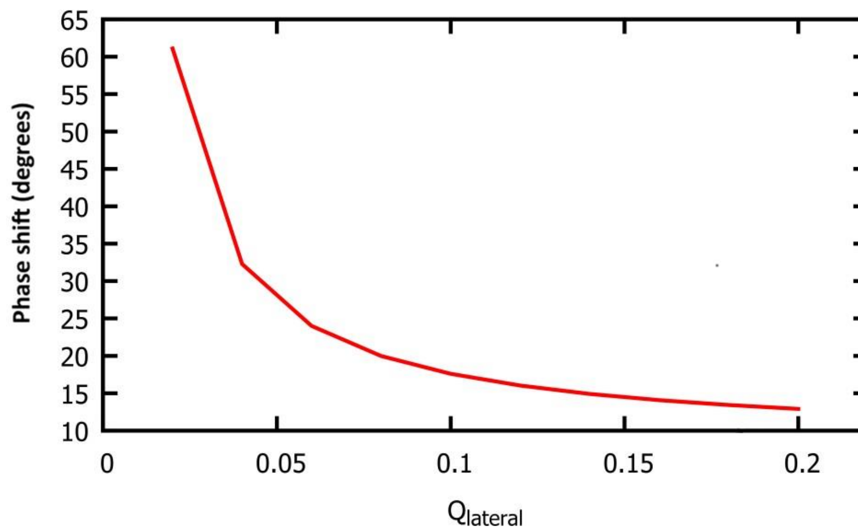

Figure 5.11 Plot of AFM cantilever phase against Q_{lat} at a fixed setpoint amplitude showing that as the value of Q_{lat} increases the phase shift decreases and it is a non-linear relationship.

5.3.2.3 Thickness of the near-surface damping layer

The thickness of the damping layer is a potentially significant parameter and was varied at intervals of 2.5 Å, which is of the order of the thickness of a single water molecule[114], in order to understand the damping contribution to AFM phase change values. Figure 5.12 shows a plot of AFM cantilever phase change against AFM cantilever amplitude during approach curves towards a damping layer thicknesses ranging from 2.5 to 10 Å. The plot in Figure 5.12 shows that increasing the thickness of the damping layer significantly increases the phase shift recorded at each cantilever amplitude and causes a shift in the positive phase shift peak to lower amplitudes. A shift in the minimum phase shift value to higher amplitudes with increasing layer thickness is clearly observed in Figure 5.12, which suggests that the region of the curve between the maximum and minimum AFM phase values becomes shorter as the layer thickness is increased. Figure 5.13 plots the AFM phase change against damping layer thickness at a constant setpoint amplitude and shows a positive correlation with a slightly positive curve upwards as thickness increases. The data presented in figures Figure 5.12Figure 5.13 would suggest that by increasing the thickness of the damping layer, the phase shift curve, as seen in Figure 5.1, is being stretched horizontally, so that the phase inversion occurs over a greater frequency range, as if reducing the Q factor of the AFM cantilever.

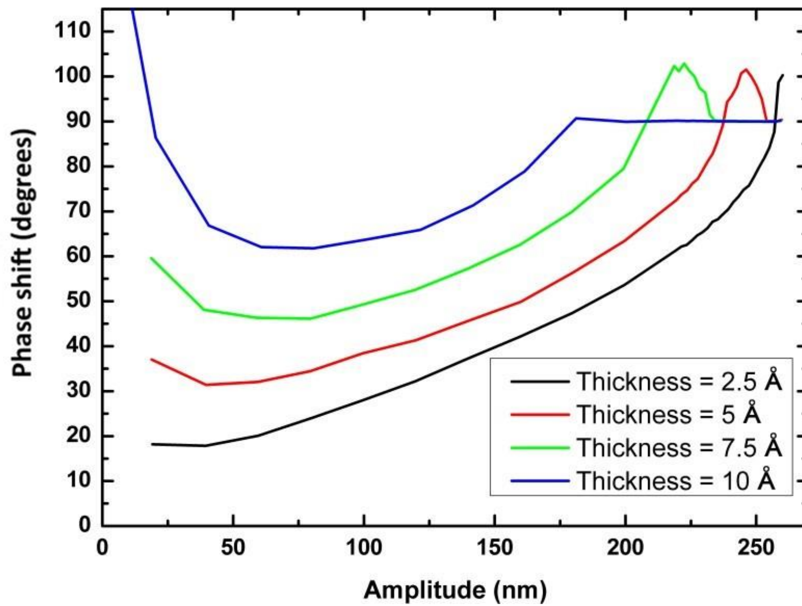

Figure 5.12 AFM cantilever phase vs AFM cantilever amplitude plot showing the effects of varying the thickness of the near surface damping layer. Increasing the thickness of the near surface damping layer causes a corresponding increase in the AFM cantilever phase shift and the positive phase shift peak (above 90° while the attractive forces dominate) moves to the left.

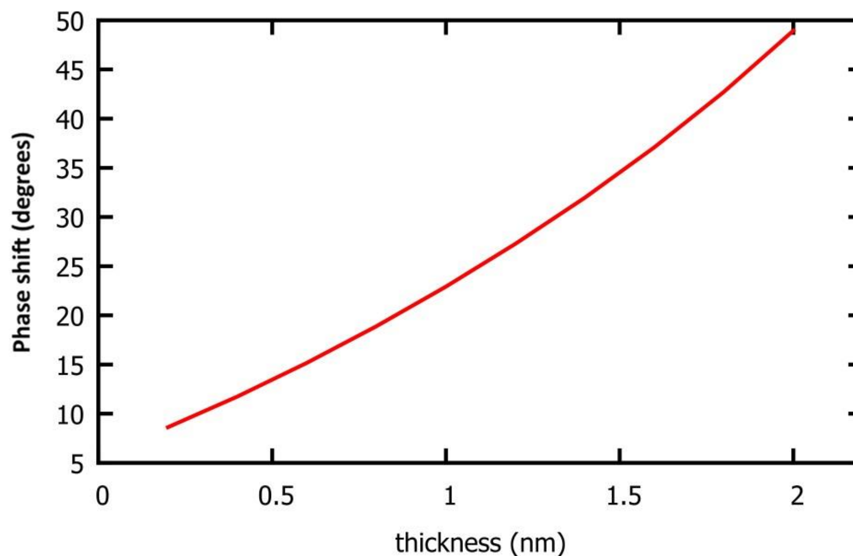

Figure 5.13 Plot of AFM cantilever phase against the thickness of the near surface damping layer when at a constant setpoint amplitude showing a positive correlation between the thickness of the layer and the phase shift value. The relationship is almost linear within the range examined

5.3.2.4 Radius of curvature of the AFM tip

The radius of curvature of the AFM tip is a significant parameter that influences the amount of interaction between the AFM tip and the sample's surface. The AFM tip can be measured by several means but is most directly found from imaging the tip apex using electron microscopy and fitting a circle to the end of the tip to give an estimate of the radius[115]. Indirect methods of determining the AFM tip radius of curvature include using the AFM tip to image a grating containing high aspect ratio features such as fibres/spikes. The resultant AFM image will give a reconstruction of the AFM tip shape as it scans over each high aspect ratio feature and is able to give a suitable radius of curvature estimation.[116]

Imaging high aspect ratio features with an AFM tip is a relatively simple method for estimating the AFM tip radius of curvature, however the actual radius of curve can vary during imaging as contamination and/or wear of the AFM tip, especially when scanning harder samples, often occurs. Because of the variability in the absolute value of the radius of curvature of the AFM tip a set of approach curves were produced to test the effect AFM tip radius has on the recorded AFM phase shift. The complete approach curves themselves were difficult to distinguish, but Figure 5.14 shows the effect varying tip radius, R, has on the phase at a fixed setpoint amplitude. As can be seen in Figure 5.14, the effect of varying the tip radius is slight compared to the variations seen when altering the parameters of the near-surface damping layer; by altering the value of R from the typical radius of an AFM probe, 10 nm, to a value 20 nm the phase is reducing by less than 1°, and the non-linear nature of the relationship means that further increases in the radius of curvature of the tip will have less effect of the resulting phase shift.

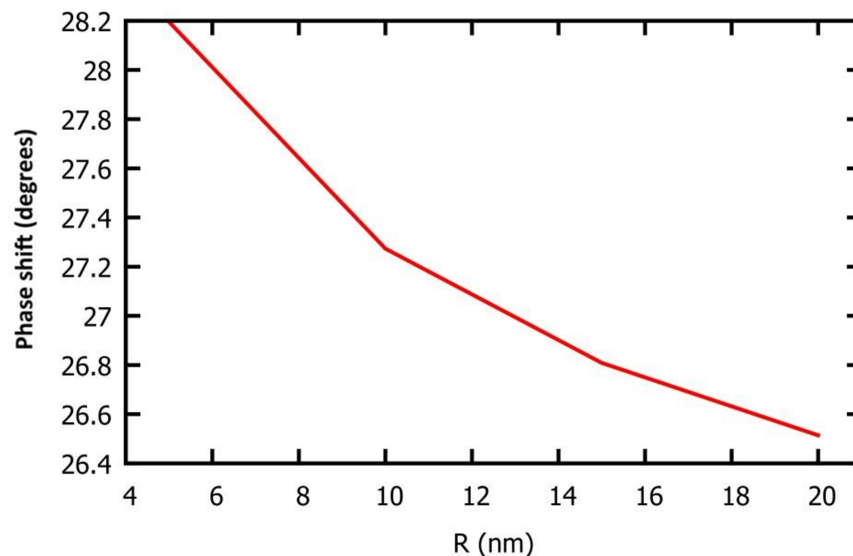

Figure 5.14 Plot of AFM cantilever phase against the radius of curvature of the AFM probe at a fixed setpoint amplitude. Increasing the radius of curvature of the AFM tip causes a decrease in the phase of the AFM cantilever.

5.3.2.5 Sample tilt angle

The sample tilt angle will have several subtle effects on the dynamics of the cantilever. By altering the angle at which the tip approaches the surface the apparent thickness of the near-surface damping layer alters. Also, the ratio of the two quality factors that contribute to the near-surface damping will be altered. In addition to the considerations about the damping layer, as the approach angle of the tip becomes shallower, the effective rate at which the tip approaches the surface will go down. Figure 5.15 is a plot of AFM phase vs. AFM cantilever amplitude showing the effect that sample tilt angle has on the shape of the approach curve. The value of the sample tilt angle was varied between -6 and 9° (remembering that the AFM has a positive offset angle to keep the cantilever base clear of the sample) to assess the effect of the sample being mounted at an offset relative to the AFM head. From Figure 5.15 it can be seen that increases in the sample tilt angle result in an increase in the phase shift for any given amplitude, and similar to the effect of layer thickness (though far less pronounced), the difference in AFM cantilever amplitude between the maximum and minimum phase shift values is reduced, as both extremes of the AFM phase shift data move

towards the centre of the plot. This effect would imply that the phase shift curve, seen in Figure 5.1, is again being stretched horizontally as the specimen tilt angle is increased, as if the Q factor of the cantilever were being reduced.

Figure 5.16 is a plot of the AFM phase shift against the value of sample tilt angle at a setpoint amplitude and shows the non-linear positive correlation between the two variables.

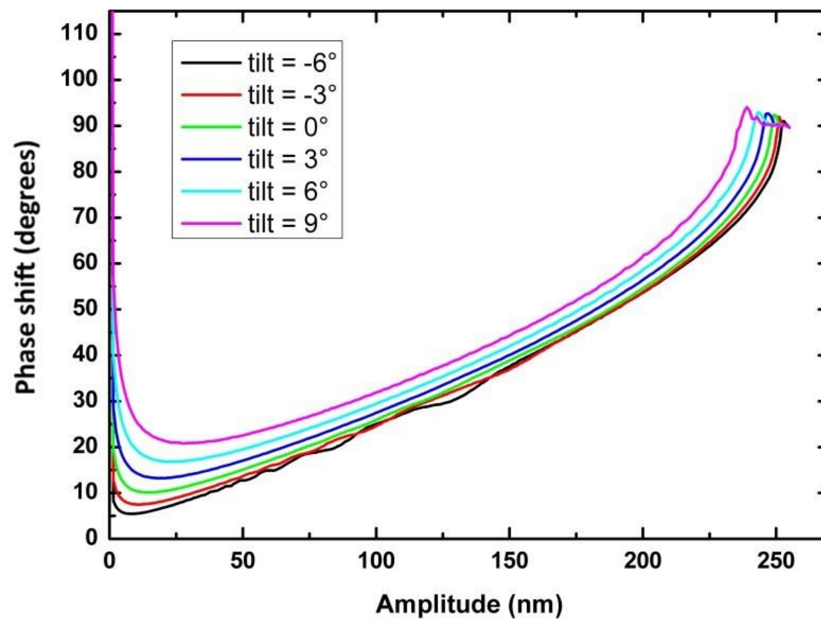

Figure 5.15 AFM cantilever phase vs AFM cantilever amplitude plot showing the effect of varying the sample tilt angle relative to the AFM tip. Increasing the tilt angle sample surface relative to the long axis of the AFM cantilever causes a corresponding increase in the phase of the AFM cantilever and the positive phase peak shifts to the left. Increasing the tilt angle also causes a softening or rounding off of the approach curve around the AFM phase minimum.

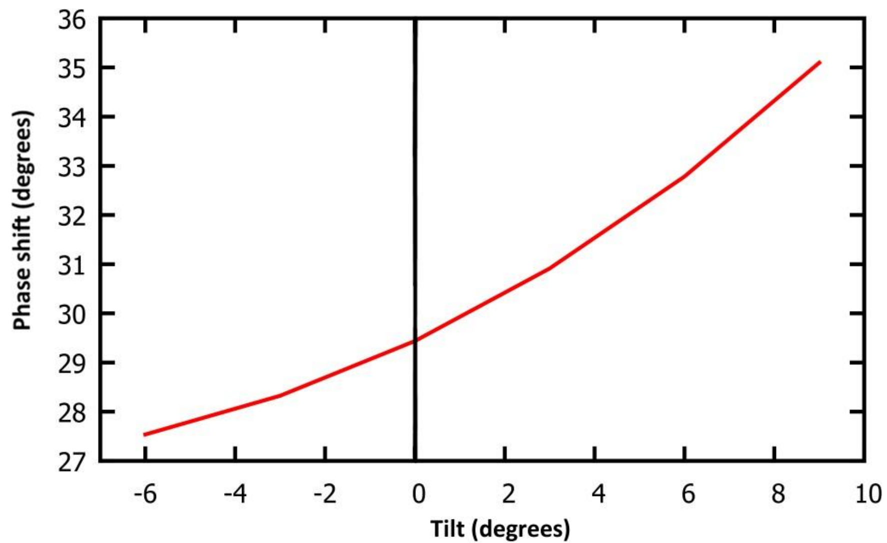

Figure 5.16 Plot of AFM cantilever phase against sample tilt angle at a fixed setpoint amplitude showing that the phase of the AFM cantilever tends to increase as the sample tilt angle is increased.

5.3.2.6 Equilibrium separation between the AFM tip and the sample surface

The equilibrium separation, xi, is the distance between the AFM tip and the sample surface when the repulsive and attractive forces are balanced, and the net force is therefore zero. The value of xi is typically of the order of 200 pm but varies depending on the materials. The effect of xi on the phase response of the AFM cantilever was simulated to assess if the use of a single, arbitrary value could be used for all sample materials. The values of xi used were in the range of 50 to 400 pm. Figure 5.17 is a plot of AFM phase against equilibrium separation as predicted by the MatLab simulation. The values of xi in this range appear to have an insignificant effect on the AFM phase signal, with the magnitude of the variation in the AFM phase being less than 0.04°, which is within the level of noise expected from an experimental setup.

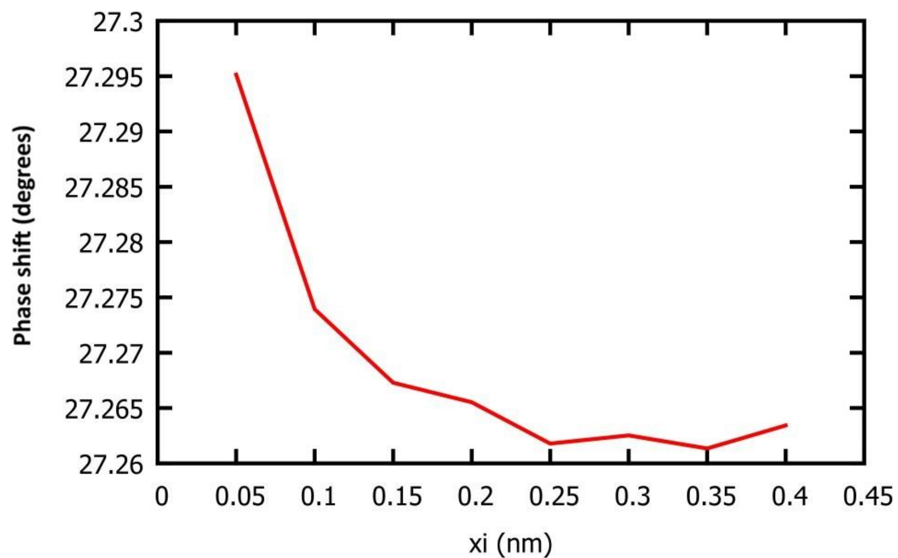

Figure 5.17 Plot of AFM cantilever phase against equilibrium separation of the AFM tip and the sample surface at a fixed setpoint amplitude. Varying the equilibrium separation has little effect on the phase value (falling within the noise expected in an experimental setup).

5.3.3 Fitting simulations to experimental data

The simulation variables considered in section 5.3.2 were each varied through a series of simulation trials in order to produce a set of AFM approach curves of phase shift against cantilever amplitude that were a match for equivalent approach curves produced experimentally. The simulation parameters used in this fit were used to investigate the effects of reduced contact modulus of AFM phase.

5.4 The effect of reduced contact modulus on AFM phase

Simulations were conducted using MatLab to study the influence of reduced contact modulus on the phase shift of the AFM cantilever. By using the feedback approach loop, AFM phase shift values were recorded for a range of values of reduced contact modulus, K, whilst

maintaining a constant setpoint amplitude. The data from these simulations are presented in Figure 5.14, which has been fitted with an exponential decay function. Figure 5.18 shows that as the value of K is increased the expected AFM phase shift will decrease, levelling off as the modulus approaches infinity. As the reduced contact modulus between the AFM tip and the sample surface decreases the phase of the oscillating AFM cantilever increases, tending towards infinity as K approaches zero. In reality, though, the phase of the oscillating cantilever is by definition constrained between 0 and 180°.

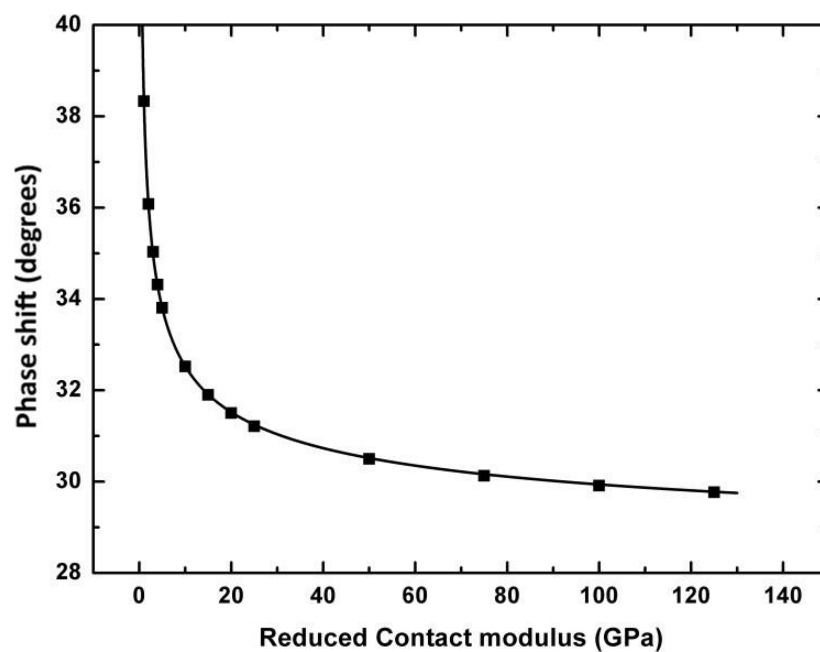

Figure 5.18 Plot of AFM cantilever phase against reduced contact modulus between AFM tip and sample showing that the value of the AFM phase shift decays exponentially as the reduced contact modulus increases.

5.5 Conclusions

In this chapter the dynamics of the AFM cantilever have been examined and modelled using the equations of motion presented by D’Amato et al.[102] MatLab was used to simulate the oscillations of the AFM cantilever by solving the equations of motion, and then extract the phase of the oscillating cantilever be means of a Fourier transform. The AFM cantilever and sample parameters were tuned to match those of an experimental setup by simulating the

cantilever response during a number of Z-spectroscopy approach curves, using ranges of values for the variables of equilibrium separation, near-surface damping layer quality factors, sample tilt angle, AFM tip radius of curvature, and near-surface damping layer thickness. Using the assigned values for the simulation parameters the AFM phase was predicted for sample materials with a range of Young's elastic moduli, as shown in Figure 5.18, which relates the AFM phase signal directly to the reduced contact modulus of the system. The simulation results of AFM phase against reduced contact modulus can be used to assign values of K to each pixel in an AFM phase contrast image and subsequently the Young's elastic modulus of the sample can be mapped at resolution of several nanometers.

The time taken to produce Figure 5.18 through the execution of the MatLab code was approximately half a day, running on a standard desktop computer. This means that the model would be too costly and time-consuming to include in a surface mechanics package in order to calculate contact mechanics while imaging. However, it could possibly be adapted for inclusion in an offline data analysis toolbox.

6 Quantitative phase imaging of nanocomposite materials

6.1 Aims

Methodology developed in Chapter 5 is able to quantify a standard AFM phase image into mechanical information, specifically Young's elastic modulus, using FIB to prepare relatively flat sample surfaces. Thus, the mapping of elastic modulus of any material can be achieved in principal, provided a suitably flat surface is prepared. This Chapter demonstrates the effectiveness of quantitative phase imaging by applying the AFM and FIB techniques to a composite material containing discrete nanoscale phases. As the AFM can image at nanometre resolution, a nanocomposite material is perhaps a suitable test of quantitative phase imaging where high resolution mechanical mapping over micron areas is required.

6.2 Preparation of a model polymer nanocomposite

In order to test and utilise quantitative AFM phase imaging, samples of a model polymer nanocomposite were prepared and imaged using the quantitative technique. The nanocomposite used was a layered tape consisting of two components, polypropylene (PP) and an elastomer (Versify 2300, DOW). Such phases in the composite are used as the polypropylene is a relatively hard polymeric phase whereas the elastomer is expected to be considerably softer. The tape was fabricated at Nanoforce Technology Ltd by coextruding two polymer components together to form a two-layered tape as described in chapter 3. The bilayer tape was then multiplied up by repeated stacking across heated rollers to produce a drawn, multi-layered tape as shown in Figure 6.1. The specific tape used went through 12 of

these mixing/drawing steps, and so should contain up to 2^{13} = 8192 layers. Some variation will be present in the total number of layers if the orientation of the tapes as they were being combined was such that two layers of the same material were at the join. The thickness of the polymer nanocomposite tape was measured to be of the order of 630 μm, therefore the thickness of each individual layer is expected to be $(6.3 \times 10^{-4})/8192 \approx 7.7 \times 10^{-8}$ m.

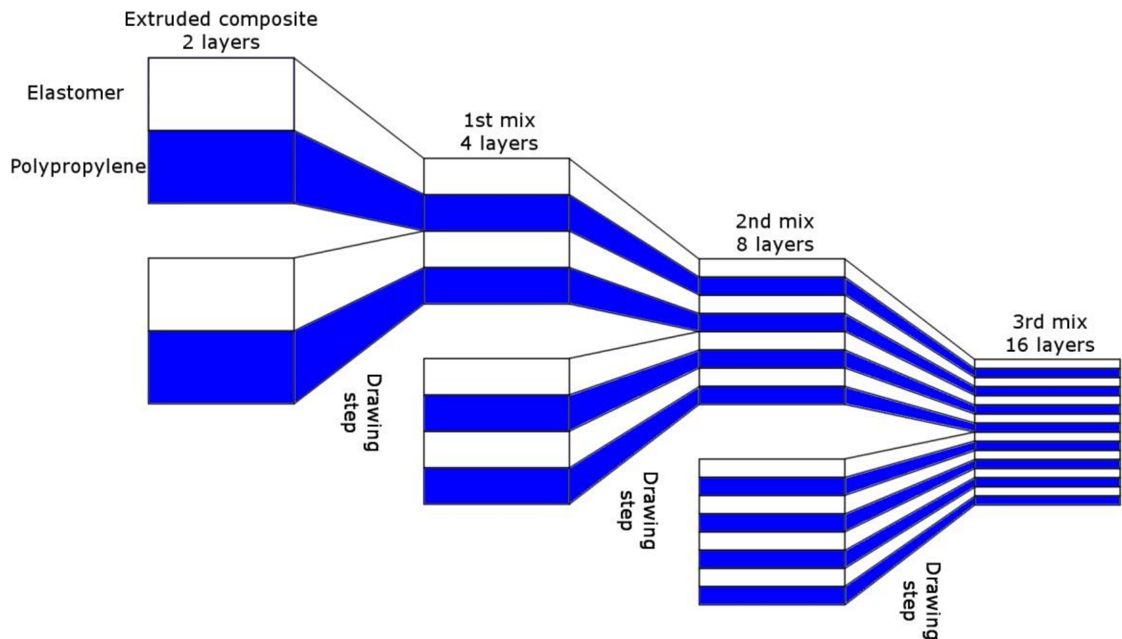

Figure 6.1 Schematic of the layering process used to generate a polymer nanocomposite from a macroscopic coextruded polymer tape. At each drawing step two composite tapes are combined and drawn over hot rollers, thereby extending the length of and thinning the layers of the tape, and causing the two tapes to adhere together. By recombining and doubling the number of layers of tape in this way, thousands of layers can be quickly achieved. The equipment used, and final tape can been seen in Figures 3.3 and 3.4 respectively.

The polypropylene and elastomer were chosen for the model material as the difference in their elastic moduli should offer sufficient contrast during AFM phase contrast imaging to easily resolve the two components, whilst at the same time the length scale of the layers and the relative softness of the materials offer a challenge in terms of the quantification of the results.

The elastic modulus of the nanocomposite tape was measured through the use of AFM phase contrast imaging, AFM force-displacement spectroscopy and tensile mechanical testing. The results of all three techniques were compared in order to test the accuracy and reliability of AFM phase contrast imaging as a method for quantitative mechanical measurement.

6.3 AFM phase imaging of the nanocomposite

6.3.1 Sample preparation and imaging

The fabricated nanocomposite tape was prepared so that a relatively flat cross-section could be imaging using the quantitative phase AFM. The nanocomposite tape was first fractured under liquid nitrogen in order to produce flat fracture surface without the shear and tool damage that would be present if cut with a blade or scissors. The freeze-fractured tape sample was inspected under SEM and polished using FIB milling approaches as described in section 3.5.2, in order to produce a flat cross-section. The nanocomposite tape was prepared for FIB milling by first mechanically mounting the tape within the AFM-SEM vertical clamp holder described in section 3.3, and coating with gold. AFM imaging of the FIB polished tape surface was achieved by first removing the nanocomposite fixed to the vertical clamp holder from the dual-beam instrument. The holder was considered to be mechanically stable so that removing the tape from the holder to fix to another holder can be deemed an unnecessary additional step.

Therefore, the holder was modified by removing the stub pin so that the clamp holder could then be placed onto the sample stage of the AFM (NTegra, NT-MDT, Russia) and imaged using the scanning head. The AFM topography and phase contrast images in Figure 6.3 were obtained using a VISTAprobes T-190 with a calibrated spring constant of 29.6 Nm^{-1} and a resonance frequency of 183.5 kHz.

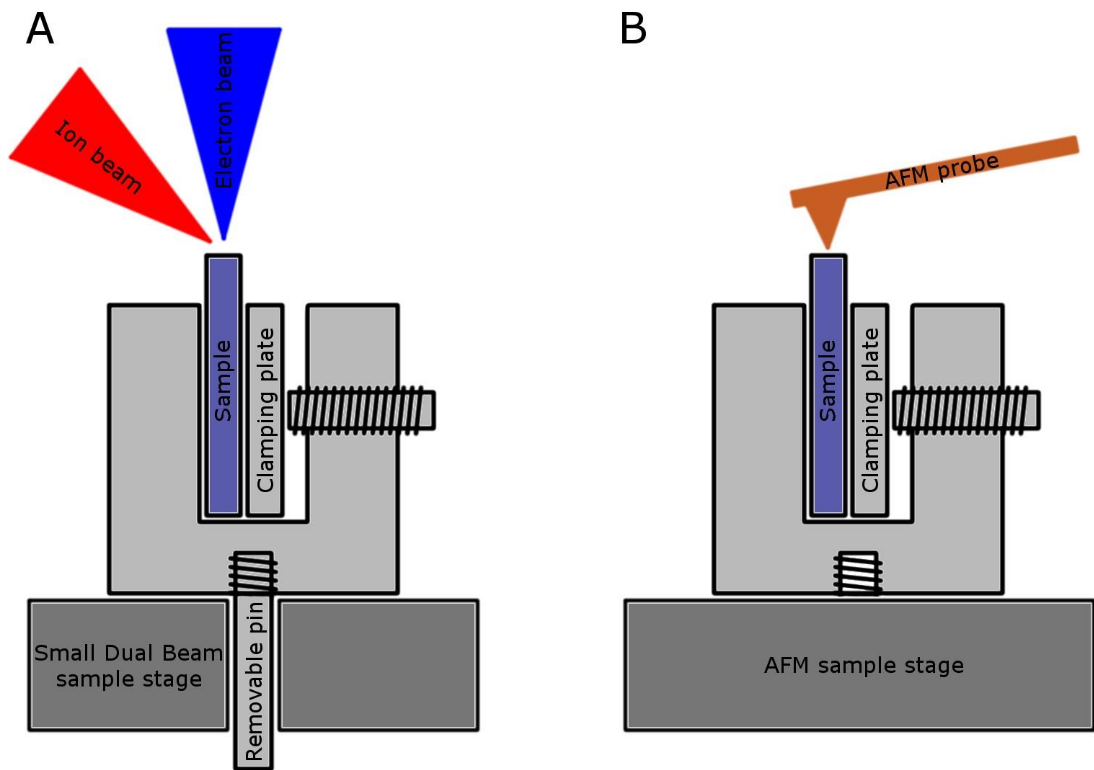

Figure 6.2 Schematic of the clamping sample holder in relation to the a) FIB-SEM and b) AFM. A) shows the sample holder with the removable SEM mounting pin in place. B) shows the sample holder with the SEM pin removed

6.3.2 Results of AFM phase imaging

The topography image of the surface in Figure 6.3a shows that the FIB polished surface is smooth; the total Z range of the image is 55 nm (which appears to be due to long range curvature in the baseline correction), and from the topography an average roughness (R_a) of 6.0 nm and an RMS roughness (R_q) of 7.6 nm. The low regions observed in the topography image are likely to be imaging artefacts due to the fact that the elastomer is an order of magnitude softer than PP, but could also lead to convolution of the phase shift signal, as there will be an associated increase in contact area. During semi-contact AFM imaging the AFM tip makes intermittent contact with the sample surface. During the AFM tip-sample contact a force is applied to the surface, which results in deformation of the sample surface. The force applied by the AFM tip will be constant for a given AFM cantilever amplitude, however the as

the Young's modulus of the sample surface decreases, the amount of deformation due to the applied force will increase. Figure 6.4 is a plot of compression depth as a function of reduced contact modulus as predict by MatLab simulation, using the Carpick model for AFM cantilever dynamics. The compression data in Figure 6.4 is plotted on a logarithmic scale and the linearity suggest that the relationship between compression depth and reduced contact modulus a power law with a reduction in the compression depth as the reduced contact modulus is increased. The phase contrast image in Figure 6.3b shows clearly resolved layers in the cross-section of the nanocomposite, which cannot be seen in the topography image. The dark bands in the AFM phase image are regions where the phase shift is low, and therefore suggests a stiff contact between the AFM tip and the sample, and the light bands represent larger phase shifts that suggest soft contacts. The layers present in the AFM phase image typically have a thickness of the order of 50 to 100 nm, which fits with the expected layer thickness described in section 6.2 of 77 nm.

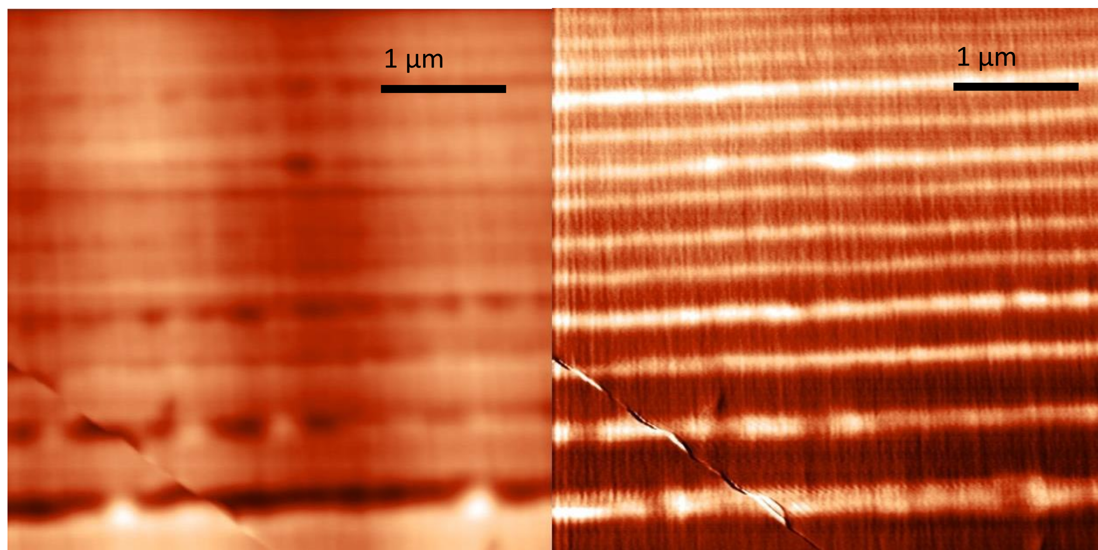

Figure 6.3 a) AFM Topography image and b) phase contrast AFM image of polymer nanocomposite after FIB polishing.

The variation in the visibility of layers present in the topography image compared to the phased contrast image in Figure 6.3 highlights the importance of mechanical contrast in AFM

phase imaging. As there is little sample topography due to FIB preparation, quantification of the phase image in Figure 6.3b) can be attempted so that a mechanical map of the variation in elastic modulus across the nanocomposite surface can be made. The remaining topography artefacts due to FIB milling can be faintly seen in the phase contrast image as the fine vertical lines, parallel to the FIB direction. These are referred to as curtaining, or waterfall lines, and typically result from uneven starting surfaces, and higher beam currents.

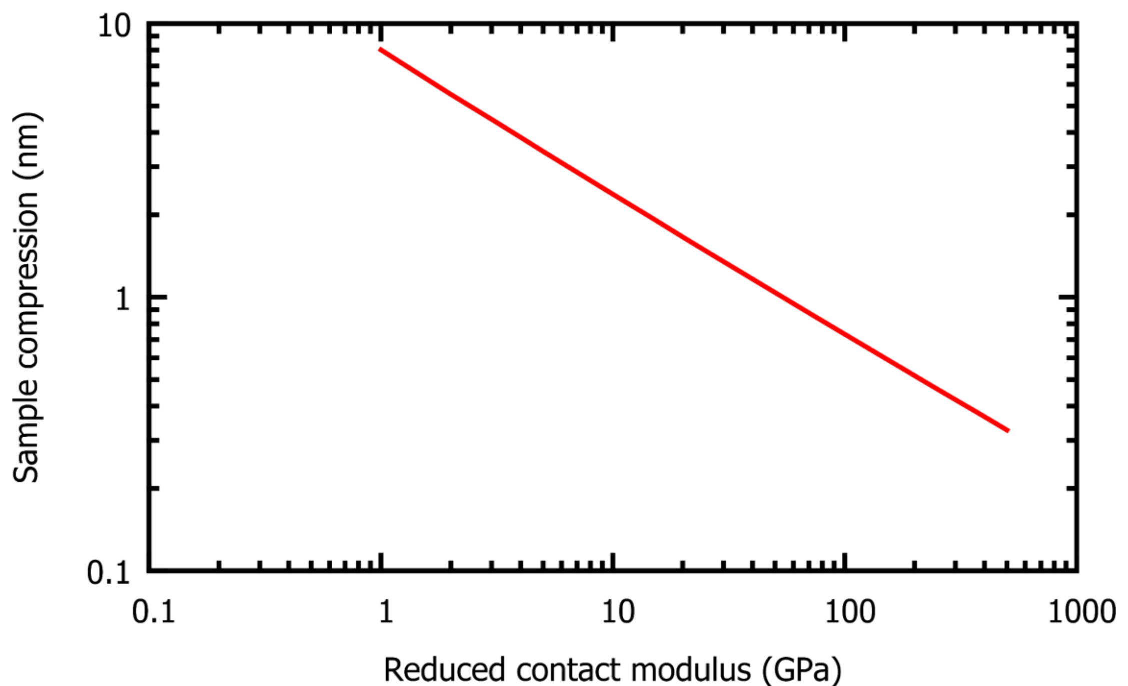

Figure 6.4 Plot of sample compression during AFM tip contact against reduced contact modulus of the AFM tip-sample contact predicted by MatLab using the Carpick model for AFM cantilever dynamics. The data is plotted on a logarithmic scale. The linearity of the data means that the compression depth of the AFM tip-sample contact is increasing exponentially as the reduced contact modulus is lowered.

6.3.3 Quantification of the nanocomposite AFM phase image

In order to assign values of Young's elastic modulus to each of the two components of the polymer nanocomposite tape, the average AFM phase shift obtained for each component has to be calculated and converted using the relationship defined in chapter 5.

The AFM phase image of the polymer nanocomposite was treated as a dataset of 256 x 256

(65536) individual data points. The distribution of phase values in Figure 6.3b is represented in Figure 6.5 as a histogram with an interval size of 0.01°, and shows two clearly resolved populations within the AFM phase image. The distribution of phase values obtained by AFM phase contrast imaging was plotted in Origin 8 (OriginLab Corporation) and the Multiple Peaks Fit function was used to fit Gaussian curves to the two peaks within the distribution. The Gaussian fits were used to characterise the two populations of phase values within the AFM phase image of the polymer nanocomposite. The two peaks present in Figure 6.5 are centred at 37.45 ± 0.01° and 39.50 ± 0.01°, as stated by the peak fitting software, and were assigned to PP and the elastomer respectively, as an increase in the AFM phase suggests a decrease in the reduced contact modulus of the AFM tip-sample interaction and the elastomer is expected to have the lowest of the two moduli. The Full Width Half Maximum (FWHM) values of the fitted peaks in Figure 6.5 were used to define the spread of data in each population, calculated as 1.17° for the PP peak and 1.99° for the elastomer peak, and were subsequently used in defining the error margins when converting the AFM phase to the reduced contact modulus of the system.

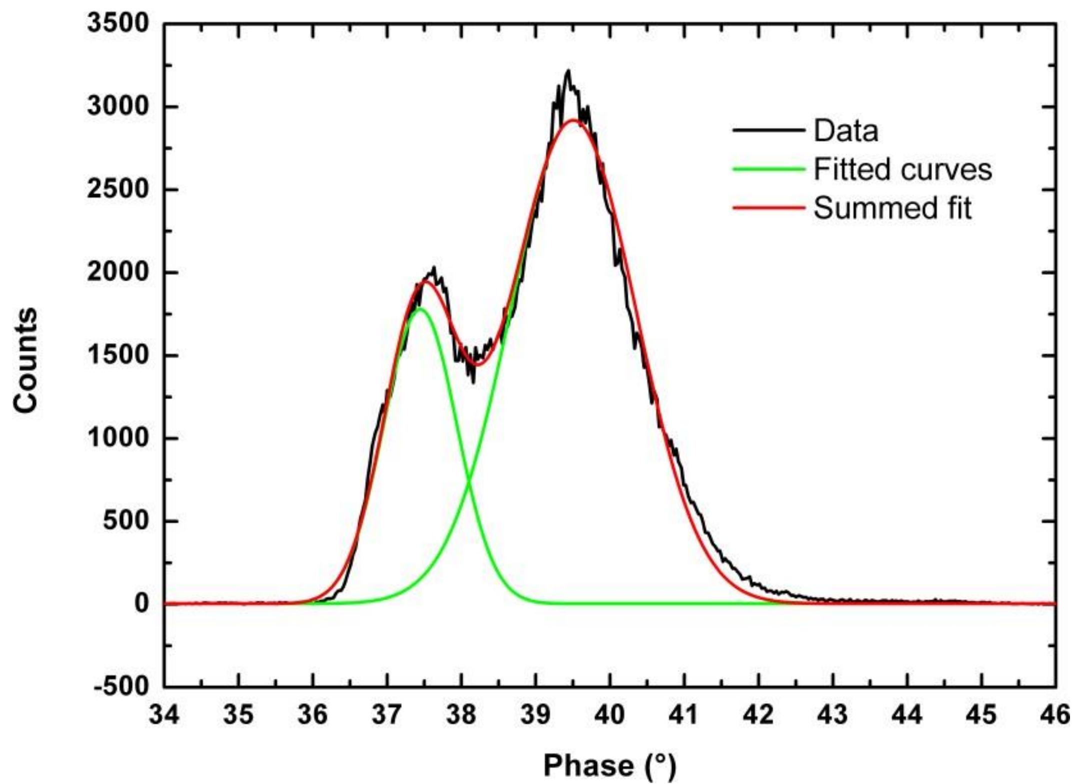

Figure 6.5 Distribution of phase signal values for the phase contrast image in Figure 6.3b

The measured phase values taken from the fitted data in Figure 6.5 were quantified to reduced contact modulus by fitting to the curve of AFM phase against reduced contact modulus produced from the MatLab simulation of the Carpick model in chapter 5 and presented in Figure 6.6. The measured phase shifts in Figure 6.6 were compared with predicted values that were obtained by varying the contact modulus in the MatLab simulation. From this conversion, we obtain reduced contact modulus (K) values of 755 ± 150 MPa for the elastomer and 1.288 ± 0.2 GPa for the PP. The Young's modulus of elasticity (E) can be calculated from K using Equation 9. The quantification of the phase signal therefore produces values of 426 ± 85 MPa for the elastomer and 816 ± 128 MPa for the PP in the nanocomposite material.

Using the values of Young's elastic modulus obtained from quantitative AFM phase imaging, predictions can be made about the behaviour of the composite as a whole. Predicting the

Young's elastic modulus of the whole composite also allows for the values calculated from AFM phase imaging to be verified against macroscopic testing techniques. One such method of predicting the behaviour of a composite material based on the properties of its components is the rule of mixtures. The simple rule of mixtures assumes that the components of the composite are continuous along the axis of the material that is to be tested, and that the applied strain for each component is equal during testing. These are reasonable assumptions in the case of the nanocomposite tape, as the layers are expected to be continuous and axial loading of the tape would strain each component equally. Given these assumptions, the rule of mixtures is a simple case of multiplying the Young's modulus by the volume fraction for each component and summing the results for all components. By applying a simple rule of mixtures to the polymer nanocomposite tape, estimating the volume fractions of the two components to be 0.6 for polypropylene and 0.4 for elastomer, based on AFM phase data and the expected ratio achieved when coextruding the two components, we can estimate the elastic modulus of the composite to be 660 ± 106 MPa

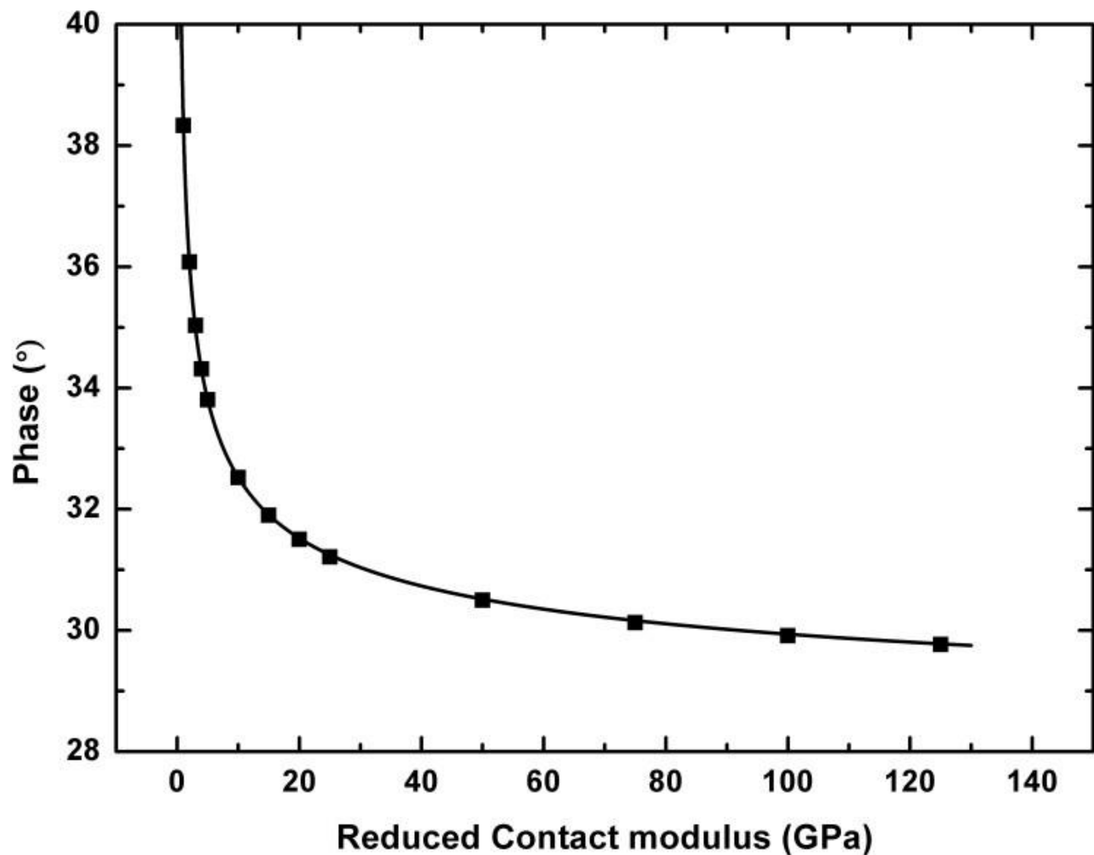

Figure 6.6 Calibration curve of AFM phase against reduced contact modulus as predicted by the Carpick model using MatLab simulation

6.4 AFM Force-distance measurements of a polymer nanocomposite

AFM force-distance spectroscopy was used as a comparative technique to measure the mechanical properties of the nanocomposite material at specific points on the sample surface and thus verify the results obtained using quantitative AFM phase imaging. Samples of the nanocomposite tape were prepared in the same manner as for AFM phase imaging, described in section 6.3.1. The method of AFM force-distance spectroscopy is described in section 3.2.5. The cantilever used for these measurements was a VISTAprobe T-190 with a spring constant of 30.0 Nm^{-1}.

6.4.1 Calibration of the AFM cantilever

The deflection signal recorded by the photodiode of the AFM is an arbitrary value (nA) and the AFM cantilever deflection (nm) that this signal relates to is dependent on where on the cantilever the laser is being reflected. The deflection signal must therefore be calibrated before any quantifiable measurement can be taken. The AFM cantilever was first used to record deflection-displacement curves against a flat sapphire substrate, which can reasonably be assumed to be an infinitely stiff surface, in order to calibrate the deflection signal recorded by the AFM (NTegra, NT-MDT, Russia). The cantilever deflection signal is output as the current recorded by the photodiode (nA) and needs to be converted into a cantilever deflection distance (nm) as the cantilever deflection is used to measure the force of the AFM-tip-sample interaction. Figure 6.7 shows the calibration curves for the cantilever against sapphire. The cantilever deflection is measured against the displacement of the piezo scanner in the Z direction, perpendicular to the sample surface, onto which the AFM cantilever is mounted. The displacement values in Figure 6.7 show a convention where more negative values correspond to the movement of the sample towards the AFM tip. The sapphire sheet is considered to be infinitely stiff relative to the cantilever and the polymer sample, as the sapphire has a Young's modulus orders of magnitude greater than polymer samples and the spring constant of solid sapphire is orders of magnitude greater than that of an AFM cantilever. Displacement of the piezo-scanner following contact between the AFM tip and sapphire sheet will cause AFM cantilever deflection that is equal to the piezo-scanner displacement due to sample deformation under the AFM tip being ignored. The average gradient of the calibration curves are therefore used to convert the cantilever deflection signal from the photodiode response, in ampere, to the physical AFM cantilever deflection distance in nanometres.

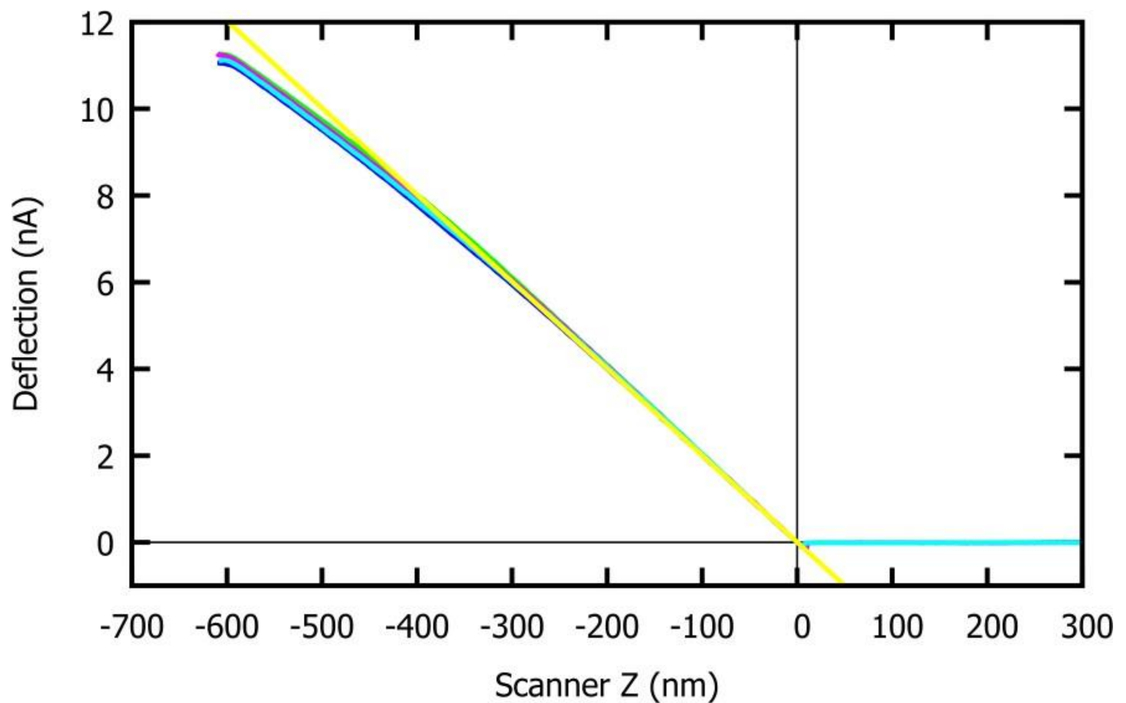

Figure 6.7 Plot of the AFM cantilever deflection with piezo-scanner displacement when calibrating against sapphire.

We note that Figure 6.7 shows the calibration curves become non-linear at large AFM cantilever deflections due to the effect of the laser in the AFM's optical system being reflected towards the edge of the photodiode. Therefore, only the linear region was considered when calculating the conversion factor of cantilever deflection signal with deflection distance and all force-distance experiments were kept within this initial region by imposing limits on the cantilever deflection during testing.

6.4.2 AFM force - displacement spectroscopy of the nanocomposite sample

Samples of the nanocomposite tape were prepared as described is section 6.3.1, mounted in the vertical clamp holder described in chapter 3.3 and placed on the AFM stage in the orientation shown in Figure 6.2b. Phase images of the nanocomposite tape cross-section were taken as in section 6.3.1 in order to verify the presence of both phases of the material. A total

of 625 force-distance curves were taken over a square grid of 25 x 25 points positioned equally across a nanocomposite sample surface as shown in Figure 6.8.

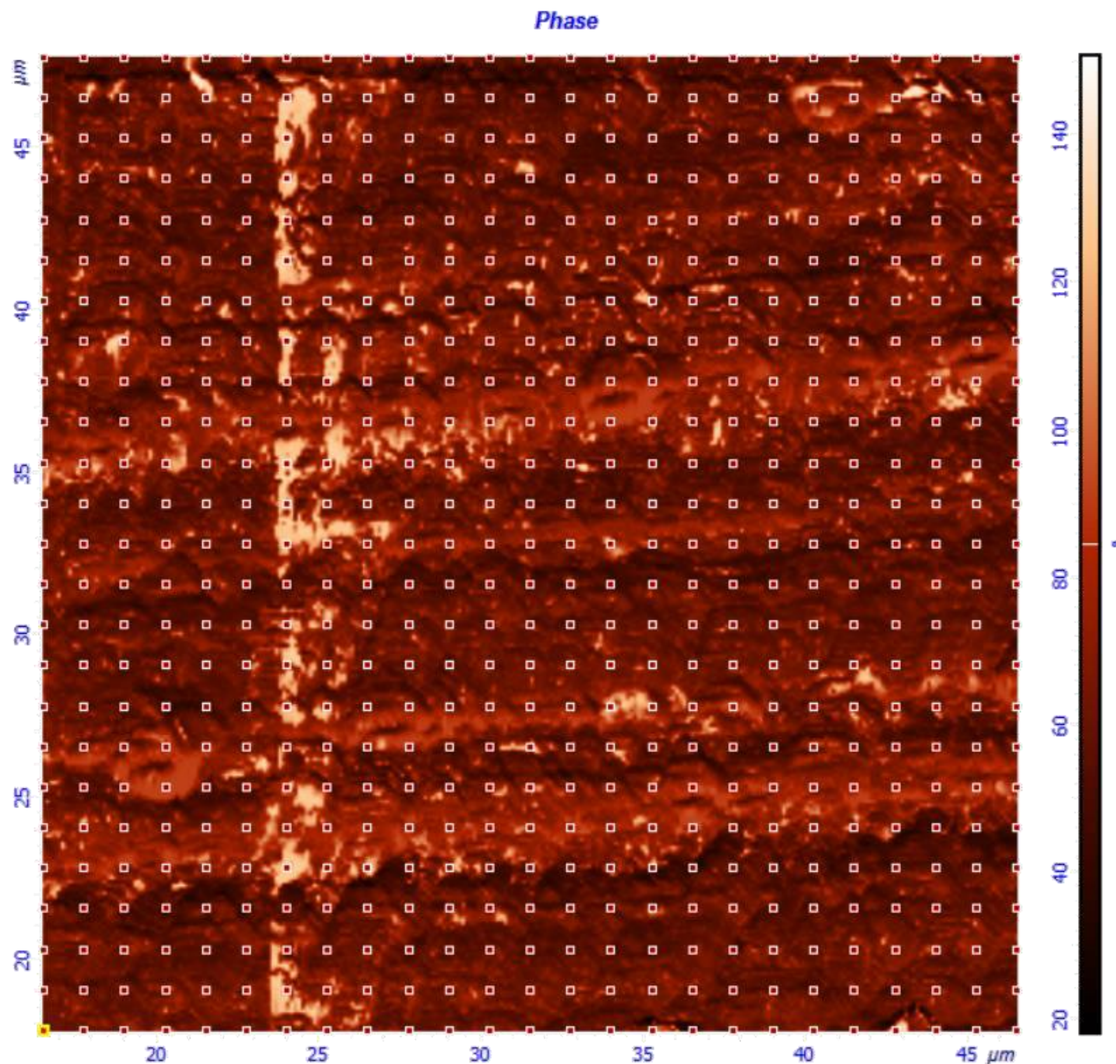

Figure 6.8 A phase contrast AFM image of the nanocomposite tape cross-section, overlaid with the sampling positions of the AFM force-distance spectroscopy

The number of force-distance curves produced across the nanocomposite sample surface ensured that both the polypropylene and elastomeric phases of the material were mechanically tested. The raw deflection-displacement data for all of the sampling on the nanocomposite is show in Figure 6.9. AFM force-displacement curves can record both the loading, as the AFM tip moves into the sample, and the unloading, as the AFM tip is moving

out of the sample. However, only the unloading curves are shown in Figure 6.9 as loading curves may contain instances of slippage on the surface and of plastic deformation of the sample; the unloading curves will only display elastic deformation. The unloading curves were therefore used to calculate the Young's modulus of elasticity for the nanocomposite tape. The data presented in Figure 6.9 has been baseline subtracted and normalised on the x-axis so that all curves pass through the origin, i.e. zero displacement occurs at zero deflection.

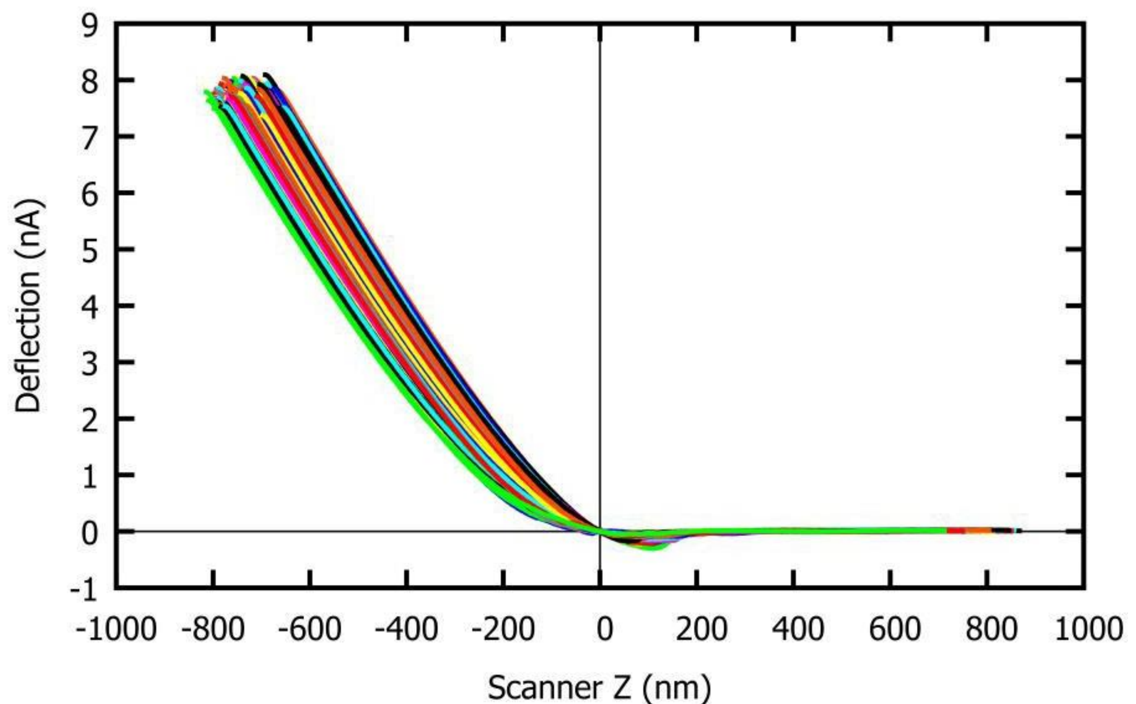

Figure 6.9 Raw AFM deflection/Scanner displacement data for the polymer nanocomposite

In order to process large datasets of force-displacement curves, a script was written in the Python programming language to automate their conversion and quantification. The user interface for this software was generated using the tkinter module of Python and is shown in Figure 6.10. The code uses the output of the AFM software, in the form of a CSV file, along with user input values of the cantilever spring constant and the half tip angle of the AFM probe and outputs files containing the results of each step of the conversion and most of the figures

presented in this section of the chapter. The code for this program can be found in the appendix.

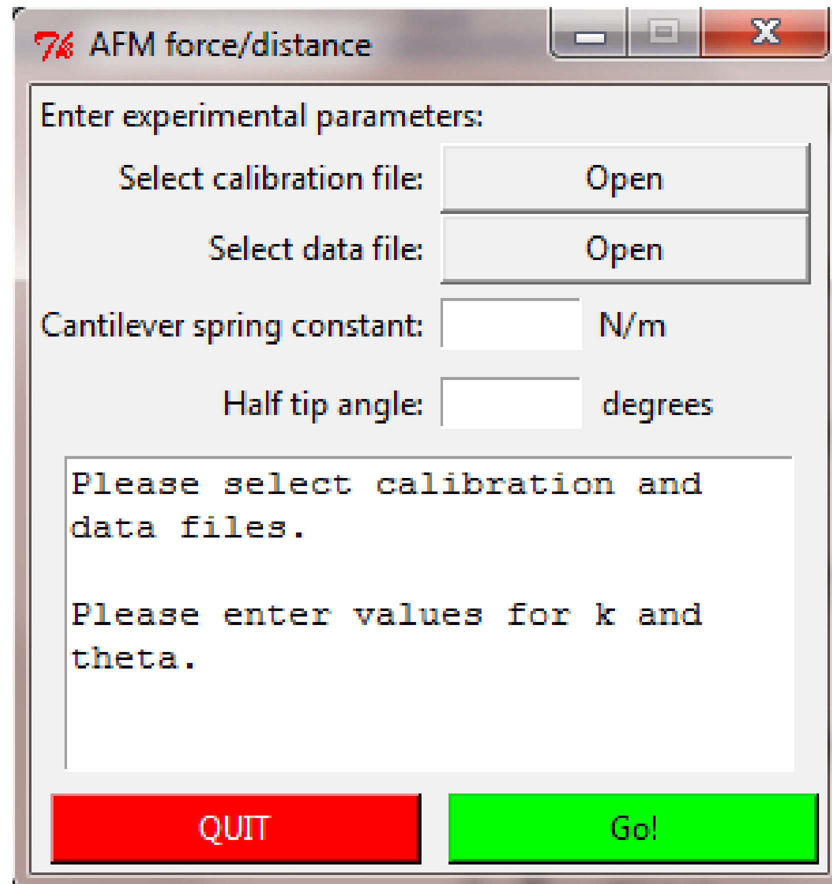

Figure 6.10 The GUI for the program written and used to convert deflection-displacement data into force-distance curves.

6.4.3 Converting data to force/distance and calculating contact moduli

The elastic modulus of the sample underneath the AFM tip producing the resultant deflection-displacement data was found by first converting into force-distance data. The first step in this conversion is to use the calibration factor for the AFM cantilever deflection when moving the AFM tip into a sapphire surface so that the cantilever deflection signal from photodiode current (nA) provides AFM cantilever deflection (nm). The sample displacement during AFM

force-displacement spectroscopy can be found from knowing the AFM cantilever deflection, taken from the photodiode signal, and the piezo-scanner displacement using:

$$Scanner\ displacement = Cantilever\ deflection + Sample\ displacement$$

Equation 18

The relationship in Equation 18 has been kept simple by not attempting to account for deformations caused by the attractive forces experienced by the surface as the AFM tip approaches. The attractive forces were ignored as we are only interested in the displacement of the sample during contact between the AFM tip and the sample surface. The scanner displacement was converted to sample displacement, or distance (nm), using Equation 18 and the cantilever displacement was converted to applied load (nN) by multiplying the cantilever displacement by the spring constant of the cantilever. The spring constant of the AFM cantilever was calculated using the method of Sader [99], as described in chapter 3.2.3. Figure 6.11 shows the calibrated force-distance data for the nanocomposite sample. The data has been truncated to only include the region during contact between the AFM tip and the sample.

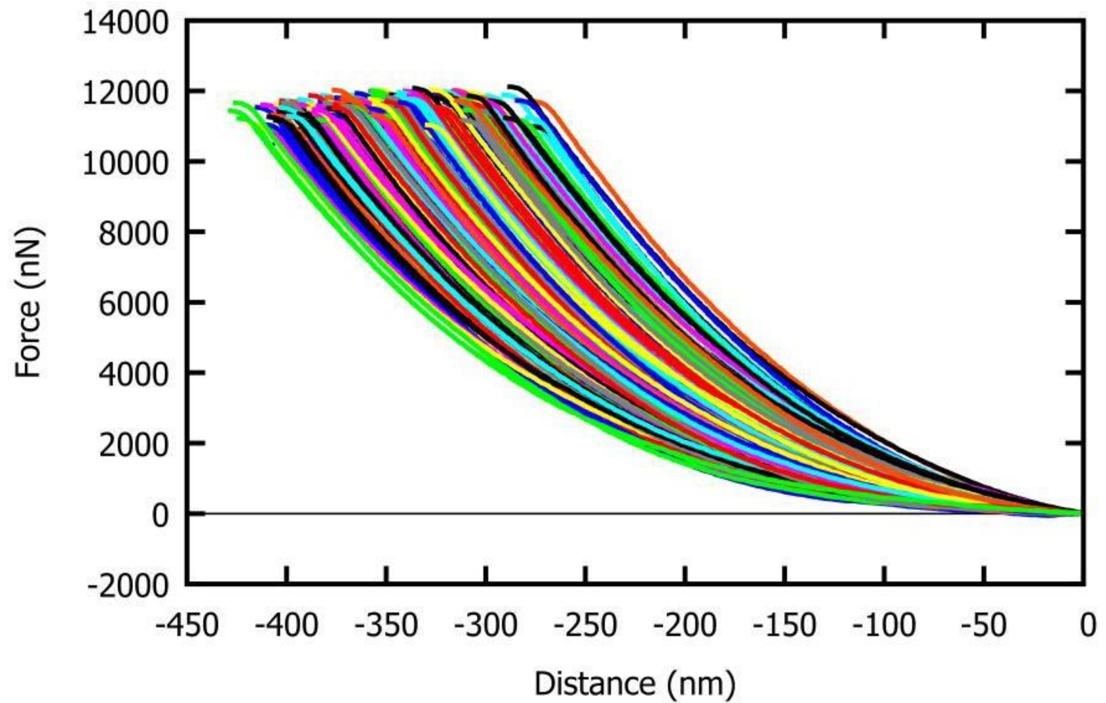

Figure 6.11 Calibrated AFM force/distance curves

The contact modulus (E^*) between the AFM tip and sample was calculated from the force-distance curves in Figure 6.11 using the following relationship described by Sneddon [117]:

$$F_N = \frac{2}{\pi}E^* d^2 \tan\alpha$$

Equation 19

Where F_N is the force normal to the surface, d is the distance and α is the half tip angle of the AFM probe.

The contact modulus, E^*, can be calculated from the calibrated data by plotting the force against $\frac{2}{\pi}d^2 \tan\alpha$ and taking the first derivative. Figure 6.12 is a plot of the force against distance squared ($\frac{2}{\pi}d^2 \tan\alpha$) used to calculate the contact modulus.

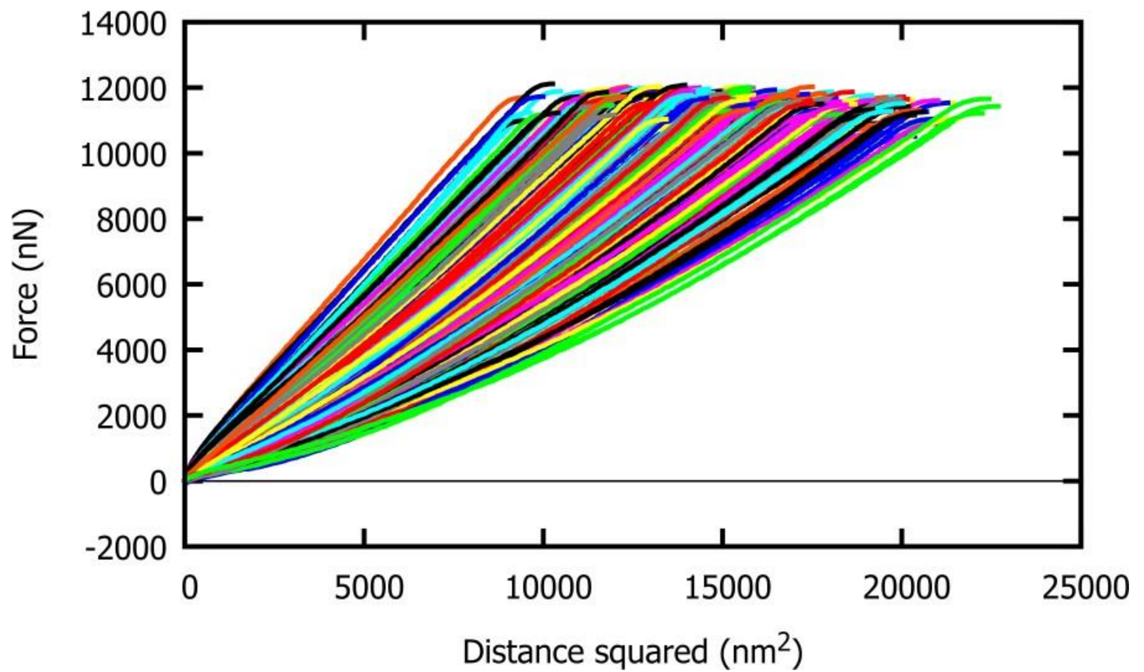

Figure 6.12 AFM force/distance squared. For the purpose of calculating contact modulus.

The values of E^* calculated from the force-distance squared plot are presented in Figure 6.13 as a histogram.

Figure 6.13 shows a unimodal distribution of the data, unlike the bimodal distribution observed from the AFM phase data in Figure 6.5, which indicates that the technique has been unable to resolve the PP and the elastomer. The E^* distribution is centred on a value of 850 MPa with a FWHM of 228 MPa. Using this contact modulus data and the relationship in chapter 5, the value of E^* can be converted into a Young's modulus of elasticity for the nanocomposite, which was shown to be 681 ± 91 MPa. The Young's modulus measured here by force-distance spectroscopy is consistent with the composite modulus predicted by phase contrast imaging and suggests that the volume being sampled by spectroscopy contains both PP and elastomer. The outlying values to the right of Figure 6.13 in the region between 1.2 and 1.4 GPa would be more consistent with the expected values for PP and could indicate that there are thicker regions of PP that are being sampled without interference from the elastomer. There are, however, no such outliers to the left of Figure 6.13, which could

suggest that there were no layers of the elastomer, either present or sampled, that were thick enough to provide a purely elastomeric response during AFM force- displacement, or that the larger displacement of elastomer compared to that of the PP in conjunction with the geometry of the AFM tip meant that the PP would always influence the results. A schematic of this hypothesis is presented in Figure 6.14. Figure 6.14a offers an explanation for the presence of outliers to the right of Figure 6.13 by suggesting that there were only layers of PP with a thickness sufficient to provide a purely AFM-tip-PP contact. Figure 6.14b represents the idea that the AFM-tip geometry, combined with the increase displacement of the elastomer compared to PP, leads to an increased contact area, and therefore an increased chance of a mixed contact, even when the layers in the nanocomposite are of equal thickness.

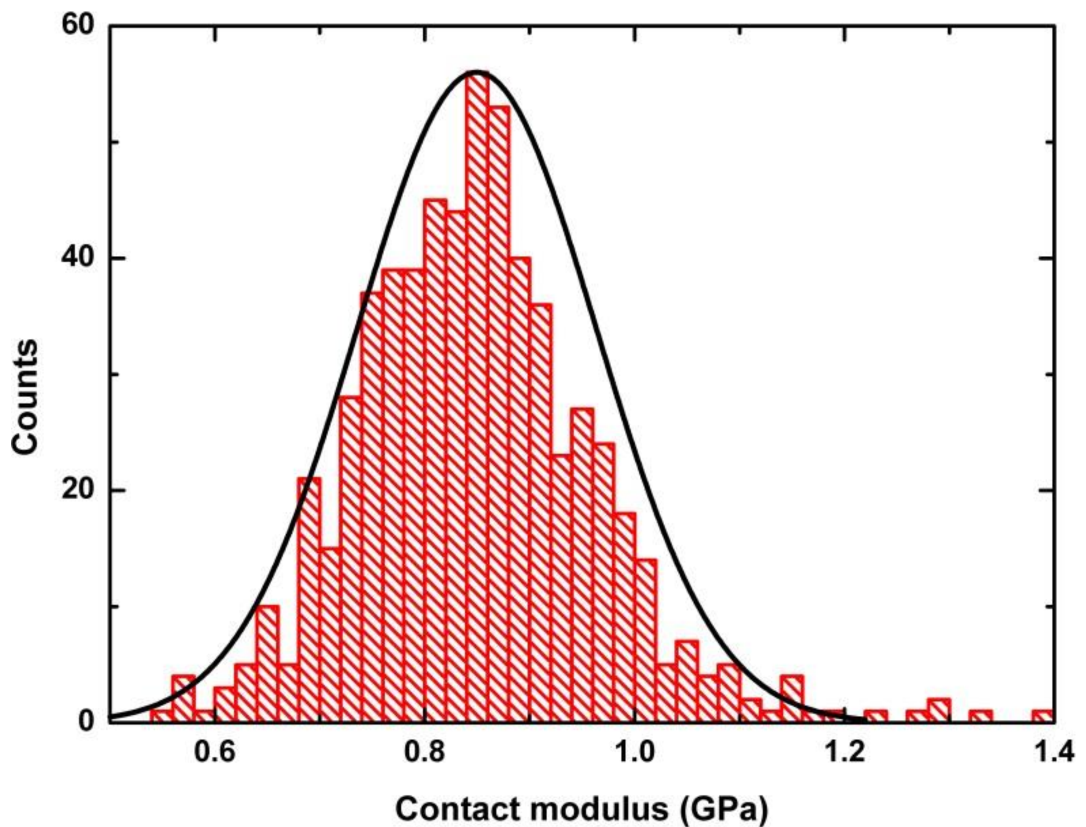

Figure 6.13 Distribution of contact moduli between an AFM tip and nanocomposite as calculated from AFM force-distance measurements. The distribution is unimodal with a slight positive skew, as evidenced by the presence of outlying data points to the right of the plot.

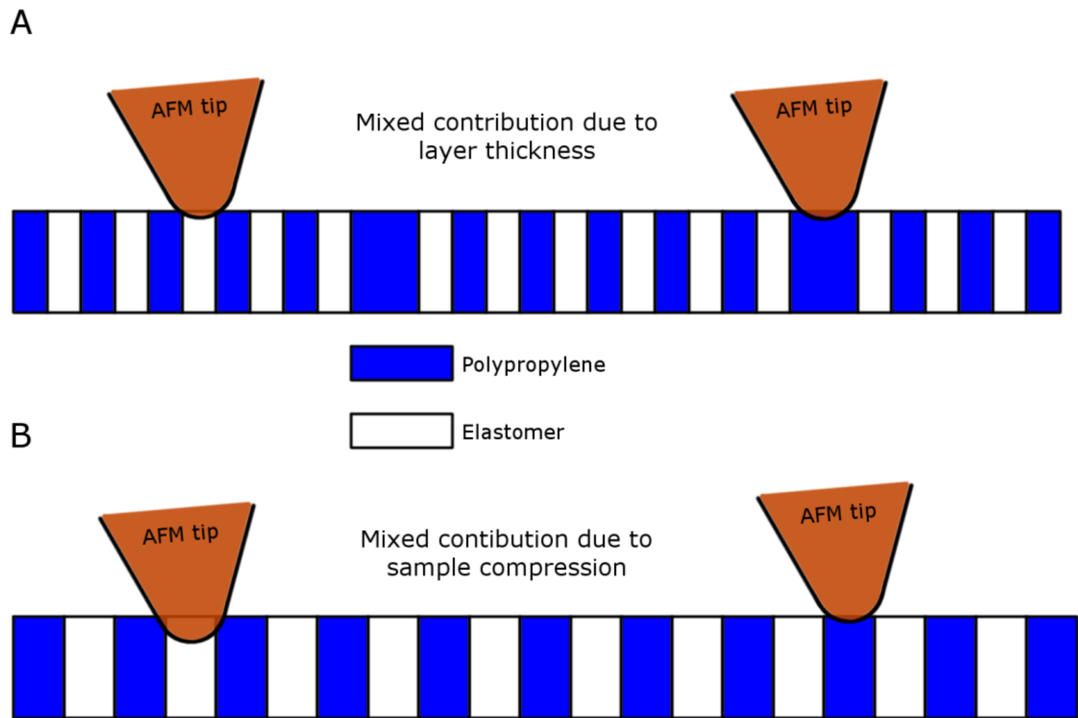

Figure 6.14 Schematic representing the mechanisms by which AFM-tip-polypropylene contacts may become more apparent in AFM force-displacement data compared to AFM-tip-elastomer contacts. A) Presence of thicker PP layers allows for pure PP contacts. B) The higher stiffness of PP compared to elastomer reduces contact area and therefore the likelihood of mixed contact.

In summary, the method of AFM force-displacement was applied to a cross-section of a polymer nanocomposite tape. The average Young's modulus of elasticity calculated 625 spectra was consistent with that calculated from quantitative AFM phase imaging, however, the distribution of moduli presented in Figure 6.13 was unimodal, which suggests that AFM force-displacement has been unable to resolve the individual component polymers. The unimodal distribution of moduli would suggest that the volume of the surface being sampled using AFM force-displacement is greater than the sampling volume of AFM phase imaging and that this has led to averaging of the two component moduli.

6.5 Measurement of elastic modulus of polymer nanocomposite by tensile testing

The Young's modulus of the polypropylene-elastomer nanocomposite material has been measured using quantitative phase imaging and a rule-of-mixtures to calculate an average modulus value, as well as AFM force-distance spectroscopy providing local Young's modulus averages of the nanocomposite. The nanocomposite material clearly exhibits nanostructural features but these features are consistent throughout the tape material. Therefore, macroscopic mechanical testing will provide a Young's modulus averaged over these nanostructured features. The calculated Young's modulus values taken from AFM techniques must be compared to macroscopic tensile tests in order to validate the approaches used and support the use of AFM phase imaging in providing quantitative small-scale mechanical testing that describes overall material mechanical performance. Macroscopic tensile testing was performed using an Instron tensile testing frame, model 5566. All the tape samples tested were below 1.0 mm in thickness and as such were tested as thin films, described by ASTM standard D882. The method of macroscopic tensile testing is described in full in chapter 3.6. Five nanocomposite tape samples were measured under tensile load. The dimensions of the five tensile samples, measured by micrometre callipers, are presented in Table 6.1. All tensile tests were carried out at strain rates of 0.1 mm/mm.min, which translates to 20 mm/min as all samples had a gauge length of 200 mm. The raw load- extension results of the tensile measurements are presented in Figure 6.15 and the calibrated stress-strain data in Figure 6.16.

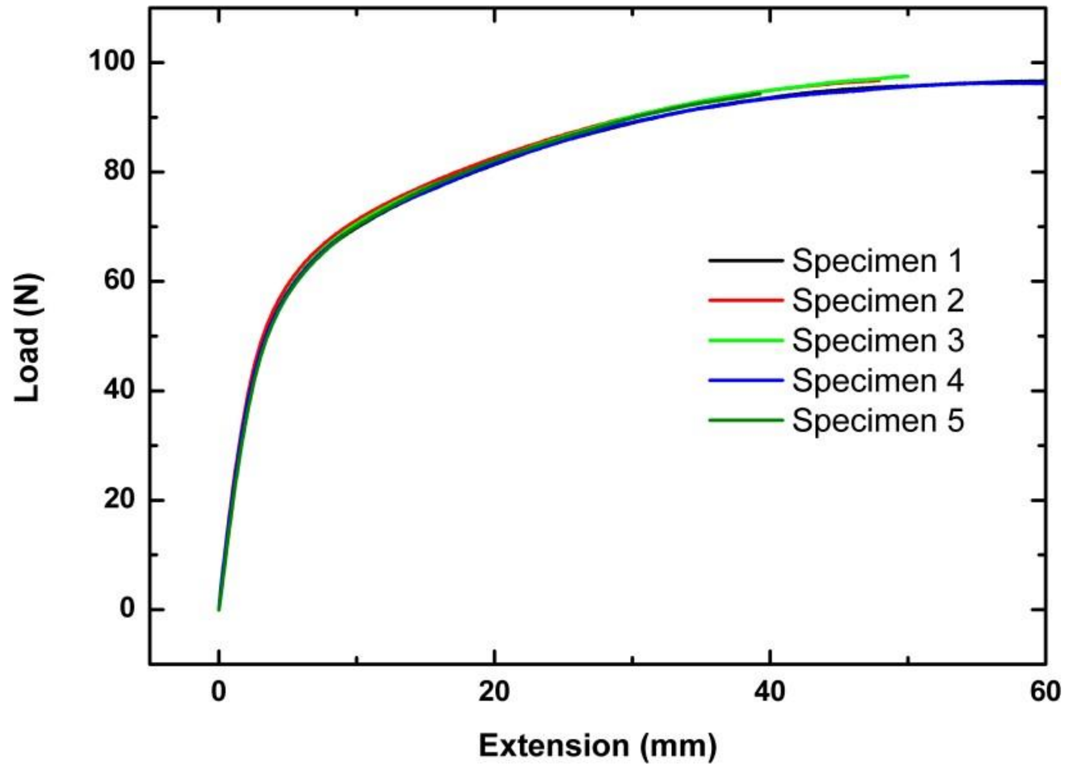

Figure 6.15 Raw load/extension data for tensile testing of the polymer nanocomposite

Sample No.	Thickness (µm)	Width (mm)	Gauge length (mm)
1	638 ± 2.5	11.09 ± 0.25	200 ± 1
2	636 ± 2.5	11.08 ± 0.25	200 ± 1
3	635 ± 2.5	11.10 ± 0.25	200 ± 1
4	633 ± 2.5	11.08 ± 0.25	200 ± 1
5	629 ± 2.5	11.06 ± 0.25	200 ± 1

Table 6.1 Dimensions of the nanocomposite tape samples used for macroscopic tensile testing. Each thickness and width value is the mean of five separate measurements. The variation in the accuracy of the measurements for each dimension is due to different size callipers being used and an extra allowance in the gauge length for the placement of the sample in the mounting grips.

Figure 6.15 is a plot of the raw load/extension data from tensile loading and shows a relatively linear elastic response of the nanocomposite up to approximately 50 N of applied tensile force followed by nonlinear plastic deformation of the nanocomposite tape. The tensile force applied to the nanocomposite tape was converted to tensile stress by dividing by the cross-sectional area of the tape, which was calculated by multiplying the mean thickness and the mean width for each sample. The tensile strain was calculated by dividing the extension of the sample by the original gauge length of the sample.

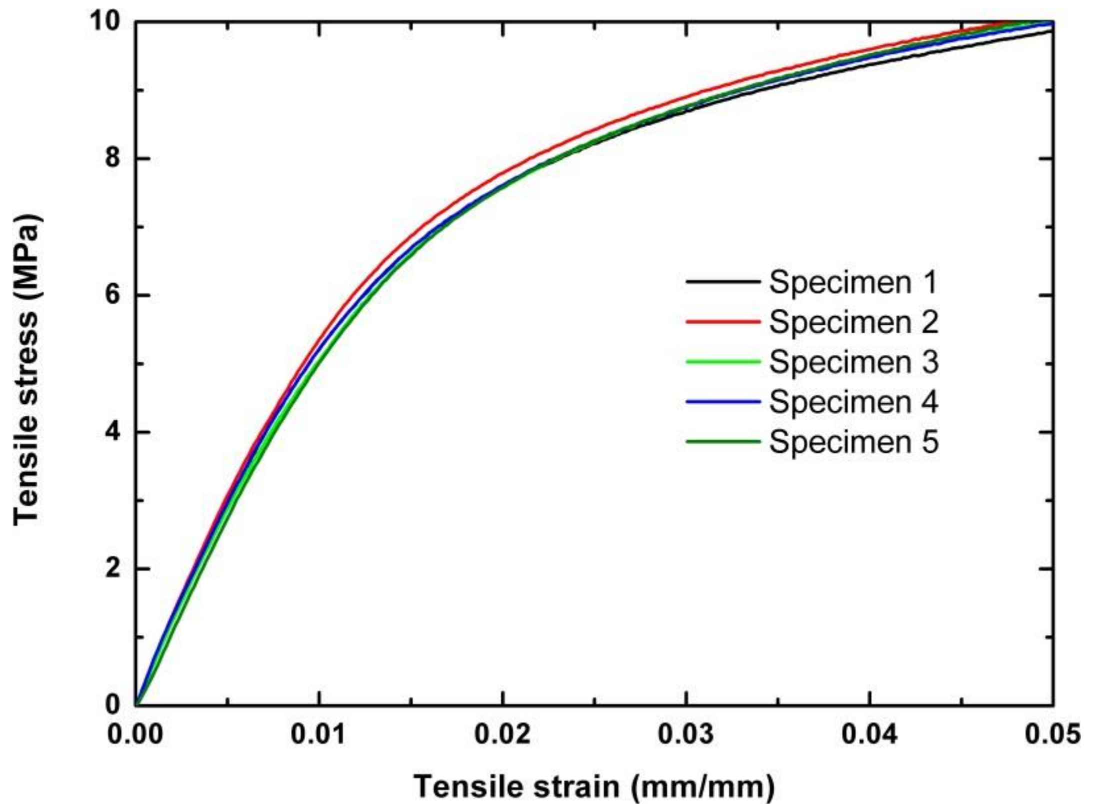

Figure 6.16 Tensile stress/strain data for the polymer nanocomposite

Figure 6.16 is a plot of the stress/strain data calculated from the load/extension data and indicates that the yield stress of the tape occurs at approximately 6 MPa. The linear region of the stress/strain plot between 0.00 and 0.01 mm/mm strain represents the region of the data where the deformations in the sample are elastic, prior to yielding and subsequent plastic deformation. It is the gradient of this linear region therefore that is used to calculate the Young's modulus for each sample of the composite tape.

Gradients were calculated from the linear, elastic region of the data, prior to yielding, and averaged to provide a measure of the Young's elastic modulus. The Young's modulus of elasticity measured from stress-strain gradient in the macroscopic tensile testing is 587 ± 16.9

MPa. The margin of error in the Young's modulus was calculated from the margins in Table 6.1 and a machine tolerance of 0.5% for the values of load and displacement.

6.5 Comparison of results from different measurement techniques

The Young's modulus of a polymer nanocomposite tape has been measured by three different techniques. Quantitative AFM phase imaging has been used to visualise the layers present in the composite and assigned reduced contact moduli to the individual components. The assigned reduced contact moduli were then converted to Young's elastic modulus a rule of mixtures used to predict the Young's modulus of the whole composite. AFM force-displacement spectroscopy and tensile mechanical testing were used to verify the results of the quantitative AFM phase imaging data. AFM force-displacement was able to provide a Young's modulus for the composite through averaging of 625 spectra, evenly spread across a cross-sectional area of the sample. The Instron tensile testing frame provided macroscopic tensile information by applying a tensile load to the whole composite tape. The Young's modulus of elasticity for the polymer nanocomposite obtained through the use of AFM phase contrast, AFM force-distance and tensile testing are presented in Figure 6.17.

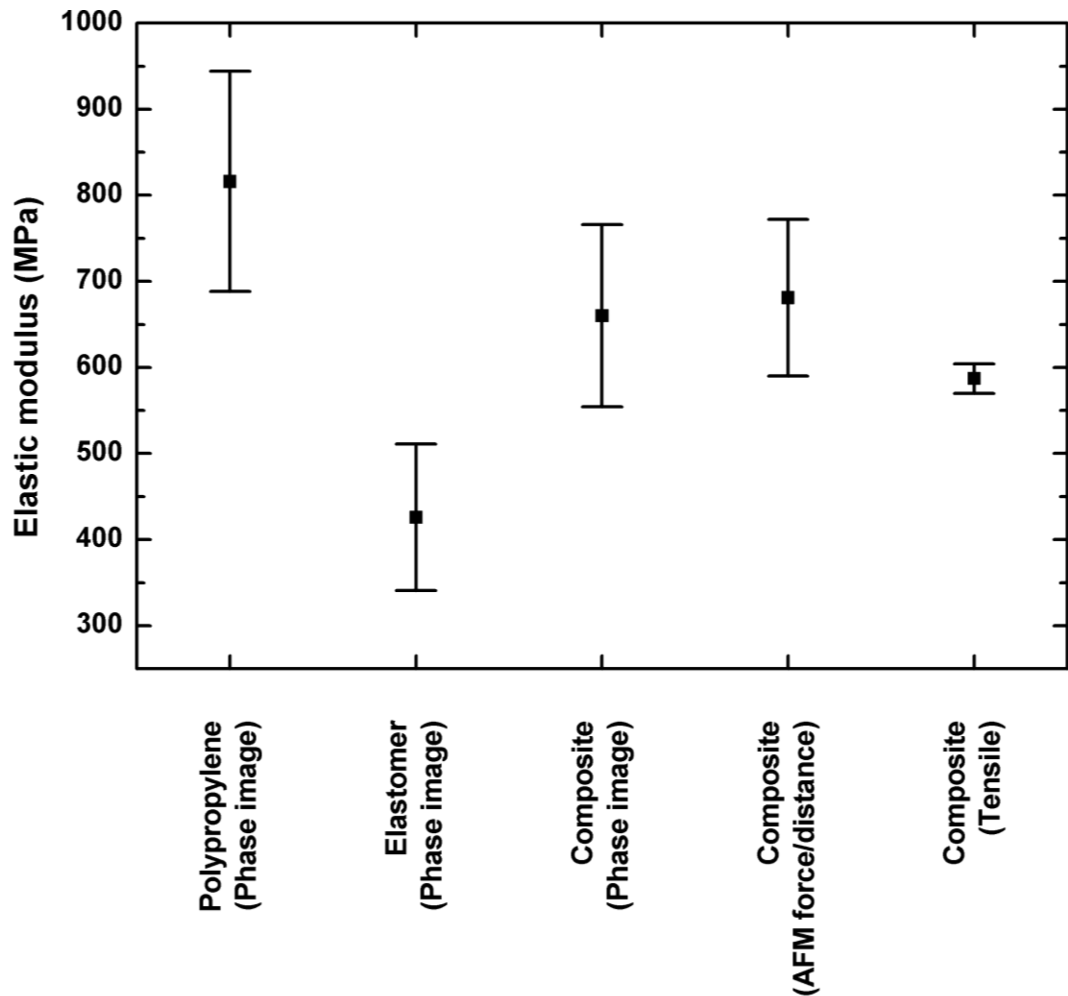

Figure 6.17 Elastic modulus of the polymer nanocomposite measured by AFM phase imaging, AFM force/distance and tensile testing

The results presented in Figure 6.17 show that AFM phase contrast imaging is capable of greater spatial and modulus resolution compared to force-distance spectroscopy, as quantitative AFM phase imaging was able to resolve the two components present in the nanocomposite tape where force-distance spectroscopy could only provide an average Young's modulus for the two components combined. However, both quantitative AFM phase imaging and AFM force-displacement spectroscopy were able to predict average Young's moduli for the composite that were in agreement with the Young's modulus measured by macroscopic tensile testing. It might be expected that the compressive axial loading of the composite tape would produce a lower stiffness compared to tensile testing, especially given the

nature of the layer composite specimen, which is more likely to delaminate under compressive loading, however the macroscopic tensile testing produced a Young's modulus at the lower end of the data range, compared to the compressive AFM techniques. This could potentially be due to the length scales under investigation in the AFM, which are less likely to be affected by the defects that would be apparent in macroscopic compressive testing.

Although quantitative AFM phase imaging was able to predict the Young's modulus of the composite and was better able to resolve the two components compared to AFM force-displacement spectroscopy, the values of Young's modulus for the individual components still are not as expected. The Young's modulus of polypropylene measured by quantitative AFM phase imaging was 816 ± 128 MPa, whereas the expected value for polypropylene found in the literature is of the order of 1.0 GPa [118], when measured by tensile testing. However, nanoindentation data reported by Nanovea in their application notes, states a measured Young's modulus for polypropylene of 810 ± 50 MPa, which is in agreement with the quantitative AFM phase data present in this work. The Young's modulus for the elastomeric component calculated from AFM phase data was 426 ± 85 MPa, whereas the modulus quoted by the manufacturer (DOW) was of the order of 50 MPa. The difference in the quoted and measured values of the Young's modulus of the elastomeric component suggests that the quantitative AFM phase measurement of this component is being influenced by the presence of the polypropylene. The influence of the polypropylene could be a genuine mechanical effect of the composition of the material, for example, the polypropylene layers could be constraining the elastomeric layers, thereby not allowing the elastomer to deform as readily as it would alone and effectively increasing its Young's modulus. Or, the polypropylene could simply be having a spatial influence on the AFM phase, for example if the sampling volume of the AFM-tip-sample contact is wider than the thickness of the elastomeric layers then the Young's modulus calculated will be a mixture of the two components. The interaction volume

of the AFM-tip-sample contact could be varied by manipulating the imaging parameters of the AFM, and by doing so could potentially increase the spatial resolution of the technique, or show that the elastomer is genuinely stiffer when constrained as a thin layer between two layer of a stiffer component. It is also possible that the measured Young's modulus of the elastomeric component is genuine, and that the processing of the material has caused some sort of work hardened that is responsible for the apparent 10-fold increase is the stiffness of the elastomer.

7 Imaging a bio-composite

7.1 Introduction

7.1.1 Aims of this chapter

Methodology developed in Chapter 5 and demonstrated in Chapter 6 enables the quantification of standard AFM phase images in order to provide mechanical information, specifically Young's elastic modulus. Chapter 6 showed that the method was capable of resolving and quantifying the Young's elastic modulus of discrete nanoscale phases in a simple, two phase polymer nanocomposite. This chapter builds on the previous chapter by applying the quantification method to AFM phase images of a more complex, biological nanocomposite. By applying the quantification method, we should therefore be able to assign values to the mechanical contributions of each component in a biological nanocomposite and make predictions about the overall mechanical behaviour of the bulk material. The biocomposite material chosen for the work in this chapter was the shell of a fresh water snail as it contains examples of regularly repeating structural units and variations in crystal orientation.

7.1.2 Complex 3D structures are ubiquitous in nature

Nature has evolved a vast array of mechanisms for solving structural and functional problems in both the plant and animal kingdoms. Mineral reinforced protein nanocomposites are commonplace in animals, and take a variety of forms depending on their functional requirements. Nanocomposites are found in support structures, such as bone; protective surfaces, such as shells; and the slicing and grinding surfaces of teeth. Figure 7.1 contains two micrographs of mineral reinforced protein nanocomposites found in humans to illustrate the ability of biology to assemble materials into complex organisations. Figure 7.1a is an unstained optical image of compact bone, as would be found at the perimeter of long bones, such as the

femur [119]. The Haversian canal shown in the centre of the image is used for fluid transport and is surrounded by concentric layers of mineralised tissue. The dark spots in the image are the osteocytes, situated in the lacunae, and radiating outwards between the osteocytes are the canaliculi, channels that allow communication between the cells. The complex geometry in bone is formed of essentially two materials that form the composite; mineral crystals of hydroxyapatite reinforcing a soft polymeric collagen matrix phase that form the structures shown in Figure 7.1.

A further example of a complex biological nanocomposite is exhibited in Figure 7.1b where a dentine fracture surface has been imaged by SEM. Dentine is found below the enamel of the teeth, between the enamel and the pulp. The dentinal tubules pass through the dentine to the pulp and contain fluid and cellular structures. The peritubular dentine surrounding the tubules is highly mineralised (hydroxyapatite), and this hard phase is potentially the reinforcing part of the composite whereas the softer phase serves as the binding matrix. The primary function of the peritubular dentine is debated; with some works suggesting the peritubular dentine provides compressive reinforcement, whereas other literature indicates a grinding surface for abrasion when exposed.

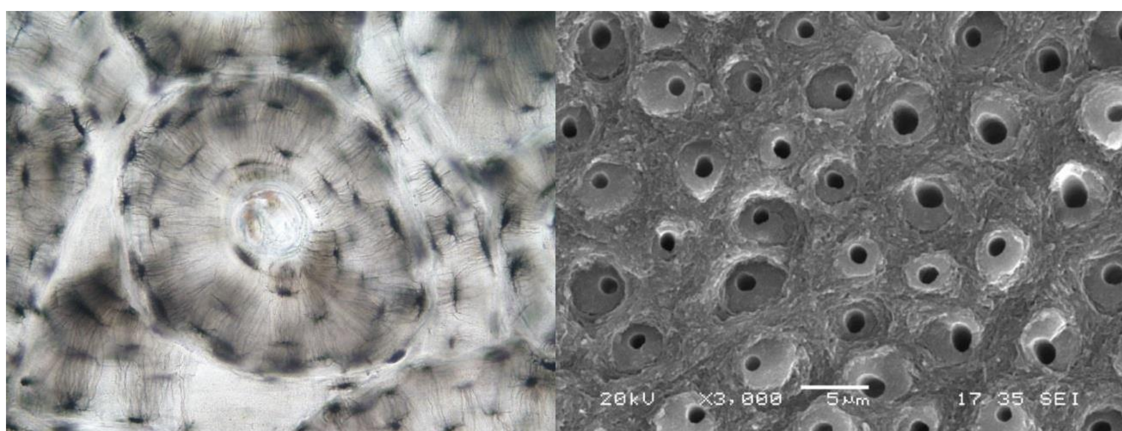

Figure 7.1 – Micrographs of naturally occurring biocomposite materials. A) An optical micrograph of bone showing the haversian system and canaliculi. [119] B) An SEM image dentine showing the peritubular dentine around the dentine tubules and intertubular dentine between. [120]

Both of these composites of bone and dentine, as is the case with most biocomposites, exhibit a hierarchical structure. Such complex structures are generally effective at supporting compressive loads, and for dissipating energy through delamination and crack deflection to reduce the risk of catastrophic failure. Considerable interest therefore remains in evaluating biological nanocomposite structures so that potentially optimised design features, which is an inherent product of evolutionary processes, can be translated towards synthetic manufacturing.

Unlike the materials observed in previous chapters, mineral reinforced protein composites exhibit a greater variation in the mechanical properties of their constituent parts. The protein phases form gel-like domains in the material, while the mineral phases are the stiffest and hardest materials that exist in living organisms. The polymer nanocomposite in Chapter 6 exhibited Young's moduli ranging from 426 to 816 MPa, whereas the expected values for the proteins and minerals found in shell are expected to range from 45 MPa to 150 GPa. A more diverse range of mechanical properties spatially distributed across the composite structure is thus anticipated.

7.1.3 Apply phase imaging to a biological nanocomposite

Evaluating the mechanical property distribution within a biological nanocomposite can be achieved by the application of the AFM quantification method in a similar way to the work in the previous chapter. Variations in the AFM operating parameters have to be considered when modelling the cantilever dynamics, and therefore a fresh set of simulations were carried out in order to produce a phase versus contact modulus calibration that was relevant to the AFM conditions used. The larger range in mechanical properties of constituents is perhaps the most demanding consideration when compared to previous work examining an all-polymer nanocomposite. Biological nanocomposites can typically contain a high volume fraction of the

hard mineral phase and a smaller volume fraction of softer proteinaceous phase. Quantitative AFM phase imaging is progressing beyond a relatively soft composite of polypropylene and elastomer as considered in Chapter 6, with mechanical Young's elastic modulus variations ranging from 426 to 816 GPa, to a biological nanocomposite where the elastic modulus variation is larger.

7.1.4 Snail shell

Snail shell has been chosen for this work as the model bio-composite system, because it has a complex, biphasic and hierarchical nanoscale 3D structure, which would be ideal for testing the application of AFM-SDB phase imaging. Snail shell also has a primary mechanical function, impact resistance, which is critically dependent on both the mechanical properties and organisation of its constituents. As such, snail shell is of interest to those developing bio-mimetic composites.

7.1.4.1 Periostracum

The periostracum is the outermost layer of a snail shell. It is mainly organic, proteinaceous, and offers a protective barrier to prevent the erosion of the mineralised layers beneath. In freshwater snails it is usually made up of two layers; the outer layer being proteinaceous and the inner layer calcified, and often brittle. As well as being protective, the periostracum plays a role in shell formation, organising the shell layers; acting as a matrix.

7.1.4.2 Crossed-lamellar layer (CLL)

The crossed-lamellar arrangement is the most frequent microstructure found in gastropods. It is formed from layers of either fine prismatic or lath like aragonite ($CaCO_3$) crystal. The layers

form interdigitating sheets at varying angles; typically between 45 and 60°. Figure 7.2 is a schematic drawing illustrating the organisation of CLL, taken from Dauphin *et al*. Aragonite has anisotropic elastic properties, which means that variation in the measured contact stiffness between the imaging AFM probe and the sample surface in a plane cross-section through a specimen shell will exist due to the orientation of the crystals in the shell. The snail shell therefore presents an interesting structural example with which to test the mechanical imaging capabilities of the quantitative AFM phase imaging technique.

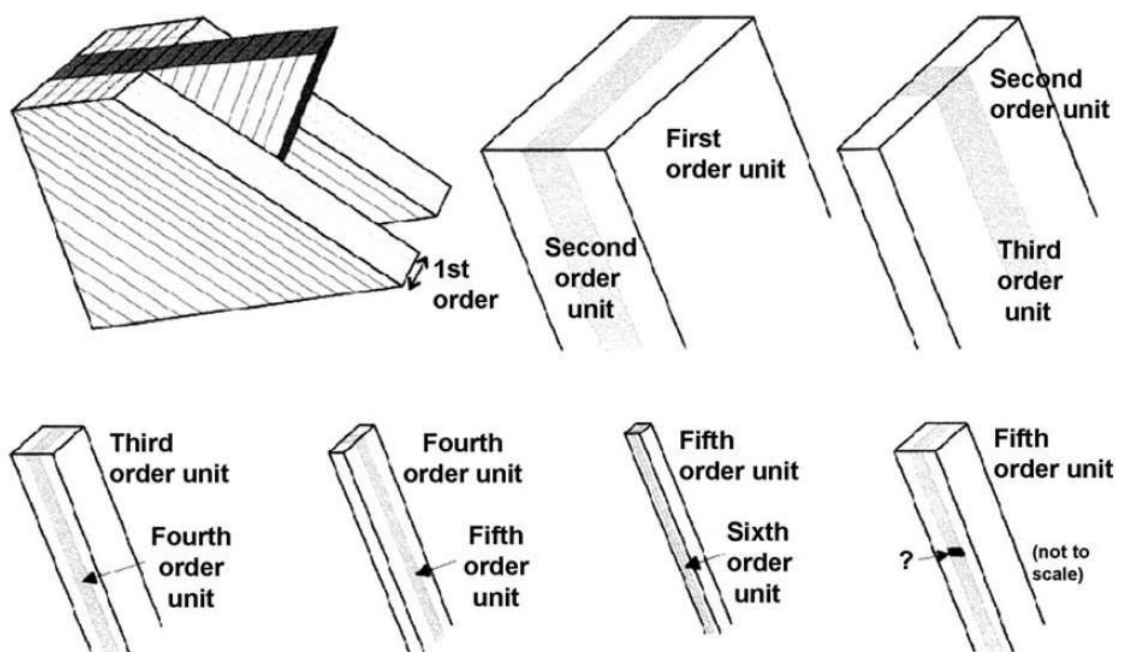

Figure 7.2 - Schematic drawing to illustrate the organisation of the crossed-lamellar layer (CLL) in shells of gastropoda. Each lamellar is made of successively smaller units, down to the individual rod-like crystals.

The first order structure forms the alternating layers. The layers are angled between 45-60°, which makes it difficult for cracks to propagate through the shell [95].

7.1.4.3 Nacreous structure

The nacreous layer is the innermost layer of a molluscan shell. It is always aragonitic in nature and forms a laminated structure. The crystals form sheets that are generally around 500nm thick and have a uniform spacing of ~30nm, which is filled with biological material. In Bivalvia and Cephalopoda the layers stack in the sheet nacre model, which resembles a “brick and mortar” arrangement. However, in Gastropoda a “columnar stacking” arrangement occurs where the newly deposited mineral plates stack directly on top of each other in vertical alignment [96]. This arrangement of stacked crystal and organic matrix (which makes up < 5% of the layer) gives nacre very high tensile, compressive and bending strengths. It is thought to be the presence of a chitin-protein complex in the organic framework of the matrix that acts as a guide for mineral deposition and gives the layer its mechanical properties [97].

7.1.4.4 The shell matrix

The shell matrix is made up of proteins, carbohydrates, polysaccharides and lipids. It is intimately associated with the mineral phase and binds the crystals together. Making up < 5% of the total volume of the shell [98]it forms the framework on which the crystals are deposited. The matrix is crucial in the process of crystal nucleation and growth and gives shell its unique physical properties. Figure 7.3 shows the model proposed by Levi-Kalisman *et al* [97] for the biological matrix. It shows strands of highly ordered β-chitin in a periodic arrangement. Between these β-chitin sheets are layers of a silk fibroin gel, which contain aspartic acid-rich glycoproteins. The glycoproteins bind and stabilise the chitin layer, forming a membrane. Upon mineralisation the aragonite crystallises in the space between the chitin sheets and forms a composite of outstanding mechanical properties.

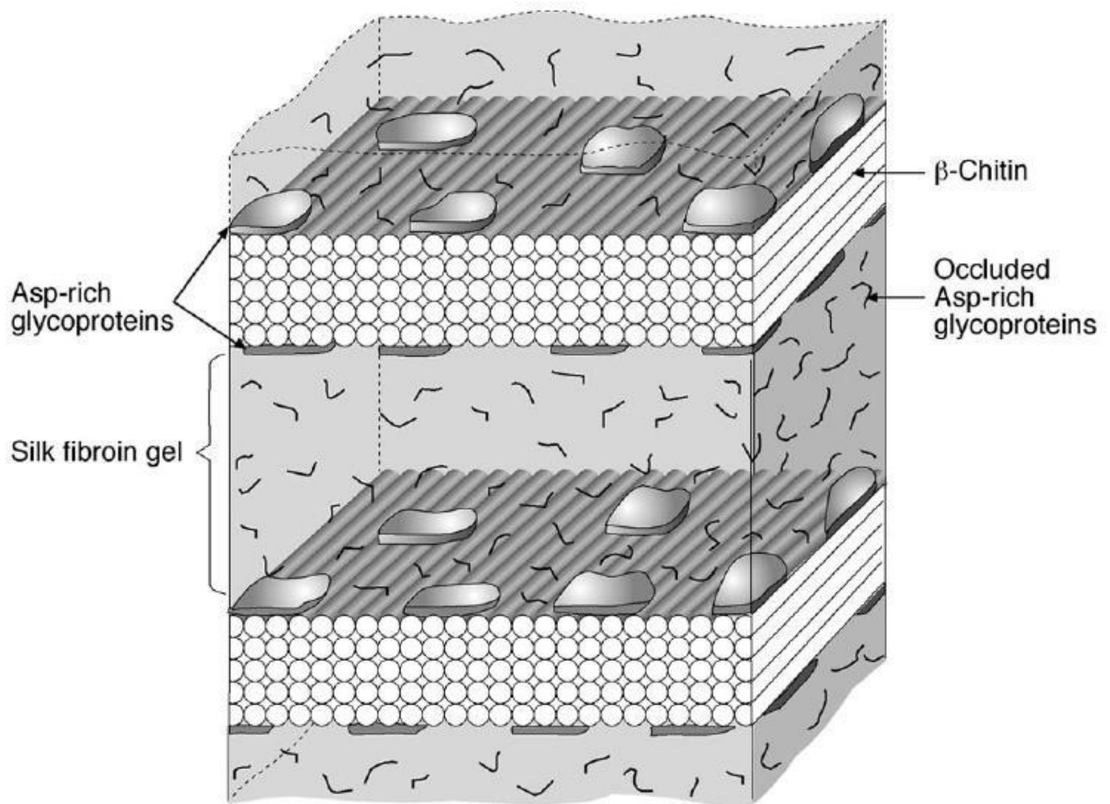

Figure 7.3 - Three-dimensional model of the biological matrix proposed by Levi-Kalisman *et al* (2001). The β-chitin forms the protein layers between the mineral layers shown in figure 7.2, which form in the fibroin gel layers. The protein typically forms ~5% of the total volume of the biocomposite.

7.2 Experimental

7.2.1 Preparation of snail shell for AFM phase imaging

A fresh water snail, *Pomacea diffusa,* or spiked-topped apple snail was purchased from a local pet shop. A small section of shell was removed as described in Chapter 3. The shell sample was fragmented by fracturing under liquid nitrogen. The shell was allowed to equilibrate to cryogenic temperature and then fractured using needle-nosed pliers, which had also been cooled in nitrogen. Figure 7.4 is an SEM micrograph of a fracture surface of snail shell. The micrograph provides evidence of a cross lamellar structure, which is typical for this kind of biocomposite. The relatively smooth top surface of the shell, at the top of the micrograph, shows a clearly layered structure. The fracture surface, and in particular the top edge,

highlights the alternating orientation of the mineral plates, as the angle of the surfaces formed during fracture is alternating.

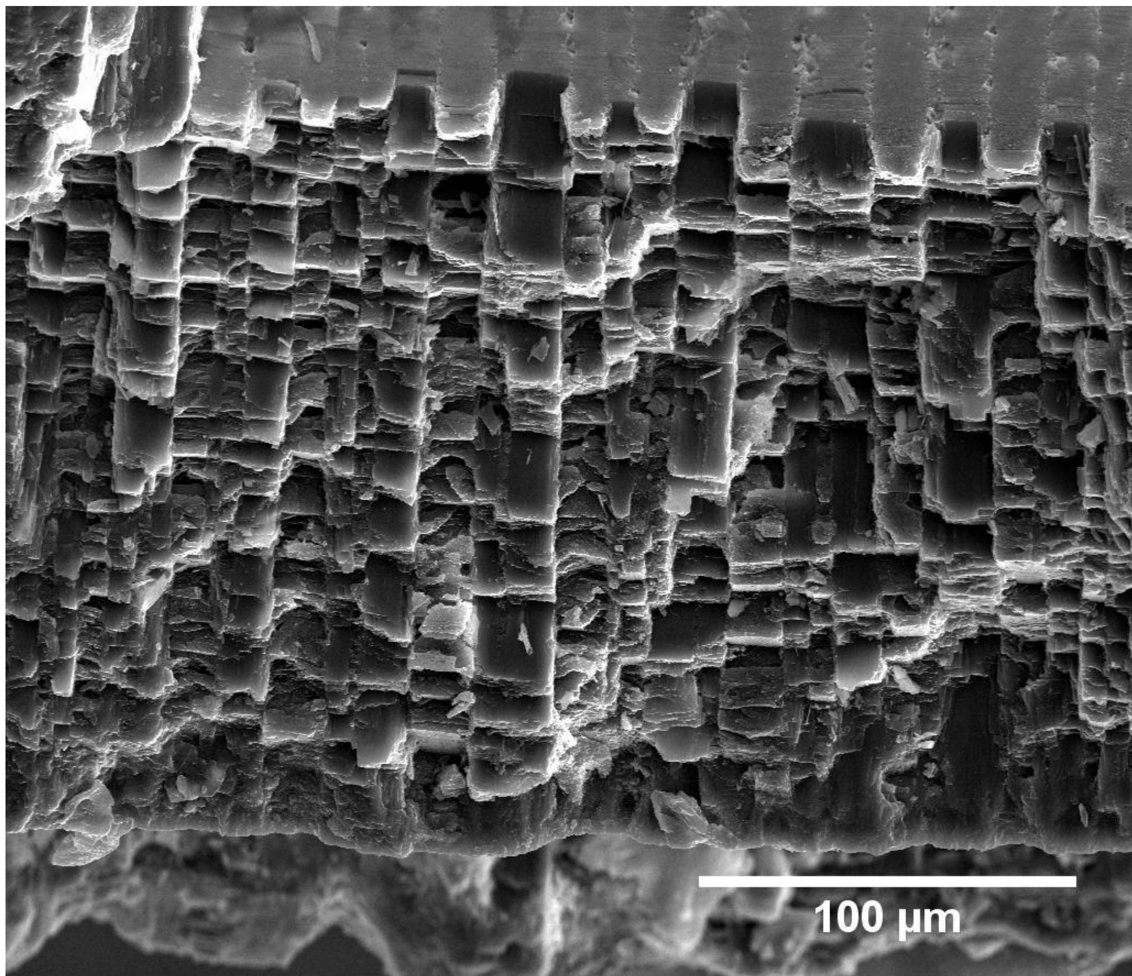

Figure 7.4 – SEM micrograph of the fracture surface of snail shell showing the cross-lamellar micro-structure. The first order layering, as seen in figure 7.2, of approximately 10 to 15 µm can be seen as the vertical striations with alternating orientations; and within each vertical stripe, second order layering can be seen.

Further structural details of the fracture surface at higher magnification using SEM are shown in Figure 7.5 . The field of view only contains one of the layers seen in the previous figure. Figure 7.5 highlights the staggered brick structure, which forms the mineral plates at the larger length scale seen in Figure 7.4. The mineral bricks in Figure 7.5 are of the order of 50 nm wide and 300 nm long and are the largest volume fraction in the composite; the protein layers are not visible in the micrograph and therefore probably only constitute a small percentage of the total volume.

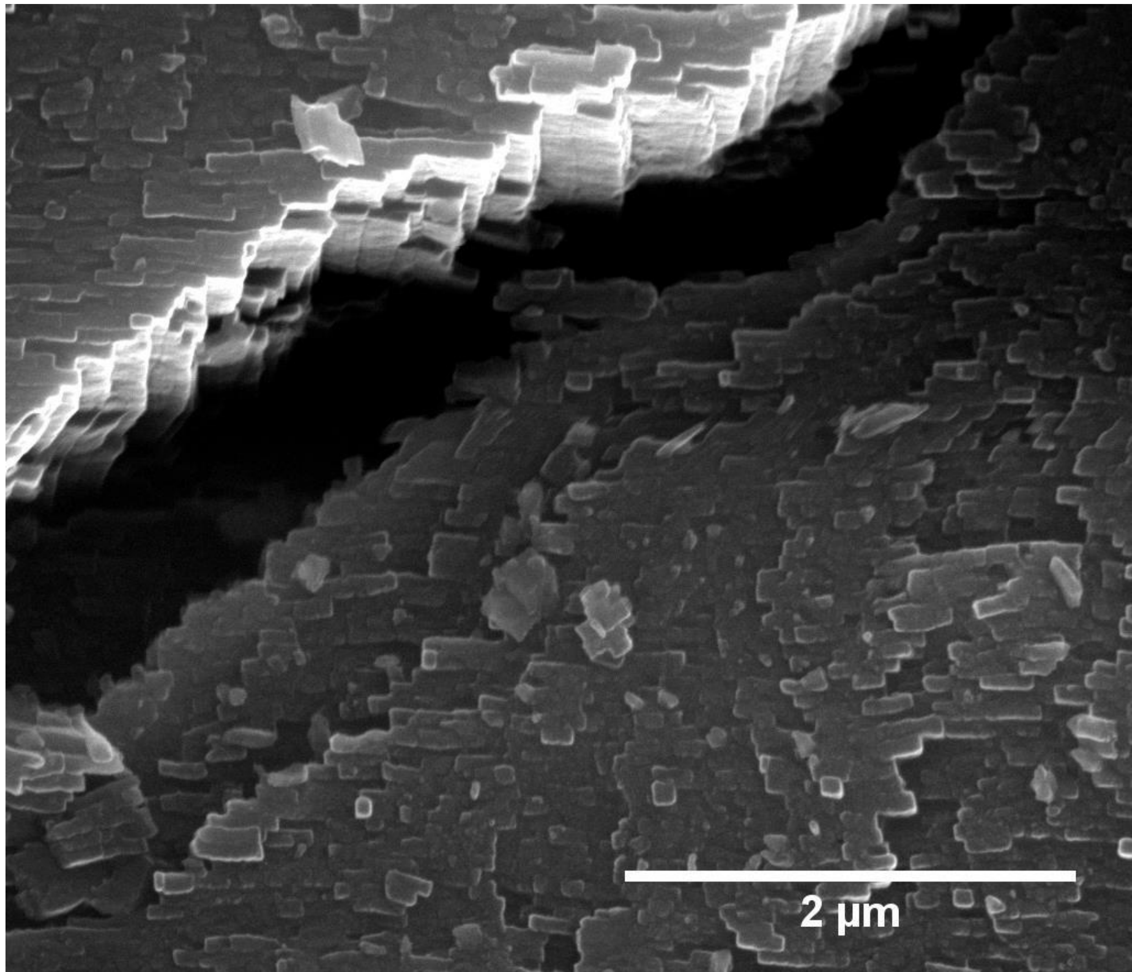

Figure 7.5 – SEM micrograph of snail shell showing the brick and mortar nano-structure, which makes up one of the higher order structures seen in figure 7.2

The fractured shell was mounted in the bespoke SEM sample holder described in Chapter 3 such that a fracture surface was parallel with the top surface of the holder. The shell sample was coated with a layer of gold as described in Chapter 3. The sample holder and shell were mounted onto the sample stage of the Quanta 3D FEG using a 45° pre-tilt stage so that with a stage tilt of 7° the fracture surface of the shell was parallel to the ion beam direction. The pre-tilt of the sample allowed for cross-sectioning and low angle polishing of the fracture surface using the FIB. The top surface of the shell relative to the FIB was coated with a strip of platinum as described in Chapter 3. The fracture surfaces produced when fragmenting the snail shell were rough in comparison to those produced for the polymer nanocomposite and

required a larger volume to be removed in order to achieve a smooth final surface. Figure 7.6 is an SEM micrograph of the snail shell after the initial large volume milling. The strip of platinum is visible near the centre of the image, and the cross-section produced cuts through the platinum.

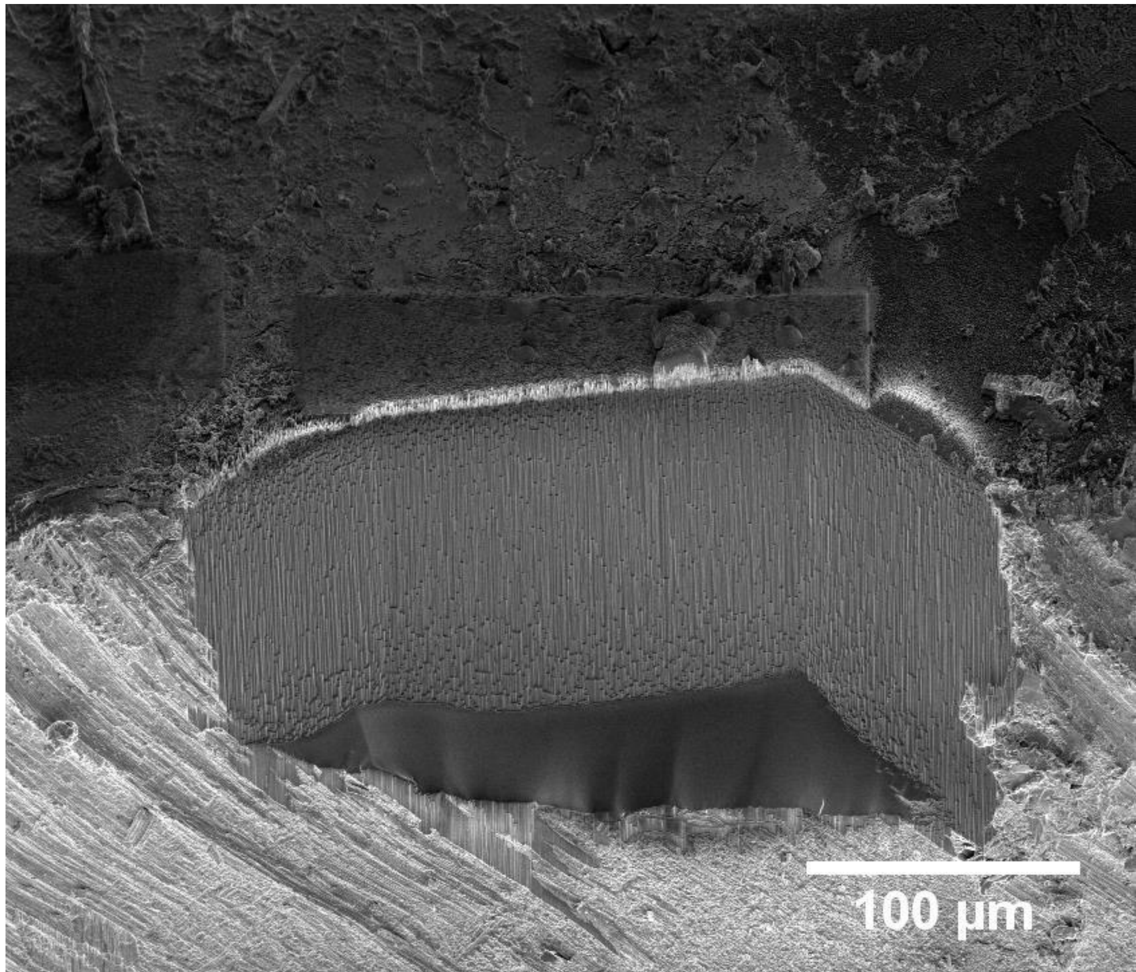

Figure 7.6 – An SEM micrograph of snail shell after coarse milling using FIB. The top surface has a layer of platinum deposited to protect the underlying shell from damage by low intensity ion beam tails. The relatively large volume has been removed in order the allow access to the final surface by the AFM probe and provides a relatively flat surface for final polishing when compared to the fracture surface.

A higher magnification image of the coarse ion beam milled cross section is shown in Figure 7.7. The top of the image is an area of deposited platinum whereas the bottom two thirds of the image shows the FIB milled cross-section area. The coarse milled surface is smoother than

the original fracture surface, but still retains some texturing. The columnar structures visible in Figure 7.7 are artefacts of the high current FIB milling step and are due to regions of preferential milling.

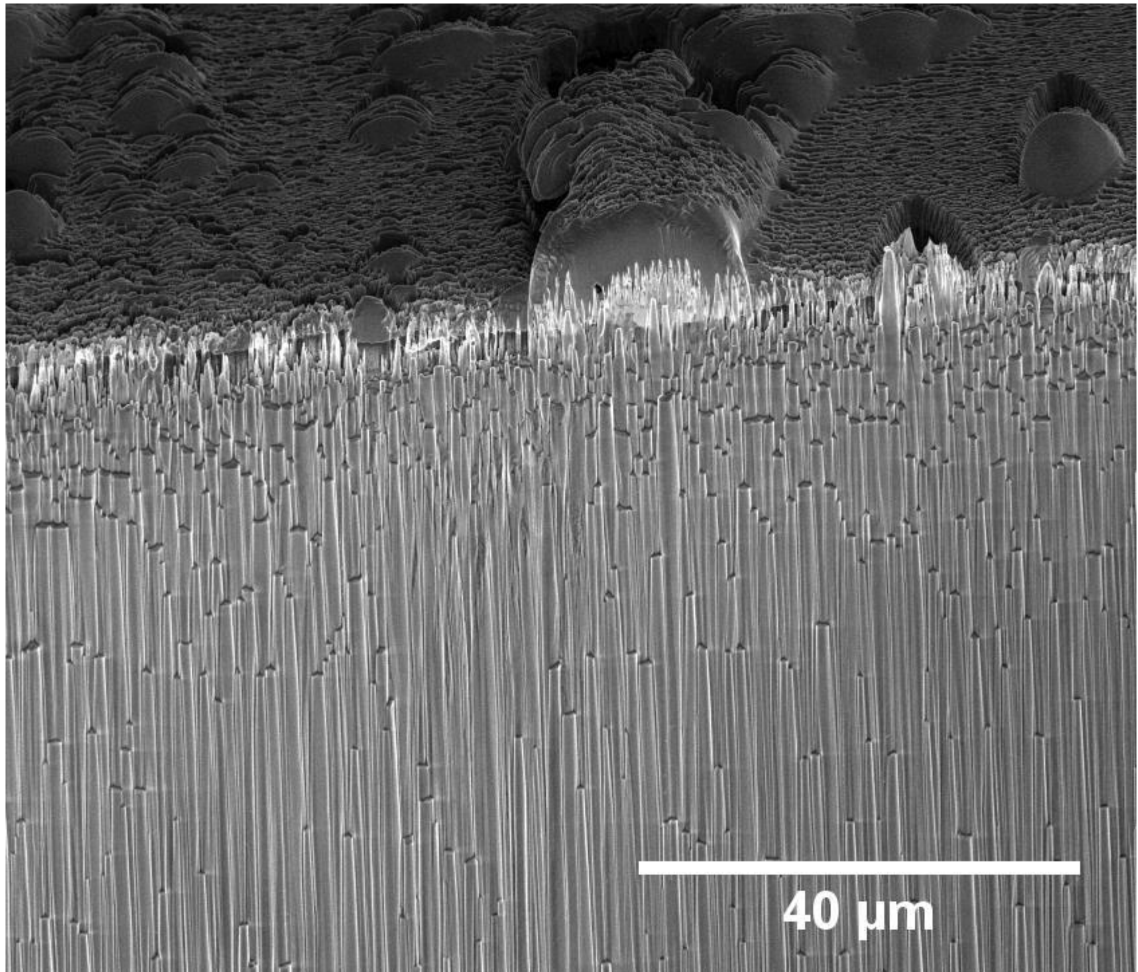

Figure 7.7 – A higher magnification image of the coarse milled snail shell. The resultant surface is flat in comparison to the fracture surface, but still has columnar type structures, which are an artefact of the milling process.

A smaller area of the shell surface was polished using a lower ion beam current in order to reduce the number of milling artefacts and provide a corresponding relatively smooth surface, as attempted with the polymer nanocomposite in Chapter 6. The step of FIB polishing at lower and lower currents was repeated until a satisfactory surface of minimal apparent roughness was observed using the SEM and could be measured using AFM to be below 5nm RMS.

Figure 7.8 is an SEM micrograph showing three successive polishing steps, each at a lower FIB current. It can be seen from Figure 7.8 that with each subsequent polishing step the resulting surface has a reduced roughness with fewer milling artefacts.

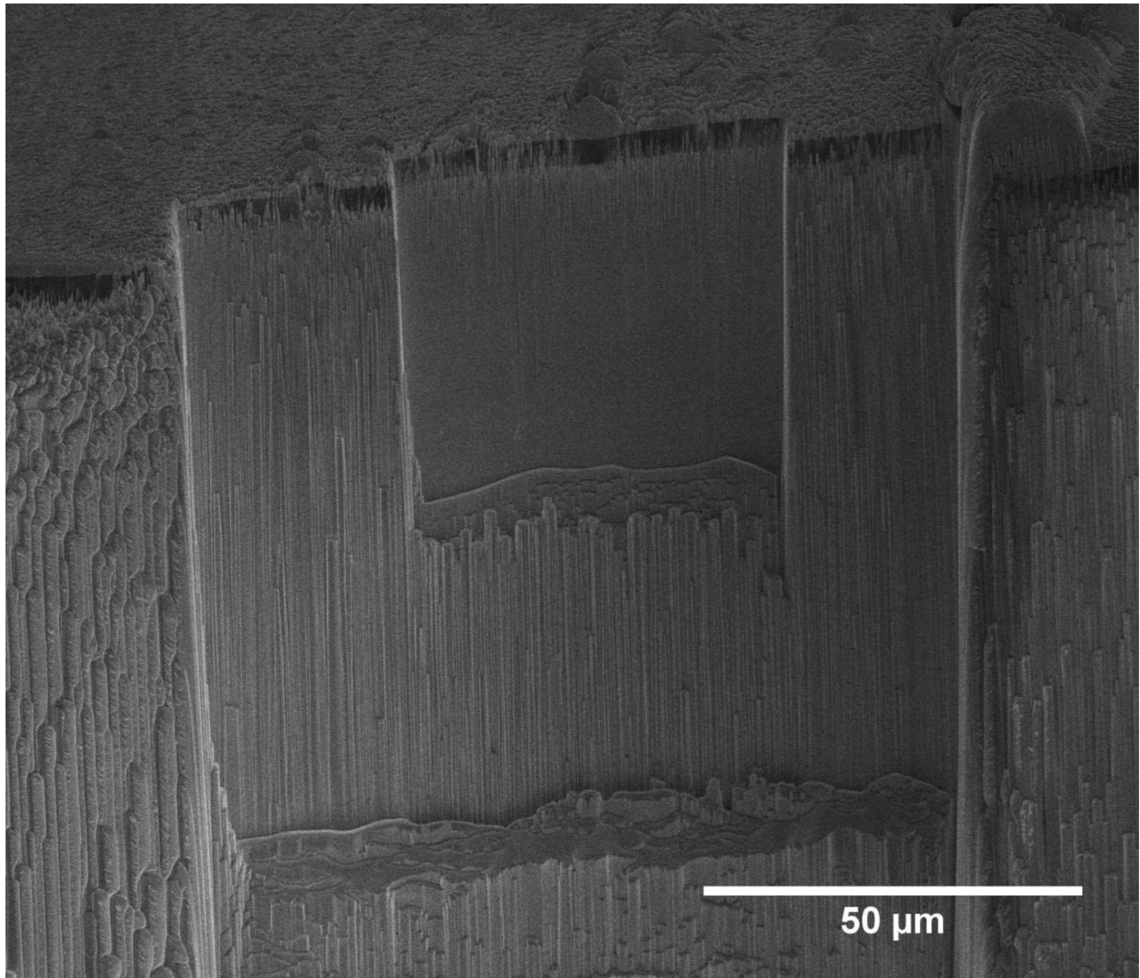

Figure 7.8 – subsequent sections milled using lower ion beam currents produce fewer artefacts and therefore a smoother finish.

Figure 7.9 is an SEM micrograph of the final FIB polished cross-section. The final surface seen in the image has no visible milling artefacts or areas of material redeposition and is therefore suitable for AFM phase contrast imaging. The sample was removed from the Quanta 3D FEG and mounted directly onto the stage of the NTegra AFM by removing the pin from the sample holder. The clamping sample holder held the shell fragment such that the FIB milled surface

was uppermost and ready for AFM imaging. AFM phase contrast images of the FIB milled cross-section were captured using the method described in Chapter 3.

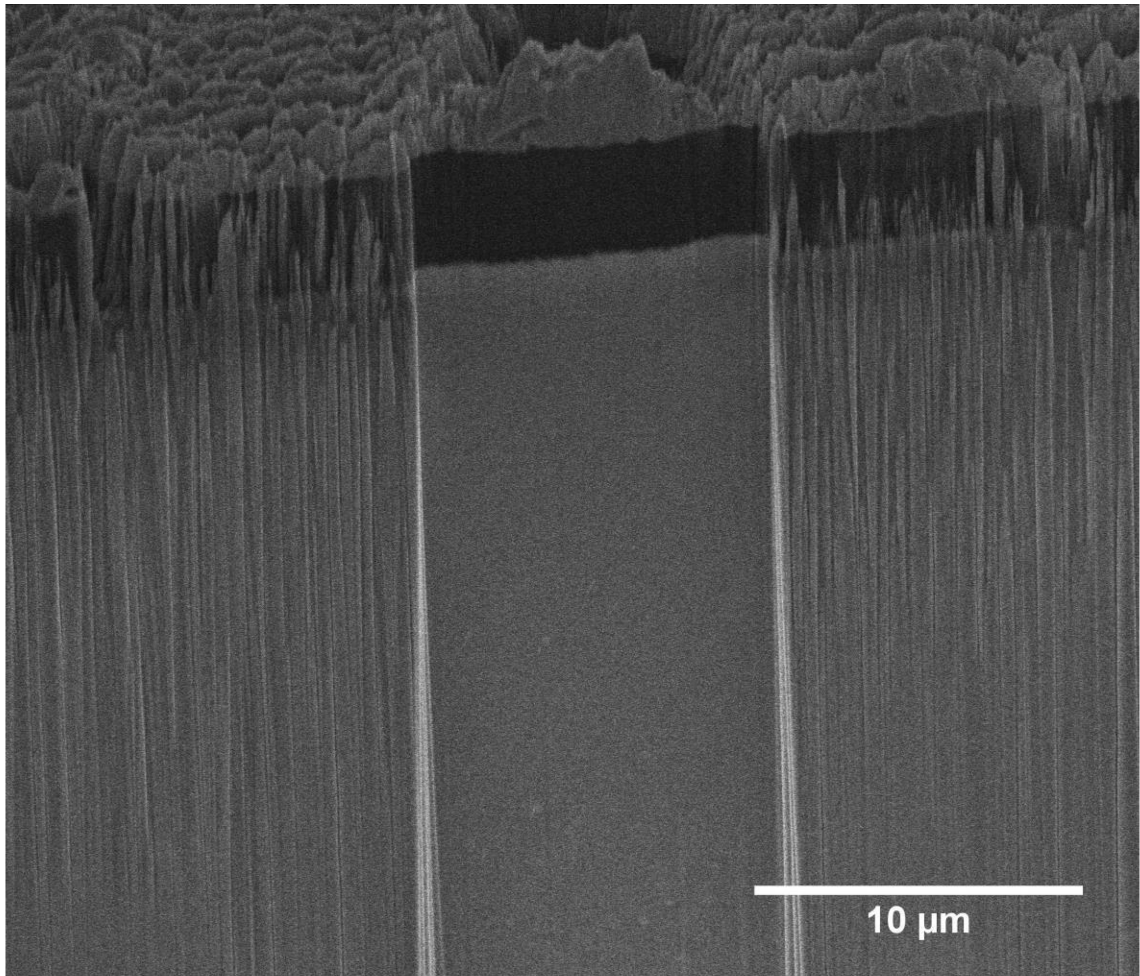

Figure 7.9 – An SEM micrograph of the final FIB polished surface. The final, low ion beam current surface has fewer artefacts compared to the previous surface to the left and right of the image, with no visible features.

7.2.2 Variations required in the model

The contrast in the phase signal recorded during AFM phase imaging is a function of the AFM cantilever dynamics and operating parameters and is therefore dependent on the resonant frequency, Q factor, spring constant, and free and setpoint amplitudes of the AFM cantilever used. A new set of simulations were performed in order to create a phase to contact modulus calibration function relevant to the snail shell AFM phase images, especially as the AFM

cantilever used to image the snail shell was different to that used for the polymer nanocomposite. Figure 7.10 is a plot of the AFM phase predictions made by MatLab simulation based on the new AFM cantilever properties and AFM operating parameters.

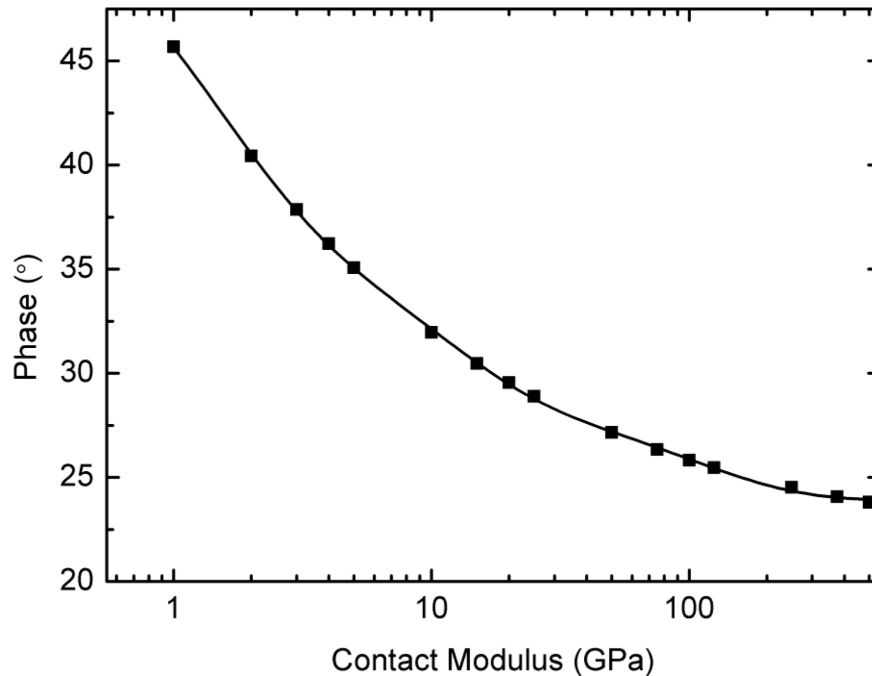

Figure 7.10 – A plot of AFM cantilever phase vs the contact modulus between the sample and the AFM tip derived from the Carpick model and used to calibrate the AFM phase images

7.3 Results

7.3.1 SEM images

Figure 7.9 is an SEM micrograph showing the final, low current FIB polished cross-section of the snail shell. The top surface, uppermost in the picture, is the platinum, which was deposited on the surface prior to FIB milling. Below the platinum is a darker layer, which is of the order of 5 µm thick. This layer is darker due to fewer secondary electrons being emitted from the sample, which is typical of an organic material and would suggest that this is the periostracum of the shell. In the centre of the image is the final polished section of the mineral region of the

shell specimen. The polished mineral region shows uniform contrast and is completely featureless, especially compared with the "roughly" milled surfaces to the left and right of the image.

7.3.2 AFM images (added contrast)

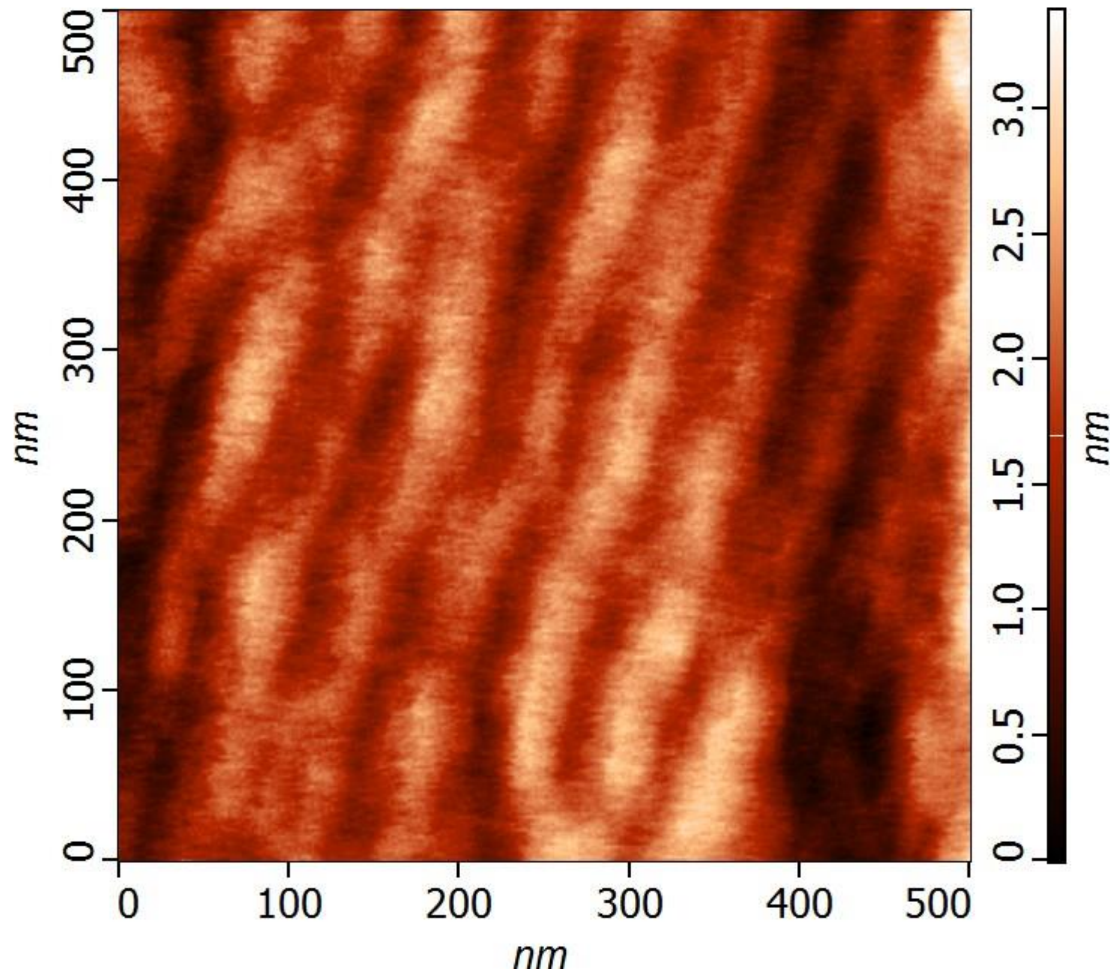

Figure 7.11 – An AFM height image of the FIB polished snail shell. The RMS roughness of the polishing surface is 0.52 nm and the variation in height recorded by the AFM is likely due to increased penetration of the AFM tip into softer regions.

The same surface that was imaged with the SEM in Figure 7.9 is shown in Figure 7.11 as an AFM topography image. Figure 7.11 shows that the surface is very smooth, with the RMS roughness calculated from the height information being 0.52 nm, but some structural features

can still be distinguished. The features visible in the AFM topography image are off axis when compared to the direction of FIB milling, so are unlikely to be artefacts from the milling process, and the layers are of the order of 50 nm, which is the same length scale as an aragonite crystal. The apparent difference in height between the layers is possibly due to preferential milling of certain crystal orientations, or due to differing AFM tip penetration depths during imaging due to the anisotropic elasticity of the aragonite crystal.

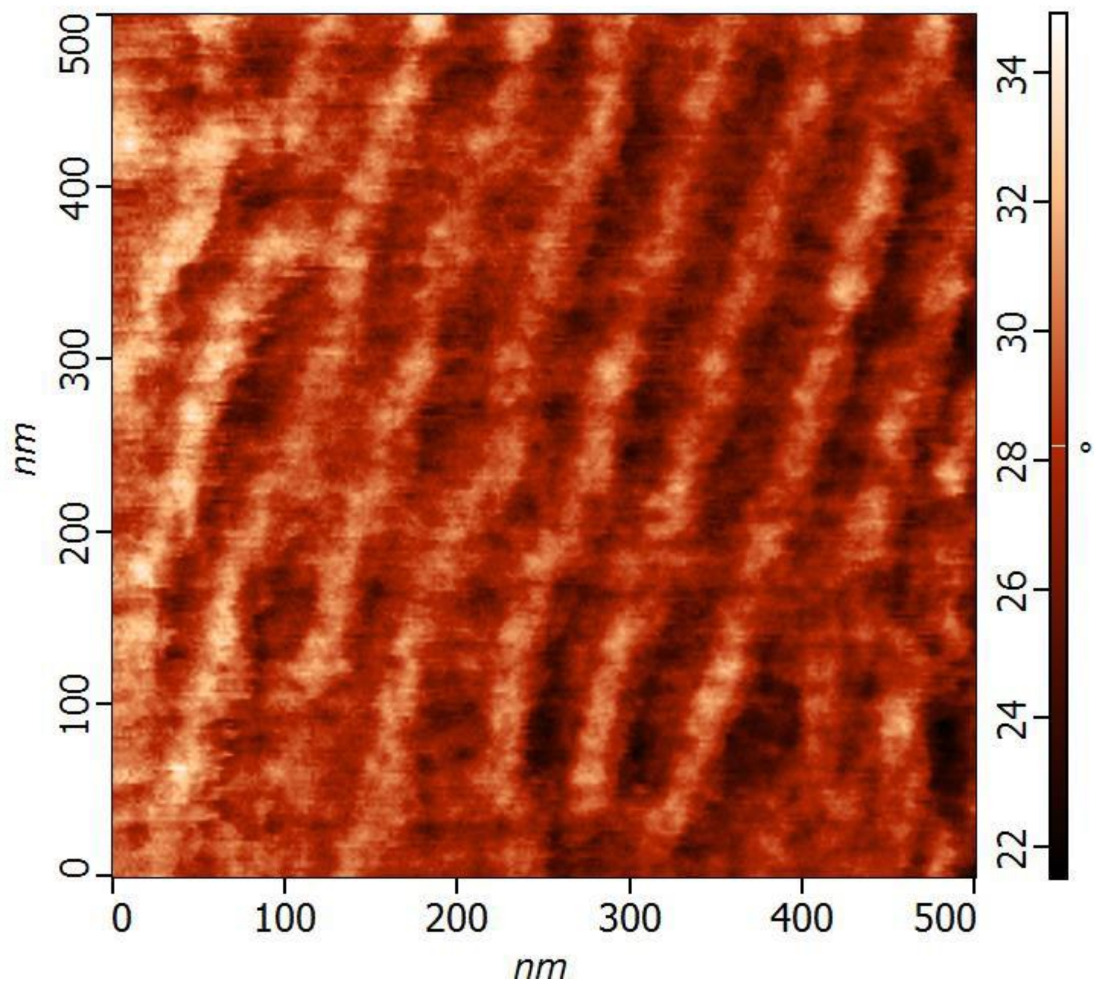

Figure 7.12 – An AFM phase contrast image of the FIB polished snail shell. The darker regions of the image represent the stiffer component in the composite, while the lighter regions represent the softer component.

Figure 7.12 is the phase contrast AFM image of the FIB polished shell cross-section, which was collected simultaneously with Figure 7.11. The phase contrast image has a greater level of

contrast between the layers in the cross-section, making them easier to distinguish. The lighter regions in the image signify a larger phase shift, which in turn implies that the contact was soft, whereas the darker regions of the phase image suggest a stiffer contact. The phase contrast image lends weight to the idea that the apparent topography in Figure 7.11 was due to differential contact stiffness, as the softer areas in the phase image marry up with the lower regions in the height image. A line profile of phase values across six layers within the AFM phase image is presented in Figure 7.13. The line profile plot shows distinct layering within the structure of the snail shell, with a period of approximately 50 nm. The phase value peaks and troughs across the layers between the values of 29 and 25° respectively. A histogram of the phase values in Figure 7.12 is presented in Figure 7.14 and shows that there is a bimodal distribution of values. The taller peak to the left of Figure 7.14 is centred around 26.12° and represents the stiffer phase of the shell, while the right peak is centred around 28.41° and comes from the softer component of the shell cross-section.

By applying the simulated calibration from Figure 7.10, the AFM phase values can be converted into contact moduli for the two different regions of the cross-section. The phase value of 26.12° is equivalent to 88 GPa, while the phase value of 28.41° equates to a contact stiffness of 28.5 GPa. Using the relationship defined in chapter 5, which defines contact modulus with respect to tip and sample Poisson's ratios and elastic moduli, these contact moduli can be translated to Young's elastic moduli values of 144.5 GPa and 32.5 GPa respectively.

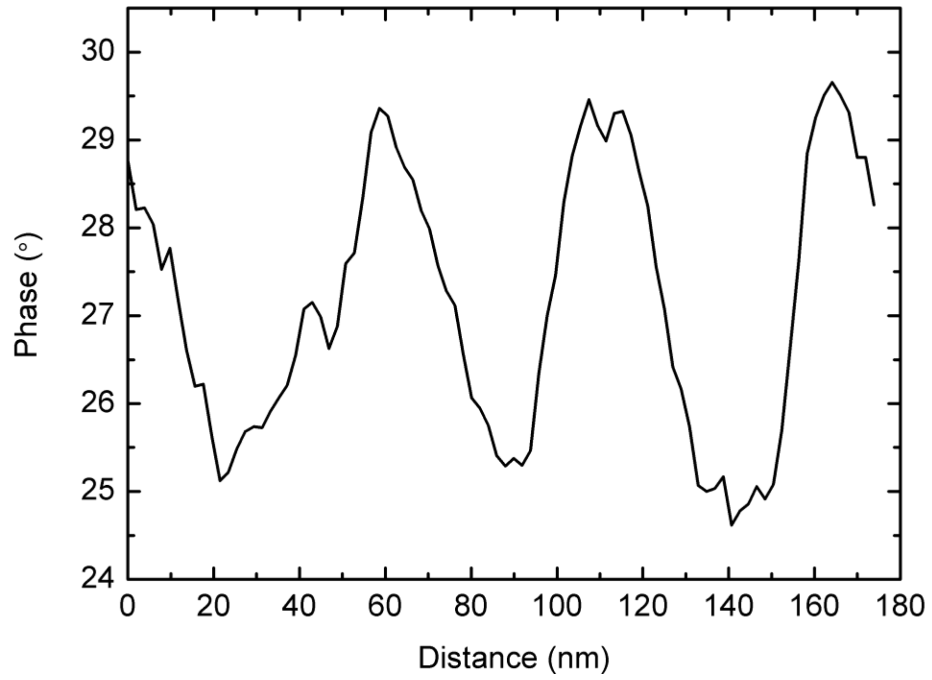

Figure 7.13 - Line profile of phase values across six layers of the snail shell biocomposite

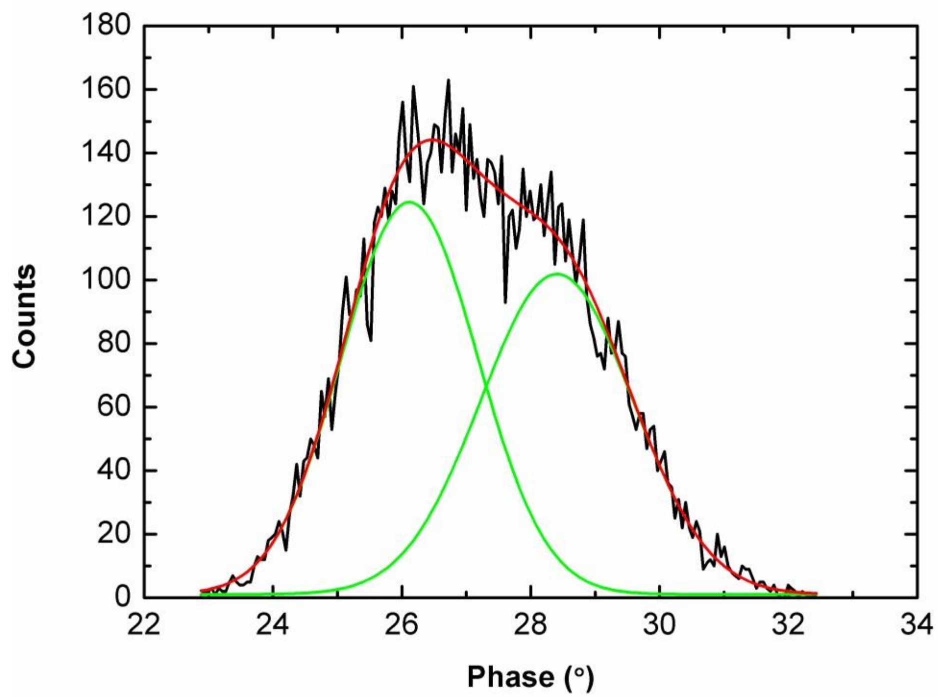

Figure 7.14 - Histogram showing the bimodal distribution of phase values in the phase contrast AFM image of the snail shell cross-section in Figure 7.12

7.3.3 Rule of mixtures approximation

The relationship between the mechanical properties of the constituent materials within the snail shell and the ability to predict the overall mechanical behaviour of the shell is a critical aim of this chapter and has been achieved previously in a simpler synthetic nanocomposite. An effective approach used in Chapter 6 is to apply a simple rule of mixtures to estimate the elastic modulus of the composite based on the contributions of the different components. As the snail shell can still be considered to consist of two distinct material domains; the two distinct layers seen in the AFM phase contrast image, and the proportions of the domains can also be estimated from the AFM phase image, a rule of mixtures approximation may still apply.

Using ImageJ, the AFM phase image was estimated to be composed of soft and stiff domains at a ratio of 49:51. Applying this ratio to the rule of mixtures, along with the elastic moduli calculated of 32.5 GPa and 144.5 GPa, the global elastic modulus for the bulk sample is reported as 89.62 GPa.

The Young's modulus of elasticity value of 89.62 GPa falls close to the range expected for aragonite-based shell biomaterials. *Fleischli et al.* (2008) studied five different seashell structures with aragonite structures, by microhardness and nanoindentation, reporting a range of values for elastic modulus of 60 to 85 GPa. The result presented in this work of 89.62 GPa falls within 6% of the upper limit of previously measured values.

7.4 Discussion

In this chapter a FIB prepared cross section of a biocomposite material was imaged using phase contrast AFM. Figure 7.12 is an example of one such AFM phase image, and shows a clearly defined layered structure, with contrast that was not present in the secondary electron SEM images of Figures 7.6 and 7.9. By simulating the AFM cantilever dynamics, using a MatLab script based on the Carpick model, a relationship between AFM cantilever phase and the

contact stiffness between AFM tip and sample was predicted and quantified. The relationship predicted by the MatLab script was then used to convert the phase contrast image into a map of contact stiffness, and subsequently Young's elastic modulus. In this way it was possible to estimate the local elastic moduli across the AFM images.

Figure 7.14 shows a bimodal distribution of phase values in the AFM phase image of Figure 7.12, with one distribution centred on a value of 26.12° and the other on a value of 28.41°. By using the MatLab script, these phase shifts can be assigned contact stiffness values of 88 GPa and 28.5 GPa, and Young's elastic moduli of 144.5 GPa and 32.5 GPa respectively.

The elastic modulus value of 144.5 GPa found in the stiffer layers of the shell structure ties in with the Young's elastic modulus of the aragonite crystal along its stiffest axis, as reported in the literature. The softer layers of the snail shell within the AFM phase image, with a Young's modulus of 32.5 GPa, are possibly formed from the fibrous protein chitin, which is reported to have an elastic modulus of the order of 40 GPa. However, fibrous protein under compressive loading would be expected to have a far lower modulus, because of buckling, so if this is a genuine compressive modulus, it would imply constraint of the fibres. Deviation from the expected modulus could also be due to the method of specimen preparation; freeze-fracture of biological specimens can cause disruption of ultrastructure if crystal ice is allowed to form. To avoid crystal ice formation, specimens are kept to small volumes and flash-frozen in supercooled nitrogen slush, to avoid the Leidenfrost effect.

The softer layers make up a larger volume fraction of the composite than expected from the protein, which is estimated to account for approximately 5% of the total. It is therefore possible that the softer layers observed in the AFM phase images are off-axis aragonite, or a convolution of aragonite and protein.

By using a simple rule of mixtures estimation, the bulk Young's elastic modulus of the snail shell was calculated to be 89.62 GPa. This bulk elastic modulus value is in keeping with values

reported in the literature, which shows that the quantitative AFM phase contrast method is capable of making predictions about a composite materials engineering performance. Phase contrast AFM can therefore be used to investigate the contribution of individual components towards the overall performance of a composite material.

7.5 Conclusions

The aim of this chapter was to demonstrate that the quantitative AFM phase contrast method outlined in chapter 5, and demonstrated on a simple binary polymer composite in chapter 6, could be effectively applied to a more complex biological composite material. In order to achieve this aim, a section of snail shell was prepared using FIB microscopy and imaged by AFM phase contrast microscopy. The resulting AFM phase images were quantified using the methods outlined in chapter 5, and the Young's elastic modulus values of the components and bulk materials were estimated.

AFM phase contrast imaging was able to highlight contrast within the biocomposite that wasn't observed in either SEM or AFM topography imaging.

AFM phase contrast information was quantified using a MatLab script based on the Carpick model of AFM cantilever dynamics and was used to calculate the young's elastic modulus of the individual of the biocomposite. The bulk properties were then calculated from the localised measurements and were in keeping with previously measured values for bulk performance recorded in the literature.

The work presented in this chapter therefore demonstrates that the quantitative AFM phase contrast method is capable of accurately measuring the elastic properties of individual components of a complex biological composite material.

8 Three dimensional reconstruction of a nanocomposite

8.1 Aims

This chapter builds on the work of chapters 6 and 7 by using focused ion beam (FIB) microscopy to extend phase contrast AFM imaging into three dimensions. A single, two-dimensional image of the surface of a complex material only tells us a fraction of the information we need to understand its structure. The aim of this chapter is to show that through the combined use of FIB to take serial sections through a sample, and phase contrast AFM imaging, it is possible to build a three-dimensional understanding of the mechanics of a complex material.

8.2 Introduction

The mechanical behaviour of nanocomposites is critically dependent on their structural composition. In this chapter I use Focused Ion Beam (FIB) microscopy to prepare surfaces from a layered polymer nanocomposite for investigation using phase contrast atomic force microscopy (AFM). Phase contrast AFM provides mechanical information on the surface examined and, by combining with the sequential cross-sectioning of FIB, can extend the phase contrast AFM into three dimensions. Nanocomposites are used in a range of applications and have been shown to be particularly effective for mechanical functions. However, this mechanical function is critically related to elucidating the structural composition of the nanocomposite material. A range of techniques are available to evaluate mechanical properties of nanocomposites and can be classified into two distinct approaches. The first approach relies on measuring the mechanical behaviour of the whole nanocomposite and then applying varies models in order to elucidate the contribution of the smaller constituents. These approaches are limited as a number of assumptions are made in terms of the mechanical

properties of the constituents and their interactions with one another. The limitations in bulk mechanical testing have led to the development of techniques suitable to measure the properties of these smaller constituents in order to evaluate composite mechanical performance more fully. Constituent evaluations in nanocomposites are relatively limited due to the constituent properties having dimensions of the order of nanometres, which are below the loading resolution of conventional engineering mechanical testing methodologies. Examples of nanocomposite constituent testing exist in the literature and range from mechanical testing of isolated individual nanomaterial constituents to indentation techniques. However, nanomaterial isolation is restricted as only one part of the nanocomposite can be considered at one time, making evaluation of a nanocomposite a lengthy process, whereas nanoindentation is able to only probe surface properties of a nanocomposite.

Phase contrast AFM is an additional technique that is able to measure the mechanical properties at surfaces but is generally infrequently used in the literature. Phase contrast AFM is a mode of amplitude modulated AFM whereby a probe attached to a cantilever is driven at its resonance frequency and periodically makes contact with the sample surface. The AFM probe is scanned over the sample surface and a predefined set-point amplitude is maintained by a feedback loop. The phase lag between the driving oscillation and the response of the cantilever whilst scanning the sample surface is recorded along with the standard AFM topographical data. Phase contrast AFM has previously been applied to evaluate changes in surface mechanical properties with high spatial resolution and model the behaviour of the AFM cantilever in order to quantify the mechanical data attained. Therefore, AFM is effective at mapping mechanical properties at a composite surface, but is hindered by being surface specific and by providing convoluted data due to surface topography effects. Indeed, surface topography is perhaps the limitation in the uptake of phase contrast AFM as a more widely used technique for measuring mechanical properties of a material at its surface.

Focused Ion Beam (FIB) microscopy is a developing technique for nanomachining and the preparation of microscopic samples. Examples of FIB use include patterning of semiconductor materials, preparation of thin samples with parallel surfaces for TEM analysis and integration into a Small Dual Beam (SDB) system for 3D imaging. This latter technique requires the sequential removal of layers of material and the capture of the exposed surfaces using SEM imaging, followed by computational reconstruction to form a 3D image of the material structure. The "Slice and View" technique is effective for 3D imaging of materials, but can suffer from poor image contrast in, for example, soft nanostructured composites. Critically, the combination of exposing composite surfaces using FIB sequential sectioning and imaging these surfaces with phase contrast AFM therefore presents an opportunity to evaluate the mechanical property distribution in a composite material. The aim of this paper is therefore to demonstrate the effectiveness of FIB preparation with the mechanical imaging capabilities of phase contrast AFM

8.3 Experiment

8.3.1 Ex situ AFM

Polypropylene/Versify 2300 composite tapes were provided by Nanoforce Technology Ltd (London, UK). The composite tapes were prepared by co-extrusion of the two components as a two-layered tape, and then repeatedly layered and drawn to produce a composite with layers ranging in thickness from 50 nm to 1 μm.

Samples of the composite tape were initially fractured under liquid nitrogen to produce a relatively flat cross-section. The freeze-fractured tape was then mounted onto a standard SEM stub using carbon cement and gold coated to ensure a good conductive pathway. The sample on the SEM stub was loaded onto the sample stage of a Small Dual Beam (SDB) system

(Quanta 3D FEG, FEI Company, Netherlands) so that the exposed cross-section was parallel to the electron beam direction. The SDB sample stage was then tilted to an angle of 52°, so that the cross-section was parallel to the FIB direction and the electron beam had an incident angle of 38° to the exposed surface. The sample was sequentially FIB milled to produce surfaces progressively through the nanocomposite and imaged, with a schematic representation of the slice and view process shown in Figure 8.1. Figure 8.1a shows a block of layered composite with an exposed cross-section. The FIB is used to mill a selected region and thus generate a new surface, as shown if Figure 8.1b. The newly exposed cross-section is then transferred to an AFM for subsequent phase imaging, as shown in Figure 8.1c.

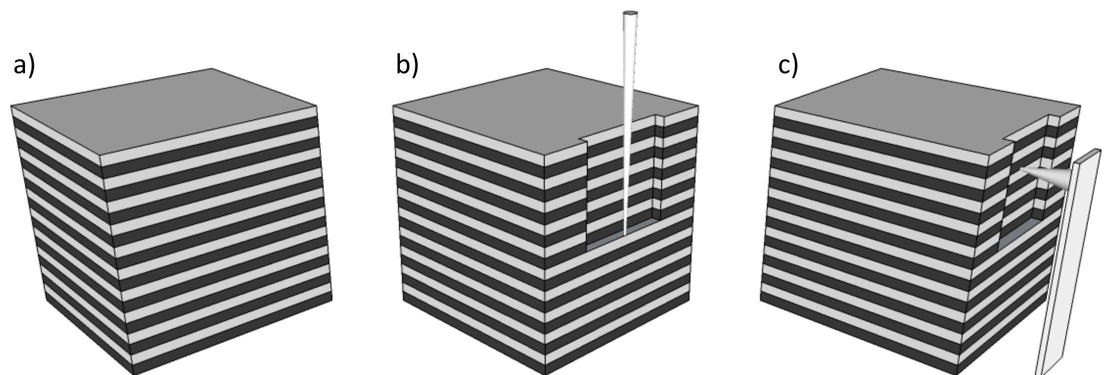

Figure 8.1 A schematic representation of the slice and view process. a) Shows a block of layered nanocomposite. b) The FIB is used to mill out a cross-section through the composite block. c) The FIB prepared composite surface is imaged using phase contrast AFM.

The process as shown in Figure 8.1 can be visualized using the SEM of the SDB system. Figure 8.2 shows a secondary electron SEM image of a region of polymer composite that has been cross-sectioned using the FIB. We note that the use of FIB preparation of the nanocomposite is particular effective in evolving surfaces that are topographically flat. Thus, subsequent phase

contrast AFM will provide information on the variation in the mechanical properties of the material and is decoupled from topography.

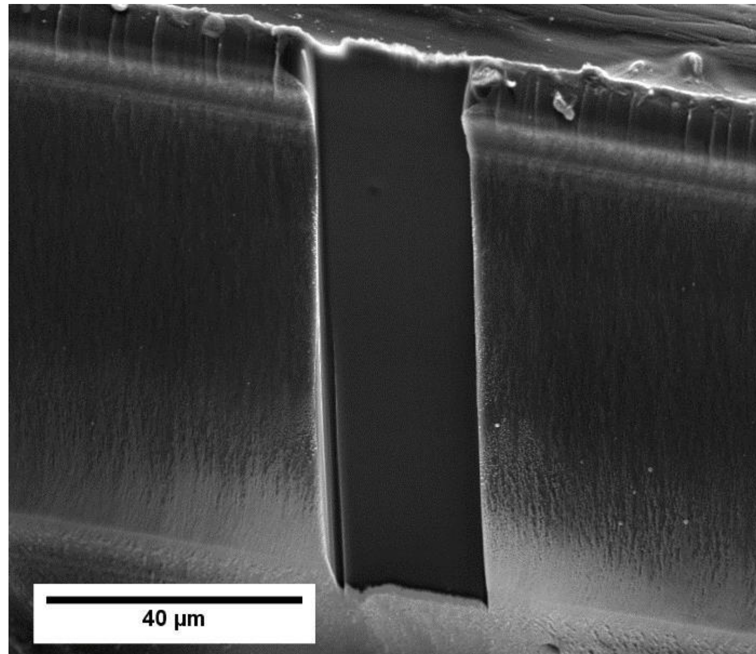

Figure 8.2 A secondary electron SEM image of a FIB milled cross-section in the nanocomposite.

8.3.2 In situ AFM

The attocube AFM, described in section 3.2.2, allowed for phase contrast AFM images to be collected in situ, without the need to remove the specimen from the microscope chamber. Figure 8.3 is an SEM micrograph showing the in-situ AFM scanning a FIB milled cross-section in the polymer nanocomposite specimen.

Figure 8.3 SEM micrograph showing the in situ AFM imaging the specimen cross-section

8.4 Results

A phase image of an exposed composite surface, prepared using FIB is shown in Figure 8.4b. The phase image clearly shows a layered structure corresponding to the different material composition within the nanocomposite that is not evident in the standard topographical image presented in Figure 8.4a. In particular, the soft elastomeric regions will provide a large phase shift whereas the higher elastic modulus polypropylene gives a smaller phase shift. Figure 8.4b correlates with the expected mechanical properties of the different regions within the composite, where the bright and dark striations represent soft and stiff regions respectively.

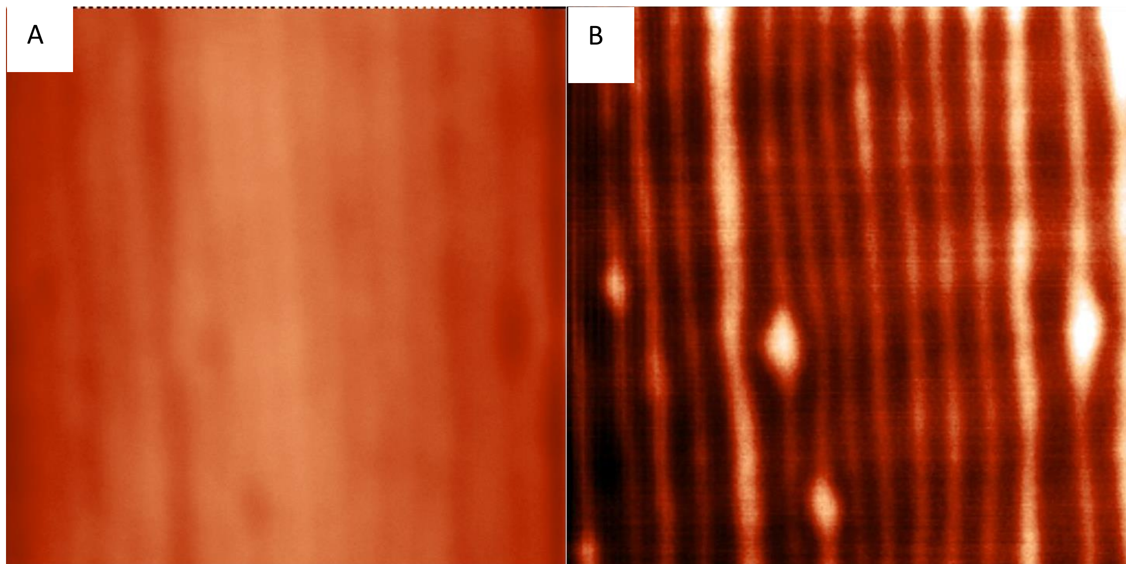

Figure 8.4 a) AFM topography image of a layered nanocomposite cross-section. b) Corresponding AFM phase contrast image showing the layered composition of the sample. Both images have a 4 µm field of view.

A series of 2D phase images collected during the progressive removal of material by the FIB is shown in Figure 8.5. A clear correlation is observed between layered features from one slice section to the next, while particulate features appear in only one or two adjacent slices. Thus, a complete mechanical evaluation of the nanocomposite structure in 3 dimensions has been achieved. While the spatial resolution in the x-y plane is of the order of 5 nm, the z resolution in the nanocomposite sample presented in this data is approximately 1 µm, but can be improved significantly to approximately 10 nm using a larger data set, containing thinner cross-sections. This improved spatial resolution would give a voxel size of the order of 250 nm^3. Figure 8.6 is an example of a Phase contrast image obtained using the in situ AFM, which demonstrates the possibility of being able to collect a 3D dataset without the need to remove the specimen from the SDB chamber.

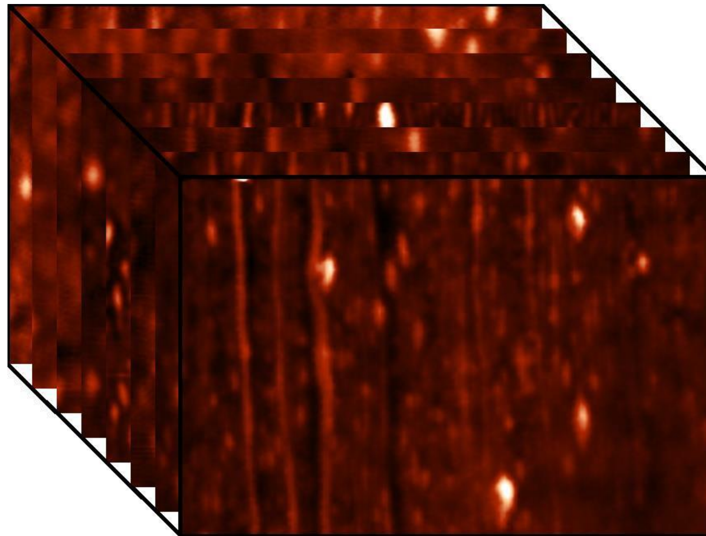

Figure 8.5 Phase contrast AFM images of sequential cross-sections through a composite surface.

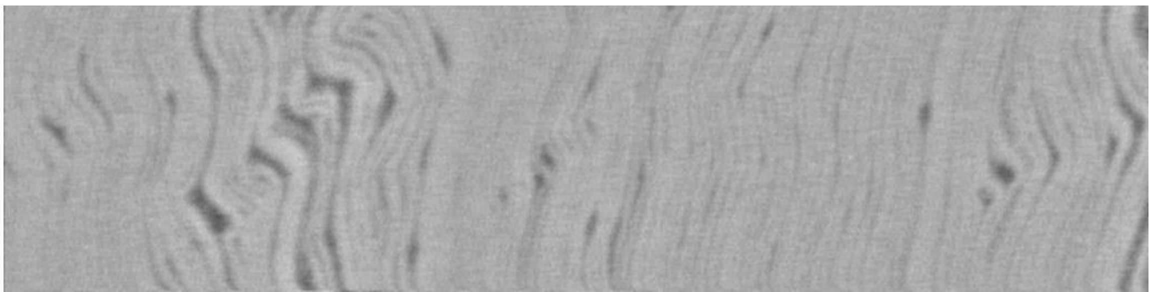

Figure 8.6 Phase contrast AFM image of polymer nanocomposite taken with in situ AFM post milling.

8.5 Conclusions

In this chapter I have used FIB to expose surfaces within a polymer nanocomposite and subsequently image these surfaces using phase contrast AFM. The imaging AFM provided clear evidence of hard and soft layered domains within the nanocomposite material. Reconstruction of 2D phase contrast AFM images was carried out to produce 3D mechanical maps of the nanocomposite and demonstrated how FIB can extend the surface evaluation of AFM to 3D. Other methods of achieving Scanning Probe Tomography (SPT) have been demonstrated, and a comparison of some of these methods has been provided by Alekseev et al. [121] Alekseev

discusses the limitations of several destructive SPT methods, including taking sections through ultramicrotomy, cryo-ultramicrotomy, chemical/plasma surface etching, and FIB. Ultramicrotomy is limited by it's potential z-resolution, and by only being realistically applicable to soft materials, with biomineralized materials being prone to severe tooling artefacts from the shear and compressive loading through the blade. Chemical and plasma etching, despite having potentially very high z-resolution, has the limitation of different materials having different etching rates, and therefore preferential etching of certain domains can be seen in composite materials.

Non-destructive methods of obtaining SPT data are potentially able to achieve very high spatial resolution, but by nature are limited to probing a very surface specific volume of the specimen, limited to the range of nanometres.

FIB was described by Alekseev as having the limitation of having unavoidable impact on the surfaces prepared by FIB mill preparation. However, the work presented in Chapter 4 demonstrates that this damage can be mitigated through careful selection of operating beam conditions. FIB therefore offers a high z-resolution method of obtaining Scanning Probe Tomographs that doesn't produce the mechanical artefacts associated with microtomy, and produces a more predictable z-step size, regardless of the material being sectioned.

9 Conclusions

In this study I have examined how AFM phase contrast imaging can be used to measure quantitative mechanical data at a specimen surface, at nanometre scale resolution. Through simulation of AFM cantilever dynamics, I have demonstrated that it is possible to estimate the contribution of contact stiffness and Young's modulus to the phase angle of the cantilever oscillation. This leads us to be able to map mechanical surface properties of a specimen, and examine how nanoscale components and structural artefacts can influence bulk behaviour.

In chapter 4, I used AFM phase contrast to assess the damage caused by FIB cross-sectioning in a polymeric material. I was able to compare the damage caused using various milling conditions through the degradation of the mechanical response of the surface, and thereby suggest beam conditions that would be most suited to cross-sectioning polymeric materials.

Through the use of the FIB, it is then possible to produce flat cross-sections in a specimen surface, in preparation for AFM phase contrast imaging, thereby removing the influence that topography has on the phase signal. This FIB preparation has been demonstrated on both a synthetic, nanocomposite material and on a biocomposite. I have also demonstrated that, by taking serial sections of the specimen surface using the FIB, and imaging each cross-section with the AFM, we can build up three-dimensional mechanical information, to examine the mechanical behaviour of a volume, rather than just a surface.

References

1. Binnig, G., C.F. Quate, and C. Gerber, *Atomic force microscope.* Phys Rev Lett, 1986. **56**(9): p. 930-933.

2. Binnig, G. and H. Rohrer, *SCANNING TUNNELING MICROSCOPY.* Helvetica Physica Acta, 1982. **55**(6): p. 726-735.

3. Binnig, G., et al., *ATOMIC RESOLUTION WITH ATOMIC FORCE MICROSCOPE.* Surface Science, 1987. **189**: p. 1-6.

4. Marti, O., B. Drake, and P.K. Hansma, *ATOMIC FORCE MICROSCOPY OF LIQUID-COVERED SURFACES - ATOMIC RESOLUTION IMAGES.* Applied Physics Letters, 1987. **51**(7): p. 484-486.

5. Albrecht, T.R. and C.F. Quate, *ATOMIC RESOLUTION IMAGING OF A NONCONDUCTOR BY ATOMIC FORCE MICROSCOPY.* Journal of Applied Physics, 1987. **62**(7): p. 2599-2602.

6. Giessibl, F.J., *Atomic resolution of the silicon (111)-(7x7) surface by atomic force microscopy.* Science, 1995. **267**(5194): p. 68-71.

7. Kitamura, S. and M. Iwatsuki, *OBSERVATION OF 7X7 RECONSTRUCTED STRUCTURE ON THE SILICON (111) SURFACE USING ULTRAHIGH-VACUUM NONCONTACT ATOMIC-FORCE MICROSCOPY.* Japanese Journal of Applied Physics Part 2-Letters, 1995. **34**(1B): p. L145-L148.

8. Sugawara, Y., et al., *ATOMIC-RESOLUTION IMAGING OF ZNSSE(110) SURFACE WITH ULTRAHIGH-VACUUM ATOMIC-FORCE MICROSCOPE (UHV-AFM).* Japanese Journal of Applied Physics Part 2-Letters, 1995. **34**(4A): p. L462-L464.

9. Zhong, Q., et al., *FRACTURED POLYMER SILICA FIBER SURFACE STUDIED BY TAPPING MODE ATOMIC-FORCE MICROSCOPY.* Surface Science, 1993. **290**(1-2): p. L688-L692.

10. Bar, G., Y. Thomann, and M.H. Whangbo, *Characterization of the morphologies and nanostructures of blends of poly(styrene) block-poly(ethene-co-but-1-ene)-block-poly(styrene) with isotactic and atactic polypropylenes by tapping-mode atomic force microscopy.* Langmuir, 1998. **14**(5): p. 1219-1226.

11. Moller, C., et al., *Tapping-mode atomic force microscopy produces faithful high-resolution images of protein surfaces.* Biophysical Journal, 1999. **77**(2): p. 1150-1158.

12. San Paulo, A. and R. Garcia, *High-resolution imaging of antibodies by tapping-mode atomic force microscopy: Attractive and repulsive tip-sample interaction regimes.* Biophysical Journal, 2000. **78**(3): p. 1599-1605.

13. Anselmetti, D., et al., *ATTRACTIVE-MODE IMAGING OF BIOLOGICAL-MATERIALS WITH DYNAMIC FORCE MICROSCOPY.* Nanotechnology, 1994. **5**(2): p. 87-94.

14. Barber, A.H., S.R. Cohen, and H.D. Wagner, *Measurement of carbon nanotube-polymer interfacial strength.* Applied Physics Letters, 2003. **82**(23): p. 4140-4142.

15. Wang, W., S. Li, and A.H. Barber, *Mechanical Evaluation of Thermal Transitions in Polymer Nanofibres Using SPM*, in *Nanoscale Phenomena in Functional Materials by Scanning Probe Microscopy*, L. Degertekin, Editor. 2008.

16. Mate, C.M., et al., *ATOMIC-SCALE FRICTION OF A TUNGSTEN TIP ON A GRAPHITE SURFACE.* Physical Review Letters, 1987. **59**(17): p. 1942-1945.

17. Albrecht, T.R., et al., *FREQUENCY-MODULATION DETECTION USING HIGH-Q CANTILEVERS FOR ENHANCED FORCE MICROSCOPE SENSITIVITY.* Journal of Applied Physics, 1991. **69**(2): p. 668-673.

18. Maivald, P., et al., *Using force modulation to image surface elasticities with the atomic force microscope.* Nanotechnology, 1991. **2**(2): p. 103.

19. Magonov, S.N., et al., *Tapping-mode atomic force microscopy study of the near-surface composition of a styrene-butadiene-styrene triblock copolymer film.* Surface Science, 1997. **389**(1-3): p. 201-211.

20. Magonov, S.N., V. Elings, and M.H. Whangbo, *Phase imaging and stiffness in tapping-mode atomic force microscopy.* Surface Science, 1997. **375**(2-3): p. L385-L391.

21. Carpick, R.W. and M.A. Eriksson, *Measurements of in-plane material properties with scanning probe microscopy.* Mrs Bulletin, 2004. **29**(7): p. 472-477.

22. Marcus, M.S., et al., *Material anisotropy revealed by phase contrast in intermittent contact atomic force microscopy.* Physical Review Letters, 2002. **88**(22).

23. Marcus, M.S., et al., *In-plane contributions to phase contrast in intermittent contact atomic force microscopy.* Ultramicroscopy, 2003. **97**(1-4): p. 145-150.

24. Schroeder, J.B., S. Bashkin, and J.F. Nester, *Ionic polishing of optical surfaces.* Applied optics, 1966. **5**(6): p. 1031-4.

25. Abrahams, M.S., C.J. Buiocchi, and M.D. Coutts, *Improvements to the ALBA machine for thinning specimens for electron microscopy.* The Review of scientific instruments, 1968. **39**(12): p. 1944-5.

26. Abrahams, M.S. and C.J. Buiocchi, *CROSS-SECTIONAL SPECIMENS FOR TRANSMISSION ELECTRON-MICROSCOPY.* Journal of Applied Physics, 1974. **45**(8): p. 3315-3316.

27. Yoshida, K. and T. Yamada, *Ion Thinning Apparatus for the Preparation of Transmission Electron-Microscopy Specimens Using New-Type Ion Guns.* Review of Scientific Instruments, 1984. **55**(4): p. 551-557.

28. Escovitz, W.H., T.R. Fox, and R. Levisetti, *SCANNING-TRANSMISSION ION-MICROSCOPE WITH A FIELD-ION SOURCE.* Proceedings of the National Academy of Sciences of the United States of America, 1975. **72**(5): p. 1826-1828.

29. Orloff, J. and L.W. Swanson, *Fine-Focus Ion-Beams with Field-Ionization.* Journal of Vacuum Science & Technology, 1978. **15**(3): p. 845-848.

30. Orloff, J.H. and L.W. Swanson, *Study of a Field-Ionization Source for Microprobe Applications.* Journal of Vacuum Science & Technology, 1975. **12**(6): p. 1209-1213.

31. Seliger, R.L. and W.P. Fleming, *FOCUSED ION-BEAMS IN MICROFABRICATION.* Journal of Applied Physics, 1974. **45**(3): p. 1416-1422.

32. Chang, T.H.P., *Proximity Effect in Electron-Beam Lithography.* Journal of Vacuum Science & Technology, 1975. **12**(6): p. 1271-1275.

33. Parikh, M., *Self-Consistent Proximity Effect Correction Technique for Resist Exposure (Spectre).* Journal of Vacuum Science & Technology, 1978. **15**(3): p. 931-933.

34. Brown, W.L., T. Venkatesan, and A. Wagner, *Ion-Beam Lithography.* Nuclear Instruments & Methods in Physics Research, 1981. **191**(1-3): p. 157-168.

35. Orloff, J., *High-Resolution Focused Ion-Beams.* Review of Scientific Instruments, 1993. **64**(5): p. 1105-1130.

36. Namba, S., *Ion-Implantation in Semiconductor Processing.* Nuclear Instruments & Methods in Physics Research, 1981. **189**(1): p. 175-182.

37. Broers, A.N., *HIGH-RESOLUTION SYSTEMS FOR MICROFABRICATION.* Physics Today, 1979. **32**(11): p. 38-&.

38. Clampitt, R., K.L. Aitken, and D.K. Jefferies, *INTENSE FIELD-EMISSION ION-SOURCE OF LIQUID-METALS.* Journal of Vacuum Science & Technology, 1975. **12**(6): p. 1208-1208.

39. Giannuzzi, L.A. and F.A. Stevie, *A review of focused ion beam milling techniques for TEM specimen preparation.* Micron, 1999. **30**(3): p. 197-204.

40. Taylor, G., *Disintegration of Water Drops in an Electric Field.* Proceedings of the Royal Society of London. Series A, Mathematical and Physical Sciences, 1964. **280**(1382): p. 383-397.

41. Komuro, M. and H. Kawakatsu, *Field-Emission Liquid-Metal Ion-Source and Triode Ion Gun.* Journal of Applied Physics, 1981. **52**(4): p. 2642-2645.

42. Orloff, J. and L.W. Swanson, *Optical-Column Design with Liquid-Metal Ion Sources.* Journal of Vacuum Science & Technology, 1981. **19**(4): p. 1149-1152.

43. Krohn, V.E. and G.R. Ringo, *ION-SOURCE OF HIGH BRIGHTNESS USING LIQUID-METAL.* Applied Physics Letters, 1975. **27**(9): p. 479-481.

44. Ishitani, T., H. Tamura, and H. Todokoro, *Scanning Microbeam Using a Liquid-Metal Ion-Source.* Journal of Vacuum Science & Technology, 1982. **20**(1): p. 80-83.

45. Seliger, R.L., et al., *HIGH-INTENSITY SCANNING ION PROBE WITH SUBMICROMETER SPOT SIZE.* Applied Physics Letters, 1979. **34**(5): p. 310-312.

46. Gamo, K. and S. Namba, *RECENT ADVANCE OF FOCUSED ION-BEAM TECHNOLOGY IN MASKLESS DEPOSITION AND PATTERNING.* Nuclear Instruments & Methods in Physics Research Section B-Beam Interactions with Materials and Atoms, 1991. **59**: p. 190-196.

47. Swanson, L.W., *USE OF THE LIQUID-METAL ION-SOURCE FOR FOCUSED BEAM APPLICATIONS.* Applied Surface Science, 1994. **76**(1-4): p. 80-88.

48. *Quanta 3D FEG: Expand your boundaries for 3D nanocharacterization, prototyping and analysis*. [Datasheet] 2009; Available from: http://www.fei.com/uploadedFiles/DocumentsPrivate/Content/2007_02_Quanta_3D_FEG_Datasheet.pdf.

49. Wagner, A., et al., *Droplet Emission in Liquid-Metal Ion Sources.* Journal of Vacuum Science & Technology, 1981. **19**(4): p. 1186-1189.

50. Swanson, L.W., *Liquid-Metal Ion Sources - Mechanism and Applications.* Nuclear Instruments & Methods in Physics Research, 1983. **218**(1-3): p. 347-353.

51. Prewett, P.D., G.L.R. Mair, and S.P. Thompson, *Some Comments on the Mechanism of Emission from Liquid-Metal Ion Sources.* Journal of Physics D-Applied Physics, 1982. **15**(7): p. 1339-1348.

52. Clampitt, R., *Advances in Molten-Metal Field-Ion Sources.* Nuclear Instruments & Methods in Physics Research, 1981. **189**(1): p. 111-116.

53. Bell, A.E., et al., *A Low-Current Liquid-Metal Ion-Source.* Journal of Vacuum Science & Technology B, 1988. **6**(3): p. 927-930.

54. Swanson, L.W., G.A. Schwind, and A.E. Bell, *MEASUREMENT OF THE ENERGY-DISTRIBUTION OF A GALLIUM LIQUID-METAL ION-SOURCE.* Journal of Applied Physics, 1980. **51**(7): p. 3453-3455.

55. Galovich, C.S., *Effects of Backsputtered Material on Gallium Liquid-Metal Ion-Source Behavior.* Journal of Applied Physics, 1988. **63**(10): p. 4811-4818.

56. Galovich, C.S. and A. Wagner, *A New Method for Improving Gallium Liquid-Metal Ion-Source Stability.* Journal of Vacuum Science & Technology B, 1988. **6**(6): p. 2108-2111.

57. Swanson, L.W., et al., *Emission Characteristics of Gallium and Bismuth Liquid-Metal Field-Ion Sources.* Journal of Vacuum Science & Technology, 1979. **16**(6): p. 1864-1867.

58. Orloff, J., *Comparison of Optical Design Approaches for Use with Liquid-Metal Ion Sources.* Journal of Vacuum Science & Technology B, 1987. **5**(1): p. 175-177.

59. Narum, D.H. and R.F.W. Pease, *A Variable Energy Focused Ion-Beam System for Insitu Microfabrication.* Journal of Vacuum Science & Technology B, 1988. **6**(3): p. 966-973.

60. Narum, D.H. and R.F.W. Pease, *Applications of a Variable Energy Focused Ion-Beam System.* Journal of Vacuum Science & Technology B, 1988. **6**(6): p. 2115-2119.

61. Sugiyama, M. and G. Sigesato, *A review of focused ion beam technology and its applications in transmission electron microscopy.* Journal of Electron Microscopy, 2004. **53**(5): p. 527-536.

62. Briggs, D. and M.P. Seah, *Practical surface analysis*. 2nd ed. ed. 1990, Chichester: Wiley. 2 v.

63. Barofsky, D.F., et al., *Molecular Secondary Ion Mass-Spectrometry with a Liquid-Metal Ion Primary Source.* Analytical Chemistry, 1983. **55**(8): p. 1318-1323.

64. Kettle, S., et al., *FIB-SIMS analysis of micro-particle impacts on spacecraft materials returned from low-earth orbit.* Applied Surface Science, 2004. **231–232**(0): p. 893-898.

65. Maydell, E.A., H. Bolouri, and D.J. Fabian, *A SIMS instrument with electron and ion induced Auger electron detection.* Measurement Science and Technology, 1992. **3**(11): p. 1087.

66. Hudson, J.B., *Surface science : an introduction*. 1998, New York: John Wiley.

67. Giannuzzi, L.A. and F.A. Stevie, *Introduction to focused ion beams : instrumentation, theory, techniques, and practice*. 2004, New York: Springer.

68. Orloff, J., M.W. Utlaut, and L. Swanson, *High resolution focused ion beams : FIB and its applications : the physics of liquid metal ion sources and ion optics and their application to focused ion beam technology*. 2003, New York ; London: Kluwer Academic/Plenum.

69. Prewett, P.D. and G.L.R. Mair, *Focused ion beams from liquid metal ion sources*. 1991: Research Studies Press.

70. Harriott, L.R., et al., *Micromachining of Optical Structures with Focused Ion-Beams.* Journal of Vacuum Science & Technology B, 1987. **5**(1): p. 207-210.

71. Langford, R.M. and C. Clinton, *In situ lift-out using a FIB-SEM system.* Micron, 2004. **35**(7): p. 607-611.

72. Prenitzer, B.I., et al., *The influence of incident ion range on the efficiency of TEM and SEM specimen preparation by focused ion beam milling.* Electron Microscopy 1998, Vol 3, 1998: p. 711-712.

73. Prenitzer, B.I., et al., *Transmission electron microscope specimen preparation of Zn powders using the focused ion beam lift-out technique.* Metallurgical and Materials Transactions a-Physical Metallurgy and Materials Science, 1998. **29**(9): p. 2399-2406.

74. Singh, D.R.P., N. Chawla, and Y.L. Shen, *Focused Ion Beam (FIB) tomography of nanoindentation damage in nanoscale metal/ceramic multilayers.* Materials Characterization, 2010. **61**(4): p. 481-488.

75. Heymann, J.A.W., et al., *Site-specific 3D imaging of cells and tissues with a dual beam microscope.* Journal of Structural Biology, 2006. **155**(1): p. 63-73.

76. Kamino, T., et al., *Application of a FIB-STEM system for 3D observation of a resin-embedded yeast cell.* Journal of Electron Microscopy, 2004. **53**(5): p. 563-566.

77. Schroeder-Reiter, E., et al., *Focused ion beam (FIB) combined with high resolution scanning electron microscopy: A promising tool for 3D analysis of chromosome architecture.* Journal of Structural Biology, 2009. **165**(2): p. 97-106.

78. Lindhard, J. and M. Scharff, *Energy Dissipation by Ions in the kev Region.* Physical Review, 1961. **124**(1): p. 128-130.

79. Williams, J.S., *Materials Modification with Ion-Beams.* Reports on Progress in Physics, 1986. **49**(5): p. 491-587.

80. Prenitzer, B.I., et al., *The correlation between ion beam/material interactions and practical FIB specimen preparation.* Microscopy and Microanalysis, 2003. **9**(3): p. 216-236.

81. Kiener, D., et al., *FIB damage of Cu and possible consequences for miniaturized mechanical tests.* Materials Science and Engineering: A, 2007. **459**(1–2): p. 262-272.

82. Frey, L., C. Lehrer, and H. Ryssel, *Nanoscale effects in focused ion beam processing.* Applied Physics A: Materials Science & Processing, 2003. **76**(7): p. 1017-1023.

83. Pallecchi, I., et al., *Investigation of FIB irradiation damage in La0.7Sr0.3MnO3 thin films.* Journal of Magnetism and Magnetic Materials, 2008. **320**(13): p. 1945-1951.

84. Rubanov, S. and P.R. Munroe, *The effect of the gold sputter-coated films in minimising damage in FIB-produced TEM specimens.* Materials Letters, 2003. **57**(15): p. 2238-2241.

85. Koblischka-Veneva, A. and M.R. Koblischka, *Ion damage during preparation of nanostructures in magnetite by means of focused ion-beam (FIB) milling.* Superlattices and Microstructures, 2008. **44**(4–5): p. 468-475.

86. Rubanov, S. and A. Suvorova, *Ion implantation in diamond using 30 keV Ga+ focused ion beam.* Diamond and Related Materials, 2011. **20**(8): p. 1160-1164.

87. Brezna, W., et al., *Focussed ion beam induced damage in silicon studied by scanning capacitance microscopy.* Semiconductor Science and Technology, 2003. **18**(4): p. 195-198.

88. Kempshall, B.W., et al., *Comparative evaluation of protective coatings and focused ion beam chemical vapor deposition processes.* Journal of Vacuum Science & Technology B, 2002. **20**(1): p. 286-290.

89. Rubanov, S. and P.R. Munroe, *FIB-induced damage in silicon.* Journal of Microscopy-Oxford, 2004. **214**: p. 213-221.

90. Kolibal, M., et al., *Low energy focused ion beam milling of silicon and germanium nanostructures.* Nanotechnology, 2011. **22**(10).

91. Gamo, K., et al., *Defect Study in Gaas Bombarded by Low-Energy Focused Ion-Beams.* Journal of Vacuum Science & Technology B, 1988. **6**(6): p. 2124-2127.

92. Spoldi, G., et al., *Experimental observation of FIB induced lateral damage on silicon samples.* Microelectronic Engineering, 2009. **86**(4–6): p. 548-551.

93. Drobne, D., et al., *Surface damage induced by FIB milling and imaging of biological samples is controllable.* Microscopy Research and Technique, 2007. **70**(10): p. 895-903.

94. Dauphin, Y., et al., *Microstructure, nanostructure and composition of the shell of Concholepas concholepas (Gastropoda, Muricidae).* Aquatic Living Resources, 2003. **16**(2): p. 95-103.

95. Currey, J.D. and A.J. Kohn, *FRACTURE IN CROSSED-LAMELLAR STRUCTURE OF CONUS SHELLS.* Journal of Materials Science, 1976. **11**(9): p. 1615-1623.

96. Wise, S.W., *MICROARCHITECTURE AND DEPOSITION OF GASTROPOD NACRE.* Science, 1970. **167**(3924): p. 1486-&.

97. Levi-Kalisman, Y., et al., *Structure of the nacreous organic matrix of a bivalve mollusk shell examined in the hydrated state using Cryo-TEM.* Journal of Structural Biology, 2001. **135**(1): p. 8-17.

98. Dauphin, Y., *Structure and composition of the septal nacreous layer of Nautilus macromphalus L. (Mollusca, Cephalopoda).* Zoology, 2006. **109**(2): p. 85-95.

99. Sader, J.E., J.W.M. Chon, and P. Mulvaney, *Calibration of rectangular atomic force microscope cantilevers.* Review of Scientific Instruments, 1999. **70**(10): p. 3967-3969.

100. Garcia, R., et al., *Phase contrast in tapping-mode scanning force microscopy.* Applied Physics a-Materials Science & Processing, 1998. **66**: p. S309-S312.

101. Cleveland, J.P., et al., *Energy dissipation in tapping-mode atomic force microscopy.* Applied Physics Letters, 1998. **72**(20): p. 2613-2615.

102. D'Amato, M.J., et al., *Phase imaging and the lever-sample tilt angle in dynamic atomic force microscopy.* Applied Physics Letters, 2004. **85**(20): p. 4738-4740.

103. Behrend, O.P., et al., *Phase imaging: Deep or superficial?* Applied Physics Letters, 1999. **75**(17): p. 2551-2553.

104. Behrend, D., K.P. Schmitz, and A. Haubold, *Surface characterization of degraded biopolymers with AFM and SEM*. Electron Microscopy 1998, Vol 3: Materials Science 2, ed. H.A.C. Benavides and M.J. Yacaman. 1998. 209-210.

105. Briscoe, B.J., L. Fiori, and E. Pelillo, *Nano-indentation of polymeric surfaces.* Journal of Physics D-Applied Physics, 1998. **31**(19): p. 2395-2405.

106. Abdel-Salam, M.H., et al., *Structure and mechanical investigation of the effect of proton irradiation in Makrofol DE 7-2 polycarbonate.* Materials Chemistry and Physics, 2011. **127**(1-2): p. 305-309.

107. Gowa, T., et al., *Ion Beam Irradiation Effects on Resist Materials.* Journal of Photopolymer Science and Technology, 2010. **23**(3): p. 399-404.

108. Koizumi, H., et al., *Crosslinking of polymers in heavy ion tracks.* Nuclear Instruments & Methods in Physics Research Section B-Beam Interactions with Materials and Atoms, 2003. **208**: p. 161-165.

109. Oshima, A., et al., *Heavy ion beam induced phenomena in polytetrafluoroethylene.* Nuclear Instruments & Methods in Physics Research Section B-Beam Interactions with Materials and Atoms, 2007. **265**(1): p. 314-319.

110. Seki, S., et al., *Ion beam induced crosslinking reactions in poly(di-n-hexylsilane).* Journal of Physical Chemistry B, 1999. **103**(15): p. 3043-3048.

111. Brezna, W., et al., *Scanning capacitance microscopy investigations of focused ion beam damage in silicon.* Physica E-Low-Dimensional Systems & Nanostructures, 2003. **19**(1-2): p. 178-182.

112. Shannon, C.U., et al., *STEM analysis of FIB damage in silicon*, in *Microbeam Analysis 2000, Proceedings*, D.B. Williams and R. Shimizu, Editors. 2000. p. 177-178.

113. Derjaguin, B.V., V.M. Muller, and Y.P. Toporov, *EFFECT OF CONTACT DEFORMATIONS ON ADHESION OF PARTICLES.* Journal of Colloid and Interface Science, 1975. **53**(2): p. 314-326.

114. Darrigo, J.S., *Screening of Membrane Surface Charges by Divalent-Cations - Atomic Representation.* American Journal of Physiology, 1978. **235**(3): p. C109-C117.

115. Kopycinska-Muller, M., R.H. Geiss, and D.C. Hurley, *Contact mechanics and tip shape in AFM-based nanomechanical measurements.* Ultramicroscopy, 2006. **106**(6): p. 466-74.

116. Bykov, V., A. Gologanov, and V. Shevyakov, *Test structure for SPM tip shape deconvolution.* Applied Physics A, 1998. **66**(5): p. 499-502.

117. Sneddon, I.N., *The relation between load and penetration in the axisymmetric boussinesq problem for a punch of arbitrary profile.* International Journal of Engineering Science, 1965. **3**(1): p. 47-57.

118. Biagiotti, J., et al., *Mechanical properties of polypropylene matrix composites reinforced with natural fibers: A statistical approach.* Polymer Composites, 2004. **25**(1): p. 26-36.

119. Slomianka, L.

120. Bajaj, D., et al., *Age, dehydration and fatigue crack growth in dentin.* Biomaterials, 2006. **27**(11): p. 2507-2517.

121. Alekseev, A., et al., *Three-dimensional imaging of polymer materials by Scanning Probe Tomography*. European Polymer Journal, 2014. **52**: p.154-165.

Appendix

For clarity, references to sections of code will be highlighted through the use of a different font (e.g. `Display('Hello world')`). The complete script can be found in the appendix on page 196.

The script begins by defining a list of variables relating to the AFM setup and the sample mechanics. Reduced contact modulus (`K`), thickness of the near surface damping layer (`thickness`), lateral quality factor of the near surface damping layer (`Q_lat`), normal quality factor of the near surface damping layer (`Q_norm`), work of adhesion (`gamma`), equilibrium separation (`xi_0`), peak-to-peak free amplitude (`A_d`), cantilever drive frequency (`w_d`), cantilever spring constant (`k`), cantilever quality factor (`Q_cant`), radius of curvature of the AFM tip (`R`), initial velocity of the tip (`v_0`), start time for the calculation (`t_0`), sample tilt relative to the AFM stage (`sample_tilt`) and the number of oscillation periods to be modelled in the calculation (`NumberOfPeriods`) can all be user defined at the start of the script.

The initial parameters are then used by the MatLab script to calculate further additional values that are dependent upon these initial parameters. The angle of the AFM tip relative to the sample surface in Radians (`tip_angle`) is calculated from the user-defined `sample_tilt` and an offset due to the tilt of the AFM chip within the AFM head:

```
tip_angle = (sample_tilt + 15) * (pi/180);
```

The length of a period of AFM cantilever oscillation in seconds (**T**) is calculated from the cantilever drive frequency:

```
T = 2*pi/w_d;
```

The total calculation time over which the AFM cantilever oscillation will be modelled (**t_f**) is calculated as:

```
t_f = NumberOfPeriods*T;
```

and the Hamaker constant (**H**) is calculated as defined in Equation 13 using:

```
H = 12*pi*gamma*xi_0*xi_0;
```

The free amplitude of oscillation (**amplitude**), which is measured as the semi-amplitude, is initially given an arbitrary value, as is the initial displacement of the AFM tip (**d_0**). **amplitude** is updated with each cycle of the differential equation solver, but is used as a terminating condition for a **while** loop that calls the solver so therefore requires an initial value.

The ordinary differential equation solver (**ODE113**) is contained within a **while** loop, which reduces the value of **z_0** until the desired value of **amplitude** is reached.

```
While abs(amplitude-(A_d/4)) > 0.5E-10
        …(Body of code)

        Z_0 = z_0 + 0.1E-9;
        end
```

In this case the terminating condition for the **while** loop is when the value assigned to **amplitude**, which is updated by the solver after each calculation, is within 0.5 Å of the value **A_d/4**, which is 25 % of the peak-to-peak free amplitude or 50 % of the free amplitude. At the end of the loop the value of **z_0** is increased by 1 Å, thereby reducing the separation of the cantilever base and the sample within the simulation.

The solver (**ODE113**) is called within the loop to solve the function **DMT_Spring** with inputs of start and end time (**t_0, t_f**) and the initial displacement (**d_0**) and velocity (**v_0**) of the tip, and lists outputs of time (**t**) and displacement (**d**)

DMT_Spring is defined as a subfunction within the script by the following code:

```
function pprime = DMT_Spring(t,p)
global A_d w_d k Q_cant z_0;

z = z_0 + A_d/(2*Q_cant)*sin(w_d*t);
zprime = A_d/(2*Q_cant)*(w_d)*cos(w_d*t);
flag = DMT_Flag(p(1));
pprime = nan*ones(2,1);
pprime(1) = p(2);
pprime(2) = -w_d/Q_cant*(p(2)-zprime)-w_d^2*(p(1)-z)
+(w_d^2)/k*DMT_Force(p(1),flag)
+Near_Surface_Normal_Damping(p(1),p(2))
+Near_Surface_Lateral_Damping(p(1),p(2));
```

The function definition requires inputs of time (**t**) and a position vector (**p**) and outputs the vector **pprime**, which contains the velocity and acceleration of the tip. The function first defines the position of the cantilever base as a function of time; a sine wave with an amplitude of **A_d/(2*Q_cant)**, frequency **w_d** and an offset of **z_0** as stated at the beginning of the script. Then the velocity of the cantilever base is defined by taking the derivative of the position.

The variable **flag** is defined using the subfunction **DMT_Flag**, which calculates whether or not the AFM tip is in contact with the sample surface. As the surface is defined as being at 0 nm, with negative values of z being above the surface and positive values within the surface, **DMT_Flag** will assign a value of 1 to **flag** if the position of the tip (**p**) is greater than or equal to 0 and therefore in contact. If **p** is not greater than or equal to 0 and therefore not in contact, then **flag** is assigned the value 0.

pprime is initialised as a (2x1) column vector and then **pprime(1)** is assigned the value of **p(2)**

i.e. the initial velocity of the tip. **pprime(2)** is calculated from a rearrangement of Equation

16 with reference to 3 more subfunctions; **DMT_Force**, **Near_Surface_Normal_Damping** and **Near_Surface_Lateral_Damping**.

DMT_Force is defined by the following code:

```
function out = DMT_Force(p, flag)
global K w_d k R gamma H xi_0 tip_angle;

if(~flag)
out = (H*R*cos(tip_angle))/(6*(((p(1)
*cos(tip_angle))-xi_0)^2));
return;

else
out = -cos(tip_angle)*((K*sqrt(R)*p.^(3/2)
*cos(tip_angle)^(3/2))-(2*pi*gamma*R));
return;

end
```

If the AFM tip is not in contact with the surface and the variable **flag** therefore has a value of 0, then the output of **DMT_Force** is the out-of-contact van der Waals force. If, however, the tip is in contact with the surface then **flag** will have a value of 1 and the output of **DMT_Force** will be the non-linear DMT contact interaction, which is dependent on tip angle, tip radius, position raised to the power 3/2 and the reduced contact modulus between the tip and the sample.

The function **Near_Surface_Normal_Damping** is defined by the following code:

```
function out = Near_Surface_Normal_Damping( p, v )
global w_d Q_norm tip_angle thickness;

if (p*cos(tip_angle) > -thickness && p*cos(tip_angle) < 0)
out = -(w_d/Q_norm)*v*cos(tip_angle)^2;
return;

else
out = 0;
return;

end
```

This function outputs the near surface normal damping term to the equation of motion if the tip is above the surface, but still within the thickness of the near surface damping layer. The

code for the function **Near_Surface_Lateral_Damping** is almost the same as that of **Near_Surface_Normal_Damping**, except that **Near_Surface_Lateral_Damping** will output the lateral damping term for the AFM tip in contact with the sample surface.

All of the terms of the equation of motion defined as subfunctions are subsequently used by the ODE113 solver to output values of time (t) and displacement (d) and return control to the parent script.

As the initial part of the simulated motion of the cantilever will include a period of instability before reaching equilibrium the script calls for two new datasets to be created called **t_interpolated** and **d_interpolated**, which consist of an interpolation of the last 200 periods of the AFM cantilever oscillation. Using these interpolated datasets, the script extracts the phase of the cantilever using the subfunctions **phaseFinder_FFT** and **Fourier_Transform**, which are defined as:

```
function tip_phase = phaseFinder_FFT(t,y,f)
[freq,phi] = Fourier_Transform(t,y);
[min_val,position] = min(abs(freq-f));
tip_phase = phi(position);
```

and:

```
function [f,tip_phase] = Fourier_Transform(t,y)
t = t - min(t);
sampling_f = 1/(t(2)-t(1))
N = length(y);
y = fft(y,N)
f = sampling_f*(0:floor(N/2))/N;
tip_phase = (180/pi)*(angle(y((1:floor(N/2)+1))));
```

phaseFinder_FFT immediately calls **Fourier_Transform**, which normalises the data so that the inbuilt function **fft** can be used to calculate a new dataset containing a list of frequencies and corresponding phase shifts. The new frequency and phase dataset is output back into **phaseFinder_FFT** as the lists **[freq, phi]**. **phaseFinder_FFT** then outputs the phase that corresponds to the frequency closest to the drive frequency of the AFM cantilever. The amplitude of the cantilever oscillation is then calculated by finding the

maximum and minimum values in the interpolated position data, which gives the peak-to-peak amplitude, and dividing the difference by 2 to find the semi-amplitude (**amplitude**).

```
[max_data, index] = max(d_interpolated);
[min_data, index] = min(d_interpolated);
amplitude = abs(max_data - min_data)/2;
```

The script calculates values of sample compression under the AFM tip and penetration of the AFM tip through the near surface damping layer based on the amplitude of the AFM cantilever and maximum displacement of the AFM tip, updates the value of **z_0** and creates logs of the AFM cantilever phase and amplitude. These logs are written to files as the final script output.

```
compression = amplitude - abs(z_0);
penetration = thickness + max_data;
z_0 = z_0 + 0.1E-9
```

As stated above, the calculated value of **amplitude** is used in the terminating condition for the **while** loop, and will allow the calculation to repeat, with the position of the cantilever base stepping towards the surface, until the value of **amplitude** falls within the desired range.

6.6 Methodology and Results

6.6.1 Modifications to the model/code

The Matlab script as supplied by D'Amato et al was first adapted in order to meet the requirements of this investigation. Originally, the script would use a single set of starting conditions and output a single phase value for a particular AFM cantilever and sample setup. The simulation was initially evaluated by modifying the **while** loop around the ODE solver to simulate either a feedback landing of the AFM tip, or a Z-spectroscopy approach curve by solving the equations of motion for a range of values of z. Also, **for** loops have been added

around the **while** loop so that the calculations can be repeated while the script steps through values of various parameters, e.g.

```
for thickness = 2E-10:2E-10:2E-9
```

will cause the script to run through the **while** loop for each value of **thickness** in the range from 2 Å to 2 nm with an interval of 2 Å.

The feedback landing version of the **while** loop allows the cantilever base to quickly approach the sample until the value of amplitude reaches the desired setpoint. The first variation in this piece of code is that the starting value of **z_0** is not defined as a point far from the surface, as was the case in previous versions of the script. Instead, the value assigned to **z_0** at the beginning of the loop is dependent on the free peak-to-peak amplitude of the cantilever, **A_d**, and the value assigned to the variable **setpoint**, which has been created for this purpose.

```
Z_0 = -A_d * setpoint * 0.5;
```

If the desired end point for the calculation is a setpoint amplitude that is 50 % of the free amplitude, then the value of 0.5 would be assigned to **setpoint**. For an infinitely stiff sample, it is reasonable to assume that the amplitude of the cantilever is equal to the separation of the cantilever base and the sample, i.e. an amplitude of 100 nm would occur at a separation of 100 nm, assuming that the separation is not greater than the free amplitude. It is for this reason that the script sets the initial separation at this predicted value; for stiff samples this initial value will be close to the desired setpoint condition and for softer samples the separation will need to be reduced further as the surface will be deformed by the AFM tip and result in the amplitude of the AFM cantilever oscillation being greater than the setpoint value.

The **while** loop uses the deviation of **amplitude** from the desired setpoint value as the terminating condition and varies the value of **z_0** using a proportional feedback term.

```
while abs(amplitude-((A_d/2) * setpoint)) > 5E-11
```

…(body of code)

```
Z_0 = z_0 * (((A_d/2) * setpoint)/amplitude);
```

This version of the **`while`** loop allows us to observe the effect an experimental parameter, such as the modulus of the sample, has on the cantilever dynamics at a specific setpoint condition by adjusting the step size proportionally to the deviation from the equilibrium condition rather than the gradual approach implemented in the original code. The script will then output the phase, amplitude etc. of this final setpoint condition only before moving to the next value in the **`for`** loop.

Initial attempts to use this feedback loop resulted in the separation overshooting the setpoint and then snapping back, never reaching the setpoint amplitude. Upon outputting and plotting the displacement/time data from the solver, and thereby visualising the complete series of oscillations, it became apparent that this overshooting was due to several factors. Firstly, the amplitude of the cantilever oscillation was found to oscillate, especially for softer samples. To combat this fluctuation in AFM cantilever oscillation amplitude, the error tolerances for the ODE solver were tightened, and the maximum step size was reduced from 50 ns to 5 ns, which effectively allowed the solver more time to react to the rapidly changing forces when the AFM tip moved in and out of contact with the sample surface. The problem of the oscillating amplitude had been further compounded by the method by which the amplitude was being calculated. The original code, as described earlier, would simply divide the difference between the highest and lowest position of the tip by 2 and assign this value to **`amplitude`**. This original method for calculating **`amplitude`** meant that any instability or fluctuation in the oscillation of the cantilever would result in an artificially high AFM cantilever amplitude value, and this in turn would cause the feedback loop to overshoot. The method of calculating amplitude was therefore updated to the following code:

```
for period_index = 200:-1:0
period_t = linspace(t_f-((period_index+1)*T),t_f-
```

```
(period_index*T),500);
period_d = interp1(t,d(:,1),period_t);
max_log = [max_log; max(period_d)];
min_log = [min_log; min(period_d)];

end

amplitude = abs(mean(max_log) - mean(min_log))/2;
```

This loop separates each of the last 200 periods of the oscillation and interpolates the data for each period before finding the maximum and minimum data point and adding them to a log for each value (**`max_log`** and **`min_log`**). These minimum and maximum value lists are then averaged, and it is the mean values of the minimum and maximum that are used to calculate the amplitude of oscillation.

Plotting the full series of oscillations also made it apparent that the arbitrary starting conditions of the cantilever (**`d_0`** and **`v_0`**) were out of phase with the base of the cantilever. This meant that the initial 20-30 % of the oscillations for each cycle through the **`while`** loop were being used as the cantilever phase inverted through 180°. To rectify this, the initial values of **`d_0`** and **`v_0`** were defined as though at the peak of an oscillation. **`v_0`** was therefore defined as 0 and **`d_0`** as **`z_0 - amplitude`**. The alterations to solver tolerances, the calculation of amplitude and the starting conditions of the cantilever have resulted in the cantilever oscillations reaching a stable amplitude, and doing so more rapidly in terms of the number of oscillations (although the calculation times have increased) to ensure a more realistic feedback loop.

The z-spectroscopy loop is simpler than the feedback loop as it steps through values of **`z_0`** until reaching the predefined **`z_0`** stop point.

```
while z_0 < 1E-9

        …(body of code)

        z_0 = z_0 + 1E9

end
```

This `while` loop is similar to the original implemented by D'Amato *et al*.[102] except that the terminating condition is independent of the value of amplitude and the loop will continue until it reaches the defined separation (in this case 0 nm). The script keeps a log of `phase`, `amplitude`, `z_0`, `penetration` and `compression`, which will be output at the end of the calculations, thus allowing complete AFM tip-sample approach curves to be plotted. These new Z-spectroscopy capabilities of the code compare the phase response of the simulation as a function of tip-sample separation to AFM experimental data. Thus, comparison of the simulation with the experimental data was used to validate if the simulation was providing meaningful values of AFM cantilever amplitude and phase.

A number of problems were encountered when providing comparison of the simulation to the experimental data. Several variables, as discussed in detail below, within the model are not easily measured physically and have values set arbitrarily for subsequent tuning in order for the simulated data to match the experimental. Secondly, whilst working through the MatLab code, a significant inconsistency between the code and the equation of motion presented by D'Amato *et al* for the repulsive term was found. In the paper, the $\frac{\omega_0^2}{k}$ term was noticeably omitted and, as the term has a value in the order of 4×10^{10}, consequently impacted the magnitude of the repulsive force significantly. The equation of motion therefore was modified as highlighted below:

$$\ddot{p} + \frac{\omega_0}{Q_{cant}}\left(\dot{p} - \dot{\zeta}\right) + \omega_0^2 (p - \zeta)$$

$$= \begin{cases} \frac{\omega_0^2}{k}\left(\frac{AR\cos\psi}{6(p\cos\psi - \xi_0)^2}\right) & p \geq 0.5\text{ nm} \\ \frac{\omega_0^2}{k}\left(\frac{AR\cos\psi}{6(p\cos\psi - \xi_0)^2}\right) - \frac{\omega_0}{Q_{norm}}\dot{p}\cos^2\psi - \frac{\omega_0}{Q_{lat}}\dot{p}\sin^2\psi & 0 < p < 0.5\text{ nm} \\ -\frac{\omega_0^2}{k}\left(K\sqrt{R}p^{3/2}\cos^{3/2}\psi - 2\pi\gamma R\right)\cos\psi & p \leq 0\text{ nm} \end{cases}$$

MatLab code for simulating AFM cantilever dynamics and calculating phase lag

```
% DMT Model Simulation by Russell Bailey 27/10/2011
%
% Simulates AFM tip motion based on DMT contact mechanics and
% extracts the phase shift.

function DMT_Bailey
% Solves the 2nd differential for the equation of motion of an AFM
% cantilever based on DMT mechanics and extracts the phase shift
global K Q_lat Q_norm A_d w_d k Q_cant z_0 R T NumberOfPeriods gamma H xi_0 tip_angle sample_tilt
thickness; % List of global variables

file_counter = 1;
K = 121.47E9;                       % the reduced contact modulus
thickness = 12E-10;               % thickness of the near surface damping layer
Q_lat = 0.12;                      % lateral quality factor - in-plane damping near the surface
Q_norm = 14.0;                     % normal quality factor - out-of-plane damping near the surface
gamma = 0.15;                   % work of adhesion (J/m^2)
xi_0 = 1.65E-10;                  % equilibrium separation
% A_d = 510E-9;                     % peak-to-peak free amplitude (m)
A_d = 250E-9;
% w_d = 2*pi*183.5E3;               % drive frequency (radians * Hertz)
w_d = 2*pi*180.63E3;
k = 29.57;                        % cantilever spring constant (N/m)
% k = 40
Q_cant = 300;                     % cantilever quality factor
R = 20E-9;                        % radius of curvature of tip (m)
v_0 = 0;                          % initial velocity of tip (m/s)
t_0 = 0;                          % start time (s)
sample_tilt = 0;                % sample tilt relative to stage
amplitude = A_d/2;                % arbitrary free amplitude
d_0 = z_0 - amplitude;            % initial displacement of tip (m) (negative values are above the surface)
setpoint = 0.25;                   % amplitude set-point ratio
compression = 0;
```

```
penetration = 0;
tip_phase = 0;
phase_log = [];
amplitude_log = [];
K_log = [];
xi_log = [];
R_log = [];
tilt_log = [];
k_log = [];
gamma_log = [];
Q_lat_log = [];
Q_norm_log = [];
Q_cant_log = [];
thickness_log = [];
data_log = [];
A_d_log = [];

T = 2*pi/w_d;                                                                  % convert frequency
to period (s)
NumberOfPeriods = 500;                                                        % number of periods
per calculation
t_f = NumberOfPeriods*T;                                                       % the total time of
the calculation
H = 12*pi*gamma*xi_0*xi_0;                                                     % the Hamaker
constant
abstol = 1E-12; reltol = 1E-6; step = 5E-9;                                    % error tolerances
for the ODE solver

options = odeset('Refine',1,'RelTol',reltol,'AbsTol',abstol,'MaxStep',step);   % set preferences
in ODE solver
% for K = 63E9:25E9:88E9;

for index_1 = 0:1:3
    for index_2 = 1:1:4
        K = 1E9 * index_2 * 5^index_1;
% for R = 5E-9:5E-9:20E-9
% for xi_0 = 5E-11:5E-11:4E-10
```

```
% for Q_lat = 0.02:0.18:0.2
% for Q_norm = 2:18:20
% for sample_tilt = -6:3:9
% for gamma = 0.02:0.02:0.2
% for thickness = 5E-10:15E-10:20E-10
    tip_angle = (sample_tilt + 11)*(pi/180);                                        % tip angle
relative to sample
    z_0 = -A_d * setpoint * 0.5;
    amplitude = A_d * setpoint * 0.5 + 2E-10;
    z_log = [];

while abs(amplitude-((A_d/2) * setpoint)) > 5E-11                   % loop until within 0.5 Angstroms of a
set-point

    fprintf('K = ')
    fprintf('%g', K/1E9)
    fprintf('\n')
    fprintf('z = ')
    fprintf('%g', z_0*1E9)
    fprintf('\n')

    d_0 = z_0 - amplitude;

    [t,d] = ode113(@DMT_Spring,[t_0,t_f],[d_0,v_0],options);                    % solve DMT_Spring
ODE
    t_interpolated = linspace(t_f-(200*T),t_f,100000);                          % interpolate time
points
    d_interpolated = interp1(t,d(:,1),t_interpolated);                          % interpolate
position points
    tip_phase = phaseFinder_FFT(t_interpolated, d_interpolated,w_d/(2*pi));
    max_log = [];
    min_log = [];

    for period_index = 200:-1:0
        period_t = linspace(t_f-((period_index+1)*T),t_f-(period_index*T),500);
        period_d = interp1(t,d(:,1),period_t);
        max_log = [max_log; max(period_d)];
```

```
        min_log = [min_log; min(period_d)];
    end

    amplitude = abs(mean(max_log) - mean(min_log))/2;
    compression = amplitude - abs(z_0);
    penetration = thickness + mean(max_log);

    fprintf('amplitude = ')
    fprintf('%g', amplitude*1E9)
    fprintf('\n\n\n')

    z_log = [z_log; (z_0*1E9)];

    figure(1)
    plot(t,d(:,1))
    xlabel('Time (s)')
    ylabel('Position (m)')
    drawnow

    z_0 = z_0 * (((A_d/2) * setpoint)/amplitude);
%     display(K)
%     if abs(amplitude - ((A_d/2) * setpoint)) > 5E-10
%         display('Amplitude too high: proportional approach')
%         z_0 = z_0 * (((A_d/2) * setpoint)/amplitude)
% %         z_0 = z_0 + 5E-9
%     else if amplitude < ((A_d/2) * setpoint)
%         display('Amplitude too low: Step back')
%         z_0 = z_0 - 1E-11
%         else
%         display('Amplitude too high: Step approach')
%         z_0 = z_0 + 1E-10
%         end
    end
%     data_log_1 =[];
%     for i = 1:length(t)
%         data_log_1 = [data_log_1; t(i), d(i)];
%     end
```

```
%     data_log_1 = data_log_1';
%     cl = fix(clock);
%     cl(1) = 12;
%     cl_trunc = [num2str(cl(1)) '_' num2str(cl(2)) '_' num2str(cl(3)) '_' num2str(cl(4)) '_'
num2str(cl(5))];
%     filename_1 = ['DMT_K' num2str(K/1E9) '_' cl_trunc '_' num2str(file_counter) '.csv'];
%     output_1 = fopen(filename_1, 'w+t');
%     fprintf(output_1, '# t              d \n');
%     fprintf(output_1, '  %15.13f,%15.13f \n', data_log_1);
%     fclose(output_1);
%     file_counter = file_counter + 1;
% end
amplitude_log = [amplitude_log;(amplitude*1E9)];
K_log = [K_log;K];
xi_log = [xi_log;xi_0];
R_log = [R_log;R];
tilt_log = [tilt_log; sample_tilt];
k_log = [k_log;k];
gamma_log = [gamma_log;gamma];
Q_lat_log = [Q_lat_log;Q_lat];
Q_norm_log = [Q_norm_log;Q_norm];
Q_cant_log = [Q_cant_log;Q_cant];
thickness_log = [thickness_log;thickness];
phase_log = [phase_log;tip_phase];
A_d_log = [A_d_log;A_d];
    end
end
for i = 1:length(phase_log)
    data_log = [data_log; K_log(i), xi_log(i), R_log(i), tilt_log(i), k_log(i), gamma_log(i), Q_lat_log(i),
Q_norm_log(i), Q_cant_log(i), thickness_log(i), A_d_log(i), phase_log(i)];
end

data_log = data_log';
c = fix(clock);
filename = ['DMT_output_' num2str(c(1)) '_' num2str(c(2)) '_' num2str(c(3)) '_' num2str(c(4)) '_'
num2str(c(5)) '_T_' num2str(thickness * 1E10) '.csv'];
output = fopen(filename, 'w+t');
```

```
fprintf(output, '# Output from Bailey_DMT\n');
fprintf(output, '# ~~~~~~~~~~~~~~~~~~~~~~\n');
fprintf(output, 'K,xi_0,R,tilt,k,gamma,Q_lat,Q_norm,Q_cant,thickness,A_d,Phase\n');
fprintf(output, '%6.4G,%6.4G,%6.4G,%6.4G,%6.4G,%6.4G,%6.4G,%6.4G,%6.4G,%6.4G,%6.4G,%6.6f\n', data_log);
fclose(output);

end
%%%%%%%%%%%%%%%%%%%%%%%%%%%%%%%%%%%%%%%%%%%%%%%%%%%%%%%%%%%%%%%%%%%%%%%%%%%%%%%%%%%%%%%%%%%%%%%%%%%%%%%%%%%%
%%%%%%%%%%%%%%%%%%%%%%
% SUBFUNCTION: DMT_Spring ---------------------------------------------------------------------------------
-------------------
function pprime = DMT_Spring(t,p)                                   % define function called "HertzSpring"
with inputs t and p
global A_d w_d k Q_cant z_0;                                        % global variables in this subfunction

z = z_0 + A_d/(2*Q_cant)*sin(w_d*t);                                % position of cantilever base as a
function of time (sinusoidally driven)
zprime = A_d/(2*Q_cant)*(w_d)*cos(w_d*t);                           % velocity of cantilever base as a
function of time (derivative of position)

flag = DMT_Flag( p(1) );                                            % set flag to be either 1 or 0
depending on sign of displacement of tip, p(1)

pprime = nan*ones(2,1);                                             % p' = "not-a-number"*  ; ones(2,1)
returns a 2x1 matrix of "1"s
pprime(1) = p(2);                                                   % p'(1) = p(2) ;  p(2) is the initial
velocity of the tip (pdot)
                                                                    % this is Matlab's method of writing a
2nd order ODE in terms of 1st order ODEs so it can integrate
pprime(2) = -w_d/Q_cant*( p(2)-zprime ) -w_d^2*( p(1)-z ) + (w_d^2)/k*DMT_Force( p(1) , flag ) +
Near_Surface_Normal_Damping( p(1) , p(2)) + Near_Surface_Lateral_Damping( p(1), p(2));
end
% SUBFUNCTION:  DMT_Flag -----------------------------------------------------------------------------------
--------------------
function flag_val = DMT_Flag( p )                                   % function called "Hertz_Flag" which
takes an input, p, p(1) = d_0 = displacement of tip
```

```
                                                                    %  i.e. Is tip in or out of contact
with the surface?
if( p >= 0)                                                         % if tip is IN CONTACT with the
surface, set flag_val = 1
   flag_val = 1;
   return;                                                          % quit
else
   flag_val = 0;                                                    % if tip is NOT IN CONTACT with the
surface, set flag_val = 0
end
end
% SUBFUNCTION: DMT_Force ----------------------------------------------------------------------------
---------------------
function out = DMT_Force(p, flag)                                   % takes initial position of tip (d_0),
or p(1),
                                                                    % and outputs the DMT_Force interaction
value if tip is in contact with sample
global K R gamma H xi_0 tip_angle;                                  % global variables in this subfunction

if(~flag)
   out = ((H*R)/(6*((p(1)-xi_0)^2)))*cos(tip_angle);                         % van der Waals, out of
contact
   return;
else
   out = -cos(tip_angle)*((K*sqrt(R)*(p.^(3/2))) - (4*pi*gamma*R));   % the non-linear DMT contact
interaction, depends on tip angle, tip radius,
   return;                                                          % position of tip (to the 3/2 power),
and material (reduced modulus)
end
end                                                                 % .^ refers to raising an array to some
power (p to the 3/2)
% SUBFUNCTION: Near_Surface_Normal_Damping ------------------------------------------------------------
---------------------------------
function out = Near_Surface_Normal_Damping( p, v )                  % takes in position and velocity of tip
(as p and v)
global w_d Q_norm tip_angle thickness;                              % global variables used in this
function
```

```
if( p*cos(tip_angle) > -thickness && p*cos(tip_angle) < 0 )         % if tip is within x nm of the surface,
non-contact...
    out = -(w_d/Q_norm)*v*cos(tip_angle)^2;
    return;
else
    out = 0;
    return;
end
end
% SUBFUNCTION: Near_Surface_Lateral_Damping -----------------------------------------------------------
---------------------------------
function out = Near_Surface_Lateral_Damping( p, v )                 % takes in position and velocity of tip
(as p and v)
global w_d Q_lat tip_angle thickness;                               % global variables used in this
function

if( p*cos(tip_angle) > -thickness && p*cos(tip_angle) < 0 )         % if tip is within x nm of the surface
    out = -(w_d/Q_lat)*v*sin(tip_angle)^2;
    return;
else
    out = 0;
    return;
end
end
% SUBFUNCTION: phaseFinder_FFT ------------------------------------------------------------------------
----------------------
function tip_phase = phaseFinder_FFT(t,y,f)                         % Function finds the phase at frequency
f
[freq,phi] = Fourier_Transform(t,y);                                % call FourierTransform and perform it
on (t,y)
[min_val,position] = min(abs(freq-f));                              % find minimum frequency? (and the
index of that value)
tip_phase = phi(position);                                          % get the phase at this index
tip_phase = (tip_phase*-1)-90;
if tip_phase < 0
    tip_phase = tip_phase + 360;
```

```
end
end

% SUBFUNCTION: Fourier_Transform ---------------------------------------------------------------------------
----------------------
function [f,tip_phase] = Fourier_Transform(t,y)                       % performs Fourier Transform on the 
data (t,y), outputs f, Y, and phase
t = t - min(t);                                                       % get deviation of each time from the 
minimum time
sampling_f = 1/(t(2)-t(1));                                           % get 1 over delta(t), something like a 
step-size (sampling)
N = length(y);                                                        % get the length of the data set
y = fft(y,N);                                                         % returns the N-point discrete Fourier 
transform on data (y)
f = sampling_f*(0:floor(N/2))/N;                                      % get the frequency?
tip_phase = (180/pi)*(angle(y((1:floor(N/2)+1))));                    % computes phase angle of y (the result 
of fft'ing the data)
end
```

7 Python code for calculating Force/Displacement and moduli from AFM deflection/distance data

```
# Deflection vs distance data converter

# Created by Russell Bailey 01/08/2012

# Reads exported ASCII file and converts data to Force vs displacement

# ASCII file should be exported from nova as a table including headers and including scales and bias


from tkinter import *

from tkinter import filedialog

import time, math


global cali_x, cali_y, data_x, data_y


## setup GUI ##

class Application:

    def_init_(self, master):

        frame = Frame(master)

        frame.pack()

        Label(frame,

            text = 'Enter experimental parameters: '
```

```
    ).grid(row = 0, column = 0, columnspan = 2, sticky = W)
Label(frame,
    text = 'Select calibration file: '
    ).grid(row = 1, column = 0, sticky = E)
Label(frame,
    text = 'Select data file: '
    ).grid(row = 2, column = 0, sticky = E)
Label(frame,
    text = 'Cantilever spring constant: '
    ).grid(row = 3, column = 0, sticky = E)
Label(frame,
    text = 'N/m'
    ).grid(row = 3, column = 1)
Label(frame,
    text = 'Half tip angle: '
    ).grid(row = 4, column = 0, sticky = E)
Label(frame,
    text = '      degrees'
    ).grid(row = 4, column = 1)
self.cali_load = Button(frame, text = "Open", width = 18, command = self.load_cali)
```

```
    self.cali_load.grid(row = 1, column = 1, sticky = W)
    self.data_load = Button(frame, text = "Open", width = 18, command = self.load_data)
    self.data_load.grid(row = 2, column = 1, sticky = W)
    self.k_value = Entry(frame, width = 8)
    self.k_value.grid(row = 3, column = 1, sticky = W, pady = 5)
    self.theta_value = Entry(frame, width = 8)
    self.theta_value.grid(row = 4, column = 1, sticky = W, pady = 5)
    self.status_txt = Text(frame, width = 33, height = 7, wrap = WORD)
    self.status_txt.grid(row = 5, column = 0, columnspan = 2, pady = 5)
    text = 'Please select calibration and data files.\n\nPlease enter a values for k and theta.'
    self.status_txt.insert(0.0, text)
    self.cali_filename = False
    self.data_filename = False
    self.quit_button = Button(frame, text = "QUIT", width = 18, bg = "red", fg = "white", command = root.destroy)
    self.quit_button.grid(row = 6, column = 0, columnspan = 1, pady = 3, padx = 3)
    self.program_go = Button(frame, text = "Go!", width = 18, bg = "green", fg = "black", command = self.run_program)
    self.program_go.grid(row = 6, column = 1, columnspan = 1, pady = 3, padx = 3)
def load_cali(self):
    self.cali_filename = filedialog.askopenfilename(filetypes = (("Text files", "*.txt"), ("CSV files", "*.csv")))
    if self.cali_filename == '' or self.cali_filename == False:
```

```
            return
        elif self.data_filename != False and self.data_filename != '':
            text = 'Calibration and data files selected'
        else:
            text = 'Calibration file selected. Please select a data file.'
        self.status_txt.delete(0.0, END)
        self.status_txt.insert(0.0, text)
    def load_data(self):
        self.data_filename = filedialog.askopenfilename(filetypes = (("Text files", "*.txt"), ("CSV files", "*.csv")))
        if self.data_filename == '' or self.data_filename == False:
            return
        elif self.cali_filename != False and self.cali_filename != '':
            text = 'Calibration and data files selected'
        else:
            text = 'Data file selected. Please select a calibration file.'
        self.status_txt.delete(0.0, END)
        self.status_txt.insert(0.0, text)
    def run_program(self):

        ## Check inputs are valid ##
```

```
try:
    k = float(self.k_value.get())
    print('Spring constant of cantilever (N/m): ')
    print(k)
    try:
        theta = float(self.theta_value.get())
        print('Half tip angle (degrees): ')
        print(theta)
        if self.cali_filename == False or self.cali_filename == '':
            if self.data_filename == False or self.data_filename == '':
                text = 'Please select calibration and data files.'
            else:
                text = 'Please select a calibration file.'
        elif self.data_filename == False or self.data_filename == '':
            text = 'Please select a data file.'
        else:
            text = None
        if text != None:
            self.status_txt.delete(0.0, END)
            self.status_txt.insert(0.0, text)
```

```
  except:
    if self.cali_filename == False or self.cali_filename == '':
      if self.data_filename == False or self.data_filename == '':
        text = 'Please select calibration and data files.\n\nPlease enter a value for theta. (theta must be a real number)'
      else:
        text = 'Please select a calibration file.\n\nPlease enter a value for theta. (theta must be a real number)'
    elif self.data_filename == False or self.data_filename == '':
      text = 'Please select a data file.\n\nPlease enter a value for theta. (theta must be a real number)'
    else:
      text = 'Please enter a value for theta. (theta must be a real number)'
    self.status_txt.delete(0.0, END)
    self.status_txt.insert(0.0, text)
    return
except:
  try:
    theta = float(self.theta_value.get())
    print('Half tip angle (degrees): ')
    print(theta)
    if self.cali_filename == False or self.cali_filename == '':
      if self.data_filename == False or self.data_filename == '':
```

```
            text = 'Please select calibration and data files.\n\nPlease enter a value for k. (k must be a real number)'
        else:
            text = 'Please select a calibration file.\n\nPlease enter a value for k. (k must be a real number)'
    elif self.data_filename == False or self.data_filename == '':
        text = 'Please select a data file.\n\nPlease enter a value for k. (k must be a real number)'
    else:
        text = 'Please enter a value for k. (k must be a real number)'
    self.status_txt.delete(0.0, END)
    self.status_txt.insert(0.0, text)
    return
except:
    if self.cali_filename == False or self.cali_filename == '':
        if self.data_filename == False or self.data_filename == '':
            text = 'Please select calibration and data files.\n\nPlease enter values for k and theta. (they must be a real numbers)'
        else:
            text = 'Please select a calibration file.\n\nPlease enter values for k and theta. (they must be a real numbers)'
    elif self.data_filename == False or self.data_filename == '':
        text = 'Please select a data file.\n\nPlease enter values for k and theta. (they must be a real numbers)'
    else:
        text = 'Please enter values for k and theta. (they must be a real numbers)'
```

```
        self.status_txt.delete(0.0, END)
        self.status_txt.insert(0.0, text)
        return
if text == None:
    text = 'Running...\n'
    self.status_txt.delete(0.0, END)
    self.status_txt.insert(0.0, text)
    root.update()

    ## calibration file ##
    cali_input = open(self.cali_filename, 'r')
    raw_cali_lines = cali_input.readlines()
    curve_num_words = str(raw_cali_lines[5]).split()          # Read the 6th line (remebering that indexing starts at 0) to identify
    index_curve_num = curve_num_words.index('=')              # the number of curves in the dataset and assign it to curve_num
    curve_num = curve_num_words[index_curve_num+1]
    try:
        curve_num = int(curve_num)
        print('Numbers of curves in Calibration: ')
        print(curve_num)
    except:
```

```
    print('Invalid data')
    print(curve_num)
  points_num_words = str(raw_cali_lines[18]).split()        # Read the 19th line to identify the number of points in each curve
  index_points_num = points_num_words.index('=')            # and assign to points_num
  points_num = points_num_words[index_points_num+1]
  try:
    points_num = int(points_num)
    print('Number of points per curve: ')
    print(points_num)
  except:
    print('Invalid data')
    print(points_num)
  cali_x = []
  cali_y = []
  for i in range(curve_num):
##      start_line_index = 19 + ((2*points_num)+7)*i                # Define start of curves using either APPROACH curves...
    start_line_index = 21 + points_num + ((2*points_num) + 7)*i     # ...or RETRACT curves
    cali_xi = []
    cali_yi = []
    for e in range(points_num):
```

```
        line_index = start_line_index+e
        words = raw_cali_lines[line_index].split()        # Separate the x and y data and assign to independant lists
        x = words[0]
        y = words[1]
        cali_xi.append(x)
        cali_yi.append(y)
    cali_x.append(cali_xi)
    cali_y.append(cali_yi)

## baseline calibration in y ##
cali_y_bl = []
remove_curves = []
for i in range(curve_num):
    min_index = [float(x) for x in cali_y[i]].index(min([float(x) for x in cali_y[i]]))     # Identify y data minimum (should be adhesive pull off)
    baseline_grads = []
    baseline_index = None
    for e in range(min_index, points_num):
        try:
            grad = (float(cali_y[i][e+5])-float(cali_y[i][e]))/(float(cali_x[i][e+5])-float(cali_x[i][e]))
            baseline_grads.append(grad)
```

```
        if grad < 0.05*mean(baseline_grads):             # Identify the point at which the gradient to the right of the minimum
          baseline_index = e                            # drops to 5% of the recorded average. This marks the start of
                                                        # the baseline
          break
      except:
        break
    if baseline_index == None:                          # If the baseline can not be identified the curve is discarded
      remove_curves.append(i)
      continue
    baseline = cali_y[i][baseline_index:points_num]
    baseline_value = mean([float(x) for x in baseline])   # The baseline value is the mean of the values right of the baseline index
    bl_cali = []
    for u in cali_y[i]:
      bl_cali.append(float(u) - baseline_value)       # Subtract the baseline value from all y data points and reassign to cali_y
    cali_y_bl.append(bl_cali)
  cali_y = cali_y_bl

  ## Normalise x data so that zero deflection occurs at distance zero ##
  cali_x_norm = []
  remove_curves.sort(reverse=True)
```

```
for i in remove_curves:                        # Remove x data for discarded curves
    del cali_x[i]
curve_num = curve_num - len(remove_curves)
print(curve_num)
remove_curves = []
for i in range(curve_num):
    min_index = [float(x) for x in cali_y[i]].index(min([float(x) for x in cali_y[i]]))
    if min_index > 0.650*points_num:
        remove_curves.append(i)                # Removes curve if minimum appears to be in the wrong place. Change limit as appropriate.
        continue
    baseline_inter = []
    for e in range(min_index):
        baseline_inter.append(abs(float(cali_y[i][e])))
    inter_index = baseline_inter.index(min(baseline_inter))     # Identify index of datum nearest x-intercept and calculate the local gradient
    inter_grad = (float(cali_y[i][inter_index])-float(cali_y[i][round(inter_index/2)]))/(float(cali_x[i][inter_index])-
float(cali_x[i][round(inter_index/2)]))
    if inter_grad > 0.0:
        print(i+1)
    try:
        intercept_x = float(cali_x[i][inter_index]) - float(cali_y[i][inter_index])/inter_grad      # Calculate x-intercept
```

```
    except:
        print('curve removed')
        remove_curves.append(i)
        continue
    norm_x = []
    print(intercept_x)
    for u in range(points_num):
        norm_x.append(float(cali_x[i][u])-float(intercept_x))       # Normalise data by subtracting x-intercept
    cali_x_norm.append(norm_x)
remove_curves.sort(reverse=True)
for i in remove_curves:
    del cali_y[i]                           # Remove any curves that could not be normalised
curve_num = curve_num - len(remove_curves)
print(curve_num)
cali_x = cali_x_norm
cali_grads = []
cali_inters = []
for i in range(curve_num):
    min_index = [float(x) for x in cali_y[i]].index(min([float(x) for x in cali_y[i]]))
    inter_cali = []
```

```
    for u in range(min_index):
        inter_cali.append(abs(float(cali_x[i][u])))            # Calculate gradient between the midway point of the repulsive curve and zero force
    inter_index = inter_cali.index(min(inter_cali))
    cali_grad_step = []
    for e in range(round(min_index/2), inter_index-5):
        grad = (float(cali_y[i][e+1])-float(cali_y[i][e]))/(float(cali_x[i][e+1])-float(cali_x[i][e]))
        cali_grad_step.append(grad)
    cali_grad = mean(cali_grad_step)
    intercept = float(cali_y[i][inter_index]) + (cali_grad*float(cali_x[i][inter_index]))
    cali_grads.append(cali_grad)
    cali_inters.append(intercept)
cali_grad = abs(mean(cali_grads))            # Take the mean of all the calibration gradients
cali_intercept = mean(cali_inters)
def_dis = 1/cali_grad                        # The conversion factor is the reciprocal of the mean gradient
print('Grads:')
print(cali_grad)
print(def_dis)
print(cali_intercept)

## plot calibration ##
```

```
## Create a .txt file containing the normalised data and a .gp for generating a .png figure through GNUPlot ##
filetime = str(time.gmtime()[0])+str(time.gmtime()[1])+str(time.gmtime()[2])+str(time.gmtime()[3])
if len(str(time.gmtime()[4])) == 2:
   filetime = filetime + str(time.gmtime()[4])
else:
   filetime = filetime + '0' + str(time.gmtime()[4])


cali_outfile = 'calibration_' + filetime + '.txt'
cali_out = open(cali_outfile, 'w')
lines = []
for i in range(curve_num):
   for e in range(points_num):
      linestring = str(cali_x[i][e]) + ' ' + str(cali_y[i][e]) + '\n'
      lines.append(linestring)
   lines.append('\n\n\n')
for line in lines:
   cali_out.write(line)
cali_out.close()
plot_file = 'plot_' + filetime + '.gp'
plot_out = open(plot_file, 'w')
```

```
        plot_out.write("\
set terminal pngcairo size 7020,4962 enhanced font',150'\n\
set output'calibration.png'\n\
set style data lines\n\
set key off\n\
set xlabel('Scanner Z (nm)')\n\
set ylabel('Deflection (nA)')\n\
set title('Calibration of AFM cantilever')\n\
set xzeroaxis lw 20\n\
set yzeroaxis lw 20\n\
set border lw 30\n\
set xrange[-700:300]\n\
set yrange[-1:12]\n\n\
plot\
")
        for i in range(curve_num):
          plot_out.write('\'' + cali_outfile + '\' i ' + str(i) + ' lw 30,\\\n')
        plot_out.write('-' + str(cali_grad) + '*x+' + str(cali_intercept) + ' lw 30')
        plot_out.close()
        text = 'calibrated\n'
```

```
self.status_txt.insert(END,text)
root.update()

## data file ##
## The data file is baselined and normalised in the same manner as the calibration file ##
data_input = open(self.data_filename, 'r')
raw_data_lines = data_input.readlines()
curve_num_words = str(raw_data_lines[5]).split()
index_curve_num = curve_num_words.index('=')
curve_num = curve_num_words[index_curve_num+1]
try:
   curve_num = int(curve_num)
   print('Numbers of curves in data: ')
   print(curve_num)
except:
   print('Invalid data')
   print(curve_num)
points_num_words = str(raw_data_lines[18]).split()
index_points_num = points_num_words.index('=')
points_num = points_num_words[index_points_num+1]
```

```
    try:
        points_num = int(points_num)
        print('Number of points per curve: ')
        print(points_num)
    except:
        print('Invalid data')
        print(points_num)
    data_x = []
    data_y = []
    for i in range(curve_num):
##          start_line_index = 19 + ((2*points_num)+7)*i
        start_line_index = 21 + points_num + ((2*points_num) + 7)*i
        data_xi = []
        data_yi = []
        for e in range(points_num):
            line_index = start_line_index+e
            words = raw_data_lines[line_index].split()
            x = words[0]
            y = words[1]
            data_xi.append(x)
```

```
        data_yi.append(y)
    data_x.append(data_xi)
    data_y.append(data_yi)

## baseline the DFL data ##
data_y_bl = []
remove_curves = []
for i in range(curve_num):
    min_index = [float(x) for x in data_y[i]].index(min([float(x) for x in data_y[i]]))
    baseline_grads = []
    baseline_index = None
    for e in range(min_index, points_num):
        try:
            grad = (float(data_y[i][e+5])-float(data_y[i][e]))/(float(data_x[i][e+5])-float(data_x[i][e]))
            baseline_grads.append(grad)
            if grad < 0.05*mean(baseline_grads):
                baseline_index = e
                break
        except:
            break
```

```
##              if baseline_index == None:
##                  remove_curves.append(i)
##                  continue
            baseline = data_y[i][baseline_index:points_num]
            baseline_value = mean([float(x) for x in baseline])
            bl_data = []
            for u in data_y[i]:
                bl_data.append(float(u) - baseline_value)
            data_y_bl.append(bl_data)

        ## Normalise x data so that zero deflection occurs at distance zero ##
        data_x_norm = []
##          remove_curves.sort(reverse=True)
##          for i in remove_curves:
##              del data_x[i]
##          curve_num = curve_num - len(remove_curves)
##          print(curve_num)
        remove_curves = []
        for i in range(curve_num):
            min_index = [float(x) for x in data_y_bl[i]].index(min([float(x) for x in data_y_bl[i]]))
```

```
##            if min_index > 650:
##                remove_curves.append(i)
##                continue

        baseline_inter = []
        for e in range(min_index):
            baseline_inter.append(abs(float(data_y_bl[i][e])))
        inter_index = baseline_inter.index(min(baseline_inter))
        inter_grad = (float(data_y_bl[i][inter_index+5])-float(data_y_bl[i][inter_index-5]))/(float(data_x[i][inter_index+5])-
float(data_x[i][inter_index-5]))
        if inter_grad > 0.0:
            print(i+1)
            print(data_y_bl[i][inter_index+5], data_y_bl[i][inter_index-5], data_x[i][inter_index+5], data_x[i][inter_index-5])
        intercept_c = float(data_y_bl[i][inter_index]) - float(inter_grad)*float(data_x[i][inter_index])
        try:
            intercept_x = -intercept_c/inter_grad
        except:
            print('curve removed')
            print(intercept_c)
            print(inter_grad)
```

```
##                remove_curves.append(i)
##                continue
            intercept_x = -intercept_c/0.02
        norm_x = []
        for u in range(points_num):
            norm_x.append(float(data_x[i][u])-intercept_x)
        data_x_norm.append(norm_x)
    remove_curves.sort(reverse=True)
##      for i in remove_curves:
##          del data_y_bl[i]
##      curve_num = curve_num - len(remove_curves)
##      print(curve_num)

    ## plot normalised data ##
    data_outfile = 'data_out_' + filetime + '.txt'
    data_out = open(data_outfile, 'w')
    lines = []
    for i in range(curve_num):
        for e in range(points_num):
            linestring = str(data_x_norm[i][e]) + ' ' + str(data_y_bl[i][e]) + '\n'
```

```
            lines.append(linestring)
         lines.append('\n\n\n')
      for line in lines:
         data_out.write(line)
      data_out.close()
      plot_data_file = 'plot_data_' + filetime + '.gp'
      plot_data_out = open(plot_data_file, 'w')
      plot_data_out.write("\
set terminal pngcairo size 7020,4962 enhanced font',150'\n\
set output'normalised_data.png'\n\
set style data lines\n\
set key off\n\
set xlabel('Scanner Z (nm)')\n\
set ylabel('Deflection (nA)')\n\
set title('Raw AFM deflection v. scanner Z')\n\
set xzeroaxis lw 20\n\
set yzeroaxis lw 20\n\
set border lw 30\n\n\
plot\
")
```

```
for i in range(curve_num-2):
    plot_data_out.write('\'' + data_outfile + '\' i ' + str(i) + ' lw 30,\\\n')
plot_data_out.write('\'' + data_outfile + '\' i ' + str(curve_num-1) + ' lw 30\n')
plot_data_out.close()
text = 'Normalised\n'
self.status_txt.insert(END,text)
root.update()

## convert data to force vs displacement ##
calibrated_y = []
for i in range(curve_num):                              # y data is converted from nA to nm using def_dis
    y_calibrated = []
    for e in range(points_num):
        y_calibrated.append(float(data_y_bl[i][e])*float(def_dis))
    calibrated_y.append(y_calibrated)
displacement_x = []
for i in range(curve_num):                                   # The cantilever deflection (now in nm) is
    calibrated_x = []                                      # subtracted from the displacement data
    for e in range(points_num):
        calibrated_x.append(float(data_x_norm[i][e]) + float(calibrated_y[i][e]))
```

```
    displacement_x.append(calibrated_x)
force_y = []
for i in range(curve_num):                              # The cantilever deflection is converted to force
    forces = []                                         # using the spring constant (k)
    for e in range(points_num):
        forces.append(float(calibrated_y[i][e])*float(k))
    force_y.append(forces)
truncated_x = []
for i in range(curve_num):
    min_index = [float(x) for x in force_y[i]].index(min([float(x) for x in force_y[i]]))
    forces_zero = []
    for e in range(min_index):                          # The data is truncated to only include repulsive contact
        forces_zero.append(abs(float(force_y[i][e])))
    force_zero_index = forces_zero.index(min(forces_zero))
    if force_y[i][force_zero_index] < 0:
        force_zero_index = force_zero_index - 1
    trunc_x = displacement_x[i][0:force_zero_index]
    truncated_x.append(trunc_x)

## plot force vs displacement curves ##
```

```
    calibrated_data_file = 'calibrated_data_out_' + filetime + '.txt'
    calibrated_data_out = open(calibrated_data_file, 'w')
    lines = []
    for i in range(curve_num):
      for e in range(len(truncated_x[i])):
        linestring = str(truncated_x[i][e]) + ' ' + str(force_y[i][e]) + '\n'
        lines.append(linestring)
      lines.append('\n\n\n')
    for line in lines:
      calibrated_data_out.write(line)
    calibrated_data_out.close()
    plot_calibrated_data_file = 'plot_calibrated_data_' + filetime + '.gp'
    plot_calibrated_data_out = open(plot_calibrated_data_file, 'w')
    plot_calibrated_data_out.write("\
set terminal pngcairo size 7020,4962 enhanced font',150'\n\
set output'converted_data.png'\n\
set style data lines\n\
set key off\n\
set xlabel('Distance (nm)')\n\
set ylabel('Force (nN)')\n\
```

```
set title('Calibrated AFM force v. distance')\n\
set xzeroaxis lw 20\n\
set yzeroaxis lw 20\n\
set border lw 30\n\n\
plot\
")
        for i in range(curve_num-2):
            plot_calibrated_data_out.write('\'' + calibrated_data_file + '\' i ' + str(i) + ' lw 30,\\\n')
        plot_calibrated_data_out.write('\'' + calibrated_data_file + '\' i ' + str(curve_num-1) + ' lw 30\n')
        plot_calibrated_data_out.close()
        text = 'Converted\n'
        self.status_txt.insert(END,text)
        root.update()

        ## calculate contact modulus ##
        ## By making x equal to (2 * d**2)/(pi() * tan(theta)) and gradient should be E* ##
        modulus_x = []
        theta = float(90-theta)*(math.pi/180)
        for i in range(curve_num):
            mod_x = []
```

```
        for e in range(len(truncated_x[i])):
            mod_x.append((2*float(truncated_x[i][e])**2)/(math.pi*math.tan(float(theta))))
        modulus_x.append(mod_x)

    ## modulus curves ##
    modulus_data_file = 'modulus_data_out_' + filetime + '.txt'
    modulus_data_out = open(modulus_data_file, 'w')
    lines = []
    for i in range(curve_num):
        for e in range(len(modulus_x[i])):
            linestring = str(modulus_x[i][e]) + ' ' + str(force_y[i][e]) + '\n'
            lines.append(linestring)
        lines.append('\n\n\n')
    for line in lines:
        modulus_data_out.write(line)
    modulus_data_out.close()
    plot_modulus_data_file = 'plot_modulus_data_' + filetime + '.gp'
    plot_modulus_data_out = open(plot_modulus_data_file, 'w')
    plot_modulus_data_out.write("\
set terminal pngcairo size 7020,4962 enhanced font',150'\n\
```

```
set output'distance_squared_plot.png'\n\
set style data lines\n\
set key off\n\
set xlabel('Distance squared (nm^2)')\n\
set ylabel('Force (nN)')\n\
set title('AFM force v. distance squared for the calculation of E*')\n\
set xzeroaxis lw 20\n\
set yzeroaxis lw 20\n\
set border lw 30\n\n\
plot\
")
    for i in range(curve_num-2):
        plot_modulus_data_out.write('\'' + modulus_data_file + '\' i ' + str(i) + ' lw 30,\\\n')
    plot_modulus_data_out.write('\'' + modulus_data_file + '\' i ' + str(curve_num-1) + ' lw 30\n')
    plot_modulus_data_out.close()

    ## use force_y and modulus_x to calculate E ##
    E_values = []
    for i in range(curve_num):
        E_steps = []
```

```
        for e in range(round(0.75*len(modulus_x[i])),round(0.90*len(modulus_x[i]))):
          grad = (force_y[i][e+5]-force_y[i][e-5])/(modulus_x[i][e+5]-modulus_x[i][e-5])
          E_steps.append(grad)
          if grad < 0.8*mean(E_steps):
            del E_steps[-1]
            break
        E_values.append(mean(E_steps))
      E_out_filename = 'E_value_' + filetime + '.txt'
      E_out = open(E_out_filename, 'w')
      for i in E_values:
        E_out.write(str(i) + '\n')
      E_out.close()
      text = 'Moduli calculated\n\nComplete\n'
      self.status_txt.insert(END,text)
      root.update()
def mean(nums):
  if len(nums):
    return float(sum(nums)/len(nums))
  else:
    return 0.0
```

```
# main

root = Tk()
root.title('AFM force/distance')
root.resizable(0,0)
app = Application(root)
root.mainloop()
```